2018

Coupling Radio Frequency Energy Via the Embedded Rebar Cage in a Reinforced Concrete Structure for the Purpose of Concrete Degradation Sensing

Ryan Campiz
University of North Florida, campiz.ry@gmail.com

[THIS PAGE IS INTENTIONALLY LEFT BLANK.]

COUPLING RADIO FREQUENCY ENERGY VIA THE EMBEDDED REBAR CAGE IN A REINFORCED CONCRETE STRUCTURE FOR THE PURPOSE OF CONCRETE DEGRADATION SENSING

by

Ryan Campiz

A thesis submitted to the School of Engineering

in partial fulfillment of the requirements for the degree of

Master of Science in Electrical Engineering

UNIVERSITY OF NORTH FLORIDA

COLLEGE OF COMPUTING, ENGINEERING, AND CONSTRUCTION

July, 2018

Certificate of Approval

The Thesis of Ryan Campiz is approved by: Date

Dr. Brian Kopp

Dr. Juan Aceros

Dr. Adel El Safty

Accepted for the School of Engineering by: Date

Dr. Osama Jadaan
Director of Engineering

Accepted for the College of Computing, Engineering, and Construction by: Date

Dr. William Klostermeyer
Interim Dean

Accepted for the University by: Date

Dr. John Kantner
Dean the Graduate School

Acknowledgements

This study would not have been possible without the Florida Department of Transportation (FDOT) — namely Randy Pierce and Ivan Laza. The Florida Department of Transportation supported this study with funding and guidance.

This work supported in part by the Defense Advanced Research Projects Agency under contract HR0011-15-C-0098.

This study was conducted under Dr. Brian Kopp, who was a wealth of knowledge and information in the RF and Communication fields and helped orient efforts in the most effective way possible — and whose patience is nothing short of a saint.

Moreover, Dr. O. Patrick Kreidl, Dr. Juan Aceros, Dr. Adel El Safty, and Dr. Nick Hudyma were all tremendously supportive and charitable with their knowledge and wisdom — Dr. Kreidl and Dr. Aceros for their expertise in electrical engineering topics, and Dr. El Safty and Dr. Hudyma for their expertise in civil engineering topics.

Moreover, UNF alumni Marshall Banks, Nick Telmosse, and Juan March were extraordinarily helpful with their mechanical knowledge and CNC skills.

Moreover, Jean Loos was overwhelmingly kind with her time and patience in her role as the head of the UNF Fabrication Lab, helping with foolish fabrication mistakes and advising how to correct them.

Moreover, Clifford Poppell was also overwhelmingly kind with his time and patience as a Teaching Lab Specialist and overall Jack of all trades.

Lastly, this project would not have been possible without Dr. Murat Tiryakioglu and all of his outstanding work as the previous director of the University of North Florida College of Computing, Engineering, and Construction.

Table of Contents

List of Figures

List of Tables

1 Abstract

This study focuses on utilizing an energy harvesting system in which a dedicated Radio Frequency (RF) power source transmits RF power via rebar in a reinforced concrete column. The RF power is received and decoupled by a receiver, and is then rectified, boosted, and stored as electrical energy in a supercapacitor, later to be used to make measurements, process data, and communicate to the source via rebar. Two design attempts are presented in this study: (a) one uses single line conduction at 2.4 GHz for RF power transfer; (b) the other uses a more conventional two-line conduction at 8.0 kHz for RF power transfer. Both designs were unsuccessful: (a) the 2.4 GHz attempt demonstrated that no detectable RF power propagated through the concrete medium; (b) the 8.0 kHz attempt demonstrated that too much of the RF power was attenuated through the concrete medium for the energy harvesting circuitry work properly. A potential third design approach is posited in the conclusion of this study. In addition to investigating power transfer designs, a study on the energy harvesting circuitry was performed. A Two-Stage Dickson Multiplier was utilized in conjunction with a Texas Instruments BQ25504 Ultra-Low Power Energy Harvesting Circuit. For these two components to function best, it was shown that the BQ25504's input filtering capacitor needed to be on the same order of magnitude as the charging capacitors of the Two-Stage Dickson Multiplier, otherwise, if the filtering capacitor was comparatively too large, it would short the output of the Two-Stage Dickson Multiplier. With that said, the lowest power input observed was at 7.83 dBm, but with lower input powers expected to be achievable. Nevertheless, since the second design attempt showed power losses were too significant, it was deemed that at present, unless the power transfer design were improved, then contemporary commercial off the shelf energy harvesting approaches are insufficient.

2 Introduction

In this section, the motivation of research is discussed, followed by a thesis objective.

2.1 Motivation of Research

All things decay with time — reinforced concrete is no exception. Over time, due to expected loads and weather conditions, concrete eventually loses its strength and begins to crack, and to control where these cracks happen, reinforced steel (rebar) is embedded in concrete so that when the concrete expands and contracts, the reinforced steel will favor cracks in some regions over others [1]. However, cracks are not always mild, nor are they always visible.

In the past 15 years, several microwave tower foundations of the Florida Department of Transportation Intelligent Transportation Systems (FDOT ITS) have needed rapid repair. During routine visual inspections, severe surface cracks in the foundations were identified, which precipitated the need for repair. In most cases, these towers are in or adjacent to the FDOT right of way, so if the surface cracks had not been visible above ground level and if the tower foundation integrity had been severely compromised, it is possible that one of these towers could have collapsed without warning, causing severe harm or death.

From a larger scope, the ageing infrastructure of the United States has received increasing attention from the American Society of Civil Engineers (ASCE). Since 1998, the ASCE has given a report card for the state of the infrastructure approximately every four years; their report card grades the infrastructure in several categories from Aviation, to Bridges, to Inland Waterways and more, and their grade scale is the conventional A-to-F scale. The overall infrastructure letter grade score has not risen above a D+ since 1998. [2] Given that much of the infrastructure is comprised of reinforced concrete, it is conceivable that if a reinforced concrete structure could internally sense its own degradation, a valuable layer of safety may be added.

One approach to sense the degradation of a reinforced concrete structure is to embed sensors into the structure during its construction. Indeed, the sensors need the ability to wirelessly communicate to an outside device so that data can be accessed; however, a more primary

concern is powering these devices. For these sensors to function at all, they must have sufficient energy to perform its required functions. However, such an energy reservoir for the lifetime of a concrete structure is not practical. Therefore, these devices need to be able to harvest their own energy.

Energy harvesting is an active area of research — two approaches exist: one approach harvests ambient RF energy, the other approach harvests RF energy from a dedicated source. For either approach, when the RF source is exterior to the concrete, the RF energy needs to penetrate the concrete surface, bypass the rebar scaffolding, and then be received by an embedded sensor; however, two key concerns with this approach is the attenuation of RF energy through the concrete medium and the reflection of the RF energy by the rebar scaffolding [3]. Consequently, an alternative approach is to use single line conduction via the rebar scaffolding in reinforced concrete. With single line conduction, RF energy is coupled onto the rebar where it is entrained onto the surface of the rebar as it propagates down the scaffolding [4] [5] [6]. With this approach, it was believed that less RF energy would be lost in single line conduction versus wave front propagation, due to the concentration of the RF energy along the surface of the rebar verses the propagation of an RF wave front spreading through the concrete.

It was the hope of this research that if the single line conduction approach seemed to be plausible, then an alternative approach to delivering RF energy to a remotely embedded sensor would be established. To study the approach, this study investigated the use of a coupling method devised by Georg Goubau to couple RF energy entrained onto a single line conductor, dividing the RF power transfer into two subjects: power transmission and signal transmission.

2.2 Thesis Objective

The objective of this thesis is to investigate the efficacy of the coupling method used to transfer to or receive RF energy from a rebar scaffold in a reinforced concrete structure. Specific targets of inquiry include understanding what effect concrete has on energy transmission in single line conduction and how well signals can be sent and received due to the nature of the concrete dielectric and the multipath configuration of the rebar scaffolding.

3 Background and Theory

In the sections below, some topics are discussed to provide context and foundation for the design that this study implements. One topic is the degradation of concrete; given that concrete acts as the medium through which the RF energy propagates, the degradation of this medium may significantly alter the RF energy transfer over time, and so its role must be understood sufficiently. Another topic included is single line conduction, which is the RF energy transfer approach that distinguishes this study from other conventions. Additionally, the energy harvesting methodology that this study implements will also be discussed; the way energy is harvested may influence the overall efficacy of the energy harvesting. Lastly, because this study ended up attempting two separate approaches for RF energy transmission, a discussion on two separate communication techniques will be included: spread spectrum communications and the Bell 103 modem.

3.1 Reinforced Concrete

For the purpose of this study, there are two issues of reinforced concrete that are carefully considered: the (a) fabrication and (b) degradation of concrete. Ultimately, this research is interested in the degradation of concrete; to understand this, the fabrication of concrete must be considered. Moreover, the fabrication of concrete needed to be understood and applied in this research study.

3.1.1 Fabrication

Concrete is essentially a mixture of cement, course aggregate, fine aggregate, and water. However, additional ingredients that aid flow without adding more water may be included, such as retardants and accelerators. Water hydrates the cement to form a binder paste. The proportions of the mixed ingredients determine the strength of the concrete the most importance of which is the water-to-cement ratio. Sometimes the mixture is so viscous that it is prevented from flowing into forms and fill completely, and so in this case, vibration may be used to settle the mixture. [7]

Reinforced concrete is the combination of concrete and reinforcing steel. The steel comes in the form of reshaped bars and reinforces the concrete by providing the tensile strength that concrete lacks. The reshaped bars have ribbed projections that have been rolled onto their surfaces to provide a better connection between the concrete and the steel. Smooth-surface bars are not used very often except for wrapping around longitudinal bars, primarily in columns. [8]

3.1.2 Degradation

Two processes that contribute to the degradation of reinforced concrete are carbonation and chloride attack. Carbonation was once believed to be the main cause of corrosion; however, after some time, chloride attack was recognized as more important for structures exposed to chloride environments. When concrete is fresh, the hydration products from the cement paste (like calcium hydroxide) yield a highly alkaline environment within the concrete medium, which provides a passive layer that forms on the steel and shields the material from corrosion attack. If this passive layer is sustained corrosion will not occur. From the exterior environment, carbon dioxide and moisture react with the hydration products at the concrete

surface: this yields calcium carbonate. This process is called carbonation, and, at first, carbonation is solely at the surface level; however, as time progresses and the concrete hydrates and dehydrates with weather conditions, carbon dioxide and moisture ingresses, and by consequence the carbonation region ingresses. Coupled with this is the ingression of chloride ions. Once the ingression of chloride ions and carbon dioxide meet the rebar surface, the corrosion process starts. After some time, corrosion products (iron oxides and hydroxides) accumulate and deposit into the concrete that immediately surrounds the steel, creating expansive stresses that crack and spall the concrete cover, which results in the degradation of the reinforced concrete. [9]

It is reasonable to expect that some aspects of concrete degradation vary regionally. For instance, for concrete structures that are located near coastlines, it is conceivable that chloride from the salty sea water is carried into the air or permeated through the soil, which then ingresses into the concrete structure. Similarly, for concrete structures that are located near cities, it is also conceivable that due to emissions from a higher population of automobiles that higher levels of carbon dioxide in the air and soil can be expected, and therefore a hastier degradation of the concrete structure can be expected. [10] [9]

3.1.3 Effects on EM Wave Propagation

Because this study is investigating an untried approach for RF energy transfer, other studies that investigated the conventional approach for RF energy transfer were reviewed.

One study did some preliminary work for wireless energy transfer by simulating wireless power transfer through reinforced concrete slabs. This study illustrated that the slab's thickness, humidity condition and rebar mesh size, or period, dominated the attenuation of electromagnetic (EM) wave propagation. The study considered EM waves in the 600 MHz to 1.3 GHz range and demonstrated that EM waves needed to be normally incident to the slab for maximum power transmission to be achieved. The study also demonstrated that the thickness of the concrete slab relative to the wavelength played a vital role in energy absorption, and that the periodicity of the rebar meshing played a vital role in the energy reflected and absorbed by the rebar. [3]

Another study measured results for complex permittivity of commonly used concrete walls under different hydration conditions. One measurement in particular recorded both the dielectric constant and loss tangent from 1 GHz to 3 GHz for solid concrete from 0 hours to 47 hours subsequent to initial hydration; the study demonstrated that over this time period the relative dielectric constant dropped from ~9.25 to ~8.2 at 2.4 GHz. [11]

The permittivity of concrete is important to know because when an RF wave traverses through the concrete medium and eventually confronts the dielectric medium of an RF coupling device, the mismatches in the permittivity of both mediums (which is equivalent to an impedance mismatch) can cause reflections to occur, which will reduce the overall power transfer of an RF wave. To reduce this mismatch, it is desirable to select material for the dielectric medium of the RF coupling device that closely resembles the permittivity of concrete.

3.2 Single Line Conduction

3.2.1 General Waveguide Fields

For any waveguide, the total field can be considered to consist of two fields: (1) the regular field and (2) the supplementary field. The regular field is the idealized version of the field for the intended propagation mode; the supplementary field completes the total field at regions where the total field deviates from the ideal: these are regions where the waveguide is excited or the waveguide geometry deviates from the ideal. The single line conductor is a special type of waveguide in which the supplementary field is a radiation field. The excitation of an open guide equates to a radiation loss, and any sudden bend of the conductor results in a radiation loss. [4] [5] [6]

For a coaxial cable, when a voltage is applied at a frequency that is below the cutoff frequency, the propagating electromagnetic wave in the coaxial line is considered to be in the transverse electric-magnetic (TEM) mode. In the TEM mode, the regular field is an electric field that is radial to the center conductor and the magnetic field is circumferential to the center conductor at every point in the coaxial cable; that is, both the electric and magnetic field are transverse (orthogonal) to the direction of propagation. Any deviation from this field at any point in the coaxial cable is considered to be due to the supplementary field that results from imperfections of the coaxial line, whether it be from the center conductor, the outer conductor, the dielectric material, and so on. [12] [4]

For a coaxial cable, when a voltage is applied at a frequency that is above the cutoff frequency, the propagating electromagnetic wave in the coaxial line is considered to be in the transverse magnetic (TM) mode. In the TM mode, the regular field is an electric field that is distributed along the surface of the center conductor in a sinusoidal like manner and is not orthogonal to the direction of propagation at every region of the coaxial cable, whereas the magnetic field is still circumferential to the center conductor at every point in the coaxial cable. Only the magnetic field is transverse to the direction of propagation. Any deviation from this field at any point in the coaxial cable is considered to be due to the supplementary field which results from imperfections of a coaxial line. [12] [4]

3.2.2 Single Line Conductor Waveguide Field

The waveguide field of the single line conductor behaves identical to the scenario where the coaxial cable has a voltage source applied to it with a frequency that is above the coaxial cable's cutoff frequency. The cutoff frequency of the coaxial cable occurs when the electric field does not radially extend from the center conductor to the outer conductor due to the relationship between (1) the applied frequency, (2) the dielectric medium, and (3) the radial distance between the center conductor and the outer conductor. When the frequency applied results in a characteristic impedance that is greater than that of the intrinsic impedance of the dielectric medium (which is similar to the impedance of free space), the coaxial cable no longer favors the TEM mode and instead favors the TM mode. One can also view this from the perspective of the wavelength becoming so small that the radial distance between the center and outer conductor is large in comparison. [12]

It's worth mentioning that the TM and TEM mode can both be present when the applied frequency is below the cutoff frequency; however, the TM frequency is not favorable when the applied frequency is to low, and so is very negligible until the cutoff frequency is approached and then surpassed. [12]

Viewed another way, one can do a thought experiment in which the outer conductor of the coaxial line grows radially, while the applied frequency, the diameter of the center conductor, and the relative permittivity between the conductors stays constant. As the outer conductor grows, the characteristic impedance of the coaxial transmission line also grows to a limit: the intrinsic impedance of the dielectric material. A visualization of this thought experiment is shown in Figure 1. [12]

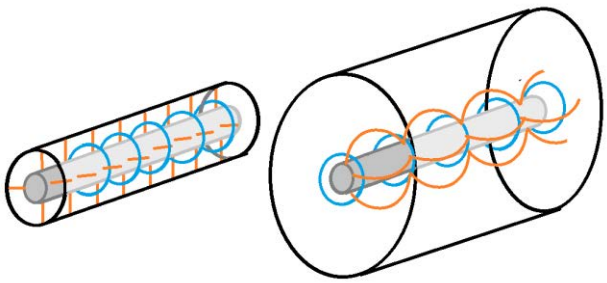

Figure 1. Visualization of TEM mode (left) and TM mode (right) — E-Field is orange, H-field is blue.

In an ideal coaxial cable with infinite conductivity, no dielectric material, and an applied frequency that is below the cutoff frequency, the regular field wave is in TEM mode. If the inner conductor is either coated with a dielectric layer or roughened, then the wave gains a longitudinal electric component, resulting in a superposition of the TEM and TM modes. If the diameter of the outer conductor becomes larger, then the amplitude of TEM mode decreases and eventually becomes negligible. Once the TM mode is the dominant mode, the outer conductor can be removed with no effect, since no electric field lines extend to the outer conductor. The result is single line conduction. The resulting wave traverses across the single line conductor as a surface wave in TM mode. [12] [4] [5] [6]

What's more, the single line conductor does not act as a typical waveguide. Typically, the ideal physical conditions for a waveguide are infinite conductivity and perfectly smooth waveguide surfaces. However, if a material like solid copper wire (high conductivity, smooth surface) were implemented as the single line conductor, it would not be suitable as a single line conductor waveguide. [4] [5] [6]

Alternatively, if the surface of such a conductor were coated with a dielectric or magnetic layer, then the desired boundary conditions for a single line conductor waveguide could be satisfied and single line conduction would result. The thickness of the layer would determine three (3) parameters: (1) the size of the field, (2) the phase velocity, and (3) the amount of energy propagated within the dielectric layer. When a dielectric coating is applied to the conductor surface, only a small amount of the energy is propagated within the coating, and so the dielectric losses are negligible in these conditions. [4] [5] [6]

Alternatively, rough surface conditions on conductors, like those conditions associated with threaded or twisted wires, can be sufficient to satisfy the boundary conditions required for the existence of the single line conduction. However, if the surface irregularities become too large, then the surface wave degenerates and is no longer the main carrier of the energy, resulting in significantly less propagation along the conductor. No matter how the boundary conditions are satisfied, there is only one wave mode guided by the single line conductor: the TM mode. [4] [5] [6]

3.2.3 Exciting the Single Line Conductor Waveguide Field

Whatever device that excites the RF TM surface wave should simulate the cross section of the RF TM surface wave. Any deviation from this distribution is compensated by a supplementary field and results in a radiation loss. A practical method of simulating the RF TM surface wave is by using a conical feedhorn. Considering the scenario of the coaxial line with the other conductor growing radially, it is easily understood why a conical feedhorn would be an excellent practice of simulating the RF TM surface wave. Starting with a coaxial line, the outer conductor gradually increases radially until it does not affect the field considerably. The field distribution then approaches that of the open line. Thus, the wave can be launched by means of a metal cone connected to the outside conductor of a coaxial feed line. The inner conductor of that line is connected to the surface waveguide. This device is referred to as a feedhorn, horn, or launcher. This study calls the developed device for the application in this study a TM Coupler. [4] [5] [6]

3.2.4 Power Losses

Losses of a single line conductor with a dielectric coating are primarily composed of three kinds of losses: conductivity losses, dielectric losses, and launching losses. Additional losses are introduced by supports, bends, and sags. Conductivity losses and dielectric losses are proportional to line length and can be calculated from the field distribution of the wave. Launching loss is independent of the line length and can be estimated by considering the fraction of the wave energy that travels within the area of the launcher's conical shaped aperture. Any launched wave energy outside this area will be lost. The ratio between the received energy and the total energy at the input determines the efficiency. An identical transmitting horn has the same efficiency, due to antenna reciprocity, so with the amount of energy input into the transmitting horn, launching loss can be determined. [4] [5]

The following set of statements summarize the key relationships for the three main sources of loss of a single line conductor with a dielectric coating along the single line conductor with one launcher at both ends:

- Conductivity loss increases little with increasing dielectric thickness. [4] [5]

- Dielectric loss increases much faster than conductivity loss. [4] [5]
- A small fraction of the energy is propagated in the dielectric for a coated single-line conductor. [4] [5]
- Dielectric loss is small compared with the conductivity loss — even for rather thick layers. [4] [5]
- Launching loss for a horn diameter decreases as dielectric thickness increases because the field is more concentrated. [4] [5]

3.2.5 A Note on Conductor Corrosion

In an experiment done by Goubau, a wire of diameter 2.6 millimeter (mm) and some length, L, was located outdoors for several months and had a thick corrosion layer on the surface. A power loss was measured to be 3.0 decibels (dB) across the transmission line. After the initial measurement was taken, most of the corrosion on the surface of the conductor was removed with sandpaper. A second measurement was then taken and resulted in an increase in power loss, with a new power loss of 3.6 dB recorded. The reason for the increase in power loss was posited to be due to an increase in the field extension due to the removal of the corrosion layer. Hence, Goubau believed that the corrosion played a key role in concentrating the field at the surface of the conductor. [4]

3.3 Energy Harvesting

A variety of energy harvesting circuit topologies were considered for this design. The stages for the selected energy harvesting circuit topology are: Impedance Matching, Voltage Rectification/Multiplication, Boosting, and Energy Storage.

3.3.1 Impedance Matching

For this application, the impedance matching network has two effects: (1) it minimizes reflections of RF power from the feedhorn to the source or load circuitry, and (2) it maximizes the power efficiency from the feedhorn to the source or load circuitry. Both effects are achieved by matching the real and imaginary components of the input impedance of the of the antenna to the source or load circuitry, which is typically 50 Ω. [13]

Maximum power transfer is necessary to achieve a sufficient voltage for the diodes in the rectifier to turn on. Maximum power transfer happens when minimum power is reflected. Minimum power is reflected when the resistive components on are equal, and the reactive components are of opposite sign. Failure to achieve this condition results in losses from power reflection and less-than-ideal power transfer from the matching circuit to the source or load circuitry. [13]

How well a matching network circuit performs depends on many factors such as component quality, chip manufacturing processes, size, and frequency; hence, no one option is not optimal for all applications. Implementing the matching impedance network can be a straightforward task using a Smith Chart. Different topologies manage the parasitic effects on the impedance in different ways. An inductor and capacitor network topology — known as an L-Network — can match a feedhorn to a rectifier circuit, canceling out stray reactance. What's more, at a specific frequency, it may appear as a resonant parallel inductive-capacitive or LC network, also known as a tank circuit, and may amplify the voltage. Other topologies known as Pi and T Networks can be implemented in ways that do not alter the final impedance but do alter the Quality Factor, potentially improving the passive voltage boost.

Inductor-Only Networks can be used when the otherwise LC matching network add much too much voltage boosting. Such a scenario happens when the load resistance is low and the antenna's radiation resistance is high. Inductor-Only Networks provide no voltage boosting, so such a topology may be useful in this scenario. What's more, Inductor Only Networks can be cheaper to manufacture and test, and they may be more efficient when paired with small resistance loads.

Similar to the Inductor-Only Networks, Transformer-based Networks make use of a pair of coupled inductors that perform voltage magnification as well as a resistive transformation. The resistive transformation is relative to their coil ratio via induction. What's more, by using an additional capacitor, the network can effectively be made into an LC network, which can provide both voltage step up and resistive matching. [14]

3.3.2 Voltage Rectifier/Multiplier

One study surveyed harvesting RF energy from the standpoint of Radio Frequency Identification (RFID) technology. In that study, rectifying the voltage was looked at closely. For a typical low power RFID system, the voltage levels after LC network matching are insufficient to drive Complimentary Metallic Oxide Semiconductor (CMOS) circuitry, so the voltage must be passed through a voltage multiplier. Voltage multipliers are often cascaded full wave rectifiers; hence, they simultaneously rectify AC voltage to DC voltage and then multiply the DC voltage to a higher voltage. Due to the voltage drop over the diode in the rectifier stages, the peak voltage at the input rectifier terminals is critical to the efficiency of the overall multiplier. Care must be taken that the number of cascaded multiplier stages is at the optimum point: too few stages and the output voltage will be insufficient, too many stages and the parasitic capacitance will detrimentally affect the preceding antenna matching. [14] [15]

The multiplier structure is potentially the most critical component of the RF energy harvester because it is where the largest source of unavoidable power loss happens. The multiplier is also the most difficult element to model, due to the nonlinear behavior. At high frequencies it can have unanticipated capacitive and resistive effects, causing changes to the behavior of the matching network and the downtream energy storage. Moreover, the diode threshold voltage affects the circuit performance. Its relationship to the peak voltage at the input of the rectifier determines the sensitivity and efficiency of the entire multiplier. Under extreme low power conditions, the diode threshold voltage is critical because providing insufficient input voltage results in starving the entire system of power. [14] [15]

3.3.3 Boosting

One group of researchers sought to harvest ambient RF energy at 2.4 gigahertz (GHz) and found that with -20 decibel-milliwatts (dBm) input power, the harvesting system could source 5.8 microjoules (μJ) into a rechargeable battery after 1 hour. In their design, the first and second stages are united: an antenna and RF rectifier are combined to form a “rectenna”. The second stage is the boost converter, which requires a cold startup at ultra-low input voltages, and then maintains high efficiency at useful output voltages. The fourth stage is an energy reservoir,

which accumulates energy from the rectenna until sufficient energy is available to run a meaningful load. [16]The same group of researchers continued their work and achieved an RF energy harvesting system that trickle charges a battery from incident power levels as low as -25 dBm at the feedpoint of an 8 decibels-isotropic (dBi) patch antenna. For this system the rectified voltages were low, so power management circuitry in the 100 millivolts (mV) range was necessary. To support this range the boost converter and battery charger circuitry were improved. The result was that at -25 dBm input RF power, the new harvesting system was able to source 150 μJ into a rechargeable battery after 1 hour. The study cautioned that boost factors up to 20 times may be required to convert rectified voltages as low as 40 mV to a useful voltage of 800 mV to run CMOS logic. [17]

3.3.4 Energy Storage

Supercapacitors have been identified as a reliable solution for use as energy storage. Performance of supercapacitors can be gauged by studying their position on the Ragone plot, which plots energy density versus power density [18]. A generalized Ragone plot can be seen in Figure 2.

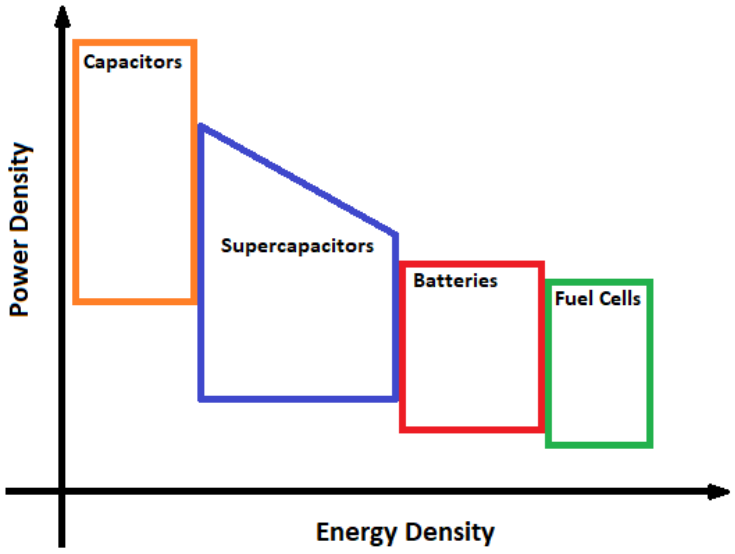

Figure 2. Generalized Ragone plot showing capacitors, supercapacitors, batteries, and fuel cells.

Supercapacitors are between ordinary capacitors and batteries on the Ragone plot, indicating higher power density than batteries and higher energy density than ordinary capacitors.

Moreover, supercapacitors do not undergo irreversible chemical reactions; hence, they have charge cycles in the order of millions. Supercapacitors require charging circuitry less complex than batteries; nevertheless, supercapacitors do have the zero-energy bootstrap problem, which is rooted in the system starting from a total lack of energy; hence, the energy harvester must generate enough energy to start from a voltage large enough for the system to operate steadily. [19]

3.4 Communications

This section discusses two separate modes of communication: Spread Spectrum Communications and the Bell 103 Standard. Two modes are discussed because during the study, it was realized that using higher frequencies was not suitable, and that lower frequencies were instead going to have to be used. The frequencies were so low, that Spread Spectrum Communications could not be used, so as an alternative the Bell 103 standard had to be adopted.

3.4.1 Spread Spectrum Communications

Spread spectrum communications is inherently able to attenuate interference. Spread spectrum communications have been applied to military antijamming tactics, guidance systems, and anti-multipath systems. A spread spectrum communications system works by using a code to spread the bandwidth of the data across more than the minimum necessary bandwidths and transmitting the resulting signal; a receiver that possesses the same spreading code and is synchronized de-spreads the signal and then estimates the resulting data. A few reasons for spreading the spectrum are for anti-jamming purposes, anti-interference purposes, low probability of intercept, multiple user random access communications with selective addressing capability, and high resolution ranging. [20]

In spread spectrum communications, how the spectrum is spread is crucial and categorizes the modulation of spread spectrum. In Direct Sequence Spread Spectrum (DSSS) modulation, a fast pseudo-random sequence causes phase transitions in the data. In Frequency Hopping Spread Spectrum (FHSS) modulation, the carrier frequency is shifted pseudo-randomly. Hybrid combinations of these techniques can also be implemented. [20]

The reason that this study is looking into spread spectrum communications, is so that multiple sensors can communicate at the same time without concern for when neighboring sensors communicate. The modulation of spread spectrum that this study considers is DSSS. Figure 3 shows a system overview for a DSSS system; it includes antennas, which will not be used in the communications tests in this research but for illustrative purposes have been included in the diagram.

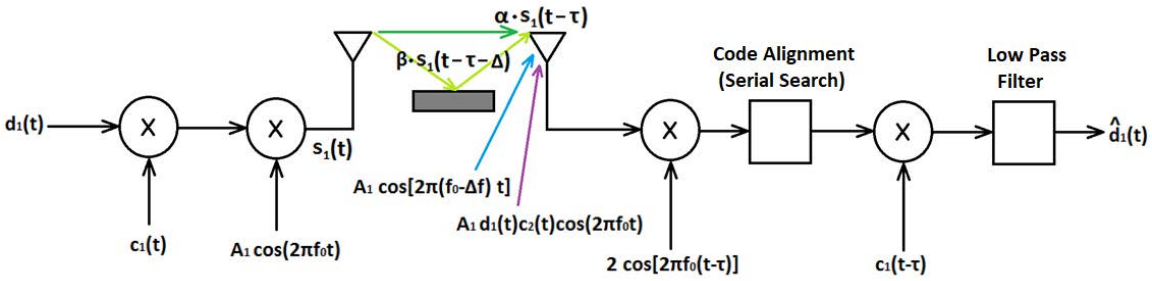

Figure 3. Simplified overview of direct sequence spread spectrum, assuming no channel noise.

3.4.1.1 Transmitter

On the left-hand side of Figure 3 a signal is inputted into the first mixer on the transmitter. This signal is a binary data stream and can be of a variety of pulse shapes. On the other input of the first mixer is a Gold Code, which is a special series of positive and negative ones that repeat indefinitely. [21]

The Gold Code is effectively pseudorandom noise. A Gold Code belongs to a family of other Gold Codes. Each Gold Code in the family spreads the waveform uniquely. The spreading of a waveform from one Gold Code is such that the spread waveform from another Gold Code in the same family will not interfere significantly with the other spread waveform. This allows for multiple signal transmissions to occur simultaneously. The Gold Code needs to be at a higher frequency than the data stream because the Gold Code chops up each pulse of the data stream. The chopping in the time domain means that in the frequency domain, the Gold Code spreads the binary data across the frequency spectrum. The significance of the spreading is not necessarily in the spreading itself but in the manner in which the waveform is spread. [21]

The second mixer on the transmitter side of Figure 3 translates the spread data to a higher frequency; in the frequency domain the same distribution of frequencies being transmitted are shifted to a higher center frequency (instead of 0 Hz). The resulting signal is transmitted across a medium. [21]

3.4.1.2 Receiver

On the receiver side of Figure 3, the first mixer re-shifts the data back to a DC center frequency. A code alignment module then performs a serial search to align the received data with its

internal clock phase. This is achieved by applying a delay of about a tenth of the Gold Code's chipping period, and then cross-correlating the delayed signal with the receiver's Gold Code; if the Gold Code contained in the signal is sufficiently in phase with the receiver's Gold Code, then the result of the cross-correlation should be essentially a DC value; if that condition is not met, then the signal is delayed again and the process repeats. After the signal is sufficiently delayed and the transmitted and received codes are synchronized, the resulting signal is run through a second mixer that de-spreads the data. A low pass filter then removes any higher order frequencies that resulted from the signal modulation and de-modulation. Finally, a receiver estimates the symbol that has been transmitted. [21]

3.4.2 Bell 103

The Bell 103 standard implements asynchronous data transmission and full-duplex operation over 2-wire lines at a baud rate of 300 bps, using frequency-shift keying (FSK) modulation. The standard is ideal for users that exchange files infrequently with other Data Terminal Equipment (DTE). The Bell 103 standard is known for performing well on the most challenging phone lines, as it is purported that communications workers would proclaim that Bell 103 modems would work on barb wire. [22]

4 Design

Two separate design approaches were made to address the problem posed in this thesis. Both approaches had the same basic structure, which can be summarized as follows:

- A coupling device receives electromagnetic power via the rebar
- Energy Harvesting circuitry harvests electromagnetic power via the coupling device
- Once sufficient energy is harvested, sub-circuitries are energized that perform a variety of tasks, such as:
    1. Receive or transmit communications
    2. Perform measurement on concrete
    3. Perform calculations on measurements

The design section of this thesis is segmented into two main subsections. One subsection is dedicated to the first design approach and one subsection is dedicated to the second design approach. The first design approach largely involves a horn referred to as a “TM Coupler”, which was employed to harvest RF power at 2.4 GHz. The second design approach largely circulates around a simpler coupling technique in which grounding clamps were utilized to harvest RF power at 8 kHz.

To discuss the first design approach, the first main subsection starts off with a discussion of the TM coupler design, and then proceeds into a discussion of the matching circuitry design, and then finally concludes with a discussion of the energy harvesting circuitry design. Additionally, a brief discussion is included at the end for the MCU SoC (System on a Chip) employed to simultaneously handle the computational and communications aspects of the design.

To discuss the second approach, the second main subsection starts off with the coupling technique employed for lower frequency operations, and then discusses the design of the energy harvesting circuitry,

4.1 First Design Approach: TM Couplers at 2.4 GHz

The first design approach involved the usage of a TM Coupler to achieve RF coupling. This approach utilized RF energy at 2.4 GHz. A basic overview is provided in the form of a schematic shown in Figure 4.

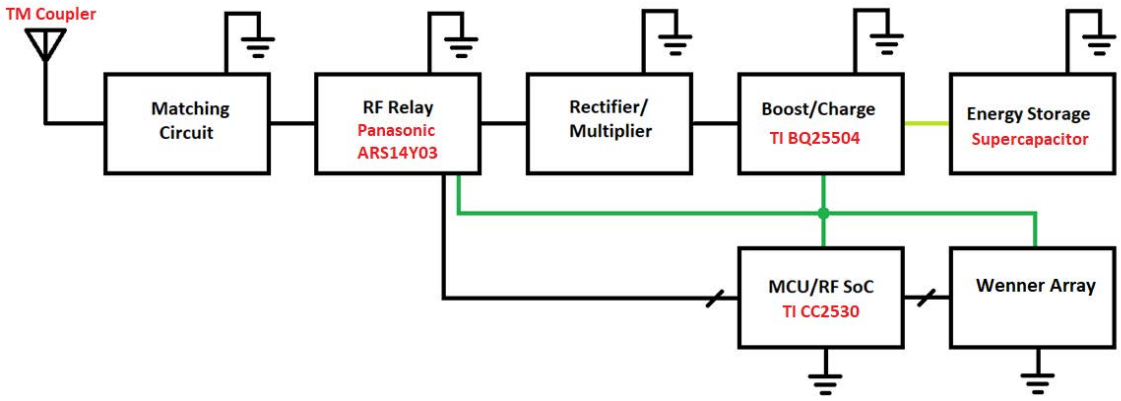

Figure 4. Overview of the entire remote sensor.

Referring to Figure 4, the TM Coupler can is represented symbolically as an antenna, which feeds into the matching circuit, which feeds into the RF relay circuitry. From there, there are two possible paths for the RF power to take: (1) the rectifier/multiplier, and (2) the MCU/RF System on a Chip (SoC). The first path is the only path intended for input RF power; this path is utilized for energy harvesting. The second path is utilized for output communications.

In the first path, the rectifier feeds into the Boost/Charge circuit, which in turn stores energy in the Energy Storage element. When sufficient energy is stored, the Boost/Charge circuit supplies energy to three circuits: the RF Relay circuitry, the MCU/RF Soc circuitry, and the Wenner Array circuitry.

The second path is reserved for power to flow towards the TM Coupler. When the system is not charging, the system interprets this as a communications-permitted state. Provided that adequate energy is stored in the storage element, the RF relay is permitted to engage, which allows the MCU/RF SoC to communicate via Spread Spectrum out through the TM Coupler. One status that would be communicated, for instance, is the measurement taken from the Wenner Array.

4.1.1 Design of the TM Couplers

The design of the TM couplers is covered with several subsections. First, the theory of the design is discussed. Then second, simulations of the design are discussed and third, the evolution of the design is discussed. In the fourth subsection, the fabrication of the design is discussed.

4.1.1.1 Theory of the Design

This section touches on the theory of the design of the TM coupler. The section starts off the theory by giving a brief introduction to single line conduction. Next, the purpose of the TM coupler is discussed, followed by the theoretical advantages of rebar as the single line conductor while immersed in concrete. Then some critical dimensions of the TM coupler are discussed. Finally, the dielectric medium within the TM coupler is discussed.

4.1.1.1.1 Purpose of the TM Coupler

The purpose of the TM Coupler is to couple the TEM mode within the coaxial cable to the TM mode on a single line conductor. The performance of single line conduction can be improved by reducing the phase velocity of the electromagnetic wave. This can be done by roughening the surface of the single line conductor, or by applying a dielectric coating to the surface of the single line conductor. Another way to improve performance of single line conduction is to reduce conduction losses by using a conductor with a large surface area (i.e. a large diameter conductor).

4.1.1.1.2 Theoretical Advantages of Rebar Immersed in Concrete

For this research specifically, the single line conductor is #5 rebar immersed in concrete. This implementation was believed to be advantageous for a few reasons. First, rebar has a rough surface, which is conducive to slowing down the phase velocity. Second, as time progresses, the rebar rusts when immersed in concrete; the rust acts as a dielectric, which slows down the phase velocity. A third reason it is believed to be advantageous is that the concrete is a dielectric medium, which slows down the phase velocity. A final reason is that relative to typical small gauge coaxial center conductors, #5 rebar is a fairly large conductor, which means that conduction losses will be smaller than if implemented with a typical smaller conductor.

4.1.1.1.3 Critical Design Dimensions for the TM Coupler

Almost all the RF power in single line conduction is confined, radially, within a half-wavelength (λ/2) distance away from the single line conductor. For this reason, when the radius of the outer conductor of the TM Coupler is increased to create the horn launcher structure, the radius need not exceed a distance much greater than λ/2, as can be seen in Figure 5. Moreover, the taper should not be sudden and provide at least a λ/2 distance for the electromagnetic field to transition from TEM to TM, as can be seen in Figure 5.

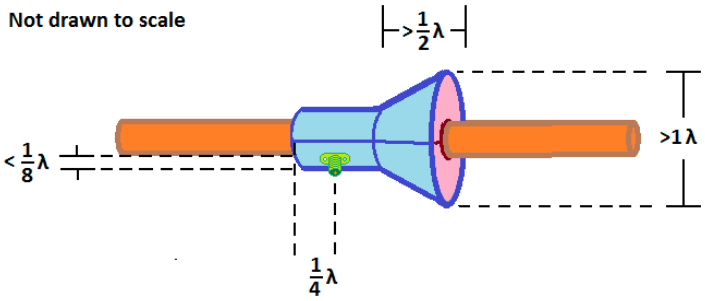

Figure 5. Pictorial representation of some critical dimensions for the TM Coupler.

The TM Coupler is to be conductively coupled to the single line conductor (the rebar). As can be seen in Figure 5, the TM Coupler has two regions: the cylindrical region and the conical region. The cylindrical region is where the TM Coupler is conductively coupled to the rebar. The point on the rebar at which the TM Coupler is conductively coupled to the rebar is referred to as the tap point. The location of the tap point on the TM Coupler is critical. Since the end of the cylindrical region is an end-cap, which reflects RF power, the tap point on the TM Coupler needs to be located a quarter wavelength (λ/4) distance away from the end to achieve constructive interference.

The λ/4 distance between the tap point and the end-cap allows for an effective total propagation distance of λ within the TM Coupler. During RF wave transmission, when the tap point radiates RF power onto the rebar, some of the RF wave propagates in the direction of the open aperture end, and some of the RF wave propagates in the direction of the end-cap. When the RF wave propagates from the tap point to the end-cap short-circuiting reflector plate, a λ/4 distance is traversed, which corresponds to a phase difference of 90°. Upon reflection, the polarity flips, increasing the phase by 180° (putting the phase at 270°). The remaining λ/4 distance back to

the tap point adds an additional 90° to the phase, causing the reflected wave to be in phase with and, therefore, to constructively interfere with a portion of the RF wave that is already propagating towards the aperture.

4.1.1.1.4 Dielectric Medium within the TM Coupler

Because the TM coupler will be embedded in concrete, the TM coupler needs to be able to survive in an environment of high pressure. To do this, a dielectric medium was chosen to tolerate such pressures. The dielectric medium that was chosen was polyvinyl chloride (PVC). When an electromagnetic wave propagates through any dielectric medium, the wavelength is going to be shortened according to Equation 1, where λ is the wavelength, f is the frequency, ϵ_r is relative permittivity of the material, and c is the speed of light.

$$c = \lambda \cdot f \cdot \sqrt{\epsilon_r} \tag{1}$$

The difficulty with PVC is that it's relative permittivity at 2.4 GHz is not readily available in research. After some experimentation, as shown in Appendix A – Refining the λ/4 Stub Distance and Determining the Permittivity of PVC at 2.4 GHz, at 2.4 GHz the relative permittivity was experimentally approximated to be 3.0969. Using this information, at 2.4 GHz in PVC the wavelength of an electromagnetic wave can be found to be approximately 7.0993 cm, compared to 12.4714 cm in air.

The shortening of the wavelength and a dielectric medium is advantageous for this application. Ideally, the TM coupler should take up as little space as possible. The effect of the wavelength shortening through the PVC medium means of the TM coupler must be reduced in size so that it can perform correctly.

4.1.1.2 Simulation of the Design

To gain an intuition about the general phenomena involved in single line conduction, a simulation of the TM coupler structure was performed in a High Frequency Structure Simulator (HFSS) software tool. The software tool allows the user to see the electric field and the magnetic field as animations. Furthermore, the software allows the user to see different planes of the electric or magnetic field (such as the XY plain, or the ρφ plane in spherical coordinates), and it allows the user to display the field as a heat map, vector field, or both. Additionally, the surface current can be displayed.

To acquire an indication of specifically how the RF wave would present when a single TM coupler perpendicularly tapped onto a length of rebar transmitted at 2.4 GHz, an HFSS simulation was run. The results are shown in Figure 6.

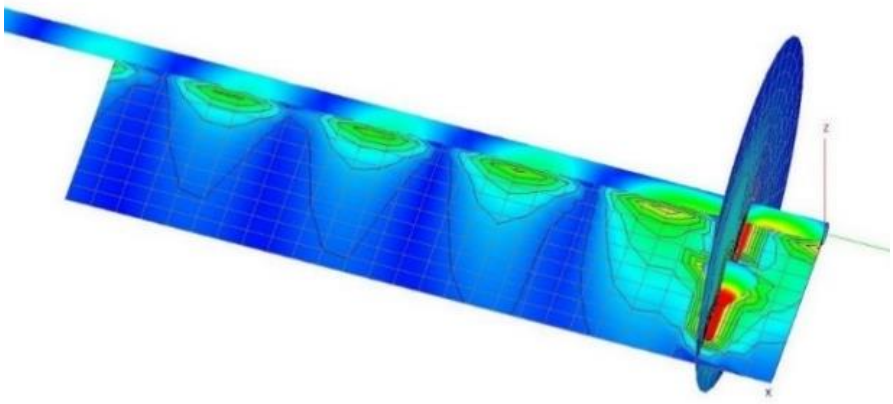

Figure 6. An HFSS simulation of one TM coupler perpendicularly tapped onto a length of conductor.

To acquire an indication of how the RF wave will be altered when an additional TM coupler terminated with a 50 Ohm (Ω) load was perpendicularly tapped onto the same length of conductor, the simulation was run, and the electric field was observed. A screenshot of the simulation can be seen in Figure 7.

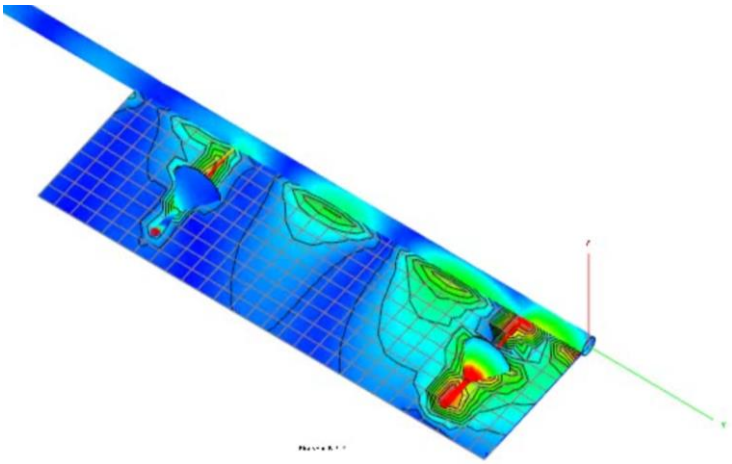

Figure 7. An HFSS simulation of two TM couplers perpendicularly tapped on the same length of conductor.

To acquire an indication of how the RF wave would present itself on a cage like structure, an HFSS simulation was run so that a voltage source at 915 megahertz (MHz) was attached to the top of one of the legs of the cage like structure, as can be seen in Figure 8. A frequency of 915 MHz was applied instead of 2.4 GHz because at the beginning of the study, it was assumed that thought that 915 MHz would be a suitable frequency from one of the Industry, Science, Manufacturing (ISM) bands, which are free for anyone to use without a license.

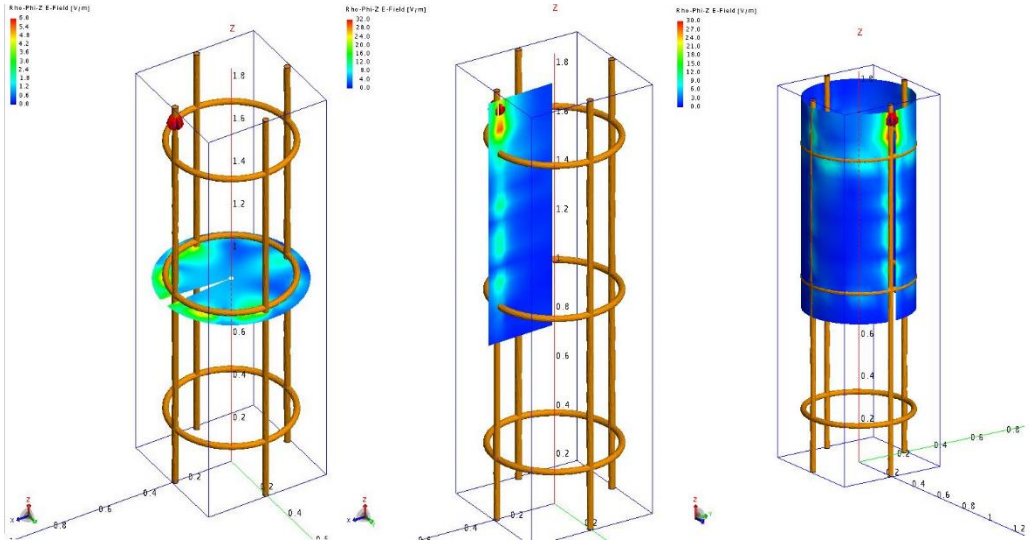

Figure 8. An HFSS simulation of the 915 MHz voltage source located at the top of one of the legs of a cage like structure.

The simulation provided a visualization for the lobe like repeating formations of the transverse magnetic (TM) mode of the electromagnetic field as it propagated down a conductor. The simulation also indicated a lobe length of λ/2. Furthermore, the simulation supported the theory that the electromagnetic field was, in fact, transverse magnetic; the HFSS software tool allowed for the electromagnetic field to be displayed in vectors (not shown in any of the figures above), which made visualizing the orientation of both the electric field and the magnetic field possible. Lastly, the HFSS software tool allowed for the user to see how the roughness of the surface of the conductor affected the formation of the TM mode surface wave by varying the number of triangular meshes that the simulation rendered for the conductor: the less triangles that were rendered, the rougher the surface would appear.

4.1.1.3 Evolution of the Design

A total of three versions existed for the TM coupler. In the subsections below, a more in depth summary will be given of each version of the TM Coupler.

The First Version was double-ended TM couplers, which was utilized for bidirectional RF transmission and reception. The Second Version served as a transition from the First Version to the Third Version; it was in the Second Version that the double-ended aspect of the design was changed to be single-ended. The Third Version became the final version, which was a single ended TM coupler that drew heavily from Goubau's work and provided unidirectional RF transmission and reception.

4.1.1.3.1 First Version

The TM Coupler started out as a double ended surface wave antenna. As shown in Figure 9, the TM coupler had the appearance of two cones facing away from each other while joined together from the pointed ends through a cylinder. The purpose of the shape of the TM coupler was to have the ability to transmit bidirectionally and allow waves originating at other couplers to pass through.

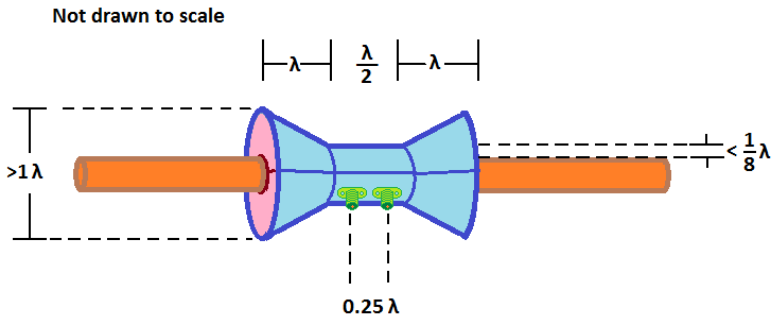

Figure 9. Conical TM Coupler Design (Not to Scale).

In theory, TM surface waves would propagate along the rebar surface until received by the TM Coupler. Once received, within the conical section of the TM Coupler, the TM surface waves would convert from TM to TEM. Within the cylindrical section, a portion of the RF power would be received by one of two tap points. Whatever RF power was not received by the tap points would then reconvert back to a TM wave RF power propagated through the rest of the TM coupler.

The TM coupler was tested by affixing two TM couplers on a single length of rebar, displaced from each other by several wavelengths as shown in Figure 10. Using a Vector Network Analyzer (VNA), the S-Parameters (S11, S12, S21, S22) were measured to evaluate the performance.

Briefly, the S-parameters are used to evaluate two important metrics: (1) the reflection coefficient at a port, and (2) the voltage gain through the two-port network. The S11 and S22 parameters respectively show the input port and output port reflection coefficient, which is a measure of how much power is reflected away from those ports. The S21 and S12 parameters respectively show the forward voltage gain and reverse voltage gain. [23]

Once the S-parameters were recorded, one of the TM couplers would then be displaced by a fraction of a wavelength, and a new set of S-Parameters would be recorded. Each measurement constituted a new test trial. The trials would be iterated until two wavelengths of distance had been traversed across the rebar, yielding a differential map of the S-Parameters with respect to

distance across the rebar. This provided fruitful data on the effects of distance between two TM couplers.

Figure 10. Experiment for the First Version of the TM coupler.

After performing several iterations of this test, the performance of both devices (in air and PVC) was deemed too poor to be of further interest. Ideally, the S11 and S22 parameters should tend towards negative infinity, and the S12 and S21 parameters should tend towards zero. The S11 and S22 parameters were close to 0 dB, which implied that a lot of the RF power supplied by the VNA was reflecting back into the VNA. Moreover, the S12 and S21 parameters were very low, which implied that a minimal amount of RF power was propagating across the rebar and being received by the other antenna. Additionally, the antenna appeared to be performing optimally near the 915MHz band, which was not the intended 2.4 GHz frequency, as shown in Figure 11. Consequently, a new design was sought.

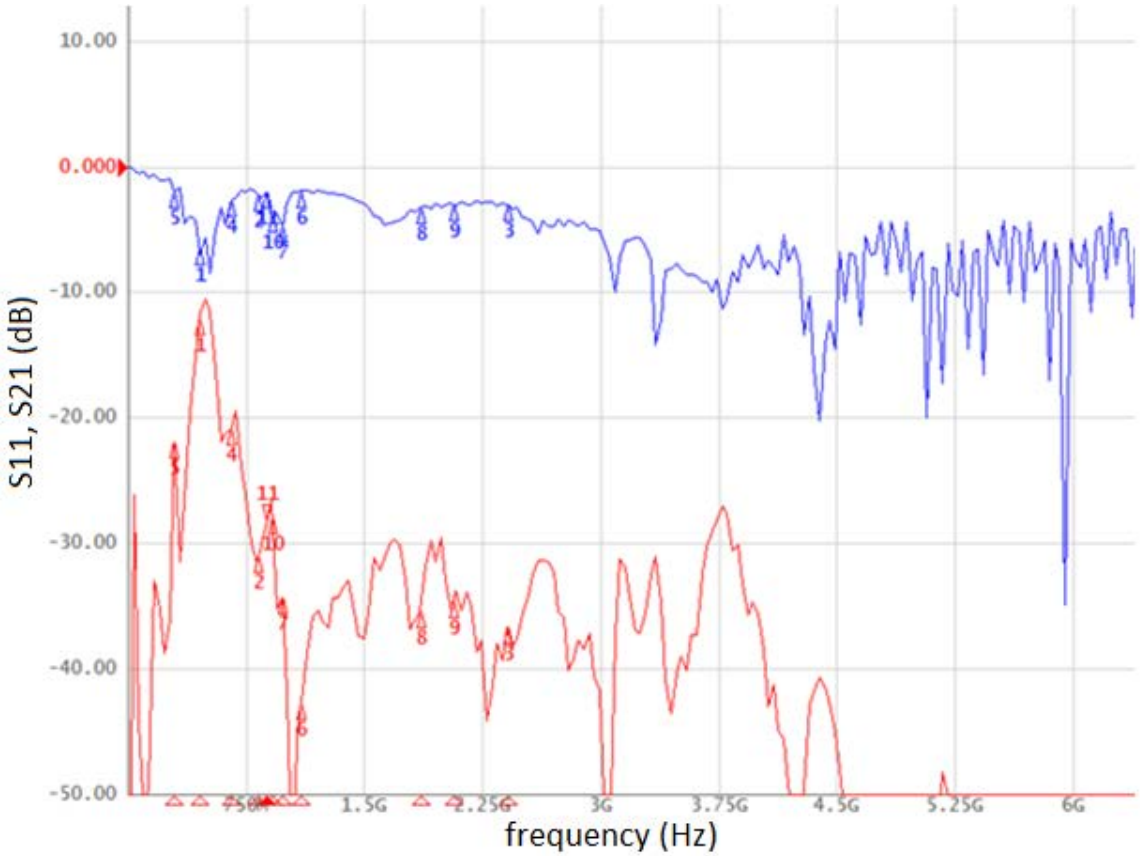

Figure 11. Results of the S11 (blue) and S21 (red) parameters for a First Version TM coupler with a PVC dielectric medium; note that the units of the x-axis is frequency and the y-axis is unitless.

4.1.1.3.2 Second Version

The length of the First Version TM coupler was about 2.5 λ: because the length was a multiple of a half-wavelength, it was posited that the length of the TM Coupler was somehow causing destructive resonance. To test this, two TM couplers were sacrificed in an experiment in which the conical sections would be iteratively shortened; for each iteration, the S_{11} parameter would be monitored — a conceptualization of the iterations is shown in Figure 12. As the TM Couplers were iteratively shortened, however, the performance did not change. Once the experimentation reached Iteration 4 and the performance showed no signs of improvement, some time was given to experiment with the set-up of the TM Coupler.

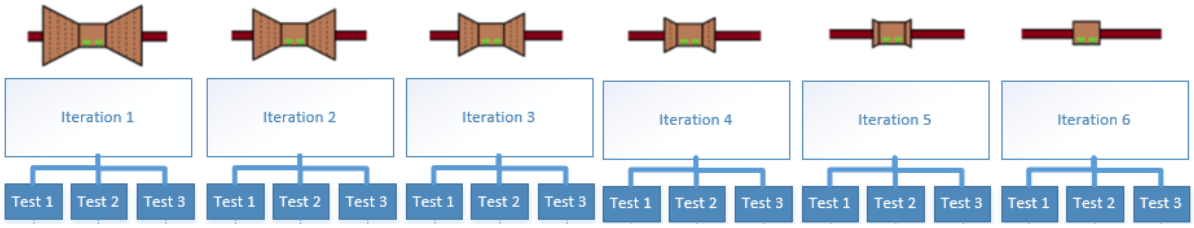

Figure 12. Conceptualization of iteratively cutting down the TM coupler.

Inspired by the work of Georg Goubau, the smaller version of the TM coupler was modified to imitate the configuration presented in his work, an example of which is shown in Figure 13.

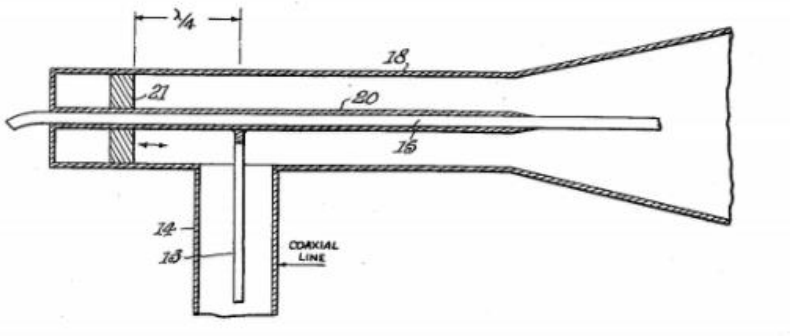

Figure 13. Goubau Cone from Georg Goubau's patent [5]

It was noticed that both tap points were approximately a λ/4 distance away from the adjacent aperture. To exploit this, a piece of copper tape was applied to one end of the TM coupler so that the whole face of the aperture was completely covered by copper tape, creating an end-

cap that would induce reflection. The TM coupler was then affixed to the very end of the rebar so that the rebar slid into the open aperture of the antenna until the rebar made contact with the copper tape in the back of the antenna. With this configuration, the S11 parameter increased dramatically. This observation gave rise to the next version of the TM Coupler, which can be seen in Figure 14, which modified the First Version by cutting off most of one of the conical sections, covering the aperture with copper, and then affixing the TM coupler to the end of the rebar.

Figure 14. The Second Version of the TM coupler.

The performance of this revision was substantially better than the prior revision. As can be seen in Figure 15, at 2.4 GHz the S12 and S21 parameters were approximately -15 dB, and the S11 and S22 parameters were also approximately -15 dB.

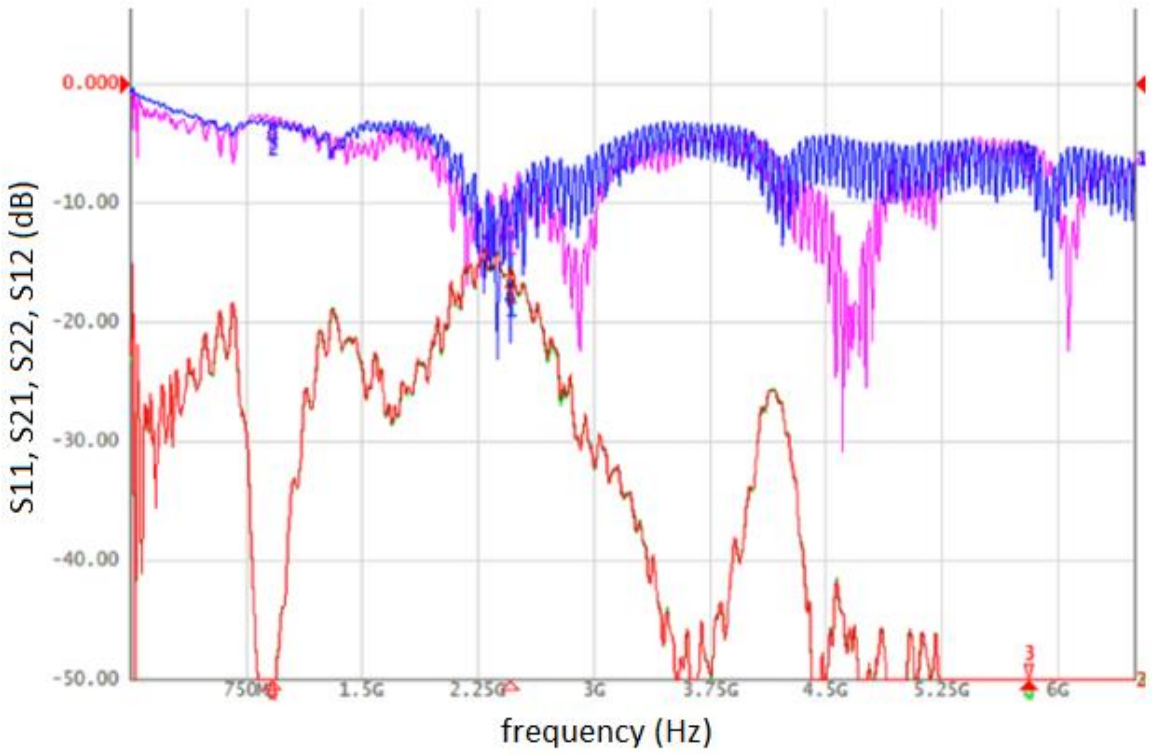

Figure 15. Results of the S-Parameters for revision one; S21 (red), S12 (green), S11 (blue), and S22 (pink) can be seen; note that the unit of the x-axis is frequency (Hz), and the y-axis is unitless.

4.1.1.3.3 Third Version

The Third Version of the TM coupler was similar to the Second Version of the TM coupler with the following exceptions: the complete removal of the cone from one side; the addition of an end-cap reflector plate on the rear of the TM coupler; the removal of the extra tap point; the repositioning of the remaining tap point to preserve the λ/4 distance between the tap point and end-cap reflector plate; the usage of a matching circuit to transform the TM Coupler input impedance as close to 50 Ω as practical; and the implementation of a new method to conductively connect the TM coupler to the rebar.

Figure 16. Fabrication (left) & implementation (right) of the Third Version TM coupler

Five TM Couplers were made in total for Experimentation, and can be seen in Figure 17

Figure 17. Five Third Version TM Couplers made for the Experiments.

The new method of conductively connecting the TM coupler to the rebar involved a filed down standoff. The threads of a standoff were filed down until a stub remained. The remaining stub was then soldered into the solder cup of a Sub-Minature version A (SMA) connector, allowing the fabrication of the TM coupler to be completed. This can be seen, in part, in Figure 18. Once the fabrication of the TM coupler was completed, the TM coupler could be affixed to the rebar.

Figure 18. Filed down standoff soldered in SMA connector (left), and finished half of TM coupler prior to affixing to rebar.

In order to affix the TM coupler to the rebar, a hole needed to be drilled into the rebar radially through the center. The diameter of the hole needed to be large enough to accommodate and Metric size 2 (M2) bolt, which would be used to mate one half of the TM coupler to the rebar, as shown in Figure 19. On the side of the rebar where half of the TM coupler affix to it, the hole needed to be countersunk such that the standoff protruding from the TM Coupler could fit in to the rebar.

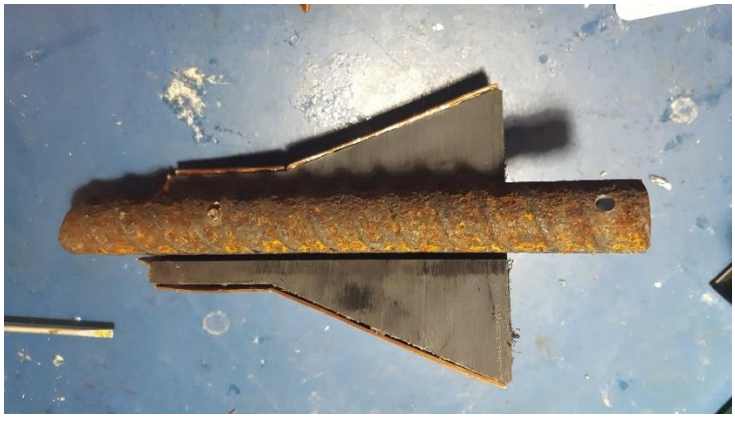

Figure 19. Using and M2 bolt to affix one half of the TM coupler to the rebar.

4.1.2 Design of the Matching Circuit

A Matching Circuit is necessary to match the input impedance of the TM Coupler to 50 Ω. On the transmitter end, a 50 Ω source will be used and at the receiver a 50 Ω load will be present. Therefore, whether being used as a transmitter or as a receiver, the TM coupler will need to be matched to a 50 Ω circuit. This is done to achieve maximum power transfer.

As can be seen in Experiment 1, the input impedance of the TM coupler had some variance, which is to say that input impedance of one TM Coupler would vary from one TM Coupler to the next. For instance, if a TM Coupler were selected from a group of TM Couplers at random, the input resistance of the randomly selected TM coupler would vary from, approximately, 30 Ω to 60 Ω; whereas the input reactance of the TM coupler would vary from, approximately, 90 Ω to 130 Ω. After some experimentation, a low pass Pi-Network was chosen to match the input impedance of the TM coupler to 50 Ω.

Due to the variance of the TM coupler's input impedance, an ideal solution could not be expected. It was impractical to construct a matching circuit for each TM coupler, so only one matching circuit was made, which meant that the matching circuit needed to sufficiently match each TM coupler to 50 Ω. Trade-offs between the performance of each TM coupler and matching circuit were anticipated.

4.1.2.1 Modeling the Matching Circuit and TM Coupler

Figure 20 depicts the circuit model used to match the TM coupler. Given that the input impedance of the TM coupler varies, the midpoint of the extremes of the variance for both the resistive and reactive components were selected: for the resistive component, 45 Ω was selected; for the reactive component, 110 Ω was selected. As shown in Figure 20, a series resistor and inductor were used to model this coupler impedance.

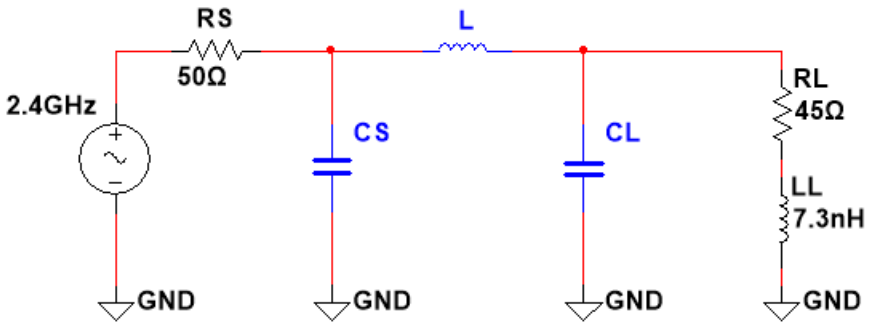

Figure 20. Circuit model used for the matching circuit and TM coupler.

Once the matching circuit is implemented, the input impedance, Z_{in}, is the impedance looking into the matching circuit (from the CS capacitor) and can be calculated using the formula shown in Equation (2).

$$Z_{in} = \left(\left((R_L + jX_L) \parallel \frac{1}{j\omega C_L} \right) + j\omega L \right) \parallel \frac{1}{j\omega C_S} \qquad (2)$$

4.1.2.2 Implementing the Matching Circuit

Using the Impedance Matching Network Designer calculator in [24], values for C_S, L, and C_L were found using the following input assumptions for the calculator: a Q-factor of 3, an input frequency of 2.4 GHz, an input resistance of 50 Ω, a load resistance of 45 Ω, and a load reactance of 110 Ω. The calculator produced a C_S of 3.98 picofarads (pF), and an L of 3.60 nanohenries (nH), and a C_L of 2.18 pF. The results of this circuit were used as a starting point to populate a matching circuit with the given circuit values.

4.1.2.3 Fabricating the Matching Circuit

Using a single-sided Printed Circuit Board (PCB) sheet, a matching circuit was created as shown in Figure 21. Using 0603 sized components, the matching circuit in Figure 19 was implemented. To conserve as much space as possible, the shunt capacitors were soldered in between the SMA ground pin and the trace originating from the SMA signal pin. The circuit, moreover, was intended for other matching circuit topologies, hence the extra pads for a center shunt component and an extra series component. For testing, the input labeled as “In” would

be connected to the VNA, which registered as a 50 Ω source; the input labeled is “Out” would be connected to the TM Coupler.

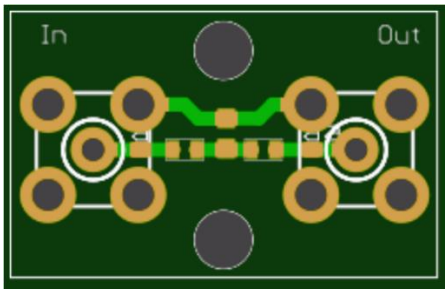

Figure 21. CAD of traces for Matching Circuit PCB

4.1.2.4 Correcting the Matching Circuit

When the matching circuit was implemented, it wasn’t registering as a 50 Ω input impedance on the VNA. After further inspection, it was noticed that when a finger was applied to the SMA pins on the “In” input of the matching circuit, the input impedance would approach 50 Ω This change was interpreted as adding shunt capacitance to the input. After some further iterative experimentation, the CS and CL capacitor values were slightly changed, eventually leading to of a new CS of 5.0pF and new CL of 1.4pF.

4.1.2.5 Design of the Energy Harvesting Circuitry

The energy harvesting segment of the overall design is composed of three stages: the rectifier/multiplier stage, the boost/charge stage, and the energy storage stage. The rectifier stage effectively turns the TM coupler and Matching Circuit pair into a rectenna, which allows for RF power to be rectified so that the energy can be stored at a later stage. The Direct Current (DC) voltage that the rectenna creates is entirely dependent on the input power received by the TM coupler. The input power will vary greatly and consequently the rectified voltage will vary greatly. Hence, a boost stage is needed to increase the rectified voltage so that the energy storage stage can be charged even at lower input power levels from the TM coupler.

4.1.2.6 Circuitry Overview

The first stage of the energy harvesting circuitry is the two-stage Dickson multiplier [14]. The Dickson multiplier rectifies and multiplies the input 2.4GHz voltage input into a DC voltage

output. The rectification process takes several Alternating Current (AC) cycles of the input to stabilize to a steady DC Voltage output. At 2.4 GHz this happens quickly, on the order of tens of microseconds after starting as shown in Figure 23. The second stage is an ultra-low power boost converter, which uses the energy provided by the Dickson Multiplier to trickle charge a Supercapacitor (the third stage of the energy harvesting circuitry). This study uses a BQ25504 ultra low power boost charger, which, in addition to boosting the rectified input voltage, also manages the supplied energy, having the ability to divert energy from the supercapacitor to a load circuit [25]. The rectified voltage needs to exceed a threshold voltage for the BQ25504 boost converter to begin trickle charging the supercapacitor.

4.1.2.7 Rectifier Circuitry

In brief, the Dickson Multiplier accumulates charge, and thus accumulates voltage, during the negative part of each cycle of the input voltage. On the positive part of the cycle, the voltage drop is distributed over some number of capacitors and some number of diodes; on the negative part of the cycle, the voltage drop is in the opposite direction and is distributed across half as many capacitors but the same number of diodes. Hence, on the negative cycle, one group of capacitors has double the voltage applied to it then during the positive cycle, and hence accumulates a small amount of extra charge that produces a small voltage directed in the positive cycle direction. On the next positive cycle the additional amount of voltage from the prior cycle contributes to the overall voltage at the output. The process for a single stage Dickson Multiplier can be seen in Figure 22. The voltage vs. time curve of a three stage Dickson multiplier can be seen in Figure 23.

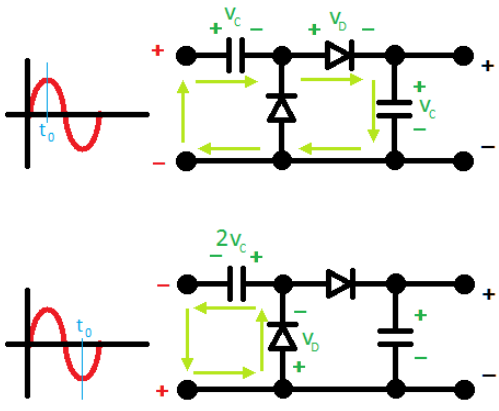

Figure 22. Positive and Negative Cycle of Single Stage of Dickson Multiplier.

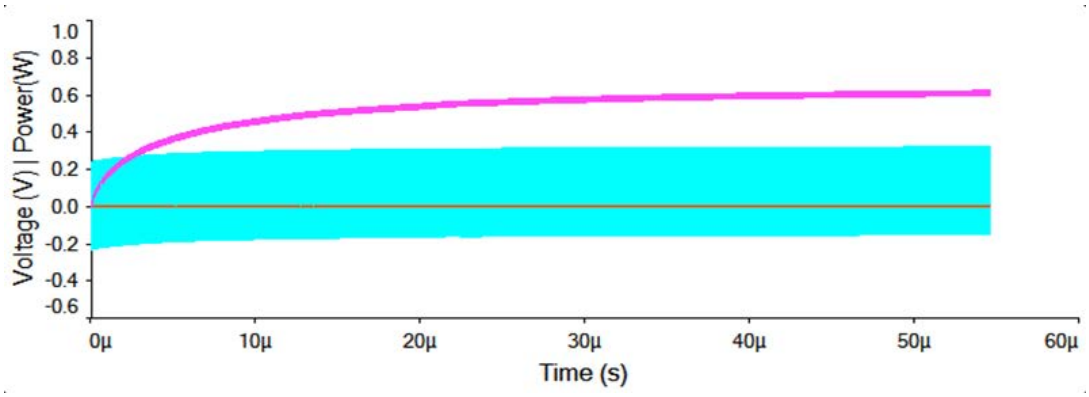

Figure 23. Voltage vs. Time Curve of a Three Stage Dickson Voltage Multiplier.

4.1.2.8 Boosting Circuitry

Texas Instruments' BQ25504 integrated circuit, which functioned as an ultra low-power boost converter with battery management for energy harvesting, was implemented into the design. This integrated circuit takes a lower input voltage and boosts the voltage to a higher level so that internal circuitry can charge an energy reservoir (i.e. super capacitor, electrolytic capacitor, lithium-ion battery). A Maximum Power Point Tracking (MPPT) sampling network is used to optimally charge the energy reservoir. Figure 24 shows an example schematic of the BQ25504 implemented with a general input power source. In Figure 24, several biasing resistors can be seen, namely the open circuit biasing resistors R_{OC1} and R_{OC2}; the overvoltage protection resistors R_{OV2} and R_{OV1}; the undervoltage protection resistors R_{UV2} and R_{UV1}; and the battery okay biasing resistors R_{OK1}, R_{OK2}, and R_{OK3}. The boosting inductor can also be seen, which is used in the switching circuitry to boost the input voltage to a sufficiently high level to charge the battery. Additionally, some bypassing capacitors can be seen as C_{HVR}, C_{BYP}, and C_{STOR}. The storage element in this example implementation is depicted as a battery. An output signal, V_{BAT_OK}, can be seen on the right-hand side of the diagram; this output signal is a logic high when the battery has been sufficiently charged and is a logical low when the battery has either (A) not yet been sufficiently charged or (B) has been discharged to the undervoltage level.

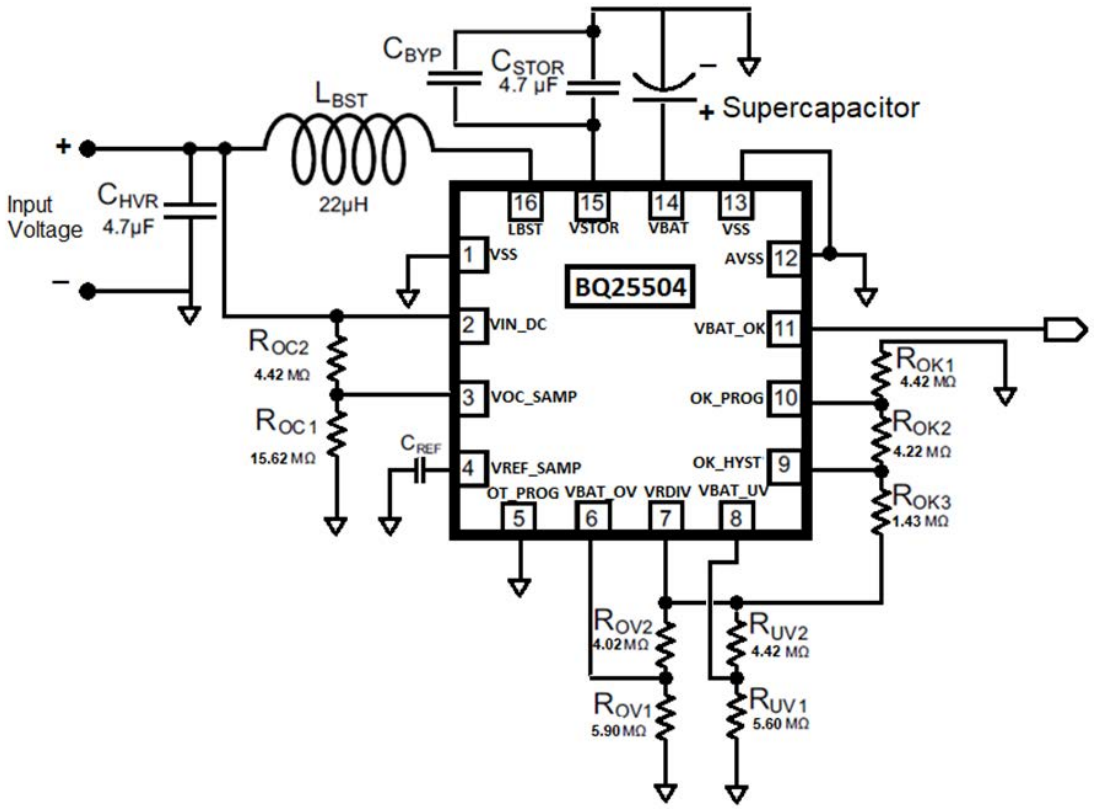

Figure 24. Diagram of the BQ25504 implemented with a general input power source [25].

The integrated circuit functions using an MPPT sampling network to optimize power transfer into the BQ25504. The biasing resistors ROC2 and ROC1 are implemented such that the series resistance across the two resistors is 20 MΩ, but the voltage at the node in between the two resistors is used to set the Maximum Power Point (MPP) percentage of the MPPT sampling network. The MPP percentage corresponds to the percentage of the open circuit voltage of the voltage source (e.g. the Dickson Multiplier) that is sought after when the BQ25504 is receiving power. The BQ25504 achieves the MPP percentage by adjusting its input impedance to achieve the set MPP percentage, which was set with the ROC1 and ROC2 biasing resistors. Recall that the output of the voltage source is connected to the VIN_DC pin. The device samples the open circuit voltage at the VIN_DC pin and retrieves the MPP voltage from the VOC_SAMP pin.

In practice, some devices operate better at particular MPPs than other devices (for instance, a solar cell might operate better at 80% of the MPP, while a thermoelectric generator might

operate better at 50% of the MPP). The exact MPP ratio can be changed by altering the values of ROC1 and ROC2.

The BQ25504 needs at least a 330 mV to cold start the circuit — if the voltage is substantially less than 330 mV, then the circuit will not begin charging. In addition, if the input power is insufficient, then it is likely that the cold start circuit will not raise the VSTOR voltage and begin charging; the datasheet indicates that the minimum power into the device is 0.01 mW (-20 dBm).

4.2 Second Design Approach: Grounding Clamps at 8 kHz

The second design approach involved the use of several pairs of grounding clamps: one pair of grounding clamps was for the transmission of power from a device called a charger/interrogator (CI), all other pairs of grounding clamps were for the reception of power per each embedded Remote Sensor (RS). For energy transmission, this approach utilized RF power at 8.0 kHz. This approach did not utilize the same theory as the first design approach. The first design approach relied on the transmission of power via single line conduction, but this approach used an approach closer to common two-line conduction.

For power transmission, as shown in Figure 25, using two legs from the rebar cage, the CI used one pair of grounding clamps affixed to these legs to supply power, and per each RS another pair of grounding clamps would be affixed to the same two legs (matching the polarity of the grounding clamps of the CI). For communications, using the same two legs from the rebar cage, Bell 103 Communications were used, with the CI acting as the originating comms, and the RSs acting as the answering comms.

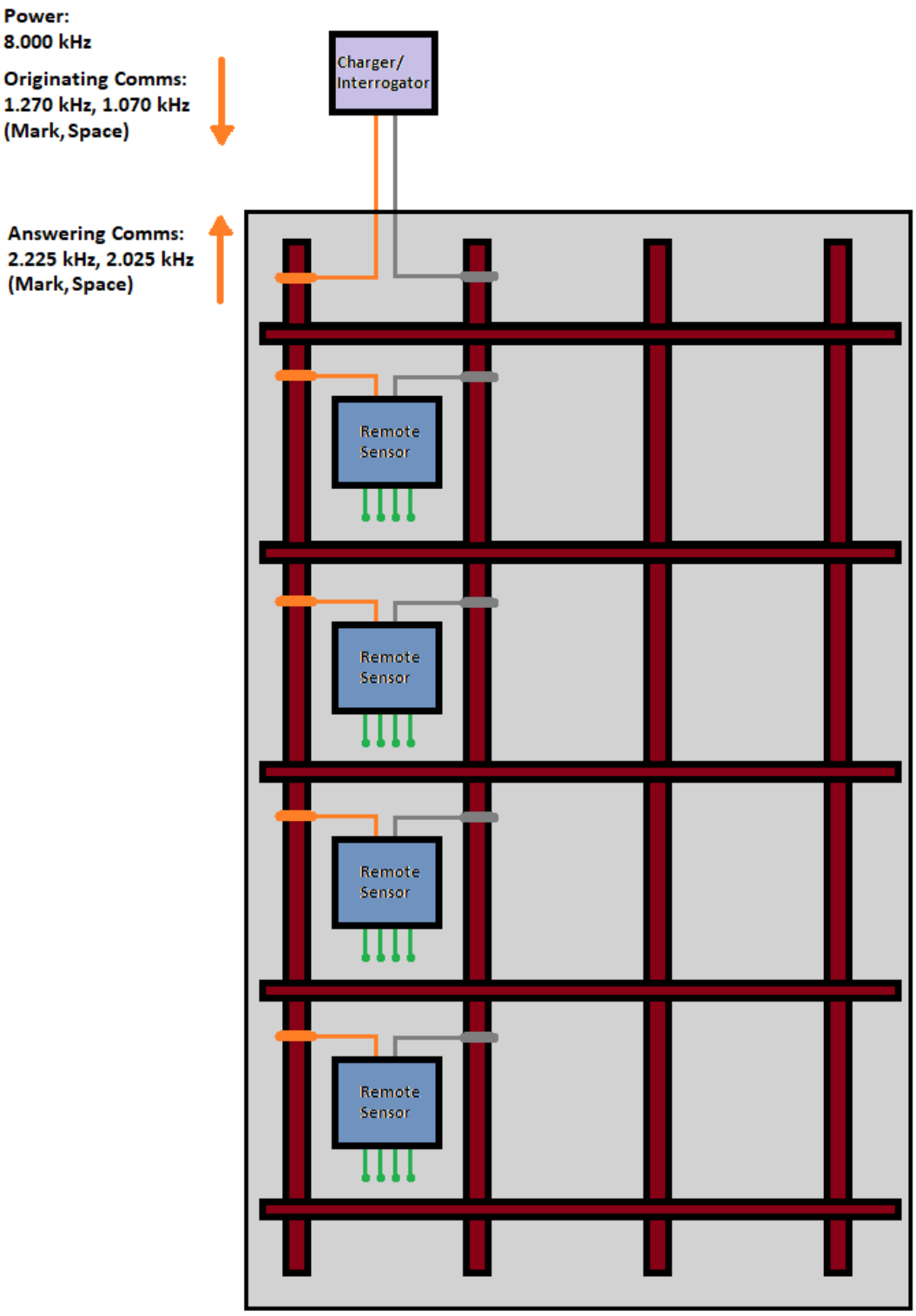

Figure 25. Diagram of the CI and RSs Implemented on Two Legs of a Rebar Cage Embedded in a Column of Concrete

4.2.1 Process

Because the second design approach used a lower frequency for energy harvesting purposes, and because there were restrictions with the frequency allocations above 8 kHz, frequencies lower than 8 kHz were sought to be implemented for communications purposes. Specifically, a Bell 103 modem was considered for the implementation. The Bell 103 modem communicates using mark tones and space tones to send binary data. The frequencies of mark tones and space tones depend on whether the device is originating communications or answering communications. As can be seen in Figure 25 If the device is originating communications, then the marks tone will be 1.270 kHz and the space town will be 1.070 kHz; if the device is answering communications, then the mark tones will be 2.225 kHz and the space tones will be 2.025 kHz. This difference in frequency sets allows for full duplex communications. However, full duplex communications are not needed for this half-duplex design.

In this design, there is a single charger/interrogator (CI) and several remote sensors (RSs). The CI charges the RSs using an 8.0 kHz signal for some duration of time; no other operations in the RSs occur during this time. After a sufficient amount of time, the CI then interrogates each RS, using originating communications tones from the Bell 103 modem (1.270 kHz, 1.070 kHz tones). In an interrogation event, the CI sends out an RS address, and then a command, and then the addressed RS responds with its address and a confirmation of the command received, and then does an action.

The first command the CI issues is for the RS to perform a measurement on the concrete. After the command is received, the RS responds with a message confirmation that the command has been received, and then the RS performs the measurement. The CI issues these commands one at a time to each RS.

After a sufficient amount of time, the CI then issues a second command, requesting for the measured value of the performed command. After the command is received, the RS responds with a message confirmation that the command has been received, and then the RS communicates the measured value. The CI issues these commands and then reads the responses one RS at a time.

4.2.2 Remote Sensor

Most of the focus for the second design approach was on the Remote Sensor (RS), given that the charger/interrogator (CI) could be easily replaced with a commercial Bell 103 modem and a function generator for testing. Figure 26 shows a detailed signal and power block diagram for the RS. In the signal part of the block diagram, it can be seen that two paths will be utilized, one for power and one for signal. For the power path, a voltage rectifier is used in the first stage, followed by the BQ25504 booster/charger, and then ending with a super capacitor as the energy reservoir. It can be seen in Figure 25 that the BQ25504 also powers all the devices in the signal line path. In the signal line path, there are three components: the first component manages the Bell 103 modem I/O management, the second component is the Bell 103 modem, and the third component is the PIC24FJ128GA204 microcontroller unit (MCU). The sensing circuit that makes the desired measurement is shown to the right side of the MCU component. The RS receives 8.0 kHz power from the CI through the RF coupler (grounding clamps), and then rectifies the RF power, boosts the rectified RF power, and then stores the rectified RF power in a super capacitor storage element. When sufficient voltages have been achieved and the super capacitor elements is charged, the BQ25504 booster/charger provides DC power to the Bell 103 I/O management, the Bell 103 modem, the MCU, and the sensing circuit.

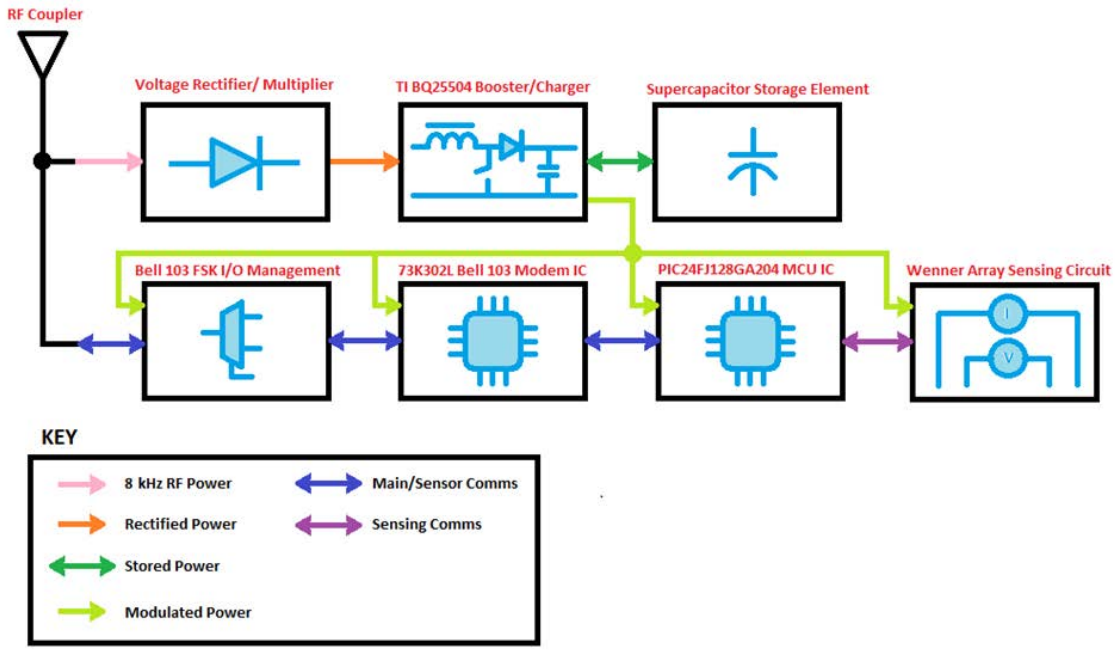

Figure 26. Detailed Signal and Power Block Diagram of the Remote Sensor (RS).

As can be seen in Figure 27, the RS is comprised of four Printed Circuit Boards (PCBs): the power board, the Bell 103 modem board, the microcontroller unit (MCU) board, and the Wenner Array board. The power board is comprised of the voltage rectifier/multiplier, the booster charger, and the super capacitor storage element. The Bell 103 modem board is comprised of the Bell 103 I/O management component and the Bell 103 modem Integrated Circuit (IC), as shown in Figure 26. The MCU board is comprised of the PIC24FJ128GA204 IC and all of the associated biasing circuitry (e.g. resistors, capacitors, pins). The Wenner Array board is comprised of the array sensing circuitry.

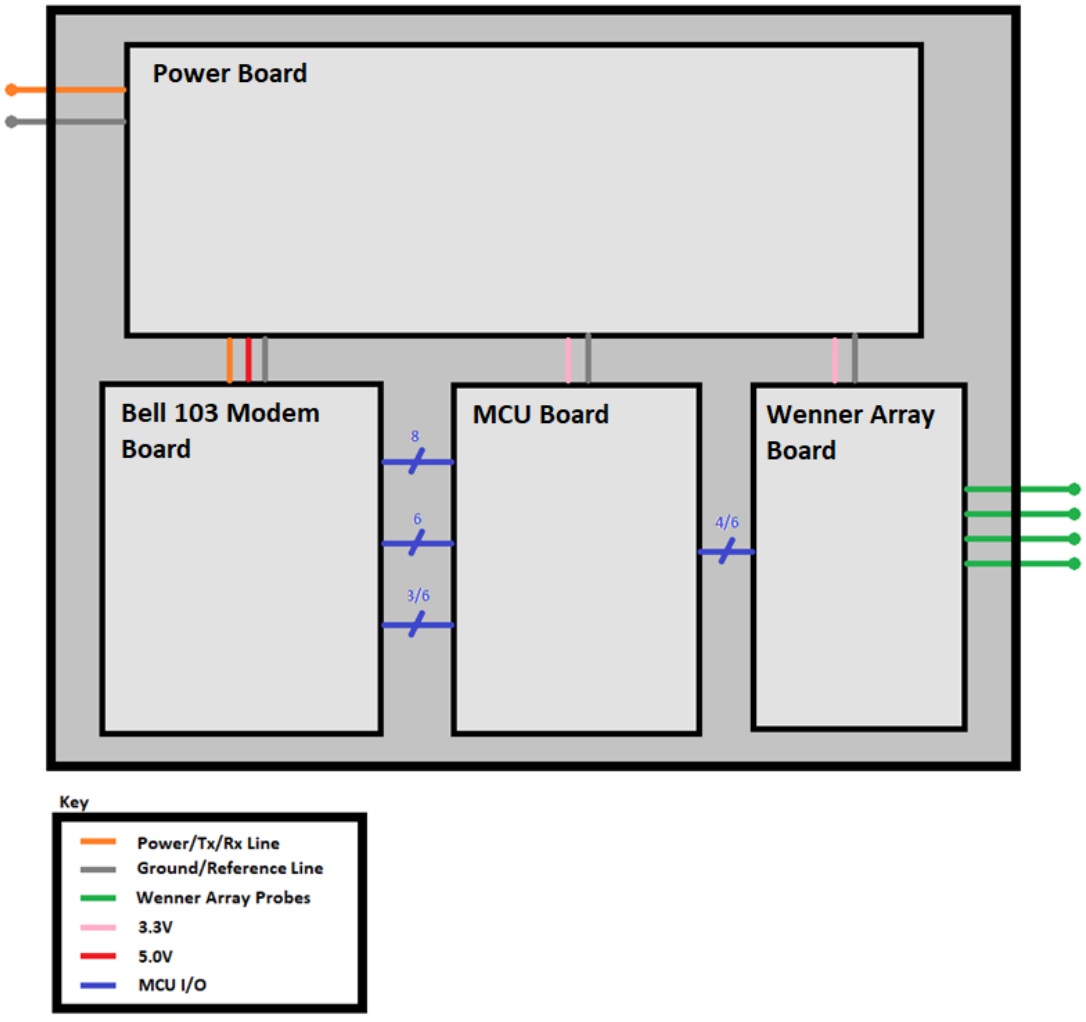

Figure 27. Layout of the Remote Sensor (RS) printed circuit boards (PCBs).

4.2.2.1 Modification to the Rectifier Circuitry

For the rectifier circuit, the 8.2 pF capacitors were changed to 2.2 µF capacitors so that the reactance of approximately -j8 Ω was preserved going from 2.4 GHz to 8 kHz. This change was necessary because if the original 8.2 pF capacitors were used, then at the low 8 kHz frequency, the impedance of the capacitors would be so high that no charge would be stored. Hence, to adjust for the change in frequencies, the capacitors were likewise adjusted so that the increase in capacitance would maintain the prior designs reactance for those particular elements.

4.2.2.2 New Biasing Resistors for BQ25504 Evaluation Board

Figure 28 shows, in red, the resistors that need to be replaced to re-bias voltages for the BQ25504. The following resistors are replaced:

- Resistors R_{UV1} and R_{UV2} are replaced with, respectively, 4.22 MΩ and 5.90 MΩ.
- Resistors R_{OV1} and R_{OV2} are replaced with, respectively, 3.74 MΩ and 6.19 MΩ.
- Resistors R_{OK1}, R_{OK2}, and R_{OK3} are replaced with, respectively, 2.55 MΩ, 4.22 MΩ, 3.09 MΩ.

By re-biasing the resistors with the values given above, the bias voltages are affected in the following way:

- Re-biasing resistors R_{UV1} and R_{UV2} cause the battery's undervoltage (V_{BAT_UV}) protection to be set to 2.998 V.
- Re-biasing resistors R_{OV1} and R_{OV2} cause the battery's overvoltage (V_{BAT_OV}) protection to be set to 4.979 V.
- Re-biasing resistors R_{OK1}, R_{OK2}, and R_{OK3} cause the comparator threshold hysteresis voltages ($V_{BAT\_OK\_HYST\_LOW}$ and $V_{BAT\_OK\_HYST\_HIGH}$) to be set to 3.319 V and 4.832 V.

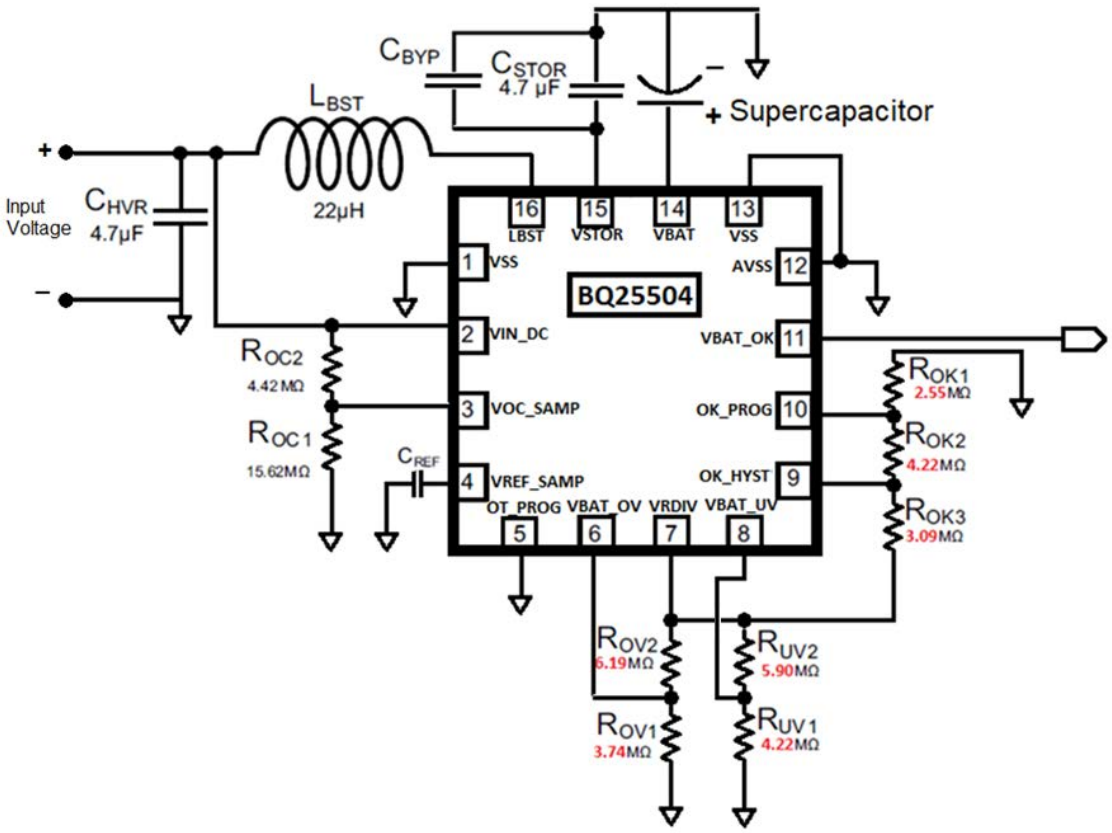

Figure 28. Diagram of the BQ25504 with resistors to be replaced denoted in red.

The effect on V_{STOR} and V_{BAT_OK} voltages after re-biasing the resistors can be seen in Figure 29. From Figure 29, it can seen that V_{STOR} will rise all the way to 4.832 V; at this point, V_{BAT_OK} is set to a logic high, equaling the same voltage as V_{STOR}. V_{STOR} continues to charge to the voltage V_{BAT_OV}. V_{STOR} remains at that voltage until the load depletes the energy storage device.

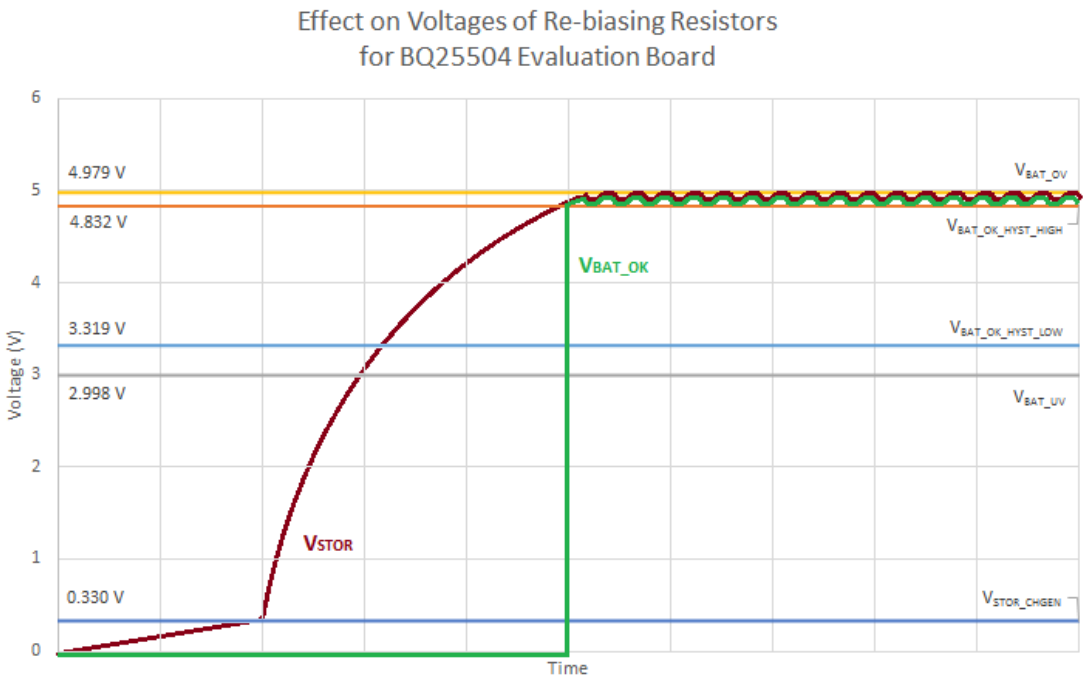

Figure 29. Effects on V_{STOR} and V_{BAT_OK} voltages after re-biasing resistors for the BQ25504

5 Experimentation

This section discusses experimentation conducted for this research project. The experiments in this section are sub-divided as follows:

- First Design Attempt: TM Coupler at 2.4 GHz
    1. TM Coupler Experimentation in Air: Experiments 1 – 9
    2. TM Coupler Experimentation in Concrete: Experiments 10 – 11
    3. Rectifier Experimentation: Experiments 12 – 15
    4. Booster Experimentation: Experiment 16
- Second Design Attempt: Grounding Clamps at 8 kHz
    1. Grounding Clamp Experimentation in Concrete and Air: Experiments 17 - 21
    2. Rectifier and Booster Experimentation: Experiment 22

The purpose of sub-dividing the experiments in this manner is to group the experiments in such a way that makes the bulk of experiments easier for the reader to organize. In total, there are 22 experiments in the Experimentation section. Each experiment will have at least three subsections included: (1) Set-Up, (2) Results, and (3) Discussion. There may be more subsections in a given experiment depending on whether the author deemed such details to be too important to not include; additionally, there may be more than one Results section depending on whether there were numerous results to discuss.

For the **First Design Attempt: TM Coupler at 2.4 GHz** section, there are a total of 16 experiments discussed. Experiments 1 – 9 are in the TM Coupler Experimentation in Air section. Experiments 10 – 11 are in the TM Coupler Experimentation in Concrete section. Experiments 12 – 15 are in the Rectifier Experimentation section. Experiment 16 is in the Booster Experimentation section.

For the **Second Design Attempt: Grounding Clamps at 8 kHz** section, there are a total of 6 experiments discussed. Experiments 17 – 21 are in the Grounding Clamp Experimentation in Concrete and Air section. Experiment 22 is in the Rectifier and Booster Experimentation section.

5.1 First Design Attempt: TM Coupler at 2.4 GHz

The first design attempt focused on utilizing the TM Coupler, as described in section 4.1.1.3.3, which discusses the Third Version of the TM Coupler. Recall that the TM Coupler functioned as a feedhorn and was designed to operate at 2.4 GHz. The TM Coupler was to be embedded in a reinforced concrete structure. More specifically, the TM Coupler would be embedded on one of two ways: (1) the TM Coupler would be mounted onto a leg of the rebar cage itself, or (2) the TM Coupler would be mounted onto a small length of rebar that was perpendicularly affixed to a leg of the rebar cage.

Before testing the TM Coupler in concrete conditions, it was deemed important to first understand the properties of TM Coupler power transmission. Hence, the antenna was first experimented with in an air medium, absent of any concrete. After a better understanding was obtained, the device was to be embedded in concrete so that its functionality in the concrete environment could be determined.

5.1.1 TM Coupler Experimentation in Air

The purpose of the experimentation in air was to characterize the behavior of the TM Coupler and to study its effects under a variety of conditions; in doing so, a "baseline" could be established so that the results in concrete could be compared against in air. Additionally, in air, adjustments can be more readily made to the experiment, whereas, in concrete, adjustments cannot be made without destroying the concrete or re-fabricating new TM Couplers and pouring another batch of concrete — a timely process.

Naturally, because most of the devices in industry for RF applications have an input impedance of 50 Ω, the input impedance of the TM Coupler was sought to be measured, understood, and matched to 50 Ω. Experiments 1 – 3 evaluate the input impedance of the TM Coupler under a variety of conditions and show the matching circuit used to match the TM Coupler to 50 Ω.

Once the input impedance of the TM Coupler was understood and matched, using a probe kit from Beehive Electronics, the electric and magnetic field strengths were investigated in Experiment 4.

Experiments 5 – 9 evaluate the performance of the TM Coupler in three different configurations. In Experiment 5 and 6, the performance of the TM Coupler is evaluated on a single length of rebar, using two TM Couplers, one at each end. In Experiment 7 and 8, the performance of the TM Coupler is evaluated on a single length of rebar, using three TM Couplers, one at each end, and one perpendicularly tapping off of the length of rebar. In Experiment 9, the performance of the TM Coupler is evaluated in a very similar configuration as in Experiment 7 and 8, but with six rungs and three additional legs tied to make a rebar cage structure.

5.1.1.1 Experiment 1: Input Impedance of the TM Coupler with Varied Mounting Pressures and without Matching Circuitry

With no matching circuitry applied to the input of the TM Coupler, it was observed that when the standoff within the TM Coupler was not making good contact with the rebar that performance suffered. To understand how the TM Coupler performed when different mounting pressures were applied (i.e. loosely secured to the rebar, firmly hand pressed to the rebar, firmly

secured to the rebar), the S11 parameters were investigated as the mounting strength was varied.

5.1.1.1.1 Set-Up

Several TM Couplers were made throughout the project, with the TM Couplers being indexed with a number written on the dielectric and the copper for identification purposes. Two TM Couplers were arbitrarily selected to perform this experiment: TM Coupler 5 and TM Coupler 8. Both TM Couplers were affixed to a length of rebar such that the tap points of the TM Couplers were separated by a distance, L_1, of 110.5 cm. A length of 110.5 cm was used to provide a sufficient number of wavelengths across this distance to eliminate near field phenomena from the experiment. A Vector Network Analyzer (VNA) was used to measure the S-Parameters. The S11 parameter tells us how much RF power is reflected by Port 1 back into Port 1; the S22 tells us the same for Port 2; this is called return loss; the input impedance of the port can be calculated with this parameter. The S21 parameter tells us how much energy was received by Port 2 from Port 1; the S12 parameter tells us the same in reverse order; this is called insertion loss. This experiment was only interested in the S11 or S22 parameter, which was used to evaluate the input impedance.

The rebar used was number 5 rebar, which has a nominal diameter of 1.7145 cm. Three different mounting pressures were applied for three different measurements: (1) no applied mounting pressure, (2) hand-pressed mounting pressure, and (3) bolt-tightened mounting pressure

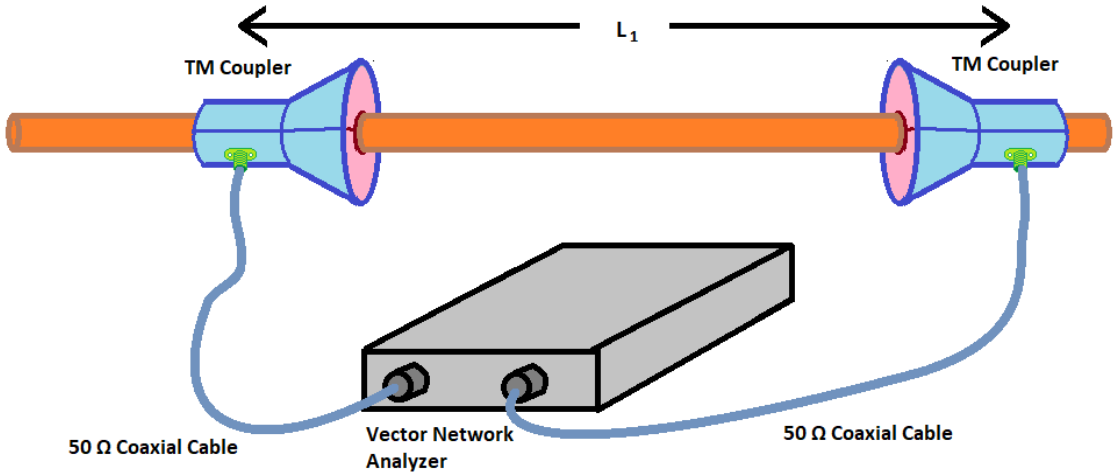

Figure 30. The set-Up for Experiment 1

5.1.1.1.2 Results

The results for three different mounting pressures are shown in the proceeding subsections, which are titled:

- No Applied Mounting Pressure
- Hand-Pressed Mounting Pressure
- Bolt-Tightened Mounting Pressure

5.1.1.1.2.1 No Applied Mounting Pressure

The input impedance and return loss for TM Coupler 8 when no applied mounting pressure was exerted on the TM Coupler system is shown in Figure 31. In this configuration, TM Coupler 8 hangs without any additional manual pressure pressing the TM Coupler against the rebar.

Figure 31 shows the input impedance of the TM Coupler on a smith chart with three markers selected: 2.40 GHz, 2.45 GHz, and 2.50 GHz. This trace indicates a mismatched antenna to the VNA, given that the impedances at these frequencies are not equal to approximately 50 Ω. This curve reads like an open or short circuit on a transmission line, with the trace following the constant Voltage Standing Wave Ratio circle (constant VSWR circle) — with a large constant VSWR. At 2.4 GHz, the input impedance for the TM Coupler was 3.44 – j15.35 Ω, with an

return loss effectively 0 dB, which meant that nearly all of the power was being reflected at the input of the TM Coupler and returning back to the VNA.

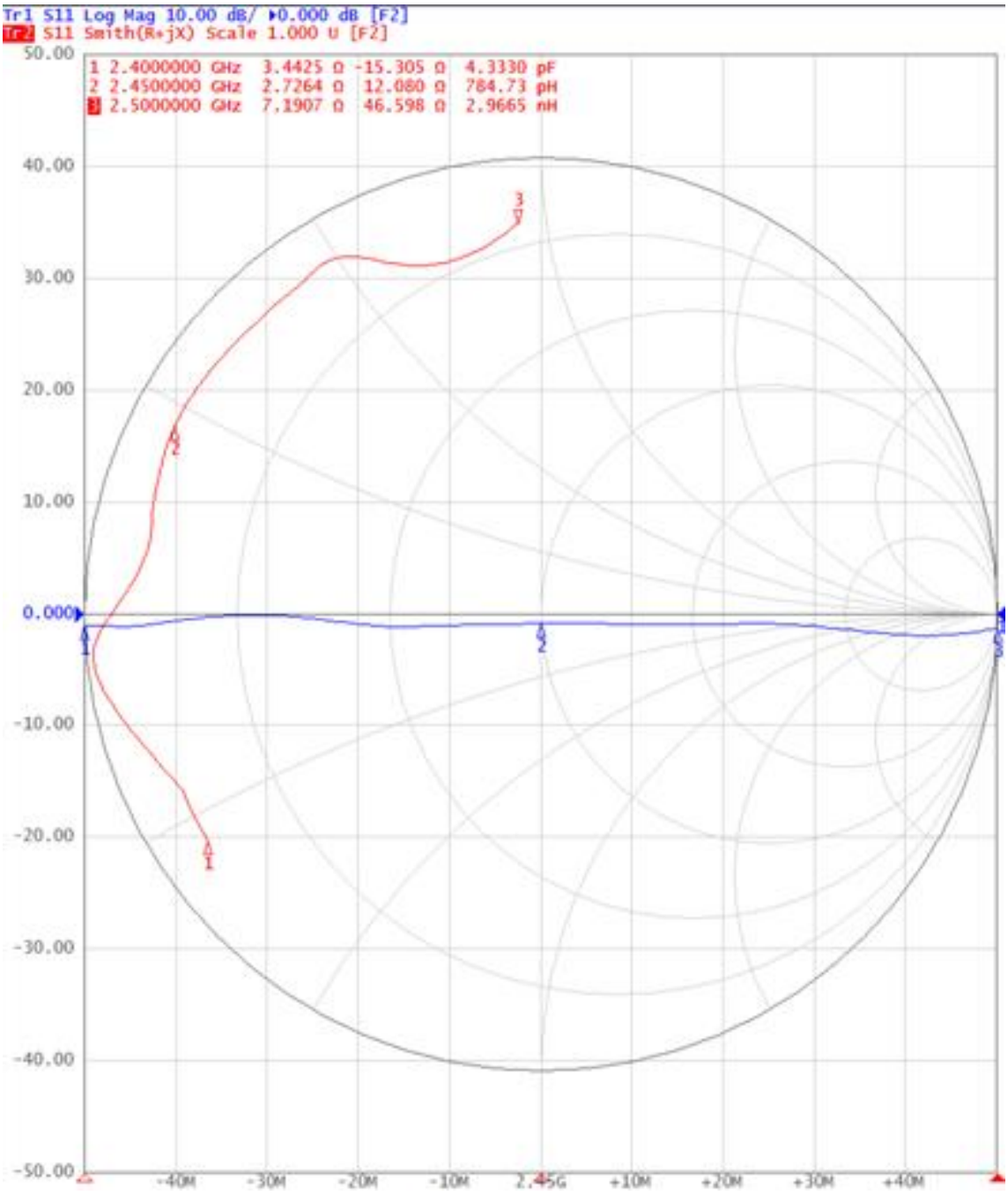

Figure 31. S11 parameter of TM Coupler with no applied pressure against rebar.

5.1.1.1.2.2 Hand-Pressed Mounting Pressure

When a sufficient amount of mounting pressure is exerted to the TM Coupler, the standoff inside the TM Coupler is believed to be making better contact against the rebar than with no applied mounting pressure (i.e. the TM Coupler's own weight supplied the mounting pressure)), the S11 parameters appear as shown in Figure 32. Figure 32 shows the input impedance of the smith chart with three markers selected: 2.40 GHz, 2.45 GHz, and 2.50 GHz. This trace indicates a less mismatched antenna to the VNA than shown in the prior measurement; however, the impedances at these frequencies are still not equal to approximately 50 Ω. At 2.40 GHz, the input impedance was 47.357 – j53.35 Ω, which is about as equally as reactive as resistive. Additionally, the return loss for this configuration was around -5 dB, which means that approximately 30% the power is being reflected back into the VNA. What's more, the trace of the input impedance hints at a VSWR that smaller in this example; however, the VSWR circle still looks choppy and inconstant.

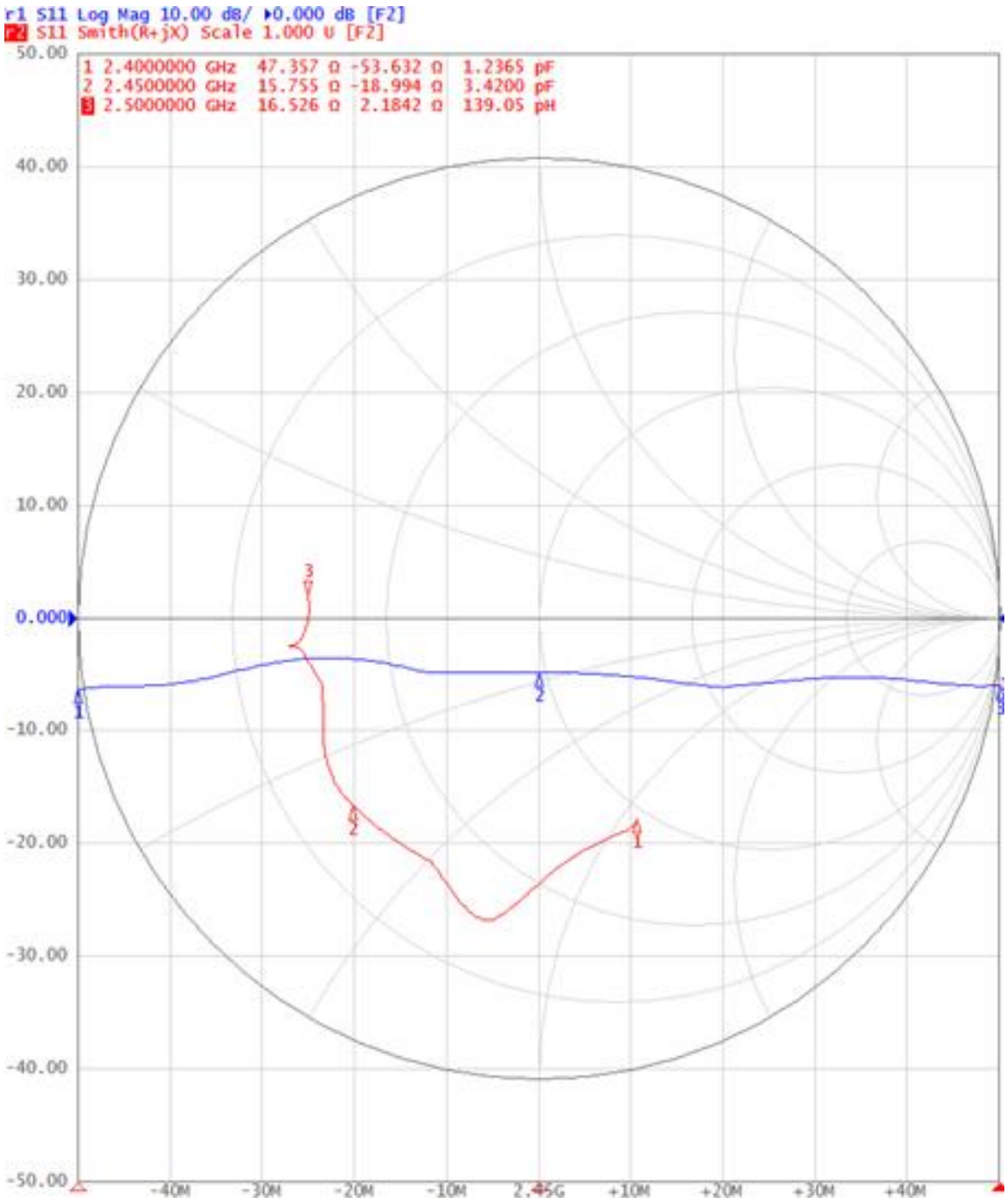

Figure 32. S11 Parameter when TM Coupler 8 is firmly hand pressed against the rebar.

5.1.1.1.2.3 Bolt-tightened Mounting Pressure

An M2 bolt was threaded into the standoff on the TM Coupler via a hole drilled through the rebar. The M2-bolt-and-standoff mechanical connection was secured onto the rebar with no jostle. The input impedance and the S11 parameter for TM Coupler 5 appears as shown in Figure 33. In Figure 33, only one marker is shown at 2.40 GHz; however, this trace appears to be much less choppy than the prior two examples.

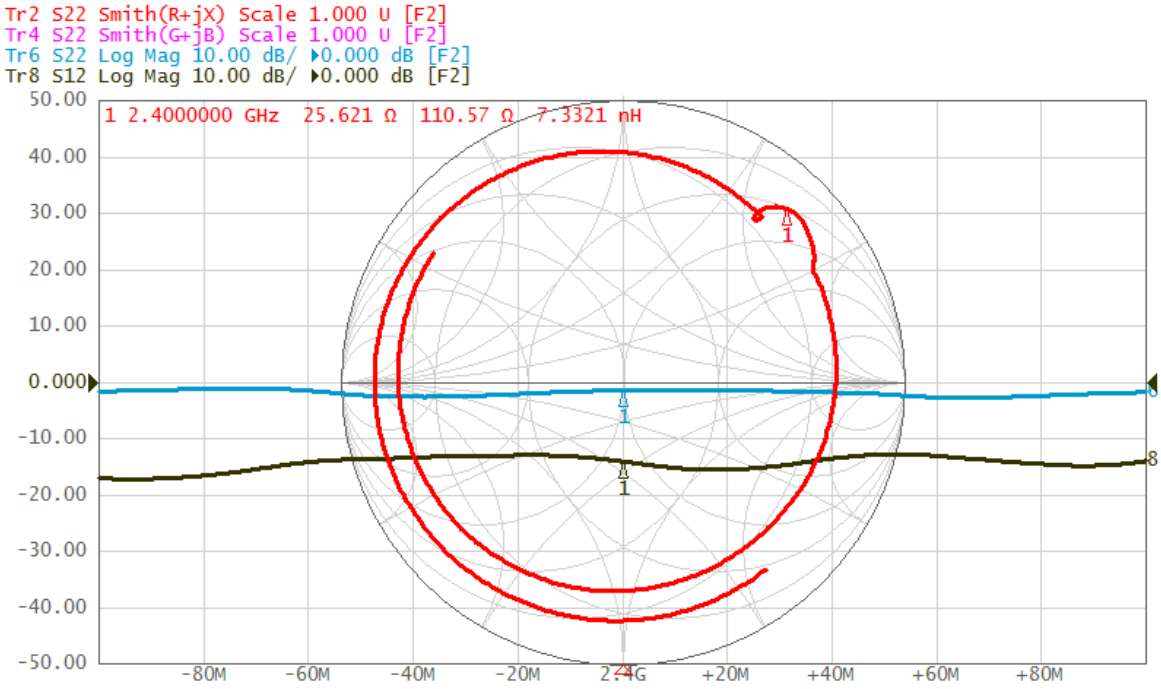

Figure 33. S11 Parameter for TM Coupler 8 when firmly secured to the rebar

The input impedance reads 25.621 + j110.57 Ω at 2.4GHz. This indicates that a lot of the power is reflected, due to the comparatively high reactance relative to the resistance. Moreover, the return loss (indicated by the S22 parameter) is shown to be almost 0 dB, which means that almost all the energy was reflected back into the VNA.

5.1.1.1.3 Discussion

When the TM Coupler is not mounted to the rebar with a sufficient amount of pressure, then the performance seems to suffer most strikingly with the appearance of the VSWR. That is, the impedance trace does not appear to be a smooth circle around the origin of the reflection coefficient. While the input impedance can be said to have improved from the no mounting pressure condition to the hand-pressed mounting pressure condition, the appearance of the VSWR cannot be said to have improved. Meanwhile, it can be argued that the input impedance of the TM Coupler decreased from the hand-pressed condition to the bolt-tightened condition; however, the appearance of the VSWR appeared to have improved due to the smoother circular trace of the input impedance.

5.1.1.2 Experiment 2: Input Impedance with the Matching Circuitry

Once it was demonstrated that the mounting pressure for the TM Coupler was important for attaining a stable and predictable VSWR circle, the objective became to match the TM Coupler to a 50 Ω load or source. To do this, a matching circuit was applied.

5.1.1.2.1 Brief Description of Applied Matching Circuitry

A schematic diagram of the matching circuit can be seen in Figure 34, which includes an input shunt capacitor of 5pF, a series inductor of 3.6nH, and an output shunt capacitor of 1.4pF.

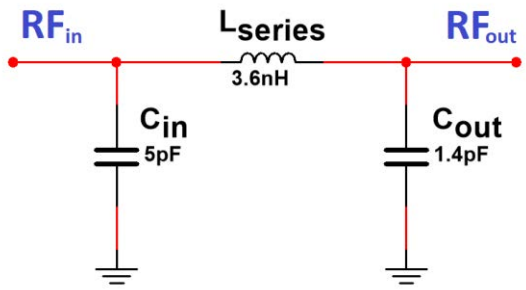

Figure 34. The Matching Circuit Implemented for all Experiments with the TM Coupler.

The matching circuit did not utilize a ground plane. Instead, a ground trace was used to provide a return path in the matching circuit.

5.1.1.2.2 Set-Up

Building off of Experiment 1, the set-up of Experiment 2 resembled that of Experiment 1 almost identically, as can be seen in Figure 35.

Two TM Couplers were arbitrarily selected to perform this experiment: TM Coupler 5 and TM Coupler 8. Both TM Couplers were affixed to a length of rebar such that the tap points of the TM Couplers were separated by a distance, L_1, of 110.5 cm. A length of 110.5 cm was used to provide a sufficient number of wavelengths across this distance to eliminate near field phenomena from the experiment. A Vector Network Analyzer (VNA) was used to measure the input impedance and return loss (S11 or S22) of a given TM Coupler. The rebar used was number 5 rebar, which has a nominal diameter of 1.7145 cm. In Experiment 2, however, two matching circuits are applied to the input of the TM Couplers.

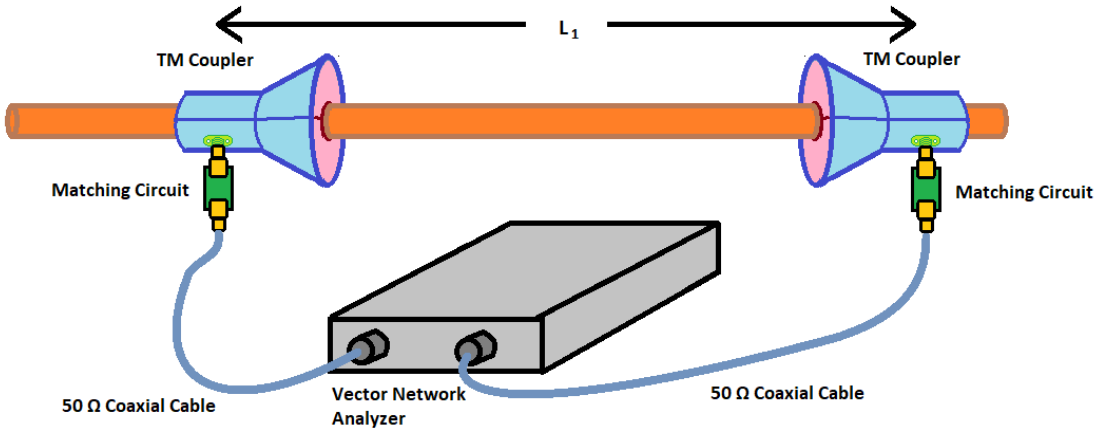

Figure 35. Set-Up for Experiment 2

5.1.1.2.3 Results

The images below show the S-parameter traces on three different graphs: (1) input impedance Smith Chart, (2) input admittance Smith Chart, and (3) a Log-Mag graph. The center frequency is 2.4 GHz; the span is 200 MHz. Figure 36 shows the results for TM Coupler 5 and Figure 37 shows the results for TM Coupler 8.

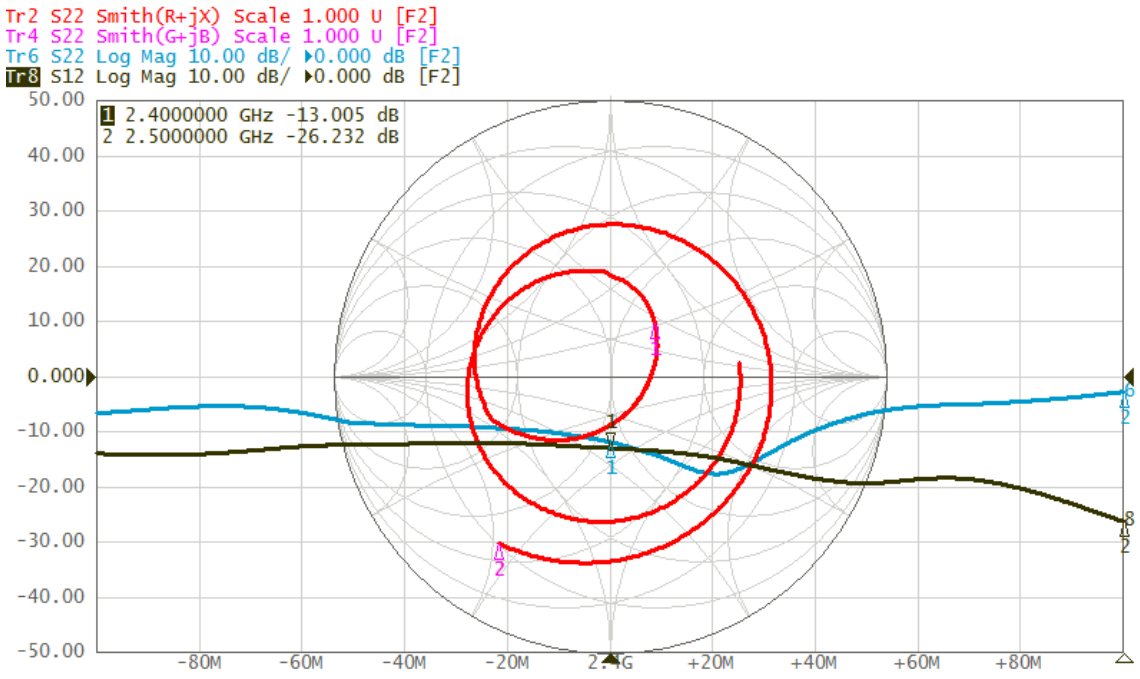

Figure 36. S-Parameter results for TM Coupler 5 with a matching circuit.

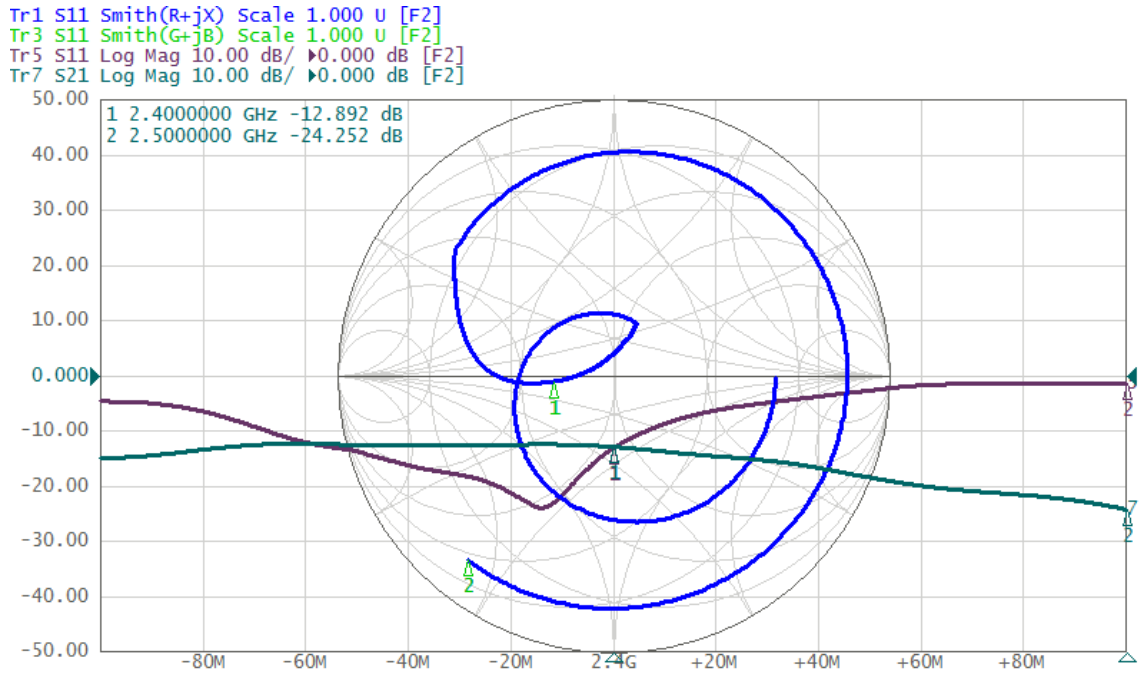

Figure 37. S-parameter results for TM Coupler 8 with a matching circuit

At 2.4 GHz, the input impedance for TM Coupler 8 is 32.4 - j1 .01 Ω; the input impedance for TM Coupler 5 is 62.6 + j27.4 Ω. The S11 and S22 parameters are approximately -10 dB. The S12 and S21 parameters read approximately -13 dB.

5.1.1.2.4 Discussion

Since the S11 and S22 parameters are approximately -10 dB, this indicates that approximately 10% of the RF power is reflected back into the VNA, in either direction. Since the S12 and S21 parameters read approximately -13 dB, this indicates approximately 95% insertion power loss occurs in both directions. This can be interpreted as the TM Couplers resulting in a 10 dB loss each.

The VNA uses a 0 dBm input power for measurements, which corresponds to 1 mW, or 1000 microwatts (µW). Using this figure, power can be calculated as various steps of the signal path. 10% of the power is reflected at the TM Coupler input; therefore, 90% of the 1000 µW input power passes through to the rebar, which corresponds to 900 µW. 95% of the input power is lost along the signal path; therefore, 5% of 1000 µW makes it through the entire signal path, which corresponds to 50 µW. Hence, of the 900 µW that makes it onto the rebar, 850 µW of

that power is lost. Neglecting power losses that occur at the receiving TM Coupler, this means that, at most, 850 μW is lost to radiation, which corresponds to 85% of the input power.

5.1.1.3 Experiment 3: The Effect of Sealant on the TM Couplers

As the TM Coupler was being developed to be embedded into concrete, sealant was being applied to the PVC face to preempt the possibility of moisture ingress into the rebar-PVC interface. Initially, it was thought that the sealant would not cause any significant power losses. However, after observation, it became clear that significant attenuation resulted.

There were significant power losses occurring when sealant was applied, resulting in a 30 dB power loss. It was posited that too much sealant was being applied, resulting in the sealant spreading too much as both halves of the PVC were pressed against the rebar, squishing the sealant. If true, then it was believed that if the sealant had spread far enough, then the sealant could have intruded into the rebar-standoff interface, which made the electrical connection between the TM Coupler and the rebar. The belief is that the sealant could be impeding the input power.

5.1.1.3.1 Why Sealant Was Used

Earlier, during the development of the TM Couplers, there had been numerous incidents where the electrical connection between the TM Coupler and the rebar had broken due to transient, unintended mechanical torqueing of the TM Coupler. This demonstrated that the electrical connection was mechanically weak and that it should not be relied on for maintaining a secure mechanical connection.

The electrical connection is formed by a standoff that had its threads filed down so that the remaining narrow stub could be soldered into the solder cup of an SMA flanged connector. The diameter of the solder cup is approximately 50 mils. It was reasoned that another agent was needed to handle any accidental torqueing loads; hence, a sealant was chosen for handling these loads.

Given that sealant was desired for handling the mechanical torque loads, the effects of the sealant on the RF performance of the TM Couplers needed to be investigated; this was done by investigating the performance of the TM Couplers first without the sealant and then with the sealant. No matching circuits were implemented in this experiment because the matching

circuits would introduce a potential error; namely, if there was a flaw with the matching circuit that was not identified, unnecessary error could be potentially introduced in the investigation.

5.1.1.3.2 Set-Up

For two separate sets of TM Couplers, the same overall test was run. For one test, TM Coupler 4 and TM Coupler 7 were mounted to the same length of rebar. For the other test, TM Coupler 8 and TM Couple 5 were mounted to the same length of rebar. For both tests, the TM Couplers separated by a distance, L_1, of 110.5 cm. No matching circuits were applied to the input of the TM Couplers so that the true input impedance of the TM Couplers could be measured. Both TM Couplers were connected to the VNA, as shown in Figure 38. For each test, two measurements were made: one with no sealant applied, and one with sealant applied to the PVC where both halves of a TM Coupler mate together.

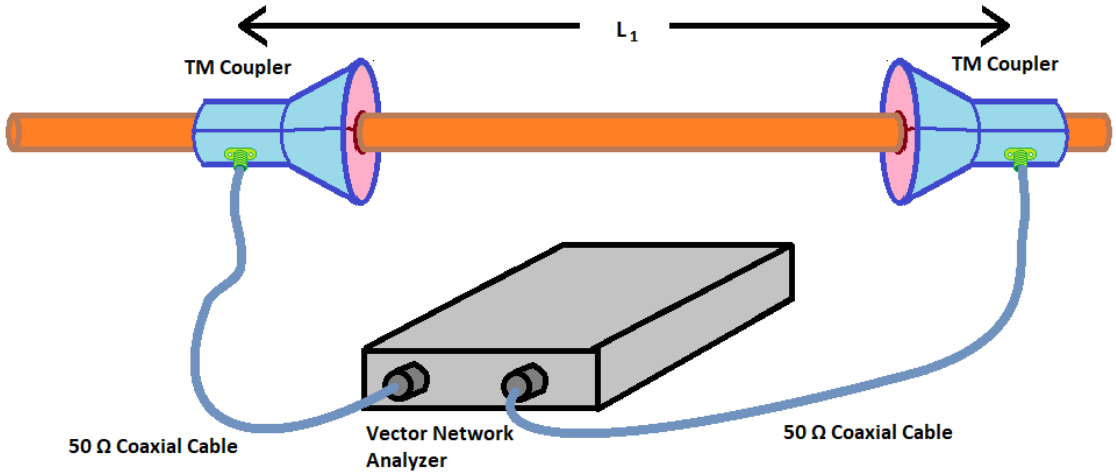

Figure 38. Diagram of the set-up of Experiment 3

5.1.1.3.3 Results: TM Coupler 4 and TM Coupler 7

This section is divided into two sub-sections: (1) without sealant and (2) with sealant.

5.1.1.3.3.1 Without Sealant

This section shows the results of TM Coupler 4 and TM Coupler 7 with no sealant applied and no matching circuit implemented. The graph shown in Figure 39 depicts the results for TM Coupler 4; this graph displays the S11 and S21 parameter. The graph shown in Figure 40 depicts the results for TM Coupler 7; this graph displays the S22 and S12 parameter.

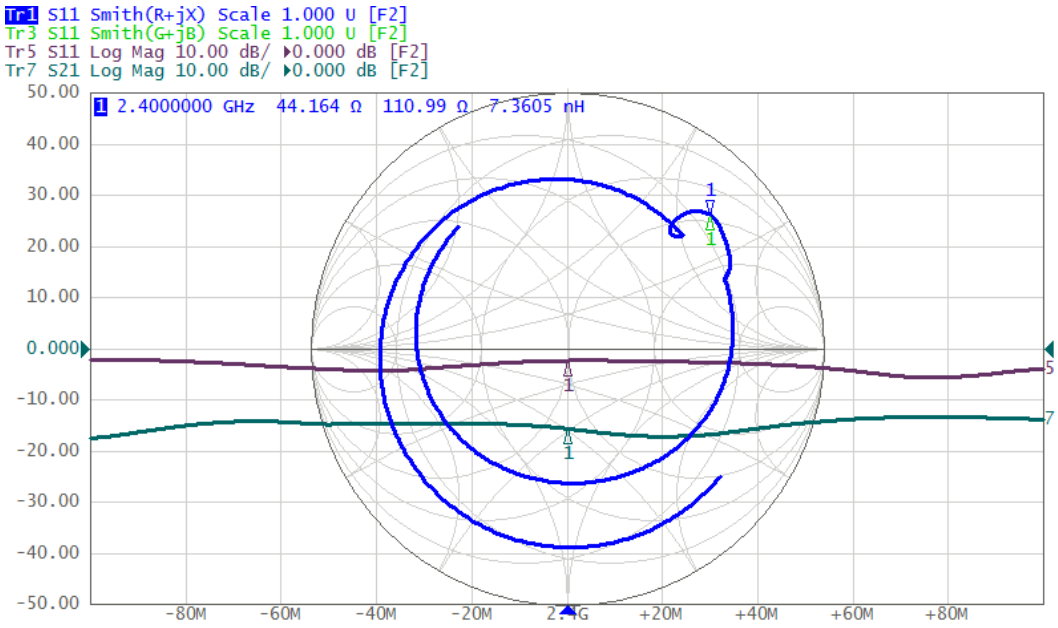

Figure 39. S-Parameter results for TM coupler 4 without sealant.

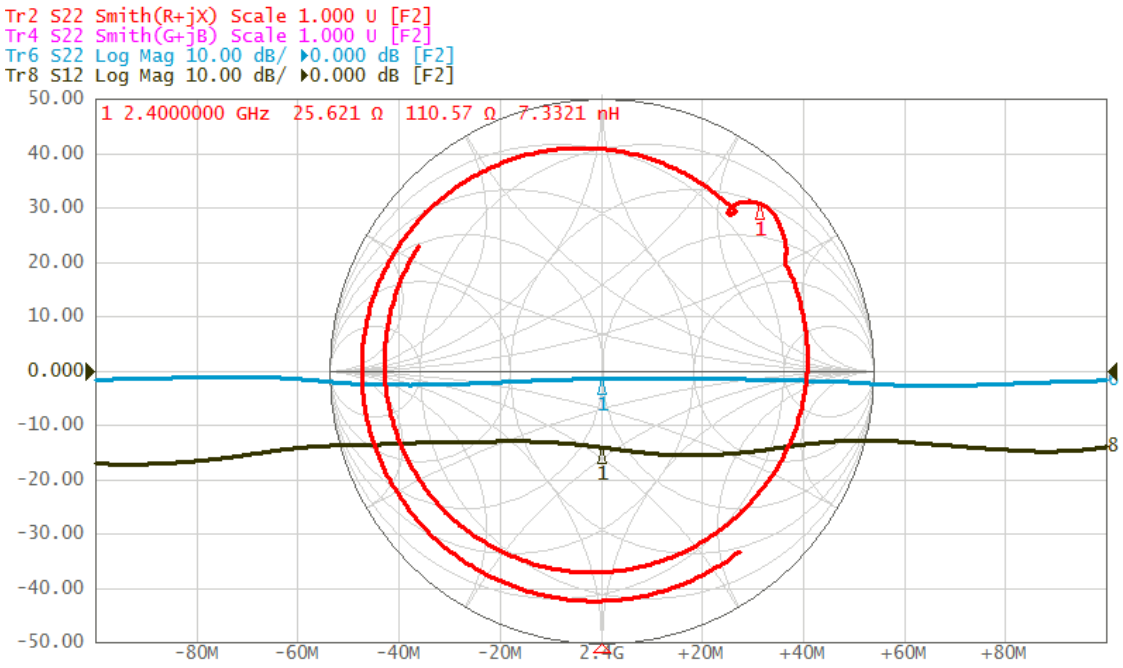

Figure 40. S-Parameter results for TM coupler 7 without sealant.

The input impedance for TM Coupler 7 is 44.2 + j111.0 Ω. The input impedance for TM Coupler 4 is 25.6 + j110.6 Ω. The S11 parameter is -2.24 dB and the S22 parameter is -1.43 dB, indicating significant return loss. The S21 in the S12 parameters, which show the insertion loss, are at respectively -15.5 dB and -13.9 dB.

5.1.1.3.3.2 With Sealant

This section shows the results of TM Coupler 4 and TM Coupler 7 with sealant applied and no matching circuit implemented. The graph shown in Figure 41 depicts the results for TM Coupler 4; this graph displays the S11 and S21 parameter. The graph shown in Figure 42 depicts the results for TM Coupler 7; this graph displays the S22 and S12 parameter.

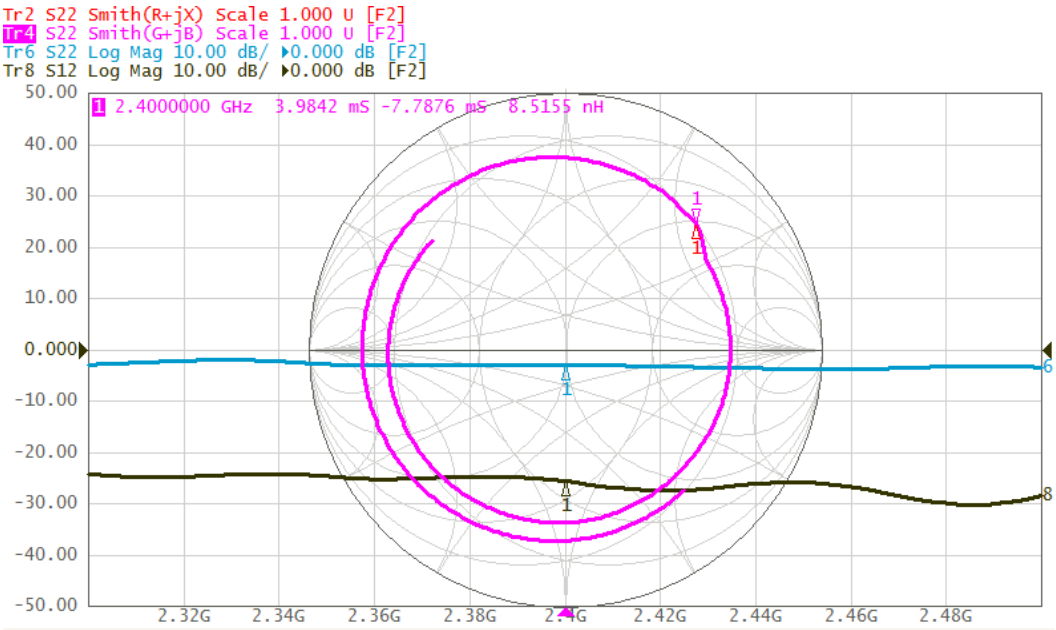

Figure 41. S-parameter results for TM Coupler 4 with sealant

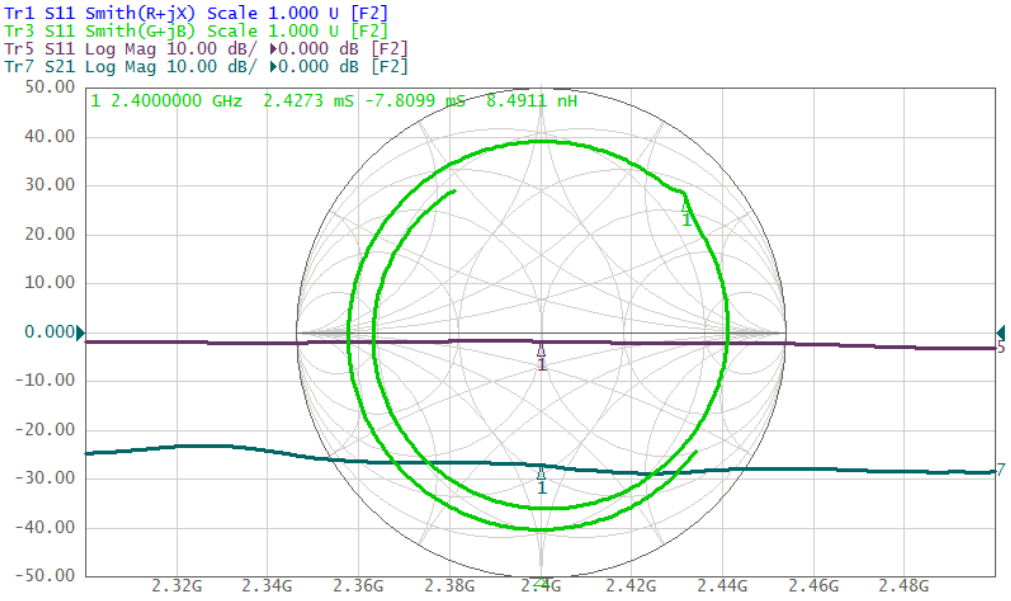

Figure 42. S-parameter results for TM Coupler 7 with sealant

At 2.4 GHz, the input impedance for TM Coupler 7 is 35.9 + j116.7 Ω; the input impedance for TM Coupler 4 is 51.0 + j102.3 Ω. At 2.4 GHz, the S11 parameter (TM Coupler 7) is -1.8 dB; the S22 parameter (TM Coupler 4) -2.9 dB. The S21 parameter is -27.1 dB; the S12 parameter is -25.5 dB.

5.1.1.3.4 Results: TM Coupler 8 and TM Coupler 5

This section is divided into two sub-sections: (1) without sealant and (2) with sealant.

5.1.1.3.4.1 Without Sealant

This section shows the results of TM Coupler 8 and TM Coupler 5 with no sealant applied and no matching circuit implemented. The graph shown in Figure 43 depicts the results for TM Coupler 8; this graph displays the S11 and S21 parameter. The graph shown in Figure 44 depicts the results for TM Coupler 5; this graph displays the S22 and S12 parameter.

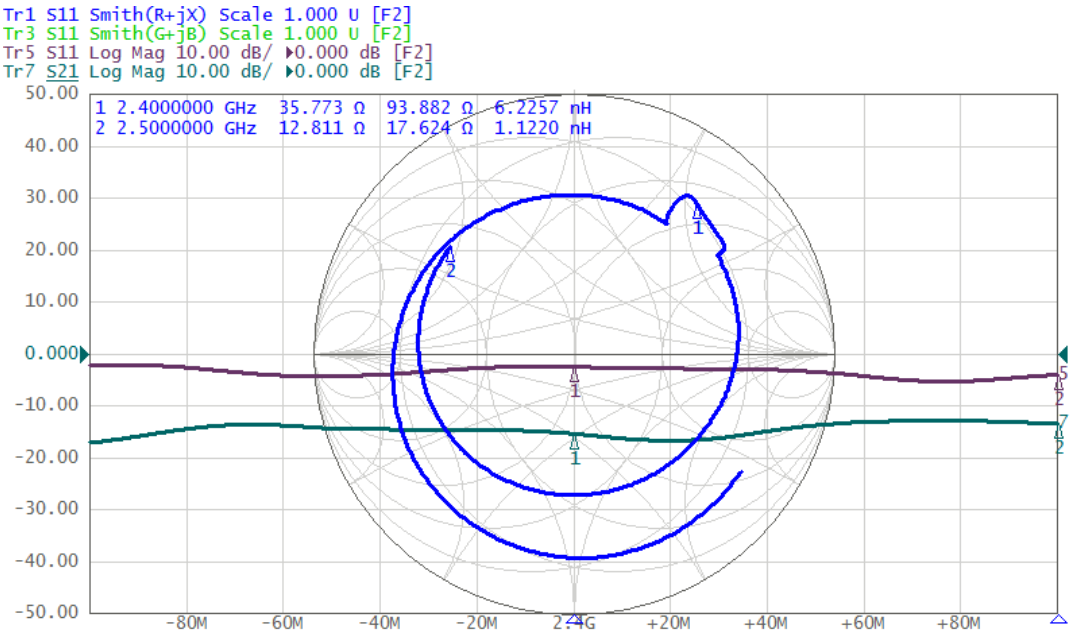

Figure 43. S-parameter results TM Coupler 8 without sealant

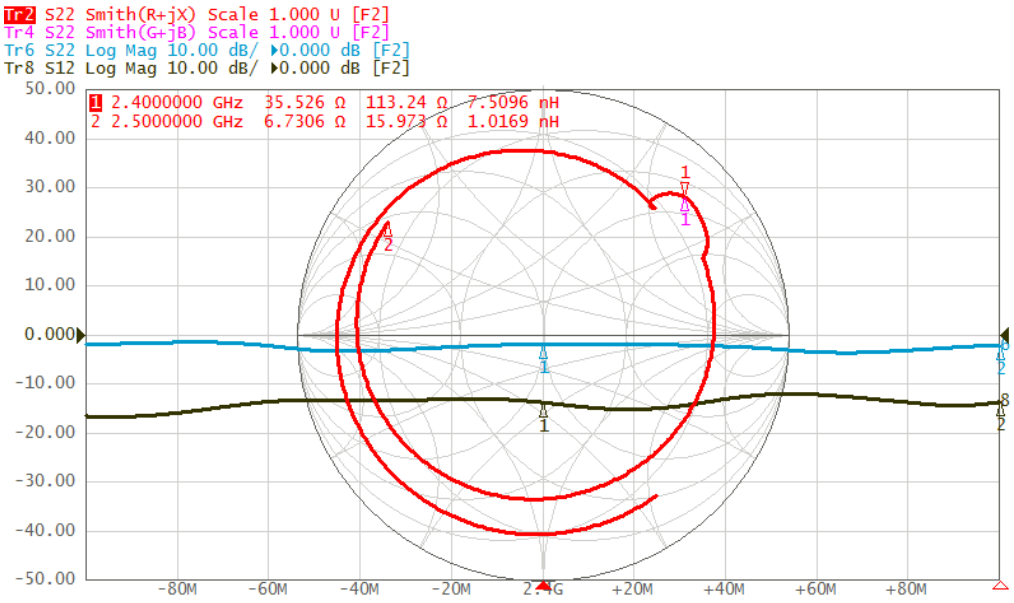

Figure 44. S-parameter results for TM Coupler 5 without sealant

The input impedance for TM Coupler 8 is 35.8 + j93.8 Ω. The input impedance for TM Coupler 5 is 35.5 + j113.2 Ω. The S11 parameter was recorded to be -2.55 dB and the S22 parameter was recorded to be -1.58 dB. The S21 and the S12 parameters were recorded to be, respectively, -16.4 dB and -14.8 dB.

5.1.1.3.4.2 With Sealant

This section shows the results of TM Coupler 8 and TM Coupler 5 with sealant applied and no matching circuit implemented. The graph shown in Figure 45 depicts the results for TM Coupler 8; this graph displays the S11 and S21 parameter. The graph shown in Figure 46 depicts the results for TM Coupler 5; this graph displays the S22 and S12 parameter.

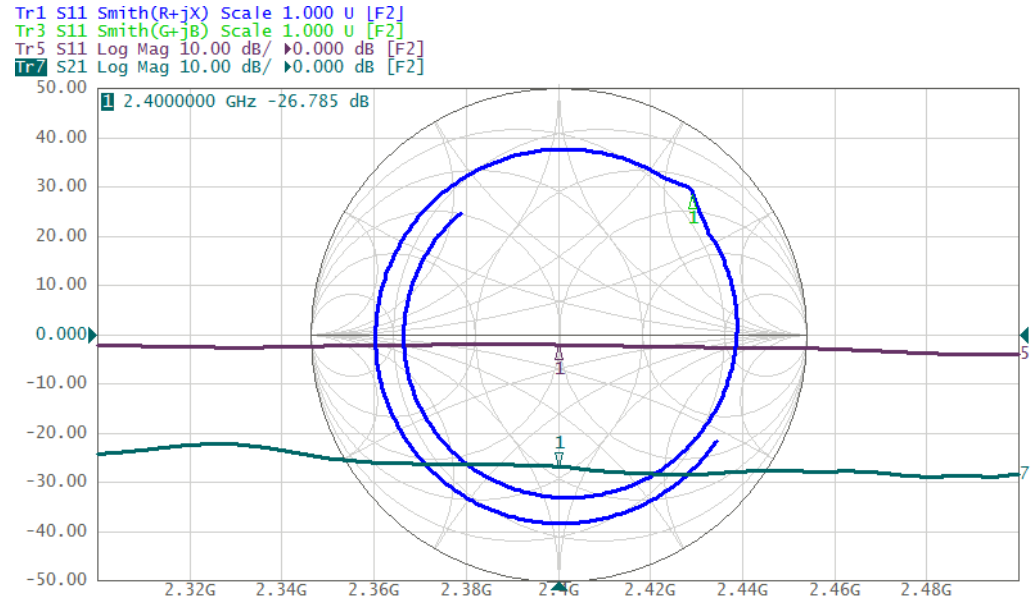

Figure 45. S-Parameters for TM Coupler 8 with sealant

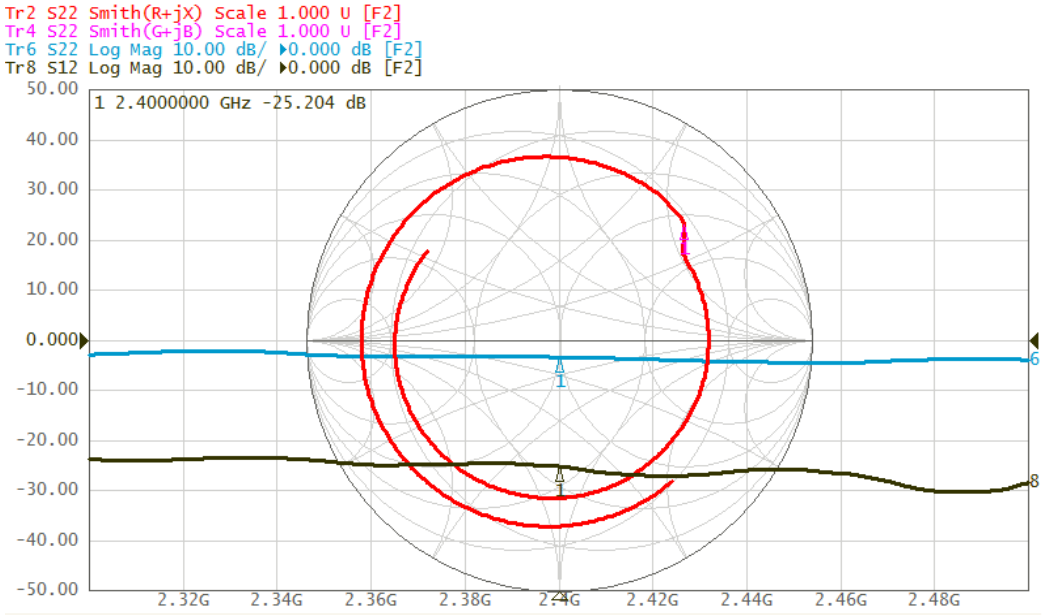

Figure 46. S-Parameters for TM Coupler 5 with sealant

At 2.4 GHz, the input impedance for TM Coupler 8 is 35.0 + j106.7 Ω; the input impedance for TM Coupler 5 is 58.3 + j100.3 Ω. At 2.4 GHz, the S11 parameter is -2.1 dB; the S22 parameter -3.3 dB. The S21 parameter is -26.8 dB; the S12 parameter is -25.2 dB.

5.1.1.3.5 Discussion

For both sets of results (TM Couplers 4 and 7, and TM Couplers 8 and 5), the application of sealant slightly affects the input impedance, in both cases causing the resistance to drop to a low value but the reactance to remain the same or drop slightly. However, the radius of the S11 or S22 curve on the Smith Chart remained almost unchanged, displaying essentially the same VSWR circle with perhaps a slightly smaller radius. It is unclear whether the sealant caused the impedance marker to made the load appear electrically closer to the generator (causing the VSWR circle to slightly rotate clock-wise). Due to these slight changes, its difficult to determine what effect the sealant had on the return loss of the system.

On the other hand, the effects of the sealant on the insertion loss on the system appears to be very pronounced. For both sets of results, the insertion loss was reduced from about -15 dB to about -25 dB. Because the only difference between the two measurements conducted in both tests was the sealant, it is believed that when the sealant is applied at the PVC interface of a TM Coupler, the sealant confers an extra 10 dB of power loss to the system.

5.1.1.4 Experiment 4: Electric and Magnetic Field Measurements

This section shows the results of the Electric and Magnetic Field measurements made along the rebar. These measurements were made to verify that the Electromagnetic field was in fact traversing along the surface of the conductor.

5.1.1.4.1 Set-Up

A ring stand was used to affix either an Electric field or Magnetic field probe above the rebar. The hoop of the magnetic field probe was always positioned so that the face of the hoop was angular to the rebar circumference so that the maximum amount of magnetic flux could be achieved through the Magnetic Field Probe. A meter length measuring stick was affixed to the table, with the zero position at the mouth of the transmitting TM coupler. A picture of this configuration (with an electric field probe) can be seen in Figure 47.

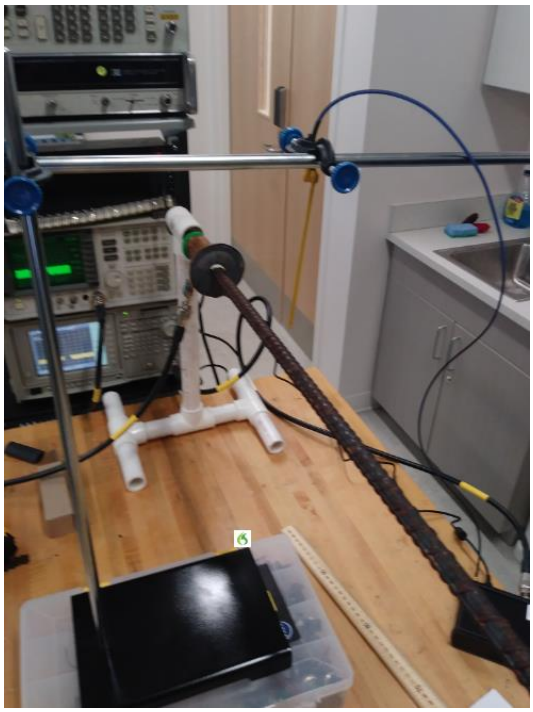

Figure 47. Electric field probe (center) affixed to a ring stand measuring the strength of the electric field at some position on the rebar.

The transmitting TM coupler, which was located at the 0-cm position, had a matching circuit affixed to its input, with a 20 dBm 2.4 GHz RF oscillator for a source. The receiving TM coupler, located 110.5 cm away from the transmitting TM coupler, was connected to a

matching circuit, which was in turn connected to a spectrum analyzer with a 50 Ω input impedance. The spectrum analyzer was just used to provide a 50 Ω load.

The Beehive Electronics probe toolkit was connected to an available Spectrum Analyzer, where the power level of the input signal corresponded to the E or H field strength measured at a particular position. The probe was swept across the rebar, maintaining the same height along the way, with the measurements recorded.

5.1.1.4.2 Results

Figure 48 shows the magnetic field strength along the rebar, 2.56-cm (about an eighth of a wavelength) away from the center of the rebar. Figure 49 shows the electric field strength along the rebar, also 2.56 cm away from the center of the rebar.

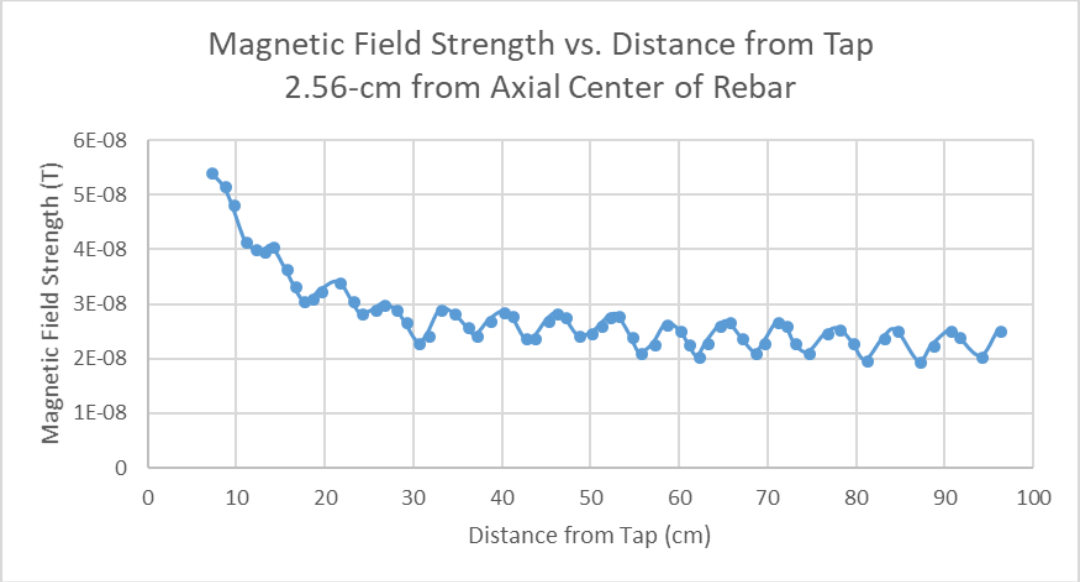

Figure 48. Magnetic Field Measurement Curve along the rebar, 2.56 cm from the center of the rebar.

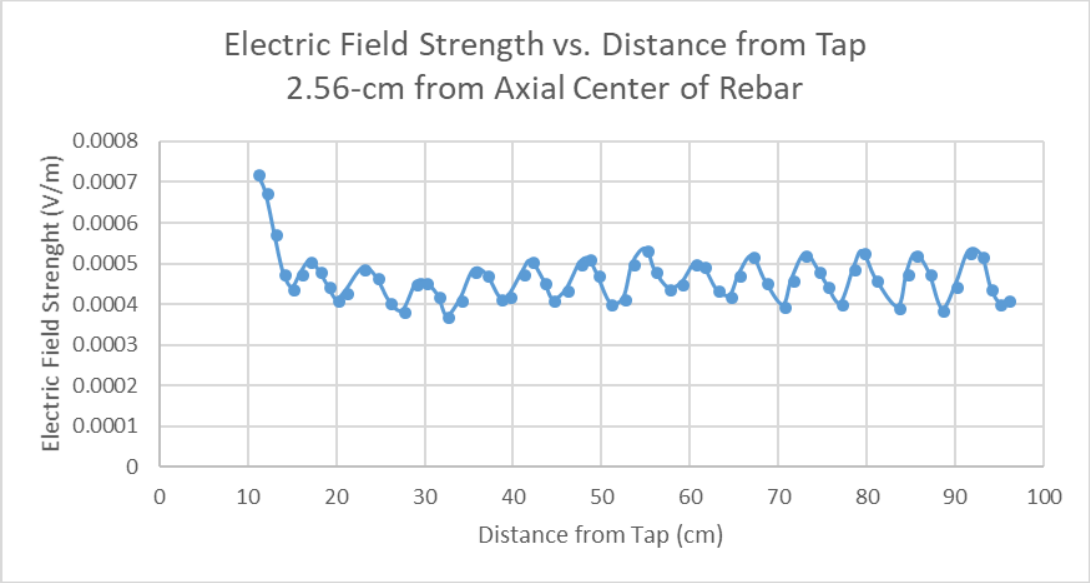

Figure 49. Electric Field Measurement Curve along the rebar, 2.56 cm from the center of the rebar.

Measurements of the magnetic field were taken at 7.24-cm away from the axial center of the rebar (which corresponds to a little over one half-wavelength). A graph of this measurement can be seen in Figure 50.

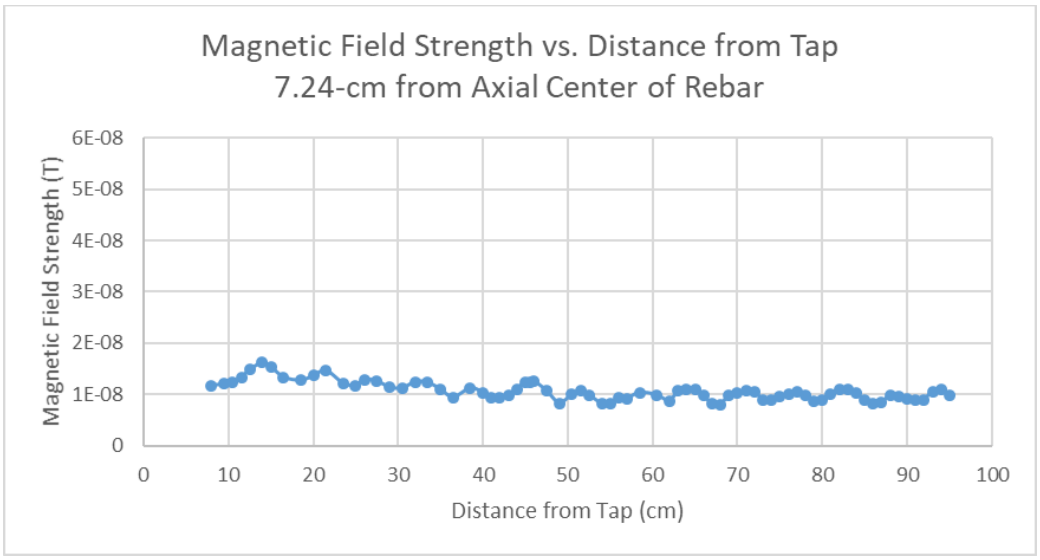

Figure 50. Magnetic Field Measurement 7.24 cm from the center of the rebar

5.1.1.4.3 Discussion

Peaks for electric field strength and eagnetic field strength tend to occur approximately 6 cm to 7 cm apart from one another, which makes sense, given that the half wavelength of 2.4 GHz is approximately 6.2 cm in free space. Moreover, when the height of the probe was raised from 2.54 cm (~1/5 λ) to 7.24 cm (~3/5 λ) above the axial center of the rebar, the measured strength of the magnetic field decreased by four orders of magnitude, lending credence to Goubau's claim that approximately 90% of the energy of the field is confined to radius of one half-wavelength around the conductor.

5.1.1.5 Experiment 5: Performance of Two TM Couplers on a Length of Rebar Using a VNA

This section shows the results of VNA measurements made on two fully constructed TM Couplers mounted to the same length of rebar. This experiment serves to evaluate the performance of this two TM Coupler system without anything else interfering with the RF power transmission. More specifically, the goal of this experiment is to eliminate the effect of the following parameters: (a) the presence of a concrete medium, (b) a rebar cage environment, and (c) a third TM Coupler tapped onto the same length of rebar, perpendicular to the rebar. Over the next few experiments, one by one, in the reverse order listed, these parameters will be added onto the experimentation.

5.1.1.5.1 Set-Up

Figure 51 shows a photograph of the set-up for Experiment 5. In this set up, TM Coupler 4 (left) and TM Coupler 7 (right) were mounted onto the same length of rebar. The TM Couplers were separated by a distance of 110.5 cm. At each end of the length of rebar, a PVC stand was used to elevate the rebar approximately 1.5 feet above the tabletop.

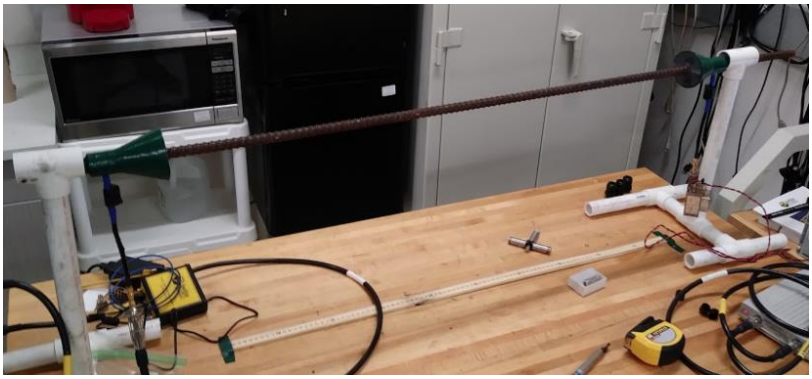

Figure 51. The Two TM Coupler Set-up for Experiment 5 with TM Coupler 4 (left) and TM Coupler 7 (right)

A diagram of the system is shown in Figure 52; in this diagram, the two TM Couplers are separated by a distance of L_1; a VNA is connected to both TM Couplers. The VNA is used to assess the S-Parameters (S11, S12, S21, S22) of the two TM Couplers system.

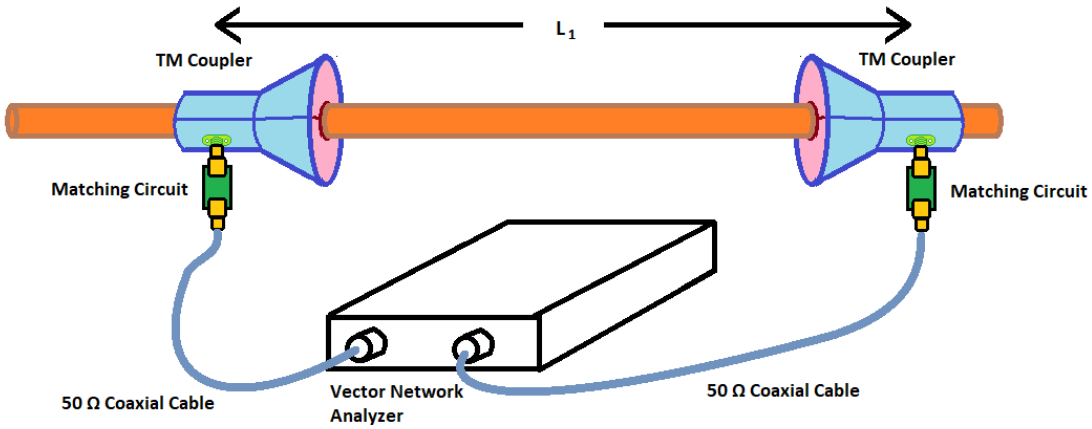

Figure 52. System diagram of Experiment 5

5.1.1.5.2 Brief description of the modification of the matching circuit.

The matching circuit was prepared for embedment in a concrete environment. In this and later experiments, the matching circuit can be seen in pictures with a black material around it — this was a result of preparing the matching circuit for concrete embedment. To prepare the matching circuit for concrete embedment, a process was undergone: (1) the matching circuit had paper placed over the 0603 components; (2) the matching circuit was wrapped with a marine-grade double-wall heat shrink, and then heat shrunk; (3) copper foil was wrapped around the matching circuit, making contact with the SMA connectors at both the input and output; (4) the matching circuit was wrapped in electrical tape to seal any openings; and finally, (5) an additional piece of marine-grade heat shrink has been applied over the copper foil wrap, and then heat shrunk.

5.1.1.5.3 Results

Using a vector network analyzer, the S-Parameters of the system were measured. Of particular interest was the input impedance. Table 1 shows the tabulated results for the TM Coupler set-up.

Port 1	**Port 2**	**Z_{in} (Ω)**	**S11 (dB)**	**S21 (dB)**	**Z_{in} (Ω)**	**S22 (dB)**	**S12 (dB)**
TM Coupler 7	TM Coupler 4	40.6 + j1.06	-19.7	-15.6	51.6 - j12.6	-18.1	-14.4

Table 1. Tabulated results for the two TM Coupler set up.

Figure 53 and Figure 54 show graphs of the S-parameter results in both log-mag and Smith Chart form.

Figure 53. Smith chart and S11 and S21 parameters of TM Coupler 7 of the two TM Coupler set up

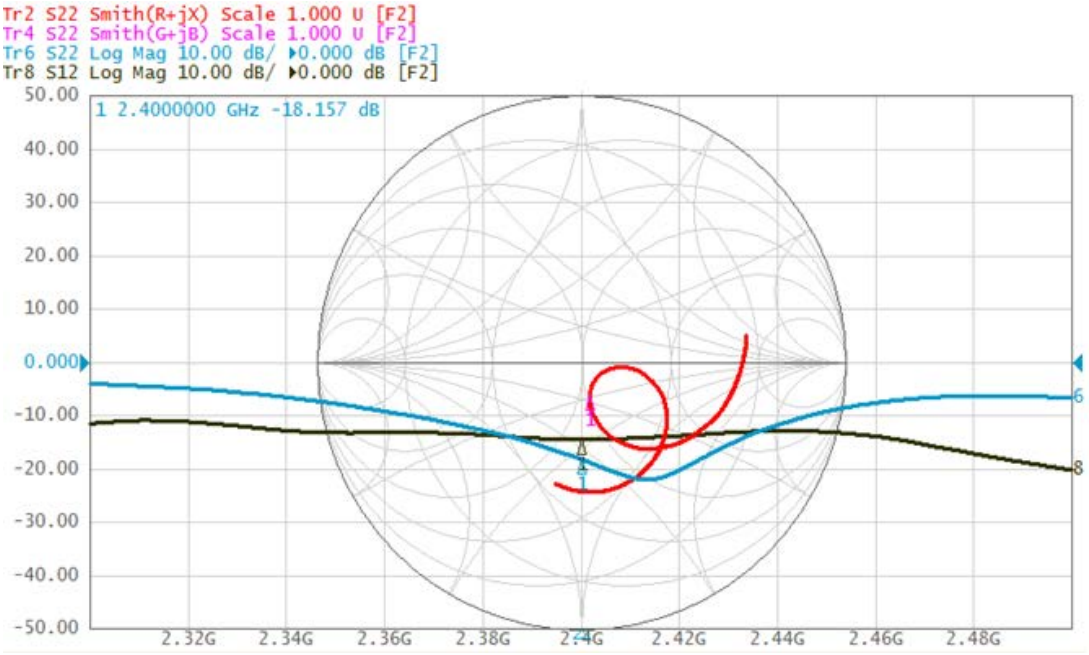

Figure 54. Smith chart and S22 and S12 parameters of TM Coupler 4 of the two TM Coupler set up

5.1.1.5.4 Discussion

For this experiment, the return loss for both TM Couplers is excellent, approaching -20 dBm, which means that almost as 1% of the power is being reflected back into the ports of the VNA. Additionally, the insertion loss of the TM Coupler system was approximately -15 dB, which means that approximately 3.16% of the input power made it through the system, from one port to the other. In comparison, the free space path loss of two isotropic antennas separated by the same distance, $L_1 = d = 110.5$ cm, would be equal to 39.1855 dB, which means that 0.012% of the power would make it from one antenna to the next. The free space path loss can be found by calculating the gain of free space, which can be found with Equation 3 [26], in which d is the distance in meters, f is frequency in hertz, and c is the speed of light in meters per second.

$$G_{free\ space}(dB) = 20\log(d) - 20\log(f) - 20\log\left(\frac{4\pi}{c}\right) \quad (3)$$

5.1.1.6 Experiment 6: Performance of Two TM Couplers on a Length of Rebar Using an Oscillator and Spectrum Analyzer

This experiment aims to confirm the performance of the insertion loss (S12 and S21) observed in Experiment 5. Insertion loss is the measurement of how much power is lost across a device or system from one port another — the metric does not inform where the power was lost to, it only refers what the amount of the loss was. Given this, if a known amount of power is inserted into a system, then by measuring the amount of power received on the other end of the system, the insertion loss can be calculated without a VNA. In this experiment, a 2.4 GHz Oven Controlled Crystal Oscillator (OXCO) that outputs power at 20 dBm is used to input power into the system, and a Spectrum Analyzer is used to measure the power received by the output of the system.

5.1.1.6.1 Set-Up

An almost identical set-up used in Experiment 5 was applied in Experiment 6: the difference is that instead of a VNA, an OXCO was used in conjunction with a Spectrum Analyzer, as can be seen in Figure 55. The 2.4 GHz OCXO was measured to output power at 19.83 dBm. The OXCO inputted power into TM Coupler 7. TM Coupler 4 received RF power, and this power was measured by the Spectrum Analyzer.

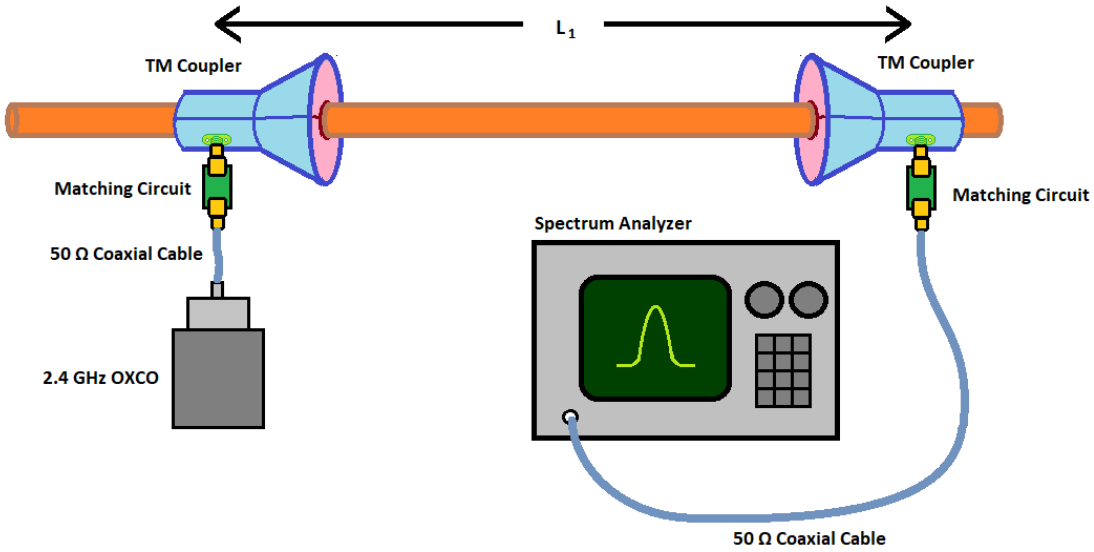

Figure 55. Diagram of the set-up for Experiment 6.

5.1.1.6.2 Results

The power received by TM Coupler 4 was 5.0 dBm, which corresponds to a 14.16 dB power loss. An image of this set up can be seen in Figure 56.

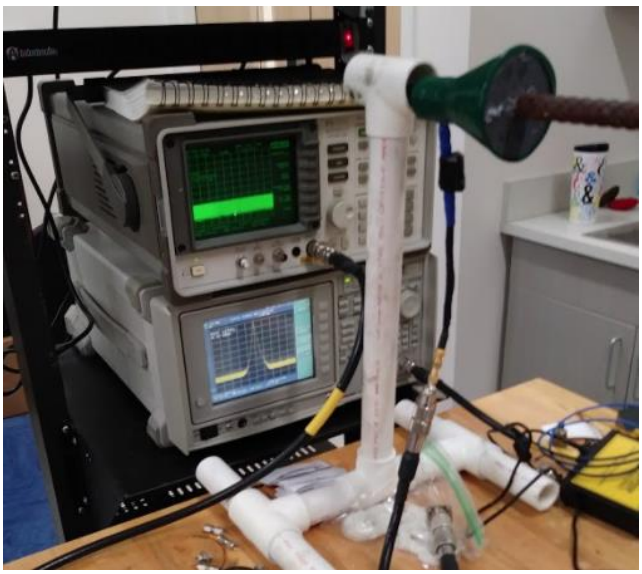

Figure 56. RF oscillator and spectrum analyzer test of the two TM Coupler set up

5.1.1.6.3 Discussion

A power loss of 14.16 dB corresponds to the results shown in Experiment 5. In Experiment 5, an S21 of approximately -15 dB was measured by the VNA, which is a power loss of 15 dB. This means that the power loss aspect of Experiment 5 was able to be replicated using an OXCO and Spectrum Analyzer.

5.1.1.7 Experiment 7: Performance of Three TM Couplers on a Length of Rebar Using a VNA

Experiment 7 is built off Experiment 5 and Experiment 6. In Experiment 7, an additional TM Coupler is added into the system. This TM Coupler perpendicularly taps off of the length of rebar that the original two TM Couplers tapped off of. The goal of this experiment is to see how an additional TM Coupler affects the system established in the prior two experiments. A VNA is used to evaluate the S-parameters of three different connections to the VNA.

5.1.1.7.1 Set-Up

Figure 57 shows the overall configuration of Experiment 7. TM Coupler 8 and TM Coupler 6 are mounted onto the same length of rebar, separated by L_1, 110.5 cm. TM Coupler 5 is mounted to a short stub of number 5 rebar, which in turn perpendicularly taps off the rebar. The tapping point of TM Coupler 5 was displaced, L_2, 61.595 cm from the tapping point of TM Coupler 8. The tapping point for TM Coupler 5 was arbitrarily selected; moreover, this position left TM Coupler 5 slightly closer to TM Coupler 6. A VNA was used to measure the S-Parameters for two TM Couplers at a time, with the unmeasured TM Coupler connected to a 50 Ω load.

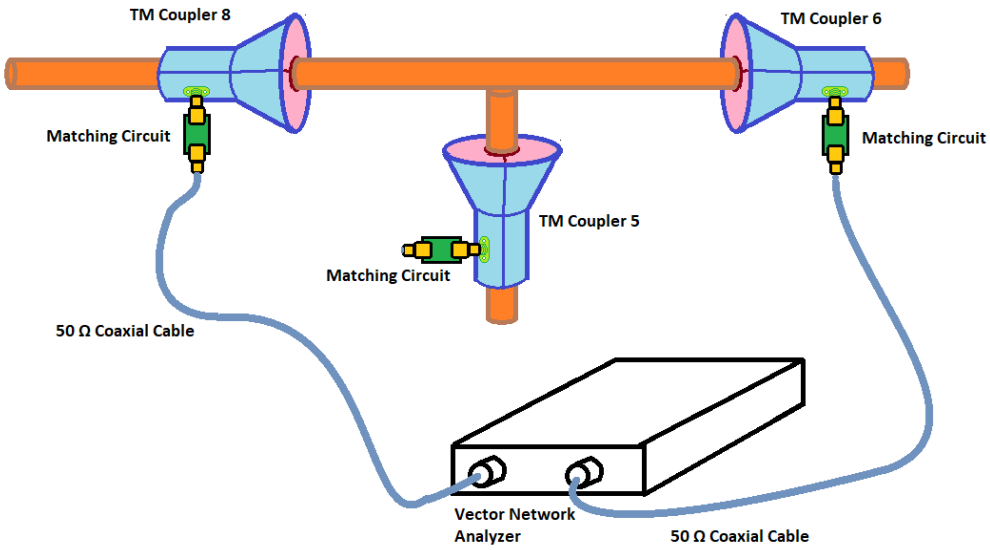

Figure 57. The overall configuration of Experiment 7

The test set up can also be seen photographed in Figure 58; in this connection, TM Coupler 5 and TM Coupler 6 are connected to the VNA.

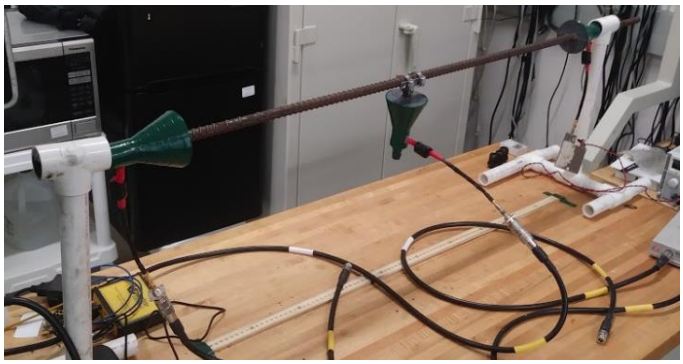

Figure 58. The Three TM Coupler set up

The S-Parameters of three different connections were measured with the connections as depicted in Figure 59. As can be seen from the figure, the following connections were made: (1) for the first connection, TM Coupler 8 and TM Coupler 5 were, respectively, connected to Port 1 and Port of the VNA; (2) for the second connection, TM Coupler 6 and TM Coupler 5 were, respectively, connected to Port 1 and Port of the VNA; (3) for the third connection, TM Coupler 6 and TM Coupler 8 were, respectively, connected to Port 1 and Port of the VNA.

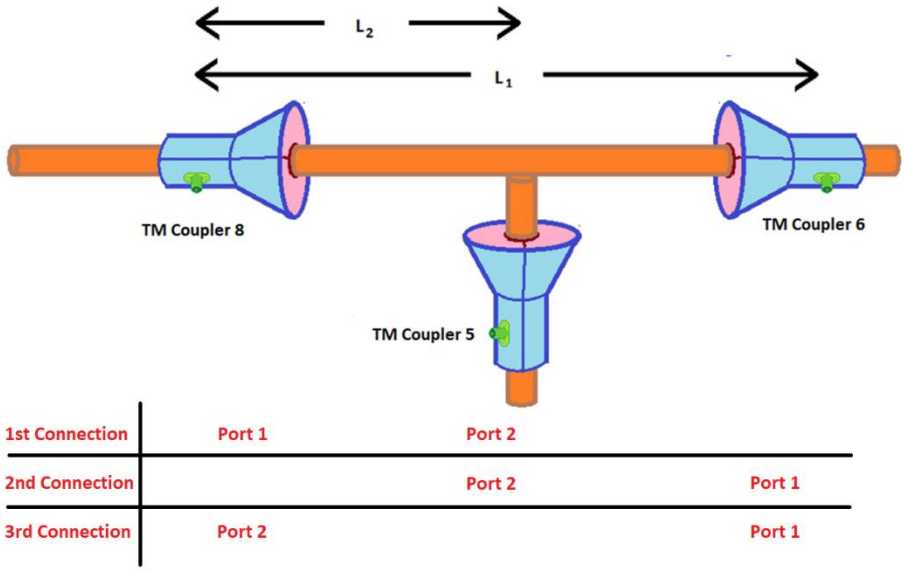

Figure 59. Diagram of the Set-Up for Experiment 7 with VNA Ports Indicated

5.1.1.7.2 Results

The results for Experiment 7 are sub-sectioned into three sections below, with each section addressing a unique connection, as shown in Figure 59.

5.1.1.7.2.1 The First Connection: TM Coupler 8 and TM Coupler 5

The results for the first connection at 2.4 GHz are shown in Table 2. The results for TM Coupler 8 from the VNA are shown in Figure 60. The results for TM Coupler 5 from the VNA are shown in Figure 61.

Port 1	Port 2	$Z_{in,1}$ (Ω)	S_{11} (dB)	S_{21} (dB)	$Z_{in,2}$ (Ω)	S_{22} (dB)	S_{12} (dB)
TM Coupler 8	TM Coupler 5	60.6 + j22.5	-13.1	-25.7	44.1 + j32.2	-9.34	-25.7

Table 2. Tabulated results for the first connection of the three TM Coupler set up

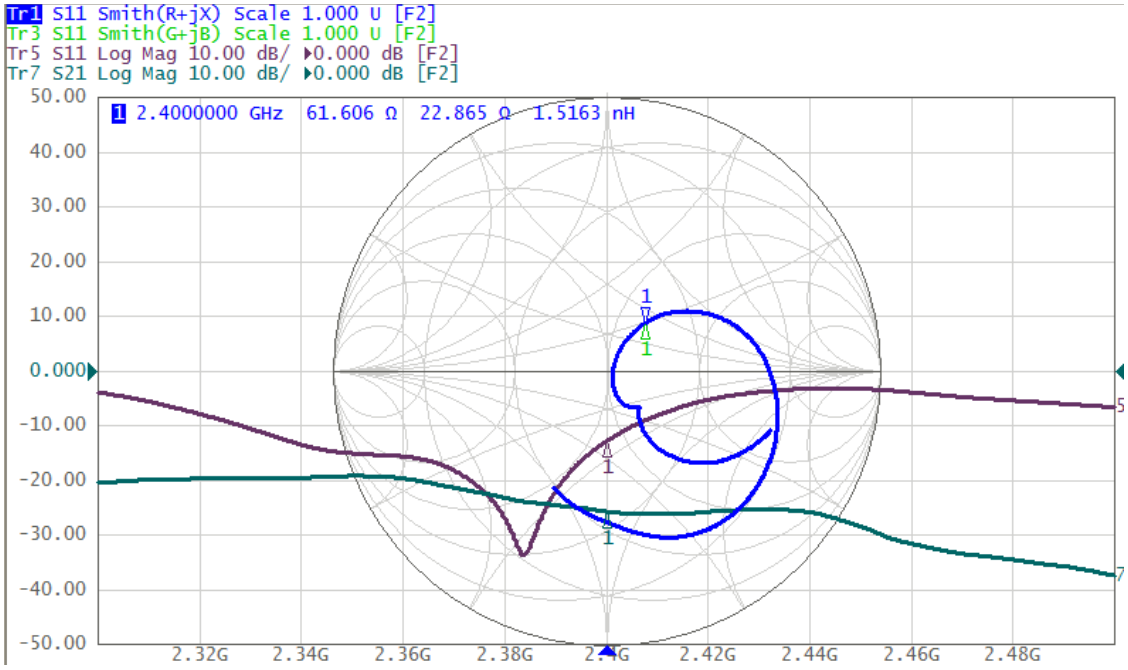

Figure 60. S-Parameters for TM Coupler 8 for the first connection

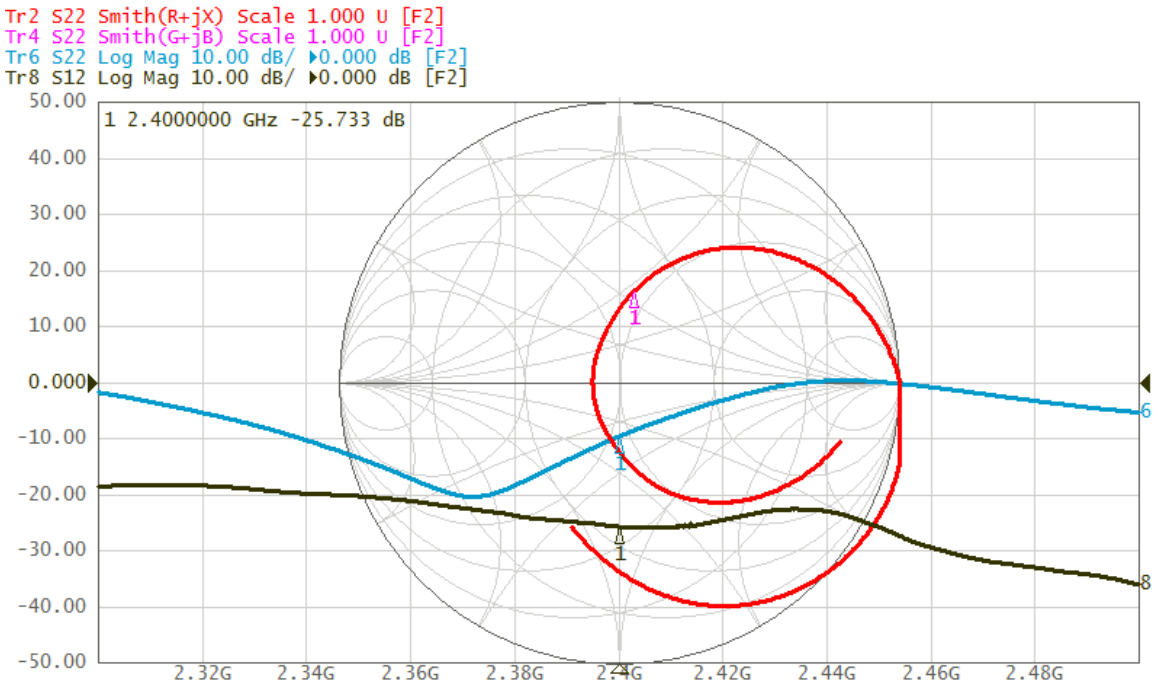

Figure 61. S-parameters for TM Coupler 5 for the first connection

5.1.1.7.2.2 The Second Connection: TM Coupler 6 and TM Coupler 5

The results for the second connection at 2.4 GHz are shown in Table 3. The results for TM Coupler 5 from the VNA are shown in Figure 62. The results for TM Coupler 6 from the VNA are shown in Figure 63.

Port 1	**Port 2**	**Z_{in1} (Ω)**	**S_{11} (dB)**	**S_{21} (dB)**	**Z_{in2} (Ω)**	**S_{22} (dB)**	**S_{12} (dB)**
TM Coupler 6	TM Coupler 5	38.4 + j3.4	-17.3	-25.2	47.1 + j30.7	-10.3	-22.8

Table 3. Tabulated results for the second connection of the three TM Coupler set up

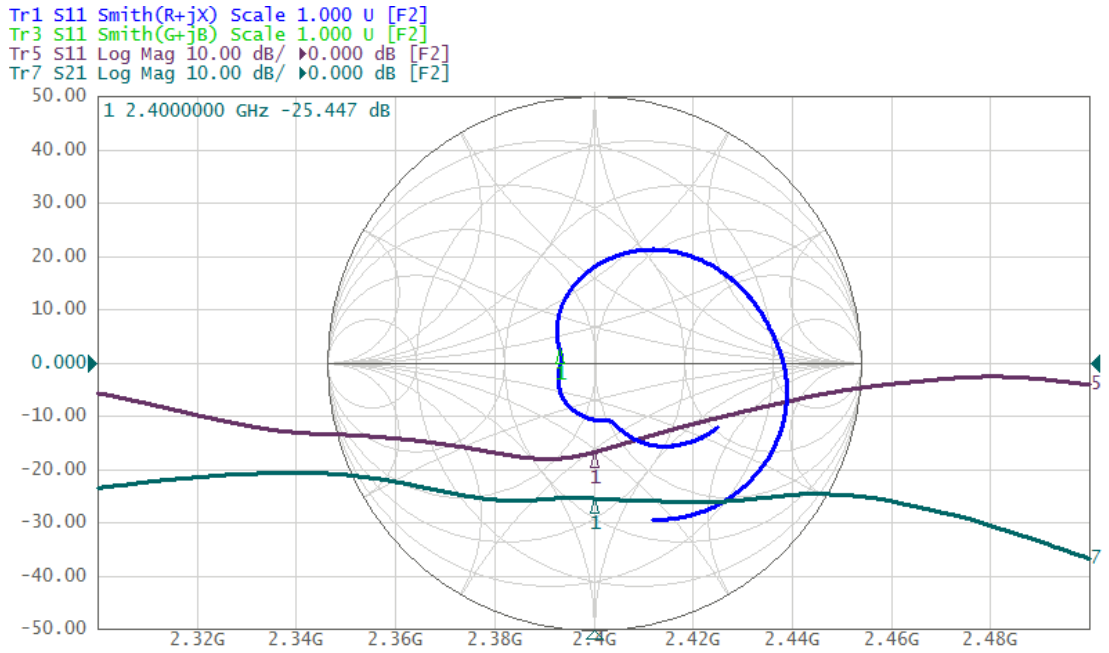

Figure 62. S-parameters for TM Coupler 6 for the second connection

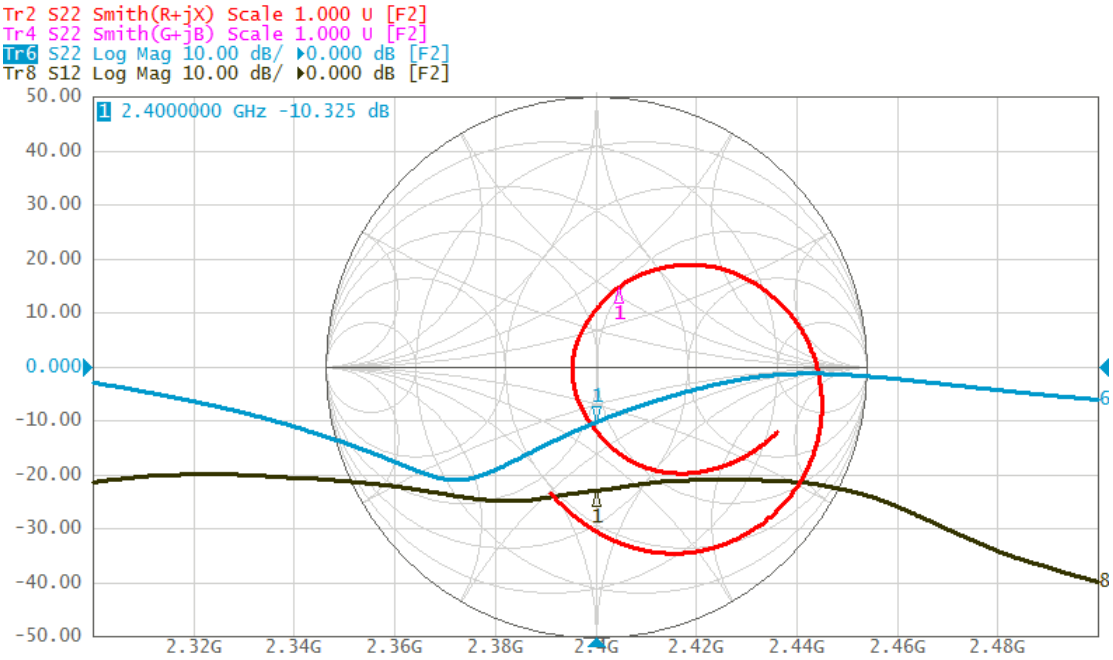

Figure 63. S-parameters for TM Coupler 5 for the second connection

5.1.1.7.2.3 The Third Connection: TM Coupler 6 and TM Coupler 8

The results for the third connection at 2.4 GHz are shown in Table 4. The results for TM Coupler 5 from the VNA are shown in Figure 64. The results for TM Coupler 8 from the VNA are shown in Figure 65.

Port 1	Port 2	$Z_{in,1}$ (Ω)	S_{11} (dB)	S_{21} (dB)	$Z_{in,2}$ (Ω)	S_{22} (dB)	S_{12} (dB)
TM Coupler 6	TM Coupler 8	37.0 + j3.8	-16.1	-16.1	63.7 + j19.6	-13.6	-13.6

Table 4. Tabulated results for the third connection of the three TM Coupler set up

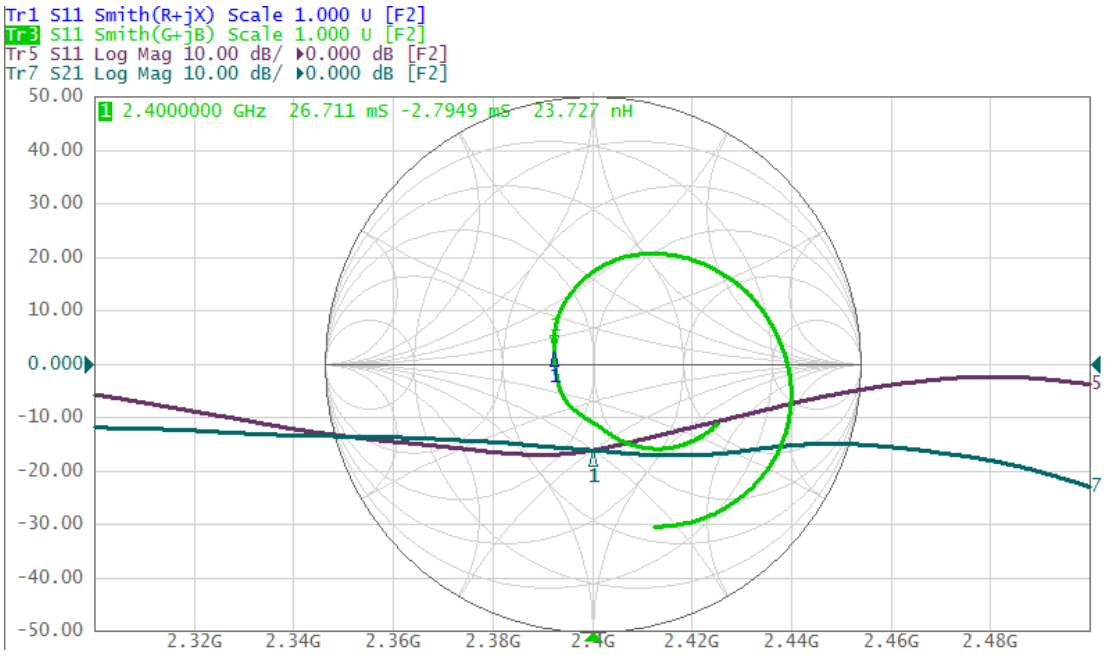

Figure 64. S-parameters for TM Coupler 6 for the third connection

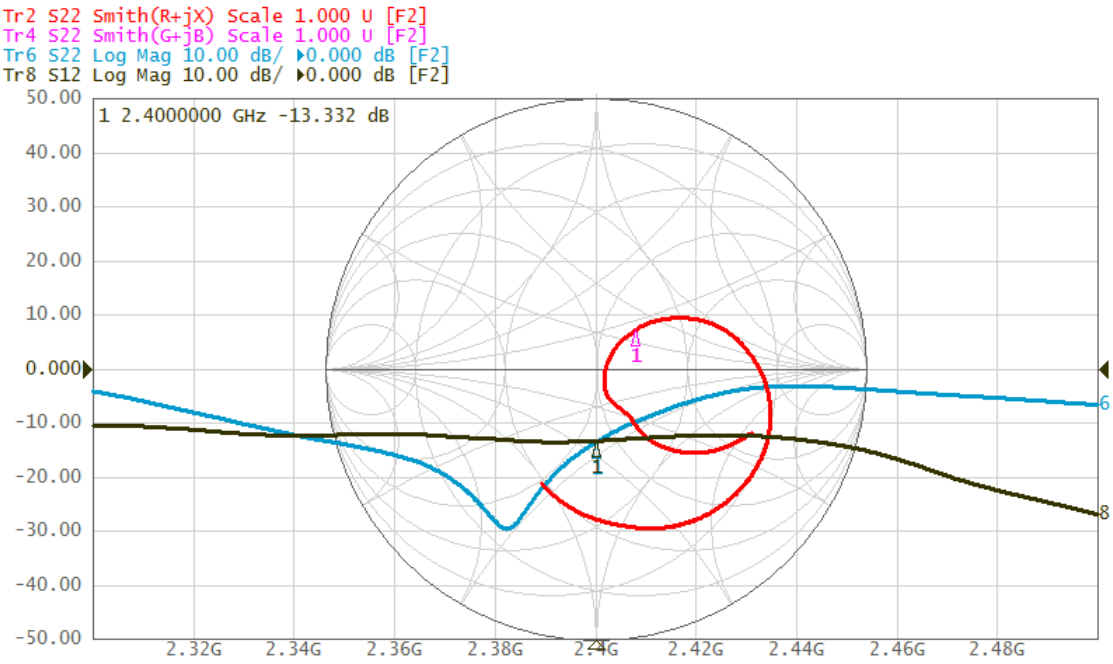

Figure 65. S-parameters for TM Coupler 8 for the third connection

5.1.1.7.3 Discussion

For the first and second connection, essentially the same configuration was applied to the VNA: (1) a TM Coupler mounted onto a length of rebar was connected to Port 1, and (2) another TM Coupler perpendicularly tapped onto the same rebar was connected to Port 2. For the third connection, essentially the same configuration as in Experiments 5 and 6 were applied to the VNA. In this manner, all three TM Couplers get measured twice.

Looking at the first and second connections, the return loss for the perpendicularly tapped TM Coupler (TM Coupler 5) was consistently measured to be around -10 dB, which means that approximately 10% of the input power into TM Coupler 5 is consistently reflected back into the VNA. What's more, the insertion loss (S12 and S21) for the first and second connection was around -25dB for all but one measurement: in the second connection, the S12 measurement was -22.8 dB, which means that almost double the power was transferred from Port 2 to Port 1 (TM Coupler 5 to TM Coupler 6) than in the reverse direction.

Looking at the third connection, the return loss for the TM Couplers appears to be consistent with the return losses observed in the first and second connection for the respective TM Coupler. That is, the return loss for TM Coupler 6 in the second and third connection is

approximately -16.5 dB, while the return loss for TM Coupler 8 for the first and third connection is approximately -13 dB. The insertion loss for the third connection, however, is considerably different from the first two connections, which is observed to be -16.1 dB for the S21 and -13.6 for the S12. This measurement is slightly alarming because it means that almost double the power was transferred from Port 2 to Port 1 (TM Coupler 8 to TM Coupler 6) than in the reverse direction.

Since TM Coupler 5 was arbitrarily positioned slightly closer to TM Coupler 6 than TM Coupler 8, it was posited that this positioning of TM Coupler 5 might have something to do with why TM Coupler 6 was receiving more power.

5.1.1.8 Experiment 8: Performance of Three TM Couplers on a Length of Rebar Using an Oscillator and Spectrum Analyzer

Experiment 8 was built off Experiment 7. In this experiment, the performance of three TM Couplers would be gauged with an OCXO and a Spectrum Analyzer. More precisely, the aim of Experiment 8 was twofold: (1) confirm the insertion loss recorded in Experiment 7, and (2) observe how the insertion loss of the system changed with the position of the perpendicularly tapped TM Coupler.

5.1.1.8.1 Set Up

The configuration for Experiment 8 can be seen in Figure 66. A 2.4 GHz OCXO was connected to TM Coupler 8. Two Spectrum Analyzers were used to simultaneously measure the received power at TM Coupler 6 and TM Coupler 5. The distance between TM Couper 6 and TM Coupler 8, L_1, was held constant at 110.5 cm. The position of TM Coupler 5 was iteratively varied (causing L_2 to vary). At each position, two sets of measurements were recorded: (a) the tap distance of TM Coupler 5, L_2, and (b) the power received by TM Couplers 5 and 6.

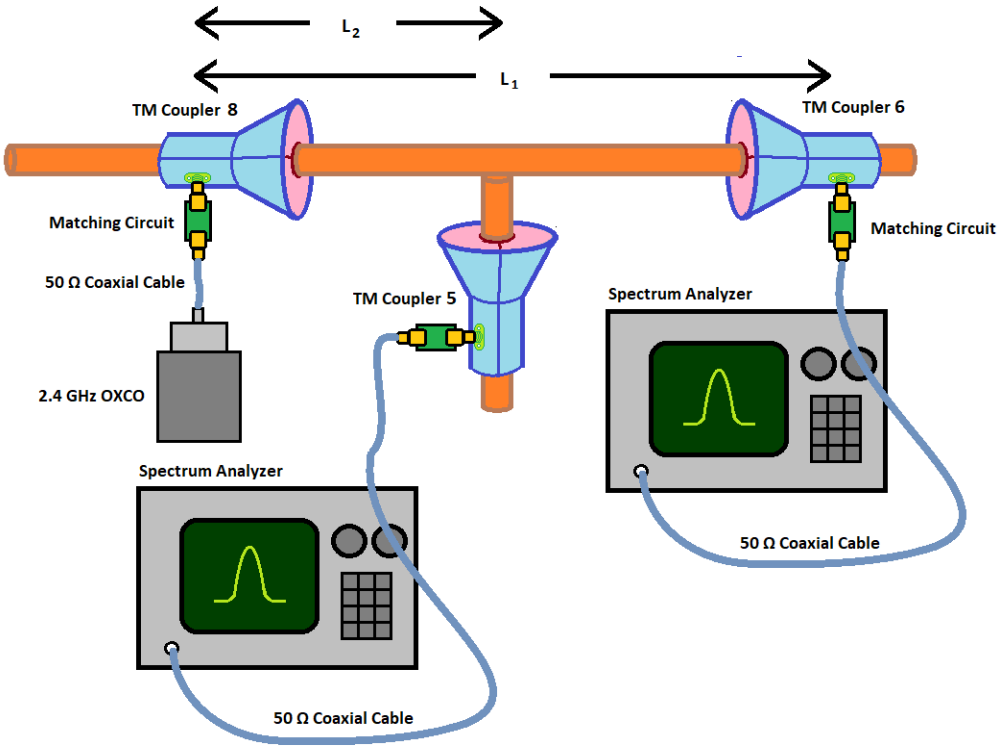

Figure 66. The configuration of Experiment 8.

A photograph of the Experiment 8 can be seen in Figure 67. In this photograph, the two Spectrum Analyzers can be seen on the left-top side, and the meter stick used to measure the tapping distance, L_2, can be seen on the table top.

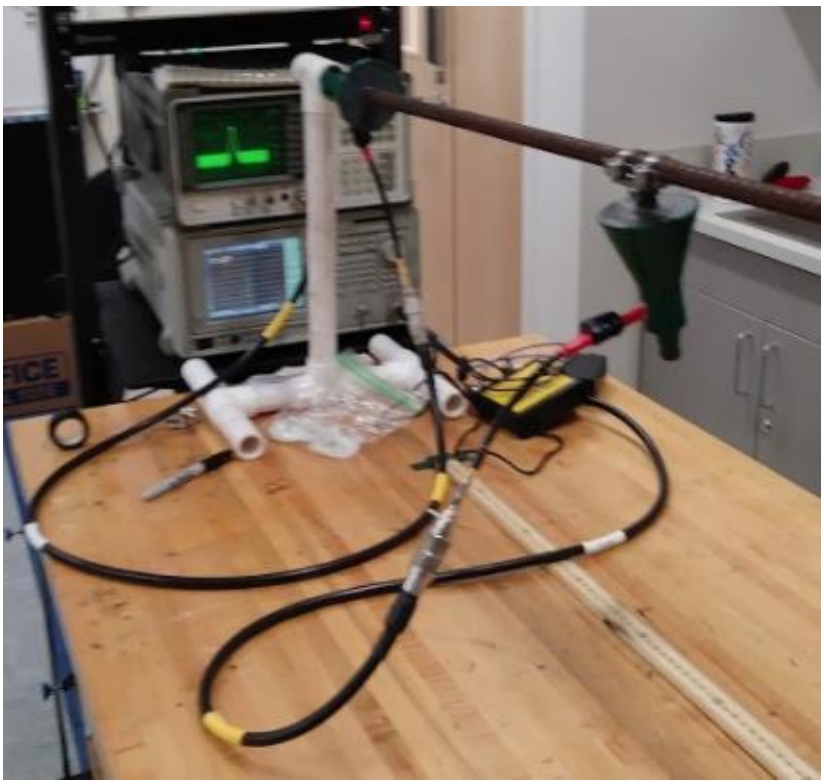

Figure 67. Photograph of Experiment 8, showing the two Spectrum Analyzers used to record the measurements.

5.1.1.8.2 Results

The results from varying the position of TM Coupler 5 can be seen in Figure 68. In this figure, the Power Gain of both measurements is displayed with respect to the tapping distance of TM Coupler 5. The power gain corresponds to the insertion loss or the S21 or S12 parameters; that is, here the insertion loss is the negative of the power gain.

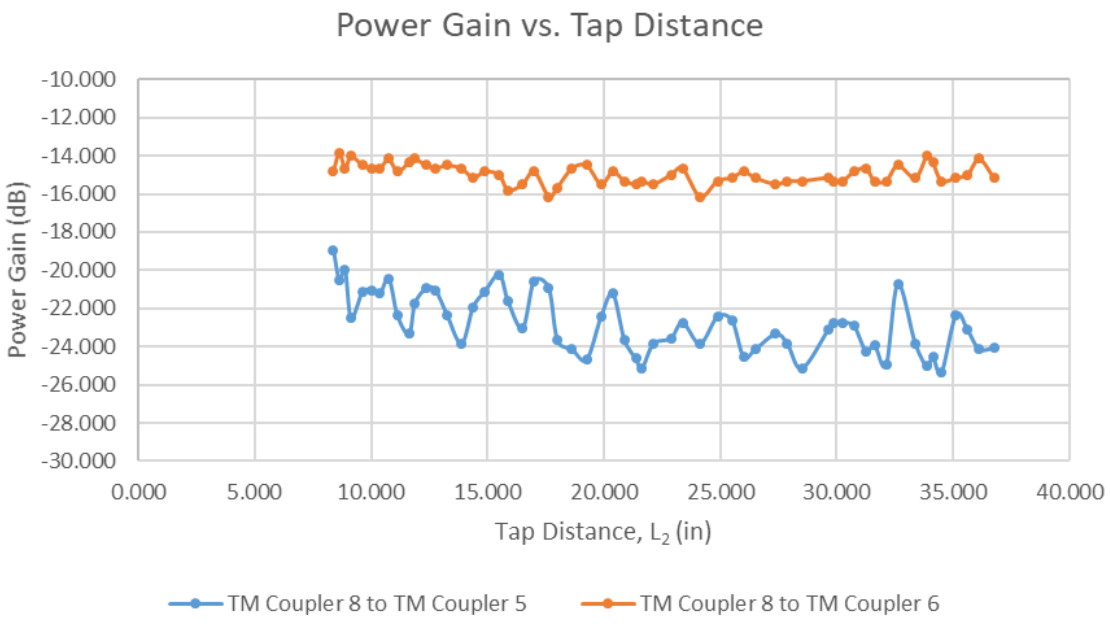

Figure 68. Power Gain of Experiment 8 with respect to varying the position of TM Coupler 5, L_2

5.1.1.8.3 Discussion

The power gain for the path from TM Coupler 8 to TM Coupler 5 varied significantly. What's more, the periodicity of the undulations this power gain appears to be double the wavelength of 2.4 GHz in free space, which shows up in Figure 68 as approximately two undulations in a 12.7 cm span. This is to be expected, because the wavelength of a field refers to the wavelength of, exclusively, the electric or magnetic field; however, the product of the electric and magnetic field is proportional to the power flux; hence, the product of two sinusoidal waveforms of the same spatial frequency will be proportional to a sinusoidal waveform of double that spatial frequency.

Another interesting feature of the graph is that the power gain of TM Coupler 8 to 5 fluctuates from approximately -20 dB to -25 dB, which means that as the position of TM Coupler 5 is varied, the lowest power received by TM Coupler 5 is 25% the maximum power received by TM Coupler 5. Nevertheless, as the position of TM Coupler 5 is varied, the power received by TM Coupler 6 is fairly constant. Therefore, the position of TM Coupler 5 has very little effect of the power received by TM Coupler 6.

5.1.1.9 Experiment 9: Performance of Three TM Couplers on Rebar Cage

Experiment 9 aimed to establish the effects of the rebar cage on the three TM Coupler system shown in Experiment 7 and Experiment 8.

5.1.1.9.1 Set-Up

Figure 69 shows the rebar cage with all three TM couplers affix to a single leg. A matching circuit was applied to each TM coupler prior to any measurements being made on the rebar cage. The input impedance is recorded using a VNA.

Figure 69. Rebar cage with three TM couplers affixed to a single leg

5.1.1.9.2 Results

The results of Experiment 9 are shown as screenshots of the VNA per each TM Coupler. Due to time constraints, only the Input Impedance and the S11 (return loss) were recorded. No losses across transmission paths were recorded for TM Couplers 11, 10, and 9.

5.1.1.9.2.1 TM Coupler 11 — Perpendicular Tap Off of Rebar Leg

Figure 70 shows the results from the VNA for the TM Coupler perpendicularly tapping off the vertical rebar leg. The input impedance is 35.8+ j0.1 Ω. The S11 parameter is -16.1 dB.

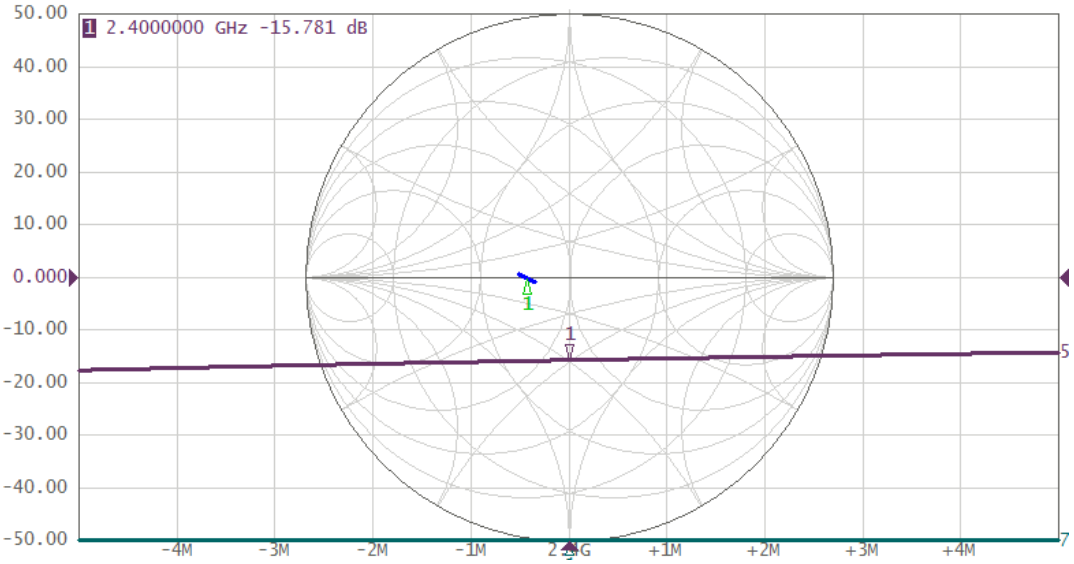

Figure 70. VNA results for TM coupler that was perpendicularly affixed to the leg (center)

5.1.1.9.2.2 TM Coupler 10 — Bottom TM Coupler

Figure 71 shows the results from the VNA for the TM coupler affixed to the rebar leg at the bottom. The input impedance is 42.4+ j 5 .9 Ω. The S11 parameter is -19.6 dB.

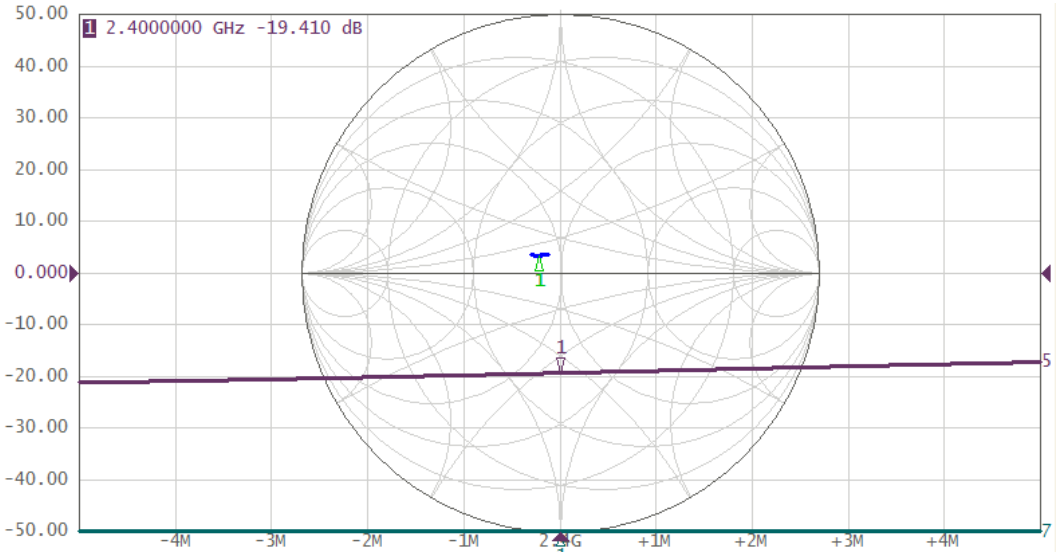

Figure 71. VNA results for TM coupler that was affixed to the bottom of the leg

5.1.1.9.2.3 TM Coupler 9 — Top TM Coupler

Figure 72 shows the results from the VNA for the TM coupler affixed to the rebar leg at the top. The input impedance is 30.3+ j8.3 Ω. The S11 parameter is -11.6 dB.

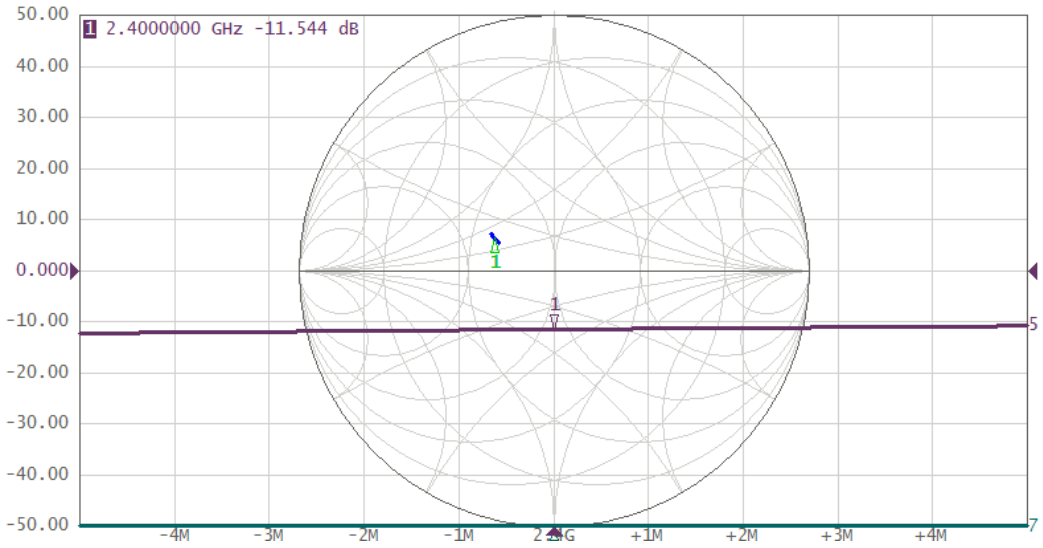

Figure 72. VNA results for the TM coupler that was affixed to the top of the leg

5.1.1.9.3 Discussion

The results of Experiment 9 indicate that the return loss for each of the TM Coupler was, at most, -11.6 dB, which means that, at worst, no more than 10% of the power was being reflected from the TM Coupler, which meant that all of the TM Couplers were fairly well matched to a 50 Ω source or load. This meant that these TM Couplers were ready to be inserted into the concrete.

5.1.2 TM Coupler Experimentation in Concrete

This section discusses the experimentation that took place when the TM couplers were embedded in concrete. The process for pouring of the concrete for Experiment 10 and 11 is described in Appendix B – Embedding the First Design Approach in Concrete.

Initially, three experiments were planned for, for the concrete medium. These three experiments were planned as so:

- one experiment would utilize two TM Couplers mounted to a length of rebar (e.g. Experiment 5 and 6)
- one experiment would utilize two TM Couplers mounted to a length of rebar with a third TM Coupler perpendicularly mounted to the same length of rebar (e.g. Experiment 7 and 8);
- one experiment would utilize two TM Couplers mounted to a length of rebar with a third TM Coupler perpendicularly mounted to the same length of rebar, but with this length of rebar as part of a rebar cage (e.g. Experiment 9).

The first two experiments were set up and run; these were Experiments 10 and 11. During these two experiments, it was found that the concrete medium provided too much attenuation for any RF energy to propagate through the medium at 2.4 GHz. After this finding, the third planned experiment was abandoned. A photo of the aftermath of the concrete preparation for Experiments 10 and 11 can be seen in Figure 73.

The results for Experiment 10 are available in this section. However, the results for Experiment 11 are so extensive that they have been shown in detail in **Error! Reference source not found.**.

Figure 73. The Concrete Preparation for Experiments 10 and 11

5.1.2.1 Experiment 10: Performance of Two TM Couplers on a Length of Rebar

The aim of Experiment 10 was to establish the effect that a concrete medium has on a single line conduction system as presented in Experiments 5 and 6. Having established the results for such a system with air as the medium surrounding single line conduction in Experiments 5 and 6, the results that would be observed in Experiment 10 would provide data to compare against, so that the effects of concrete could be teased out.

5.1.2.1.1 Set-Up

The same length of rebar with the same TM Couplers as in Experiments 5 and 6 was embedded into a concrete mixture that was poured into an 8 inch diameter concrete molding tube that was 4 feet in length. There were two holes in the concrete molding tube with cord grips installed near the TM Coupler mounting positions. SMA cables were installed onto the TM Couplers and routed through the cord grips so that electrical access could be made to the TM Couplers. After the concrete had hardened, a VNA was connected to the TM Couplers, and measurements were made. Figure 74 shows a diagram of the set-up of Experiment 10.

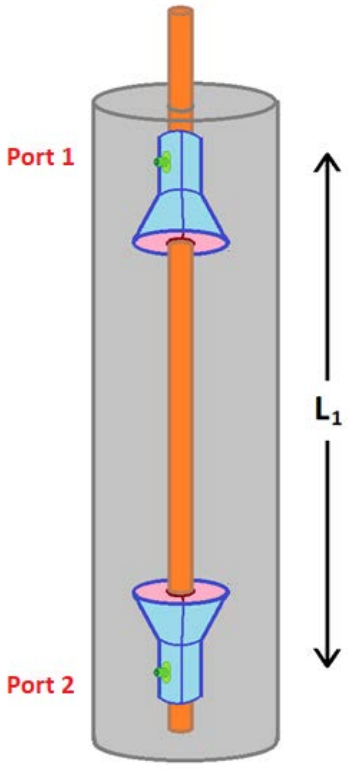

Figure 74. Diagram of the set-up of Experiment 10

5.1.2.1.2 Results

This section displays the results for Measurement 1 and Measurement 2 for Experiment 10. The results are presented in superimposed graphs. The superimposed graphs include an admittance Smith chart and an impedance Smith chart, and the XY graphs for the S-Parameters. Only two measurements were taken over the span of two days. Port 1 was connected to the top SMA cable. Port 2 was connected to the bottom SMA cable.

Eleven days after the concrete pour, Measurement 1 of Experiment 10 was conducted. The S-Parameters were recorded, centered at 2.4 GHz, and then the S-Parameters were recorded again but with the full span of the VNA.

Twelve days after the concrete pour, Measurement 2 of Experiment 10 was taken. Like in Measurement 1, the S-Parameters were recorded, centered at 2.4 GHz, and then the S-Parameters were recorded again but with the full span of the VNA. However, after a peculiarity was noticed towards the DC end of the spectrum, the S-Parameters were recorded again with the span set to 9kHz to 1.5GHz, and then again with the span set to 9kHz to 200MHz.

5.1.2.1.2.1 Measurement 1of Experiment 10, centered at 2.4 GHz

The frequency was centered at 2.4 GHz, with the span of 20 MHz. Figure 75 shows the Port 1 results. Figure 76 shows the port 2 results.

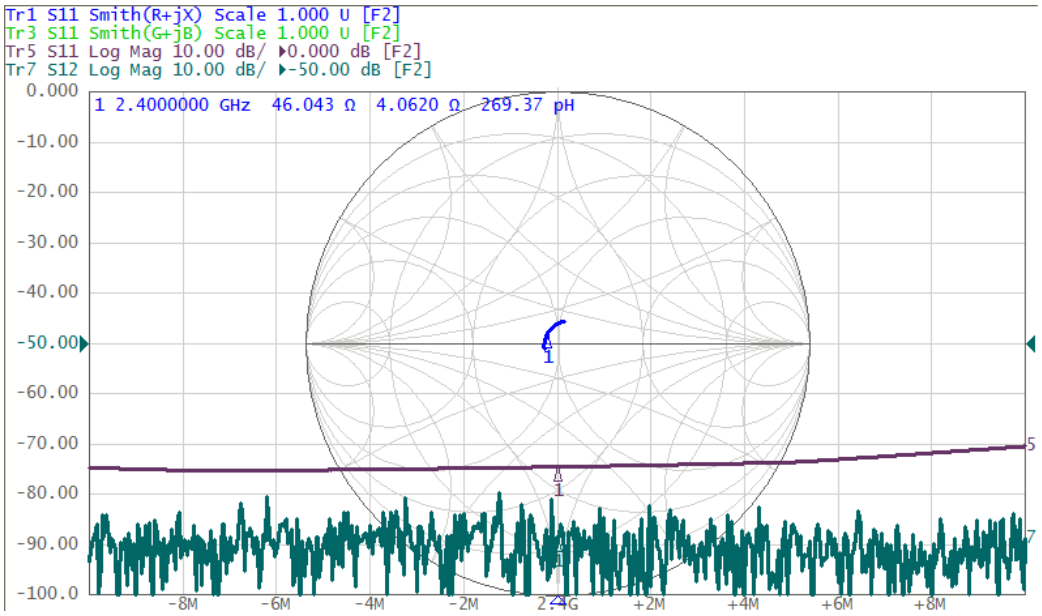

Figure 75. Port 1 results for Measurement 1 at 2.4 GHz

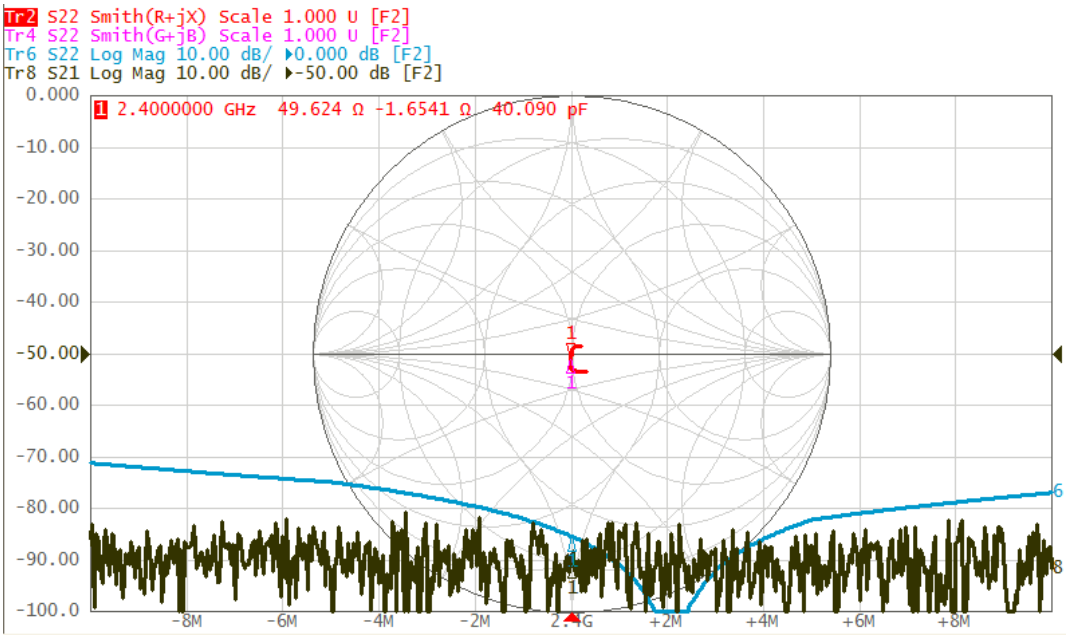

Figure 76. Port 2 results for Measurement 1 at 2.4 GHz

5.1.2.1.2.2 Measurement 1 of Experiment 10 at Full Span

The VNA was also used to determine the S-parameters across the full sweep of the frequency range available to the VNA. Figure 77 shows the Port 1 results for a full sweep for Measurement 1. Figure 78 shows the Port 2 results for a full sweep for Measurement 1.

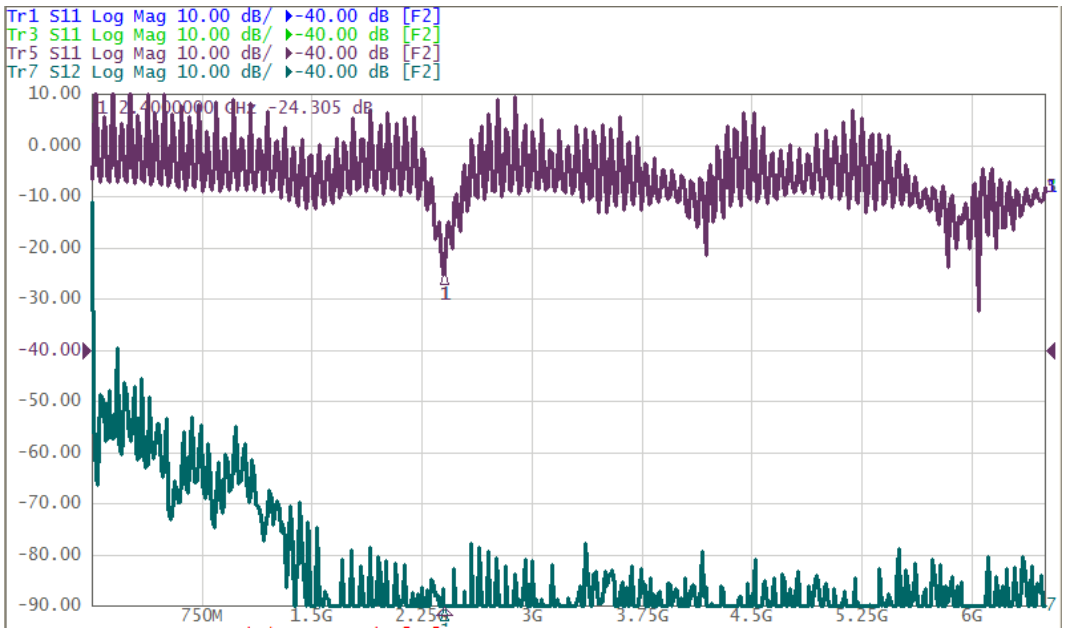

Figure 77. Port 1 results for full sweep for Measurement 1

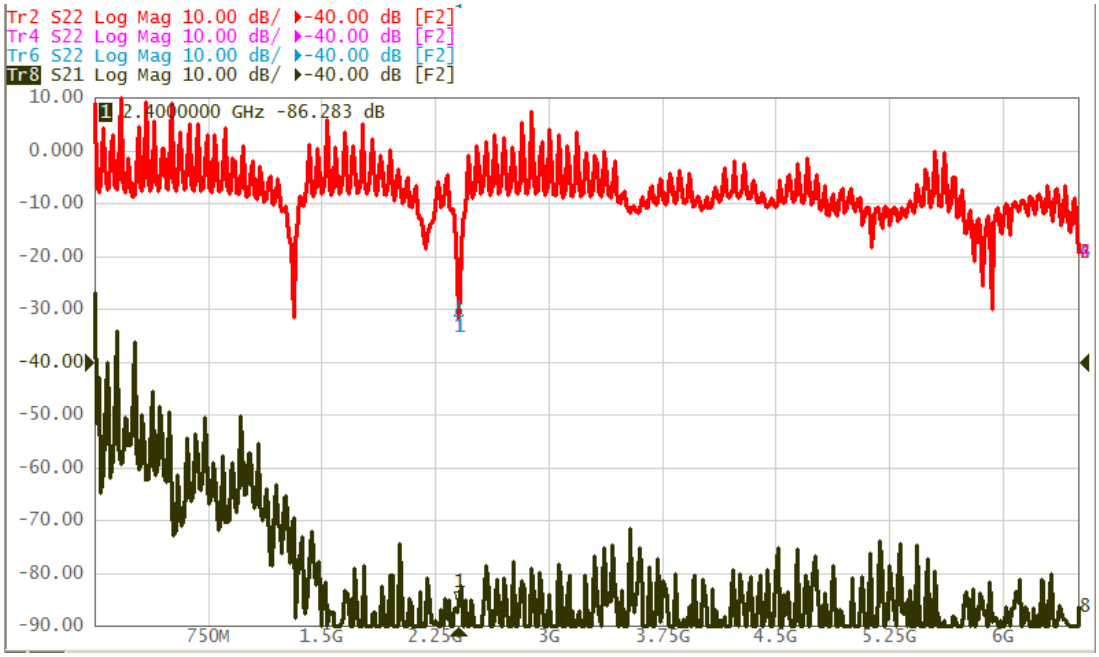

Figure 78. Port 2 results for full sweep of Measurement 1

5.1.2.1.2.3 Measurement 2 of Experiment 10, centered at 2.4 GHz

Port 2 was connected to the bottom SMA cable. The frequency was centered at 2.4 GHz, with the span of 20 MHz. Figure 79 shows the results for Measurement 2 at 2.4 GHz for Port 1. Figure 80 shows the results for Measurement 2 at 2.4 GHz for Port 2.

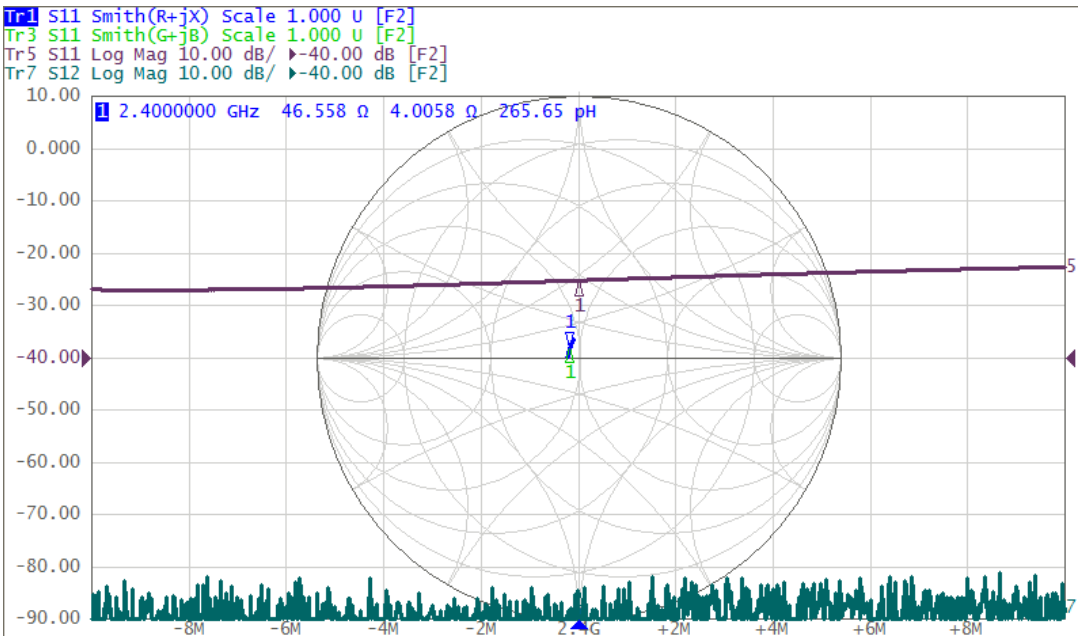

Figure 79. Port 1 for Measurement 2 at 2.4 GHz

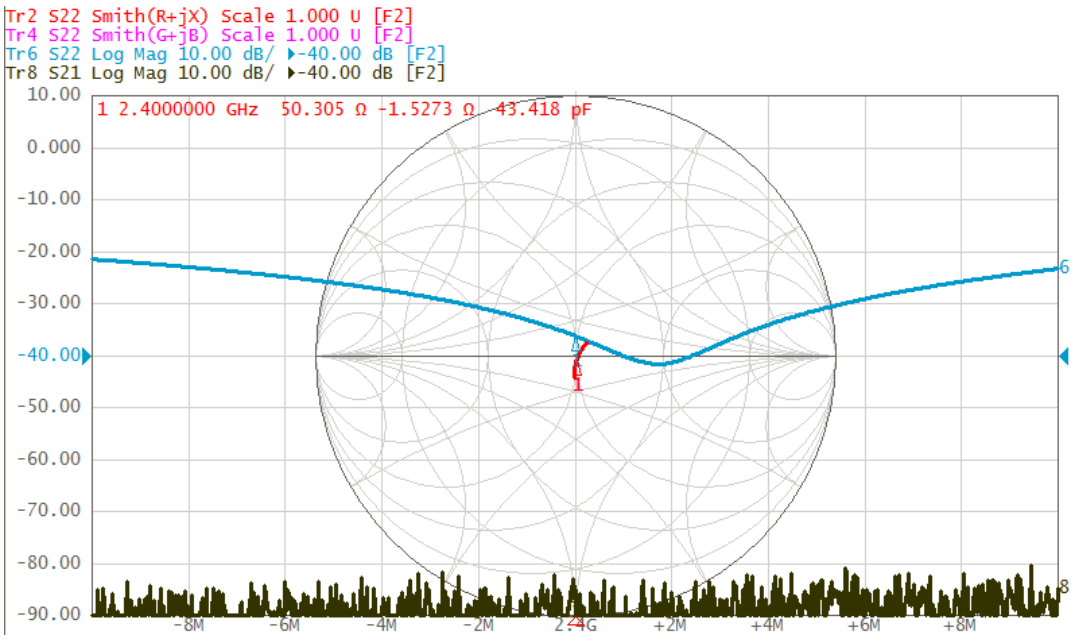

Figure 80. Port 2 for Measurement 2 at 2.4 GHz

5.1.2.1.2.4 Measurement 2 of Experiment 10 at Full Span

The VNA was also used to determine the S-Parameters across the full sweep of the frequency range available to the VNA. Figure 77 shows the Port 1 results for a full sweep for Measurement 2. Figure 78 shows the Port 2 results for a full sweep for Measurement 2.

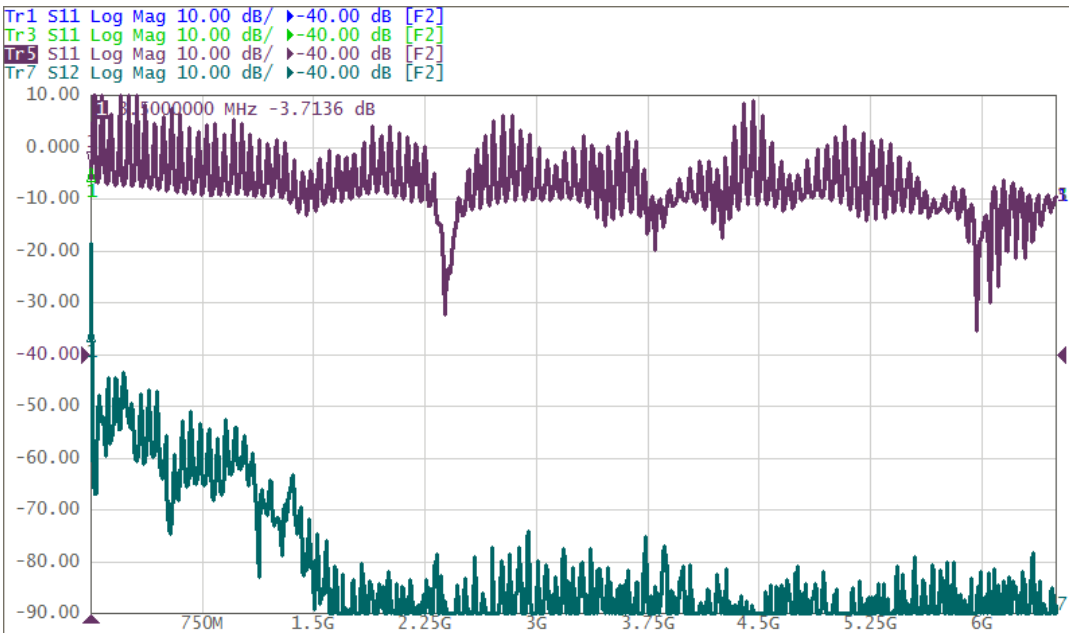

Figure 81. Port 1 for Measurement 2 at full span

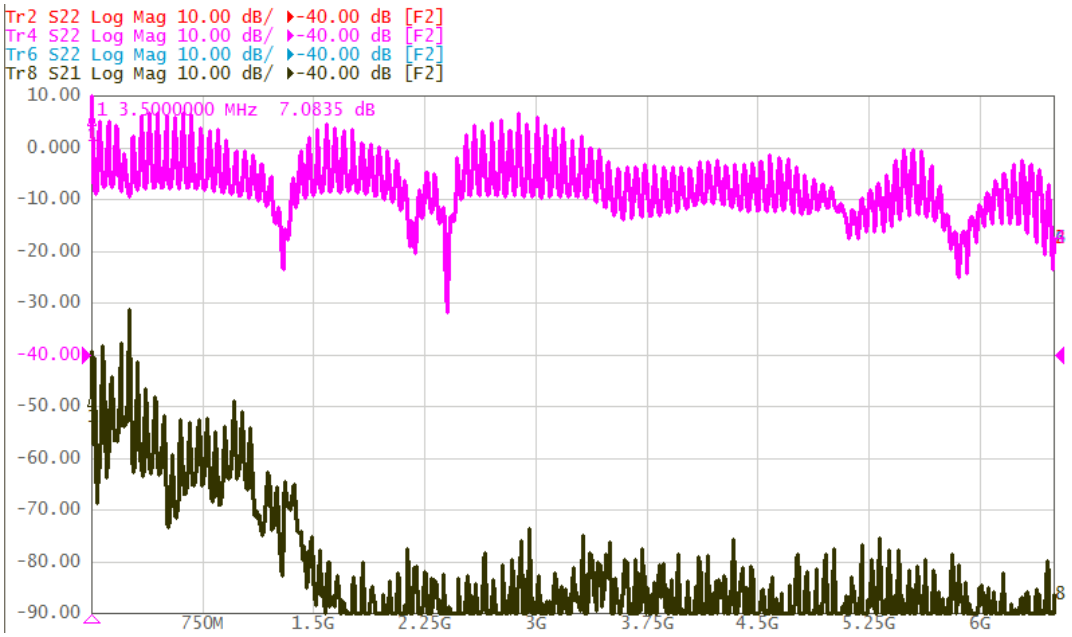

Figure 82. Port 2 for Measurement 2 at full span

5.1.2.1.2.5 Measurement 2 of Experiment 10 at 9kHz to 1.5GHz

These are the measurements taken from 9kHz to 1.5GHz. Figure 83 shows the results for Measurement 2 for a 9kHz to 1.5GHz sweep for Port 1. Figure 84 shows the results for Measurement 2 for a 9kHz to 1.5GHz sweep for Port 2.

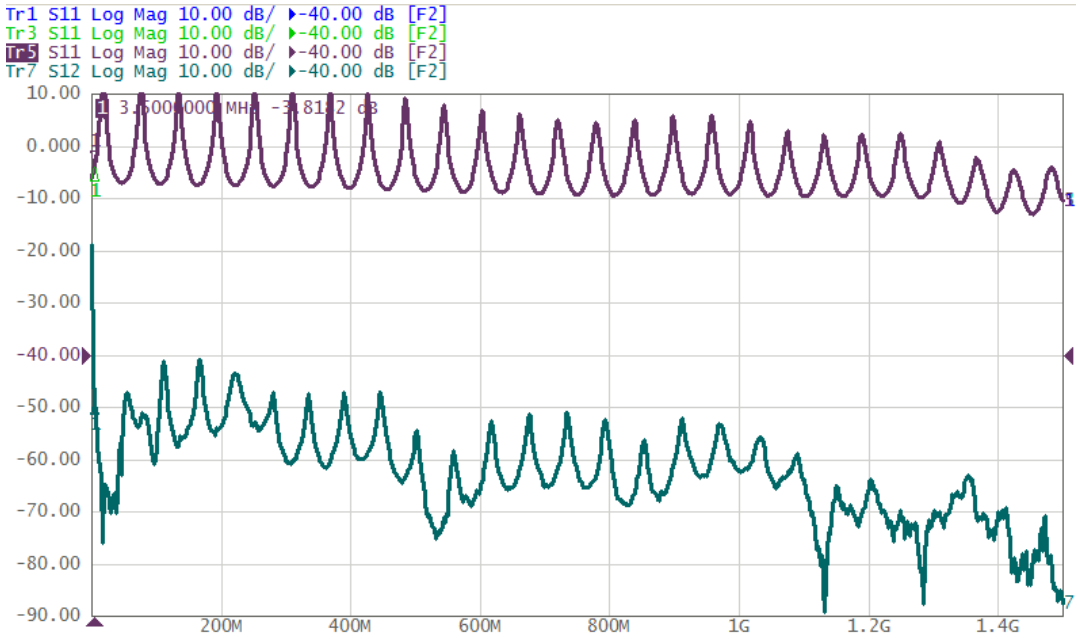

Figure 83. Port 1 for Measurement 2 at 9 kHz to 1.5 GHz

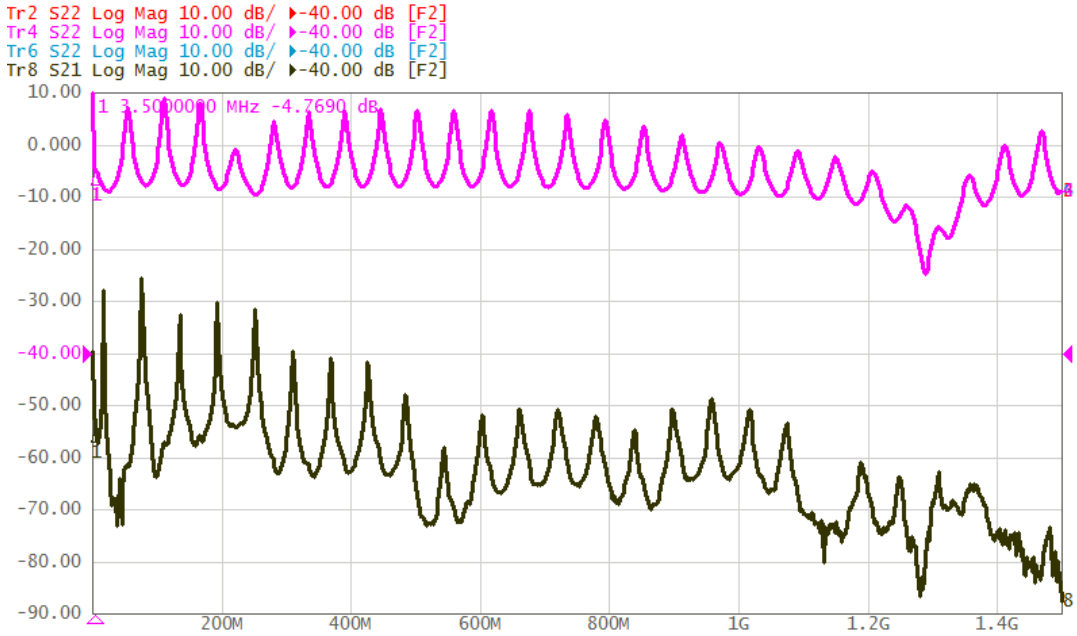

Figure 84. Port 2 for Measurement 2 at 9 kHz to 1.5 GHz

5.1.2.1.2.6 Measurement 2 of Experiment 10 at 9kHz to 200MHz

These are the measurements taken from 9kHz to 200MHz. Figure 85 shows the results for Measurement 2 for a 9kHz to 200MHz sweep for Port 1. Figure 86 shows the results for Measurement 2 for a 9kHz to 200MHz sweep for Port 2.

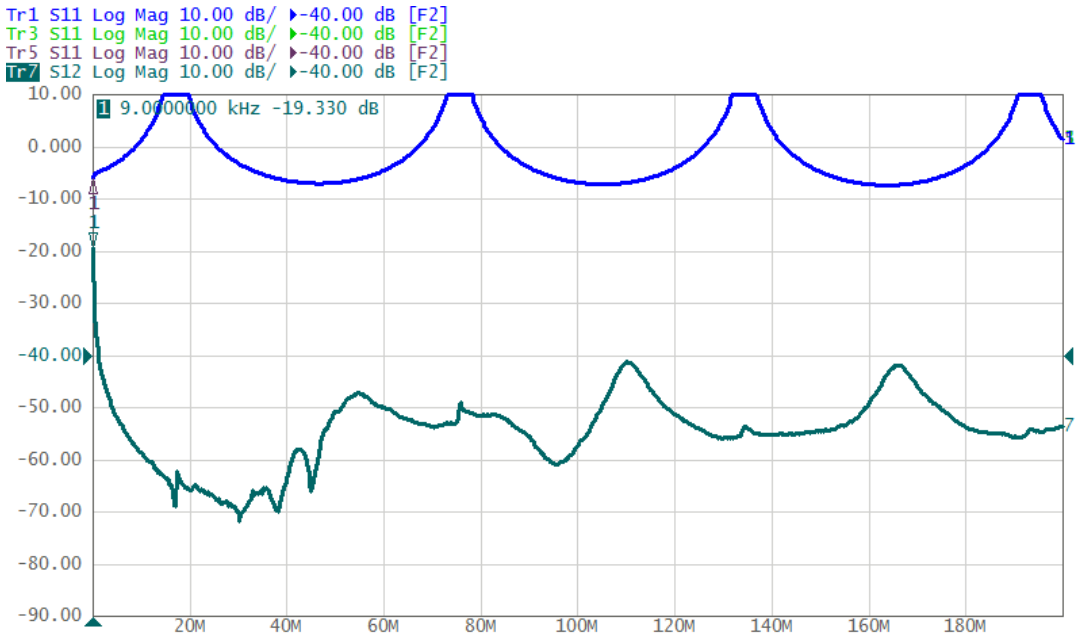

Figure 85. Port 1 for Measurement 2 at 9kHz to 200MHz

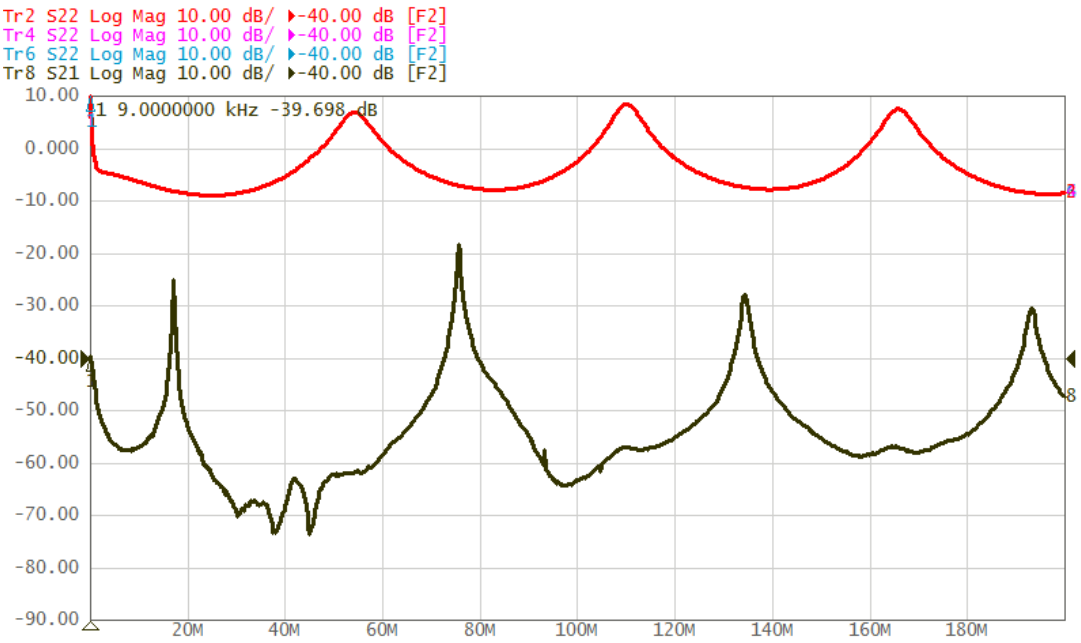

Figure 86. Port 2 for Measurement 2 at 9kHz to 200MHz

5.1.2.1.3 Discussion

The results of Measurement 1 indicated that the concrete medium attenuated the RF power at 2.4 GHz well below the noise floor of the VNA. As can be seen from Figure 75 and Figure 76, while the S11 and S22 parameters looked very good with both below -20 dB (the input impedance was almost 50 Ω, exactly!), the S12 and S21 parameters were horrible, indicating that essentially none of the RF power transmitted through the single line conduction. However, when the span of the measurement was widened, it was noticed that frequencies closer to the DC end of the spectrum were propagating through. More precisely, as can be seen in Figure 77 and Figure 78, frequencies below 1.5 GHz were detectable by the VNA. This observation gave reason to investigate more closely the behavior of the system at lower frequencies, which is what was done in Measurement 2.

The results of Measurement 2 again showed that the RF power at 2.4 GHz was attenuated well below the noise floor of the VNA, as can be seen in Figure 79 and Figure 80; and again showed that the VNA was able to detect RF power at frequencies below 1.5 GHz, as can be seen in Figure 81 and Figure 82. However, in Figure 83 – Figure 86, the insertion loss shows that as frequency decreases, in general, the amount of power detected increases. As shown in Figure 85, at 9 kHz the VNA was able to detect an approximately 19 dB loss through the concrete.

5.1.2.2 Experiment 11: Three TM Couplers in Concrete

The aim of Experiment 11 was to establish the effect that a concrete medium has on a single line conduction system as presented in Experiments 7 and 8. Having established the results for such a system with air as the medium surrounding single line conduction in Experiments 7 and 8, the results that would be observed in Experiment 11 would provide data to compare against, so that the effects of concrete could be teased out.

5.1.2.2.1 Set-Up

Several measurements were taken over the span of two days. The same length of rebar with the same three TM Couplers as in Experiments 7 and 8 was embedded into a concrete mixture that was poured into a 12 inch diameter concrete molding tube that was 4 feet in length. There were three holes in the concrete molding tube with cord grips installed near the TM Coupler mounting positions. SMA cables were installed onto the TM Couplers and routed through the cord grips so that electrical access could be made to the TM Couplers. After the concrete had hardened, a VNA was connected to the TM Couplers, and measurements were made. Figure 87 shows a diagram of the set-up of Experiment 11.

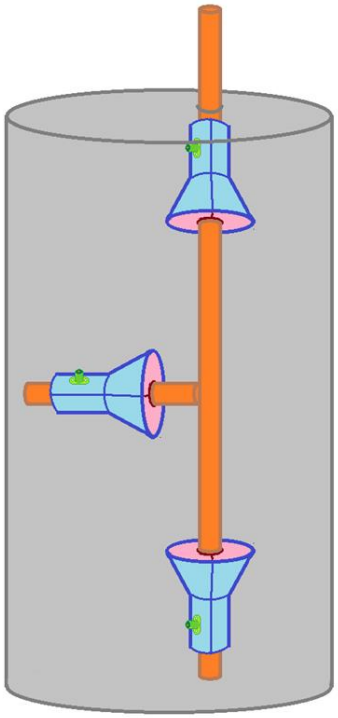

Figure 87. The set-up for Experiment 11

5.1.2.2.2 Results

The full results for Experiment 11 in concrete can be found in **Error! Reference source not found.**. The results of Experiment 11 reflect the results of Experiment 10; for example, as shown in Figure 88, at full span it can be seen that below 1.5 GHz the VNA is able to detect RF power through the rebar, and towards the DC range a significant amount of RF power is able to be detected.

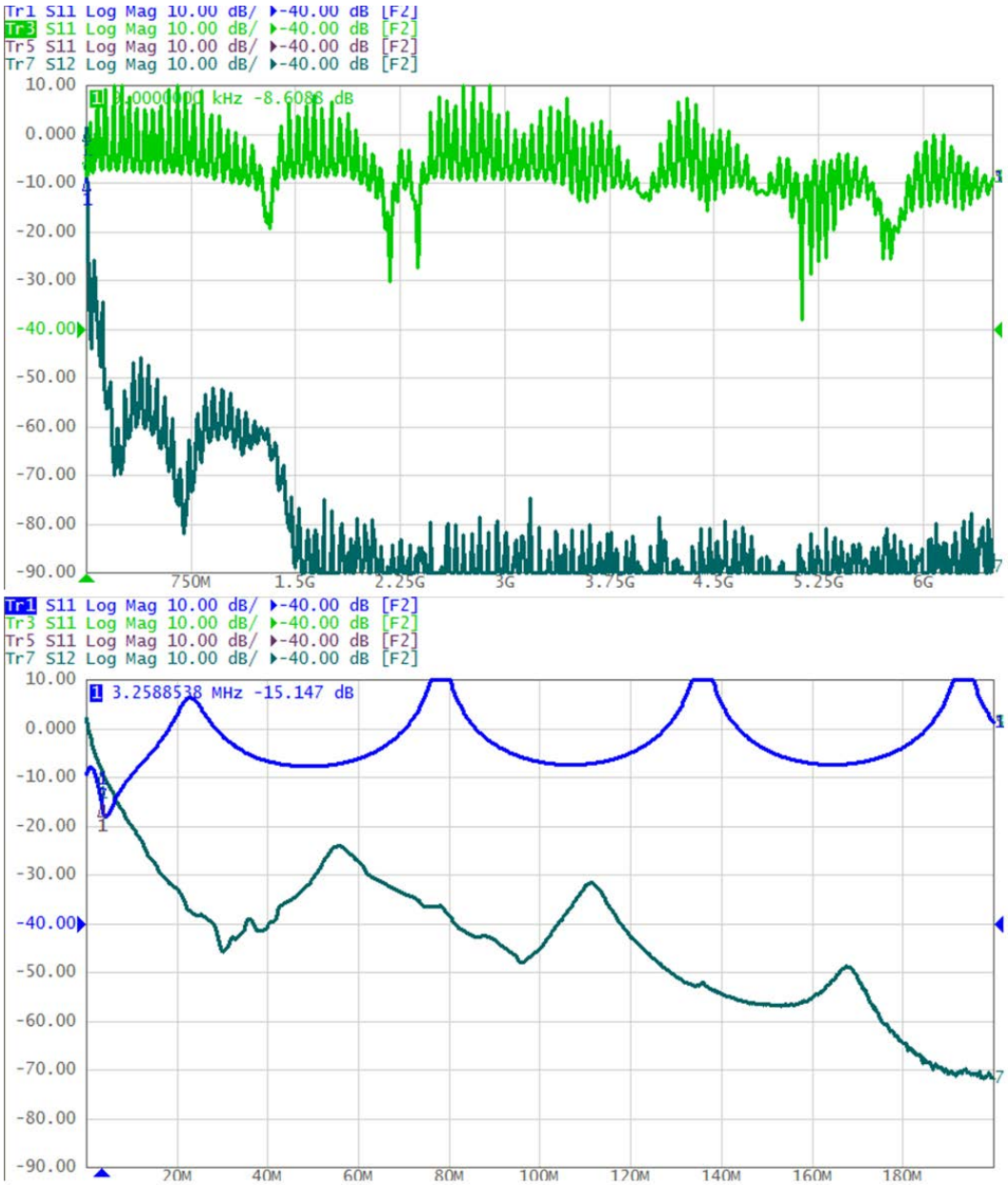

Figure 88. Measurement 2, Configuration 1 at (top) Full Span and (bottom) 9 kHz to 200 MHz range

5.1.2.2.3 Discussion

Experiment 11 essentially repeats the findings of Experiment 10: above 1.5 GHz, no detectable power transmits through the rebar embedded in the concrete; however, towards the DC end of the spectrum, a significantly greater amount of power was able to be transmitted through the rebar embedded in concrete. It appears that the concrete simply attenuates the RF power too much to be useful at the 2.4 GHz frequency that the TM Coupler was designed for.

5.1.3 Rectifier Experimentation

This section discusses the experimentation that took place for the rectifiers for the first design approach (i.e. for single line conduction).

5.1.3.1 Experiment 12: Tuning with Series Elements

For Experiment 12, a two stage Dickson Multiplier was fabricated using standard Flame Retardant 4 (FR4) Printed Circuit Board (PCB) material. No ground plane was implemented; that is, both the signal and ground traces were done on one side of the PCB. The circuit schematic of the two stage Dickson multiplier that was implemented can be seen in Figure 89.

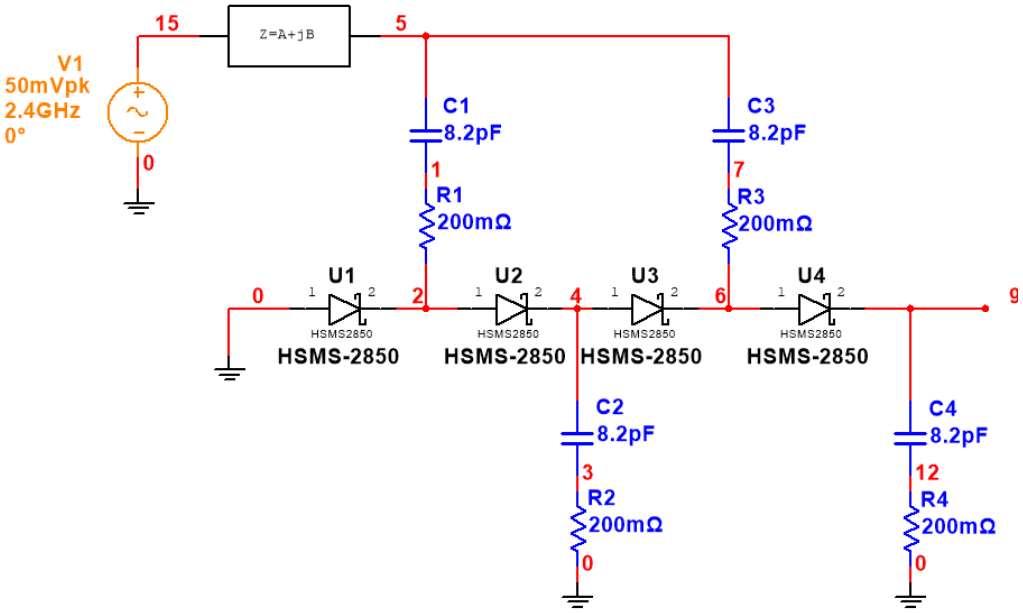

Figure 89. Circuit schematic of two stage Dickson Multiplier

5.1.3.1.1 Circuit Description

Two (2) HSMS-2850 series-pair Schottky diode components were implemented in a series connection, resulting in four Schottky diodes implemented in series. Four 8.2pF capacitors were implemented in the series of Schottky diodes; these capacitors were alternately tied to the positive voltage supply rail and the ground rail. A space was left on the PCB for a series component that was meant to cancel the reactance present in the two-stage Dickson multiplier. In Figure 89, the series component is represented as an impedance block after the source.

5.1.3.1.2 Set up

The goal of this experiment was to establish which series component would result in the maximum power transfer. This was done by iteratively replacing the series component with different values of inductors and capacitors. Small size 0603 components were selected for the series element used to tune the circuit.

A 2.4 GHz oscillator was used to input energy into the circuit. Using a range of attenuators, the input power was varied so that the performance of the circuit could be evaluated at multiple input powers. An example set-up is shown in Figure 90.

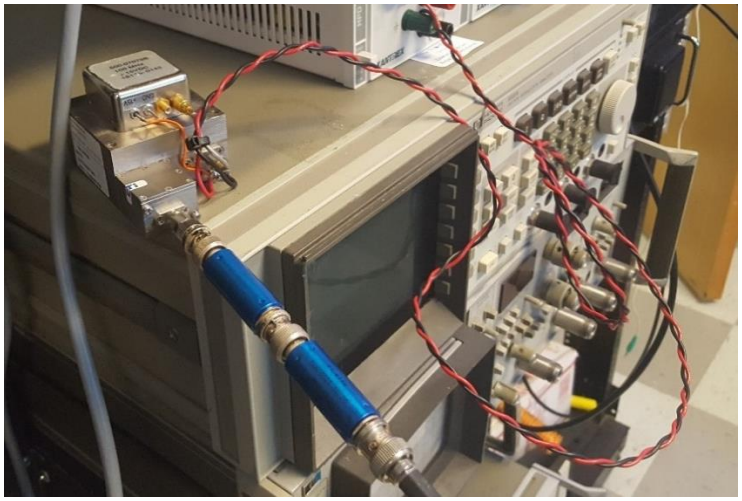

Figure 90. The 2.4 GHz oscillator with two attenuators attached in series

A spectrum analyzer was used to evaluate how much RF power was input into the two-stage Dickson Multiplier, as can be seen in Figure 91. A digital multimeter was used to evaluate the open circuit voltage output from the two-stage Dickson multiplier. Once a range of input powers were swept using the attenuators, and the resulting open circuit output voltages were measured, the component would be de-soldered and then replaced with another component to further evaluate the performance.

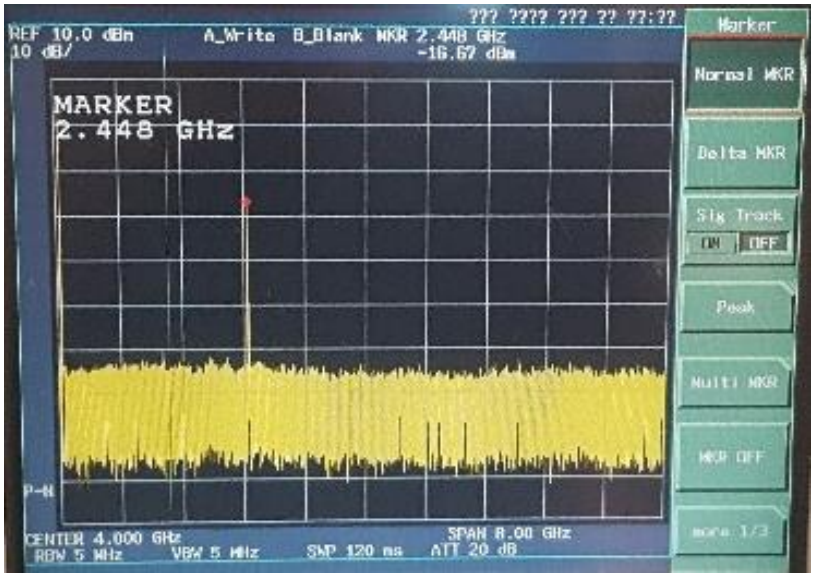

Figure 91. Example of the output of the spectrum analyzer for Experiment 12

5.1.3.1.3 Results

Initially, due to results from a simulation (Appendix F – Simulating the Rectifier Circuit), it was thought that the necessary component for canceling out the reactance of the circuit would a series inductor. However, when the circuit was built and tested, series inductor values were swept through from a high value to a lower value. It was noticed that, as the inductance decreased, the performance improved. Eventually, the smallest inductor was tested, with the improvement still increasing. Naturally, instead of using a series inductor, a series capacitor was implemented at an arbitrary 4.0 pF, and performance improved. Then the capacitance was increased to an arbitrary 8.0 pF, with slightly worse performance. Then the capacitance was decreased, to 2.0, which resulted in a marked improvement from both the 8.0 pF and 4.0 pF implementations.

The results of the measurements were graphed and can be seen in Figure 92. In this graph, the red line at the bottom denotes 330 mV, which was the minimum voltage needed to initiate a cold start for the BQ25504 boost circuit. If the output voltage did not exceed 330 mV, then it was thought that the charging would not initiate.

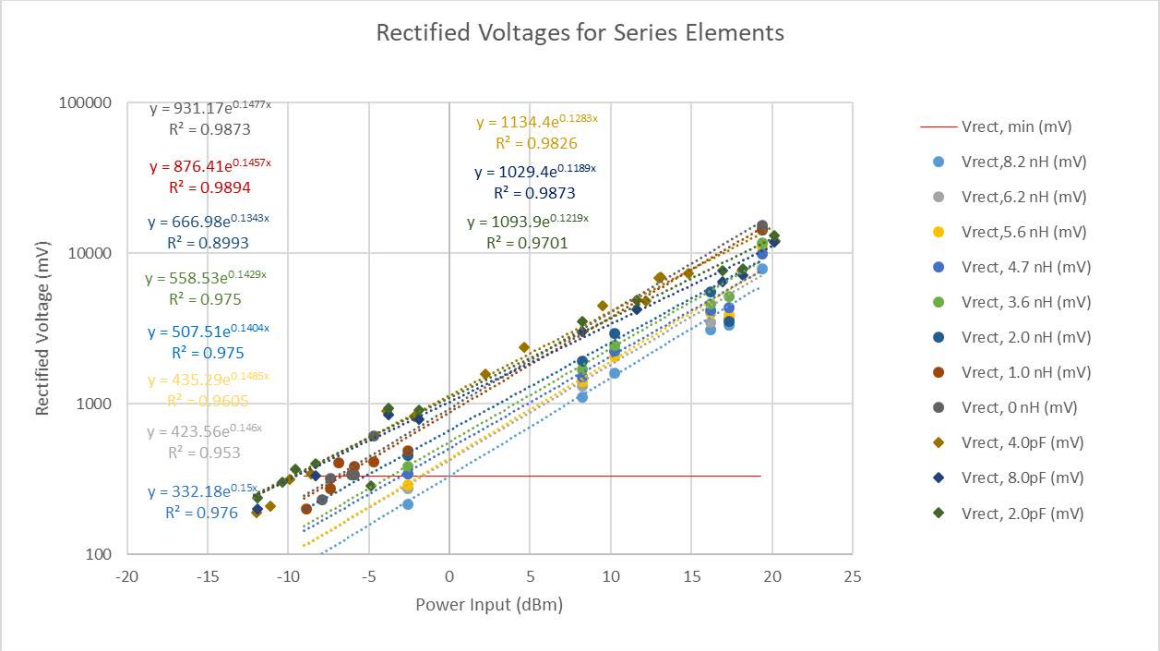

Figure 92. Results of two stage Dickson Multiplier with various series components in terms of open circuit output voltage vs input power

5.1.3.1.4 Discussion

As can be seen from Figure 92, the series component that supported the best performance for open circuit output voltage versus input power was the 2.0pF capacitor. The 2.0pF capacitor could output approximately 330mV at -10dBm input power. Observing the graph in Figure 92, note that the performance of the circuit with a given series element can be quickly evaluated by the slope of its curve and how far to the left it is shifted on the graph; that is, the less steep that the curve is, and the furthest shifted to the left that the curve is, indicates superior performance. If the curve is shifted to the left, then that indicates that the circuit can function with lower input power. If the curve is less steep, then that means that the open circuit output voltage is less sensitive to the input power.

5.1.3.2 Experiment 13: Series Capacitor Adjustments

After the results from Experiment 12 were evaluated, further un recorded-experimentation was applied to the circuit: the capacitance of the series capacitor was decreased from 2.0 pF all the way down to 0.5 pF. It was noticed that somewhere around 0.8 pF to 0.5 pF, performance was maximized. Hence, the purpose of Experiment 13 was to closely evaluate the performance of the two-stage Dickson multiplier using these three series capacitor values.

5.1.3.2.1 Set up

The two-stage Dickson multiplier circuit would be evaluated by varying the capacitance of the series capacitor with three values: 0.5 pF, 0.6 pF, and 0.7 pF. Using a Vector Network Analyzer, the input impedance and the S11 parameter were evaluated. However, these two parameters would be evaluated was varying: (a) input powers, (b) frequency, and (c) load resistance.

It was posited that the power efficiency of the two-stage Dickson multiplier would vary with load resistance; therefore, it was desired to vary the load resistance to observe if this phenomenon would result. To easily vary the load resistance, a 10 kΩ potentiometer was implemented as shown in Figure 93. The voltage across and current through the 10 kΩ potentiometer was evaluated using: (a) an oscilloscope to measure the voltage across the 10 kΩ potentiometer, and (b) a multimeter to measure the current flowing through the 10 kΩ potentiometer. Using these two measurements, the load resistance could be calculated using Ohm's law, and the output power could be calculated by taking the product of voltage and current.

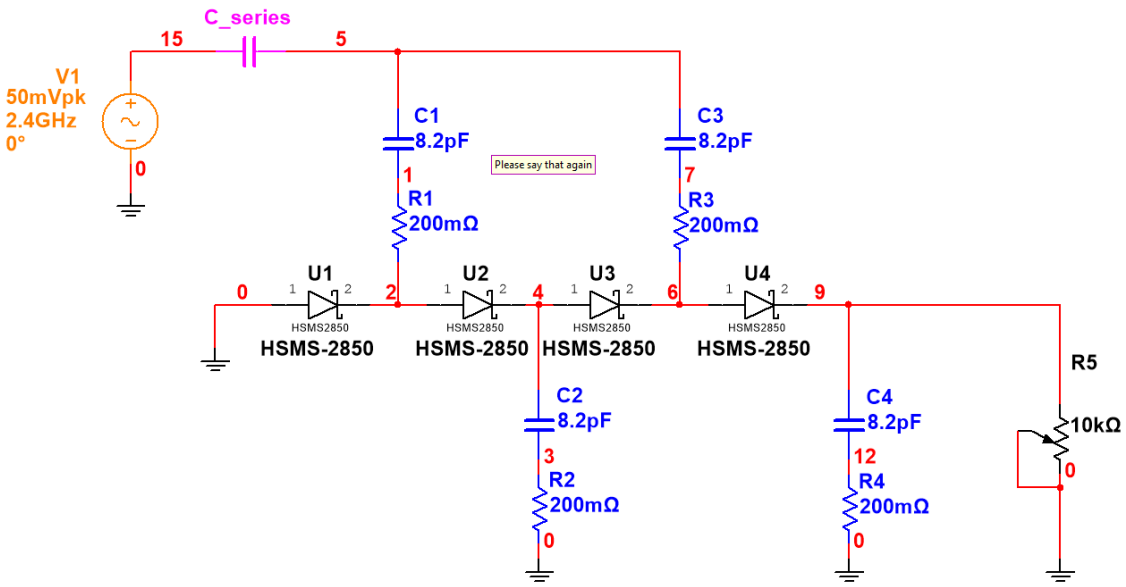

Figure 93. Rectifier Circuit with Series Capacitor as Matching Element

The VNA would act as the input power source, and the VNA had the ability to vary the input power. The maximum input power the VNA could supply was 5 dBm. For Experiment 13, the input power was varied from 5 dBm to -6 dBm. The VNA was used to measure the input impedance and the S11 parameter data.

5.1.3.2.2 Note on the Open Circuit Voltage Percentage Parameter

This subsection briefly provides explanation of the Open Circuit Voltage Percentage and why it was used. In this discussion, there are two components: the input power circuit (two stage Dickson Multiplier) and the BQ25504 Boost Circuit, which has energy harvesting battery management circuitry within it.

As discussed above, to maximize power transfer, the BQ25504 uses an MPPT circuit to modulate its input impedance to accommodate whatever input power circuit is driving it. The MPPT circuit adjusts the input impedance of the BQ25504 by periodically driving its input impedance high (emulating an open circuit) so that the open circuit voltage of the input power circuit can be approximated; the BQ25504 uses this approximated open circuit voltage to drive its input impedance to whatever value causes the voltage drop across the BQ25504 input to

equal a user-specified percentage of the open circuit voltage of the input power circuit, which is set with a voltage divider.

For this design, the input power circuit is the two-stage Dickson Multiplier. Hence, to determine what open circuit voltage percentage the MPPT circuit should be set to, the performance of the two stage Dickson Multiplier in terms of Power Efficiency should be evaluated with respect to the Open Circuit Voltage Percentage. The way that this parameter is evaluated for the two-stage Dickson Multiplier is by taking the voltage of a given load resistance and dividing it by the open circuit voltage of the two-stage Dickson Multiplier.

5.1.3.2.3 Results

The results of Experiment 13 per series capacitance is in the following three subsections below, which are named:

- 0.5-pF Series Capacitor
- 0.6-pF Series Capacitor
- 0.7-pF Series Capacitor

In each of the subsections, four different types of graphs were generated from all the data:

- With varying Input Power (dBm):
    1. Power Efficiency versus Load Resistance
    2. Power Efficiency versus Open Circuit Voltage Percentage
- With varying Input Power and Load Resistance:
    3. Input Impedance at 2.4 GHz
- With varying frequency:
    4. S11 parameter and Power Loss versus Load Resistance

5.1.3.2.3.1 0.5-pF Series Capacitor

The results for the two-stage Dickson multiplier using the 0.5 pF capacitor can be seen in Figure 94 through Figure 101.

Figure 94 and Figure 95 show the power efficiency of the two-stage Dickson multiplier. The only difference between these two graphs is the x-axis. For Figure 94, the x-axis is the load resistance; optimal power efficiency appears to occur near 2 kΩ for all tested power inputs.

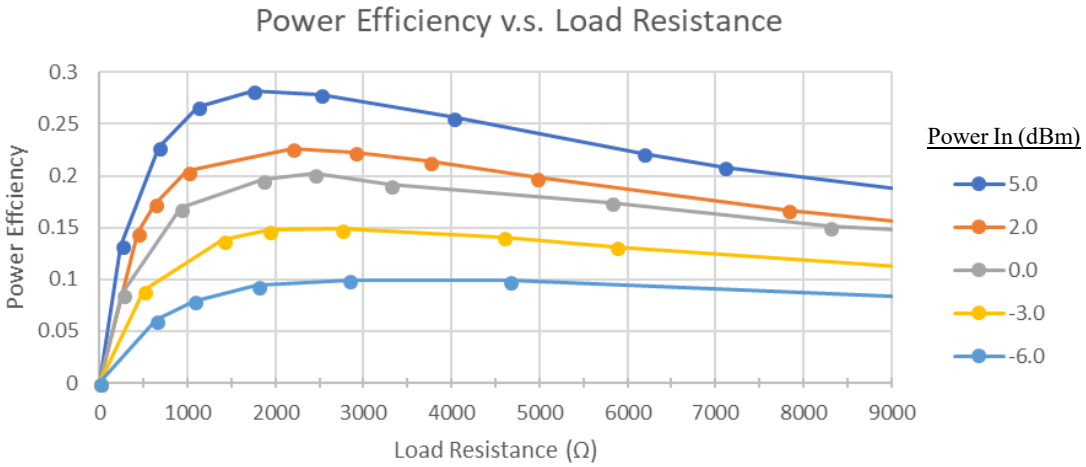

Figure 94. Power efficiency versus load resistance for the multiplier with a 0.5 pF series component.

For Figure 95, the x-axis is open circuit voltage percentage; optimal power performance appears to occur near 40% open circuit voltage percentage for all tested power inputs.

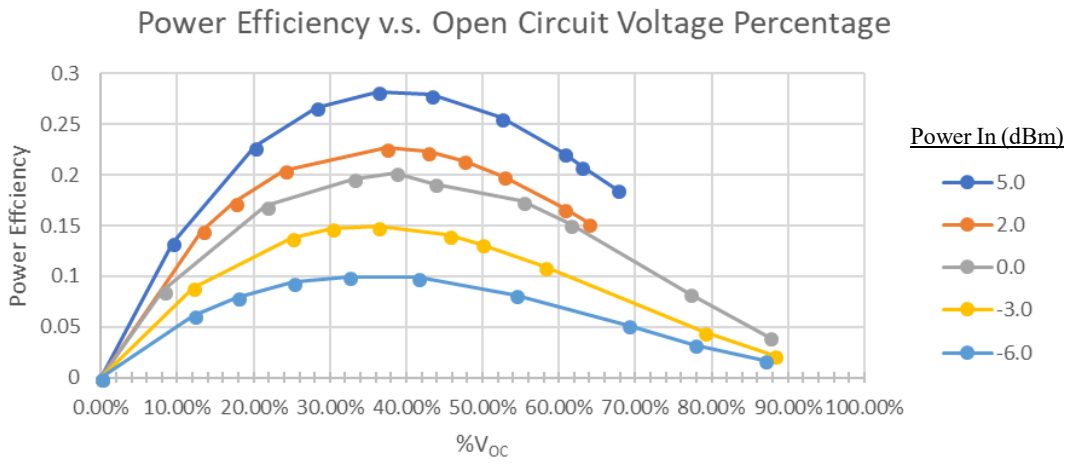

Figure 95. Power efficiency versus open circuit voltage percentage for the multiplier with a 0.5 pF series component

Figure 96 shows how the input impedance varies at 2.4 GHz for all tested power inputs. In this figure, it can be seen that at various load resistances, the input reactance varies along the same track for different power inputs.

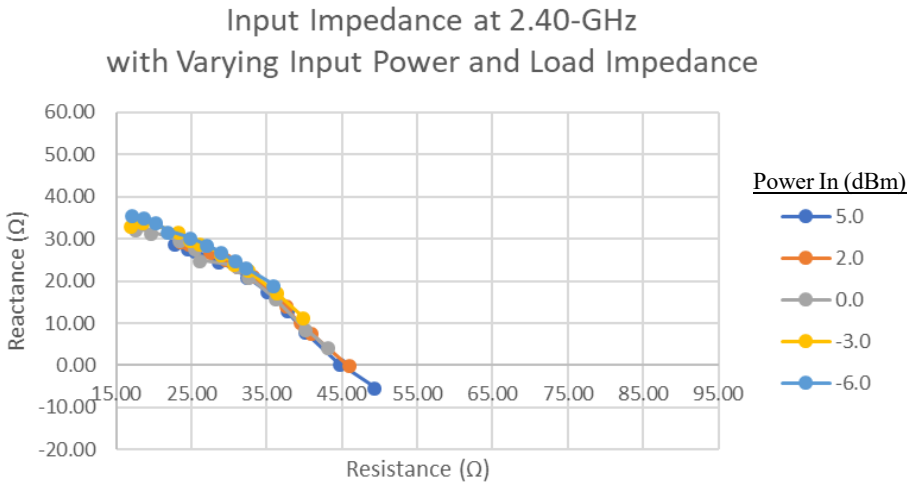

Figure 96. Input impedance of the multiplier with the 0.5 pF series component with varied load resistance and input power.

Figure 97 through Figure 101 show the S11 parameter versus load resistance for the two-stage Dickson Multiplier circuit, with each figure showing only one input power. These figures show how the magnitude of the S11 parameter changes with input power and frequency. Note that

as the input power decreases, the dip in reflected power that occurs at the higher input power shifts leftward on the load resistance axis.

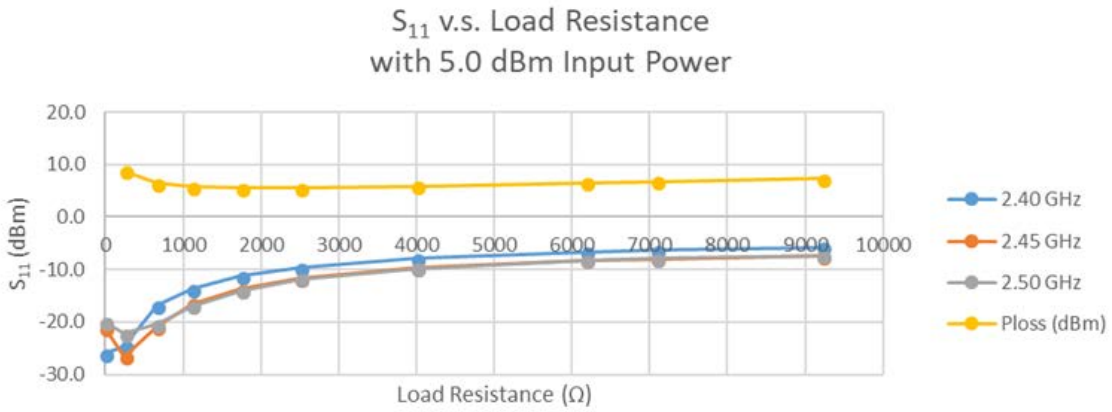

Figure 97. S11 parameter vs load resistance for the multiplier circuit with the 0.5 pF series component with 5 dBm input power at 3 different input frequencies

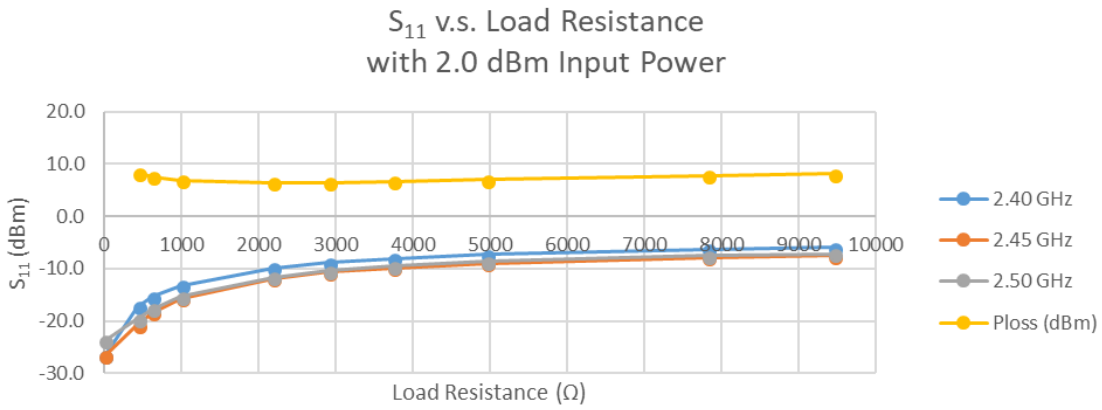

Figure 98. S11 parameter vs load resistance for the multiplier circuit with the 0.5 pF series component with 2 dBm input power at 3 different input frequencies

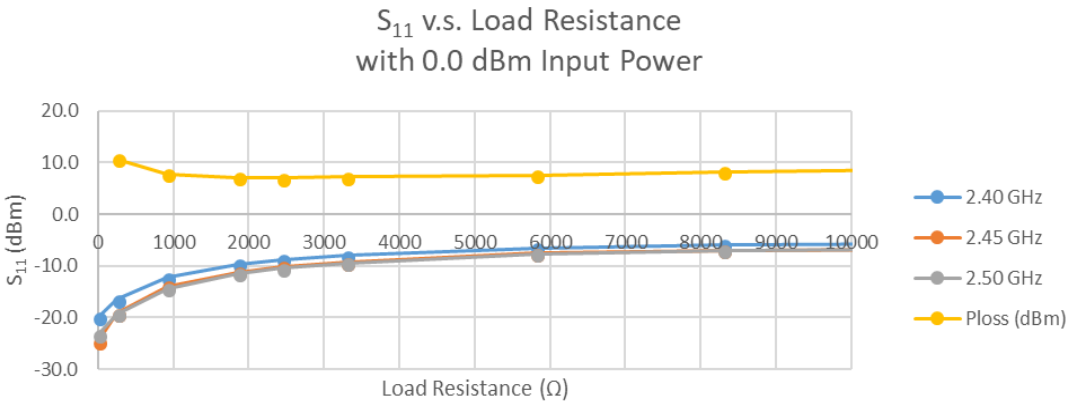

Figure 99. S11 parameter vs load resistance for the multiplier circuit with the 0.5 pF series component with 0 dBm input power at 3 different input frequencies

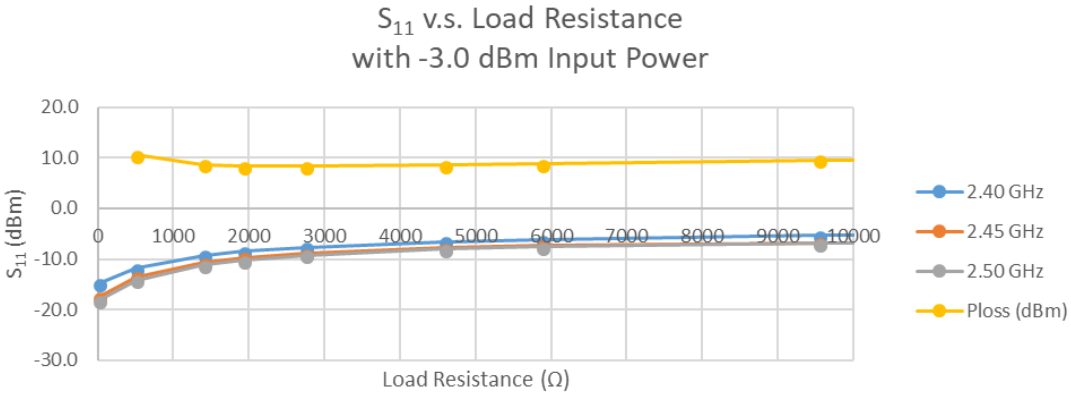

Figure 100. S11 parameter vs load resistance for the multiplier circuit with the 0.5 pF series component with -3 dBm input power at 3 different input frequencies

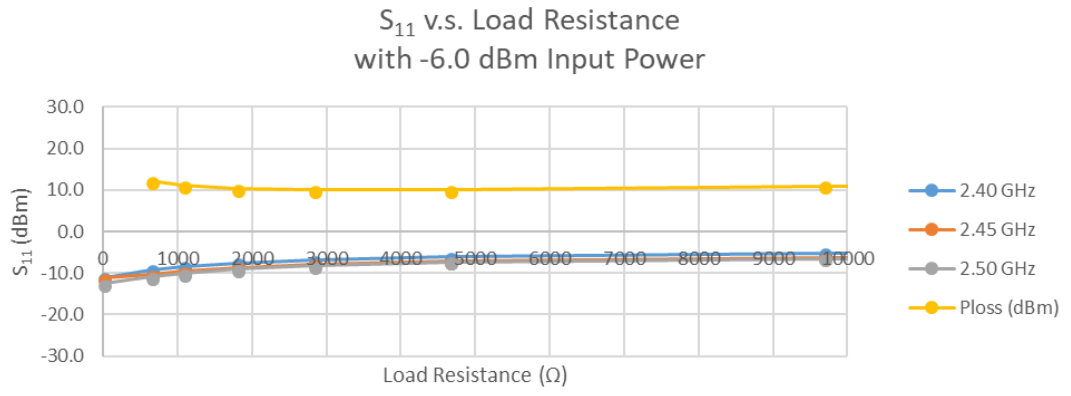

Figure 101. S11 parameter vs load resistance for the multiplier circuit with the 0.5 pF series component with -6 dBm input power at 3 different input frequencies

5.1.3.2.3.2 0.6-pF Series Capacitor

The results for the two-stage Dickson multiplier using the 0.6 pF capacitor to cancel out the reactance are shown using eight graphs, which can be seen in Figure 102 through Figure 109.

Figure 102 and Figure 103 show the performance of the two-stage Dickson multiplier in terms of power efficiency. The only difference between these two graphs is the x-axis. For Figure 102, the x-axis is the load resistance. Maximum power efficiency appears to occur near 2kΩ for all tested power inputs.

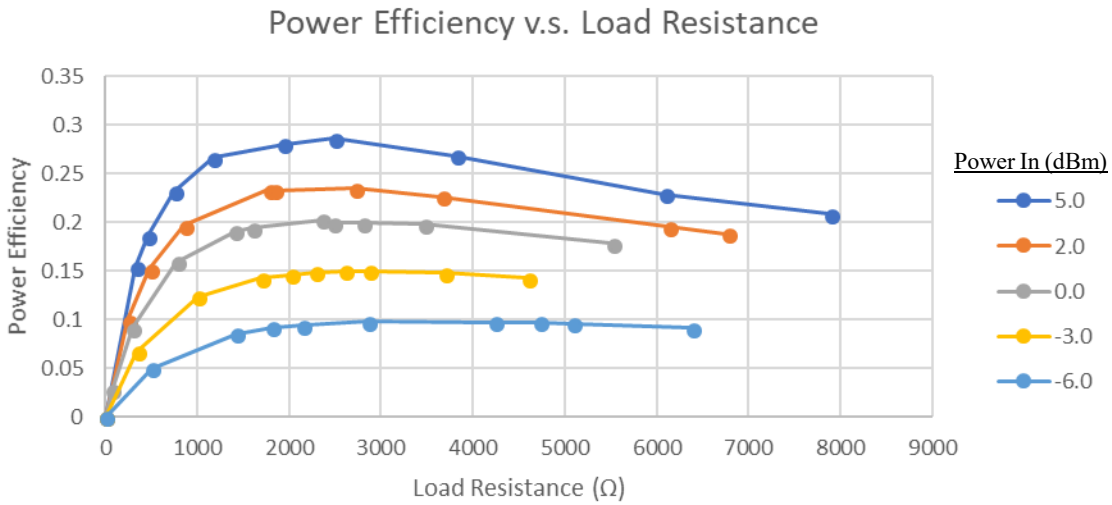

Figure 102. Power efficiency versus load resistance for the multiplier with a 0.6 pF series component

For Figure 103, the x-axis is open circuit voltage percentage. Again, optimal power performance appears to occur near 40% open circuit voltage percentage for all tested power inputs.

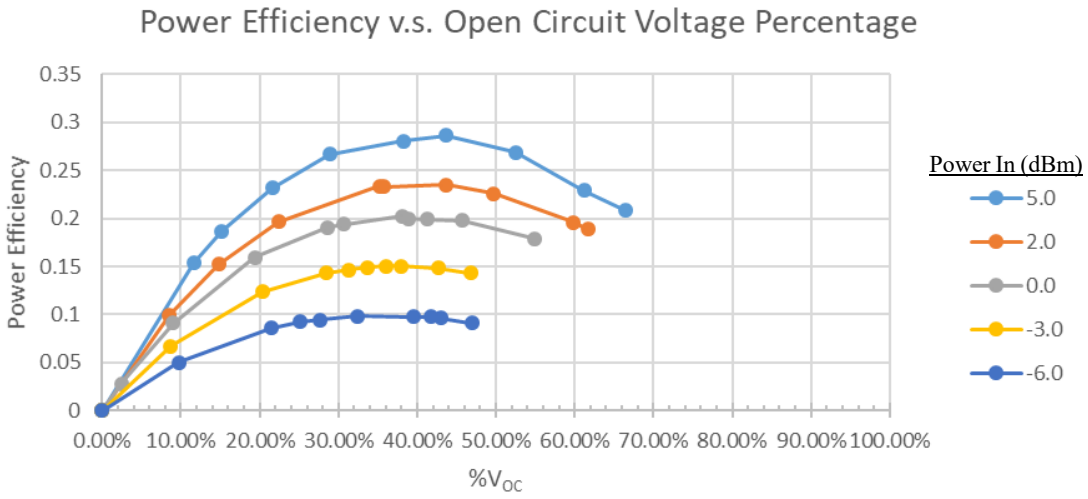

Figure 103. Power efficiency versus open circuit voltage percentage for the multiplier with a 0.6 pF series component

Figure 104 shows how the input impedance varies at 2.4 GHz for all tested power inputs. In this figure, it can be seen that as the input power decreases, the input impedance drifts upward and to the right, causing the input impedance to become both more resistive and inductively reactive.

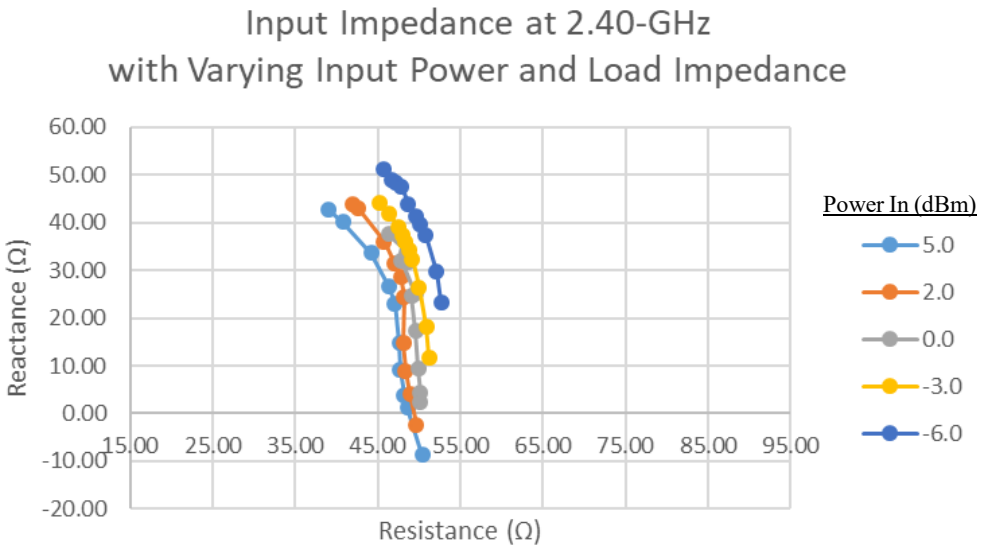

Figure 104. Input impedance of the multiplier with the 0.6 pF series component with varied load resistance and input power

Figure 105 through Figure 109 show the S11 parameter versus load resistance for the two-stage Dickson Multiplier circuit, with each figure showing only one input power. These figures show how the magnitude of the S11 parameter changes with input power and frequency. As with the 0.5 pF capacitor, note that as the input power decreases, the dip that occurs at the higher input power shifts leftward on the load resistance axis.

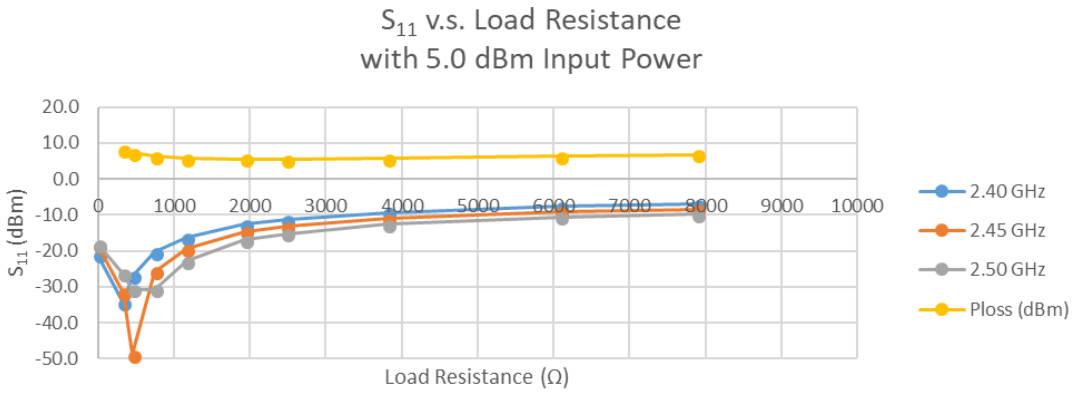

Figure 105. S11 parameter vs load resistance for the multiplier circuit with the 0.6 pF series component with 5 dBm input power at 3 different input frequencies

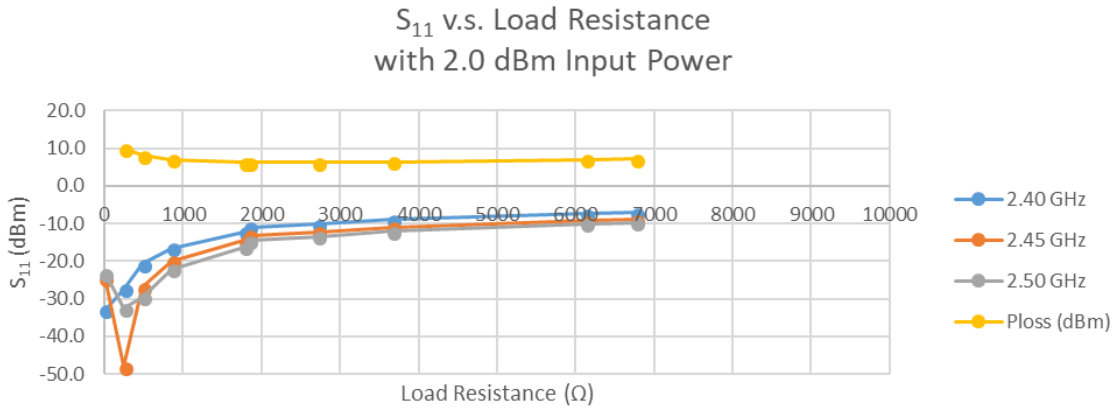

Figure 106. S11 parameter vs load resistance for the multiplier circuit with the 0.6 pF series component with 2 dBm input power at 3 different input frequencies

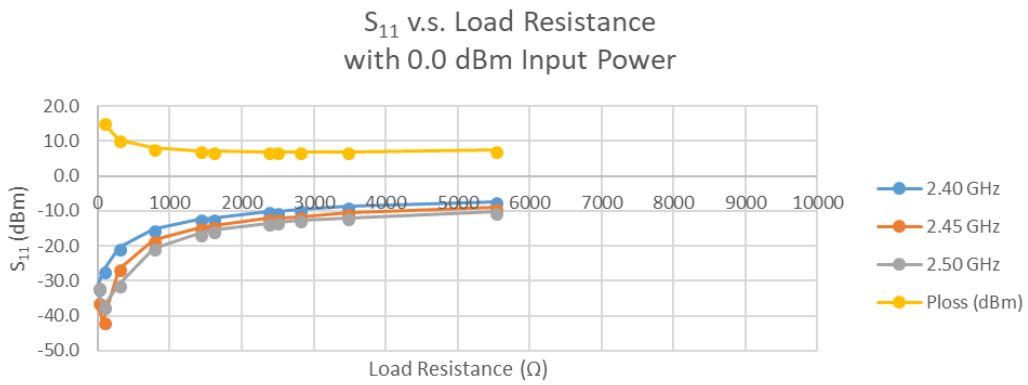

Figure 107. S11 parameter vs load resistance for the multiplier circuit with the 0.6 pF series component with 0 dBm input power at 3 different input frequencies

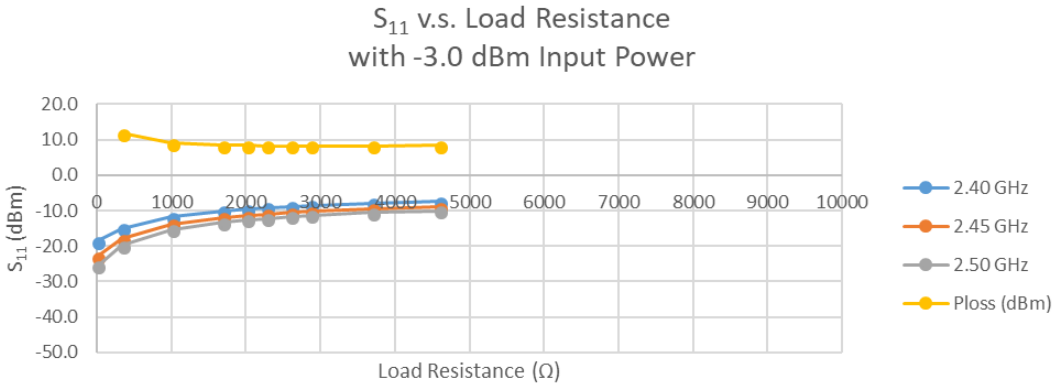

Figure 108. S11 parameter vs load resistance for the multiplier circuit with the 0.6 pF series component with -3 dBm input power at 3 different input frequencies

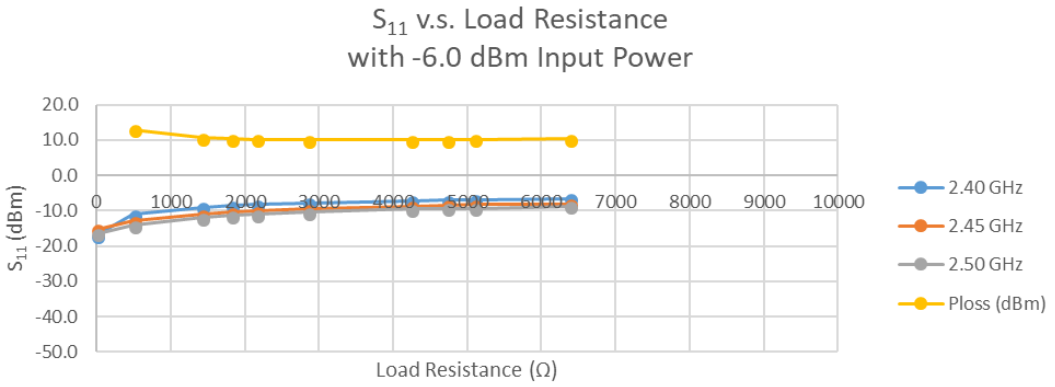

Figure 109. S11 parameter vs load resistance for the multiplier circuit with the 0.6 pF series component with -6 dBm input power at 3 different input frequencies

5.1.3.2.3.3 0.7-pF Series Capacitor

The results for the two-stage Dickson multiplier using the 0.7 pF capacitor to cancel out the reactance are shown using eight graphs, which can be seen in Figure 110 through Figure 117.

Figure 110 and Figure 111show the performance of the two-stage Dickson multiplier in terms of power efficiency. The only difference between these two graphs is the x-axis. For Figure 110, the x-axis is the load resistance. Again, optimal power efficiency appears to occur near 2kΩ for all tested power inputs.

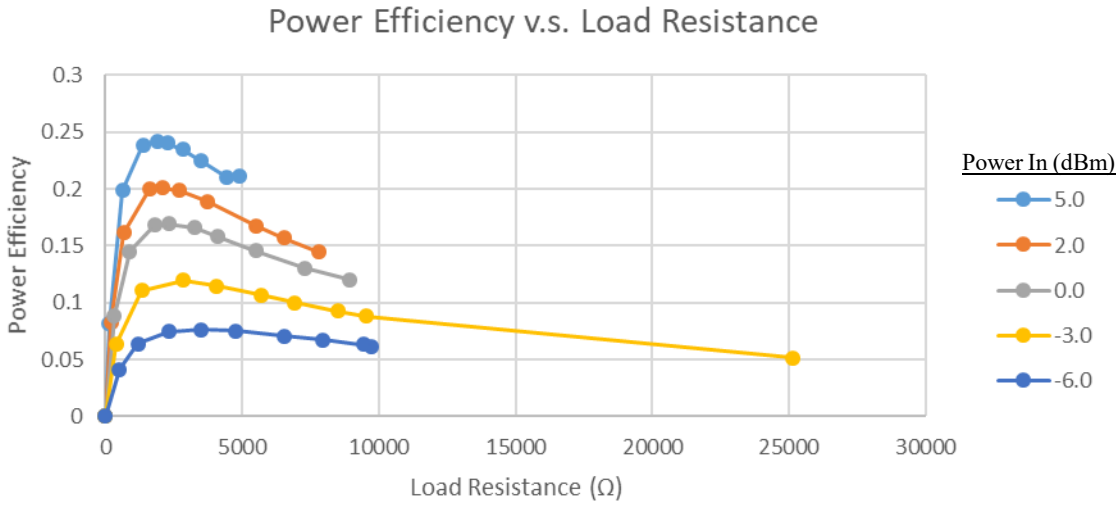

Figure 110. Power efficiency versus load resistance for the multiplier with a 0.7 pF series component

For Figure 111Figure 95, the x-axis is open circuit voltage percentage. Again, optimal power performance appears to occur near 40% open circuit voltage percentage for all tested power inputs.

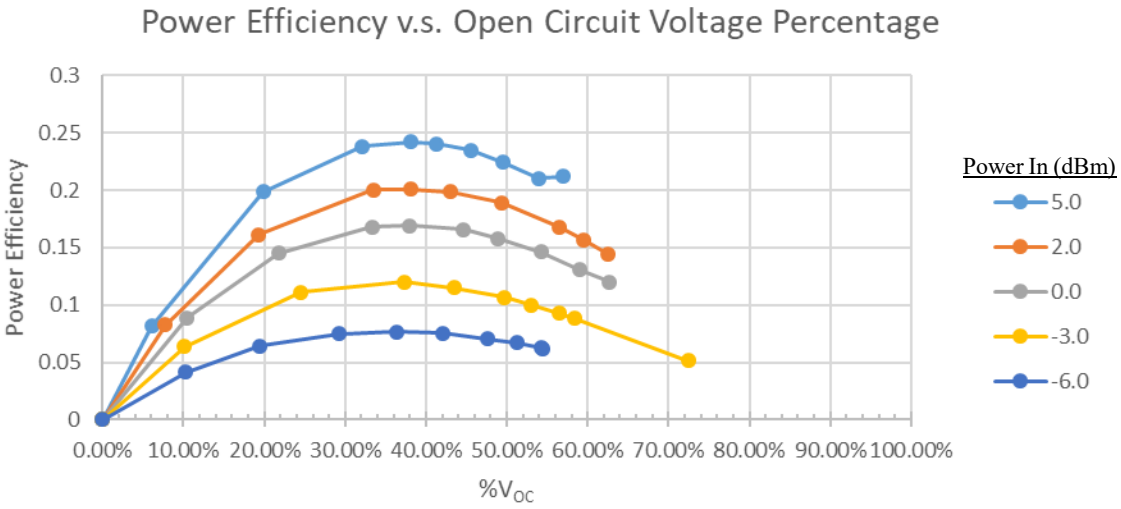

Figure 111. Power efficiency versus open circuit voltage percentage for the multiplier with a 0.7 pF series component

Figure 112 shows how the input impedance varies at 2.4 GHz for all tested power inputs. In this figure, it can be seen that as the input power decreases, the input impedance drifts upward and to the right, causing the input impedance to become both more resistive and inductively reactive.

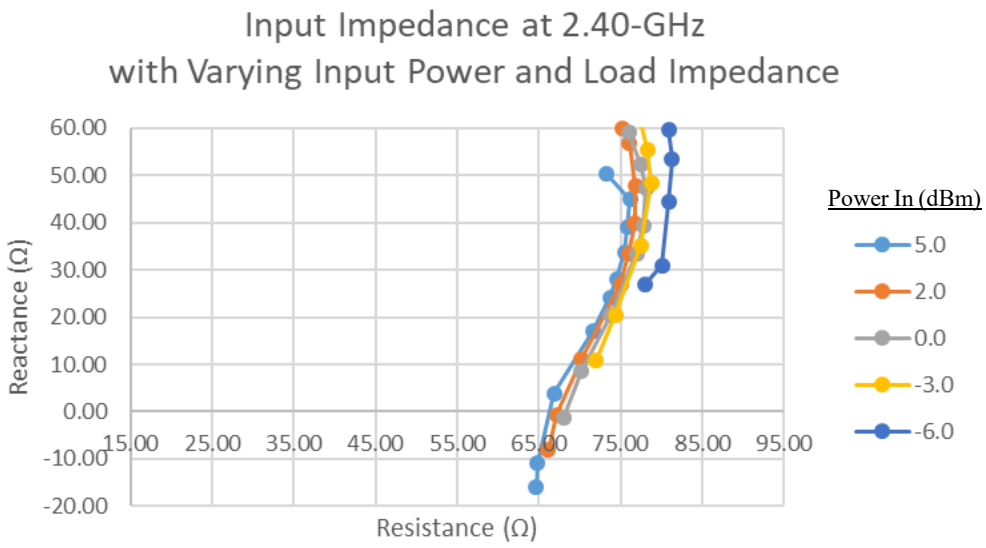

Figure 112. Input impedance of the multiplier with the 0.7 pF series component with varied load resistance and input power

Figure 113 through Figure 117 show the S11 parameter versus load resistance for the two-stage Dickson Multiplier circuit, with each figure showing only one input power. These figures show how the magnitude of the S11 parameter changes with input power and frequency. Note that as the input power decreases, the dip that occurs at the higher input power shifts leftward on the load resistance axis.

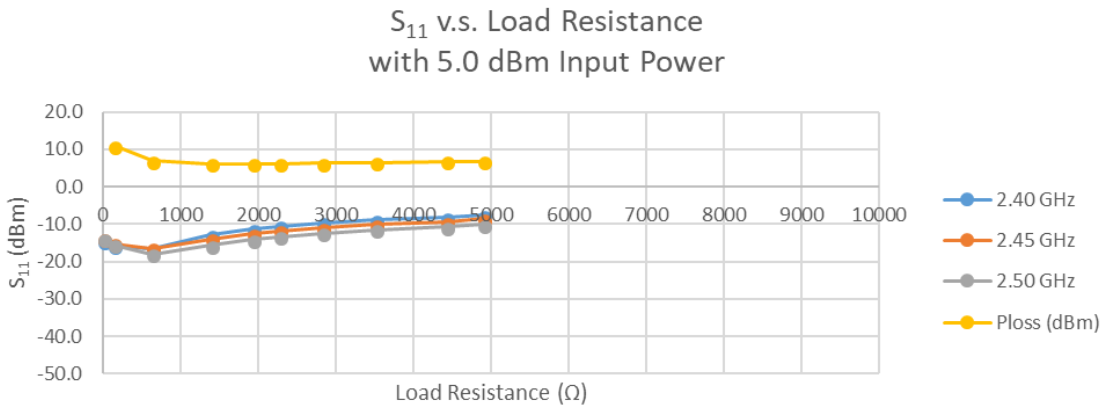

Figure 113. S11 parameter vs load resistance for the multiplier circuit with the 0.7 pF series component with 5 dBm input power at 3 different input frequencies

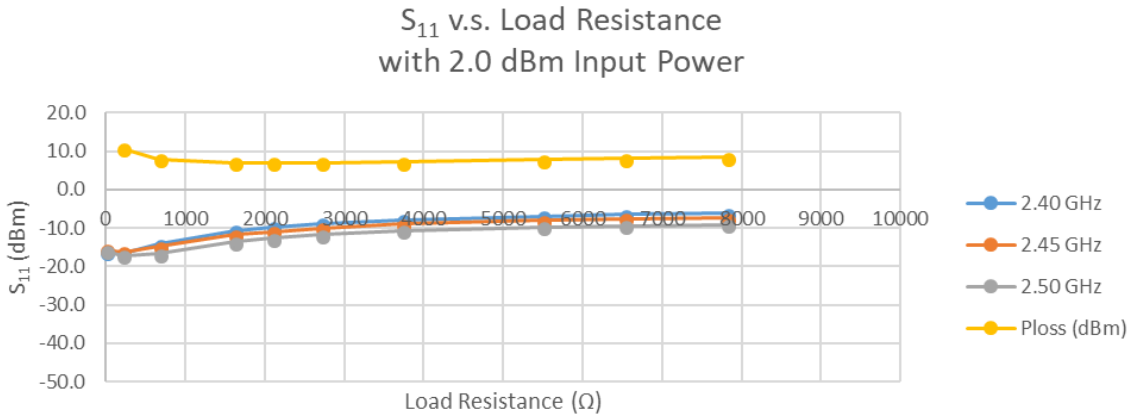

Figure 114. S11 parameter vs load resistance for the multiplier circuit with the 0.7 pF series component with 2 dBm input power at 3 different input frequencies

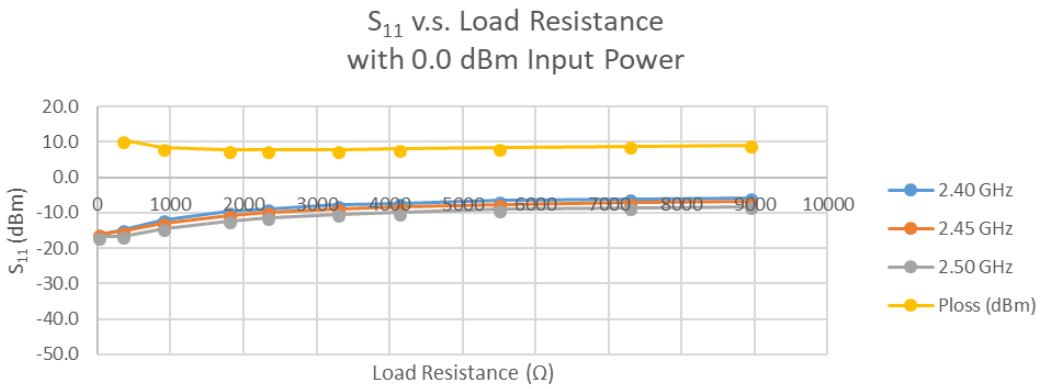

Figure 115. S11 parameter vs load resistance for the multiplier circuit with the 0.7 pF series component with 0 dBm input power at 3 different input frequencies

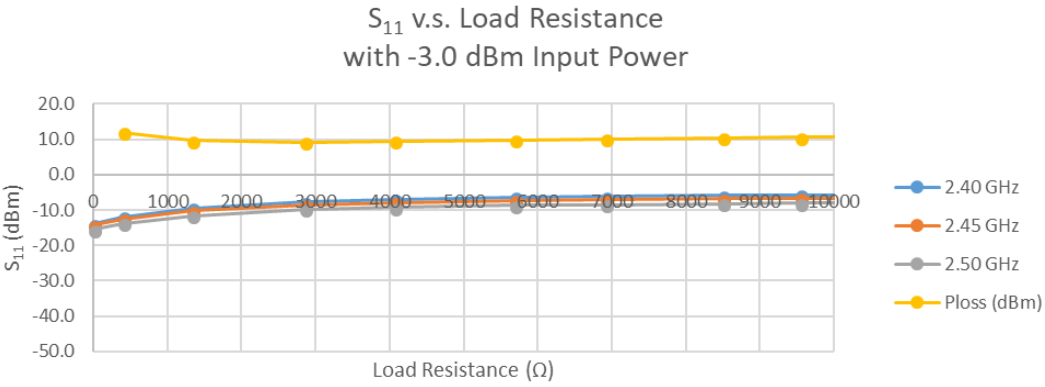

Figure 116. S11 parameter vs load resistance for the multiplier circuit with the 0.7 pF series component with -3 dBm input power at 3 different input frequencies

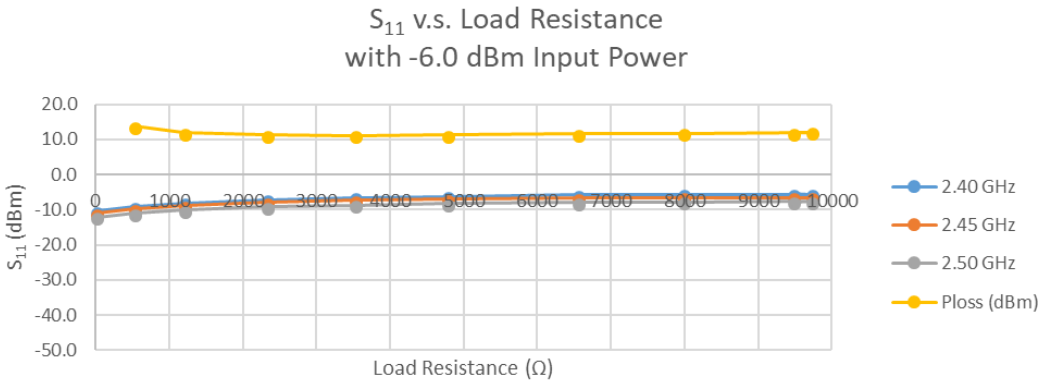

Figure 117. S11 parameter vs load resistance for the multiplier circuit with the 0.7 pF series component with -6 dBm input power at 3 different input frequencies

5.1.3.2.4 Discussion

After analyzing the (a) Power Efficiency versus Load Resistance graphs, and (b) Power Efficiency versus Open Circuit Voltage Percentage graphs, it was determined that an open circuit voltage percentage of approximately 45%, which was equivalent to an approximately 2 kΩ load for all three circuits, that that was the optimal value for the BQ25504 to be set to for maximum power efficiency.

After analyzing the Input Impedance at 2.4 GHz of the Two-Stage Dickson Multiplier for each series capacitor, it was noticed that the input impedance of the Two-Stage Dickson Multiplier with the 0.6 pF series capacitor resulted in an almost constant 50 Ω for every input power and applied load resistance, as can be seen in Figure 104. Compared to the input impedances of the Two-Stage Dickson Multiplier circuits with 0.5 pF and 0.7 pF series capacitors, for the Two-Stage Dickson Multiplier with the 0.6 pF series capacitor, the resistive component of the input impedance had much smaller spread. Because of this spread, it was judged that the Two-Stage Dickson Multiplier with the 0.6 pF series capacitor was the best topology for canceling out the reactance of the circuit.

After analyzing the S11 parameter and Power Loss versus Load Resistance graphs, it was noticed that the Two-Stage Dickson Multiplier with the 0.5 pF series capacitor behaved as well as the Two-Stage Dickson Multiplier with the 0.6 pF series capacitor. The Two-Stage Dickson Multiplier with the 0.7 pF series capacitor resulted in the most power loss through the circuit.

5.1.3.3 Experiment 14: Observing Varying S11 with Varied Input Power

After a 0.6pF series capacitor was selected for cancelling out the reactance of the rectifier circuitry, upon further investigation, which can be found in Appendix E – Improving the Rectifier Circuit, it was shown that the rectifier performed with lower S11 parameters and with a better matched input impedance with a 0.5pF shunt capacitor and a 0.6pF series capacitor, as shown in Figure 118.

5.1.3.3.1 Set-Up

In Experiment 14, the input power into the rectifier circuitry was varied at 2.4GHz using a VNA with a 2.2kΩ resistor applied as the load of the rectifier, as shown in Figure 118. A VNA was used to measure the input impedance and S11 parameter of the Two-Stage Dickson Multiplier.

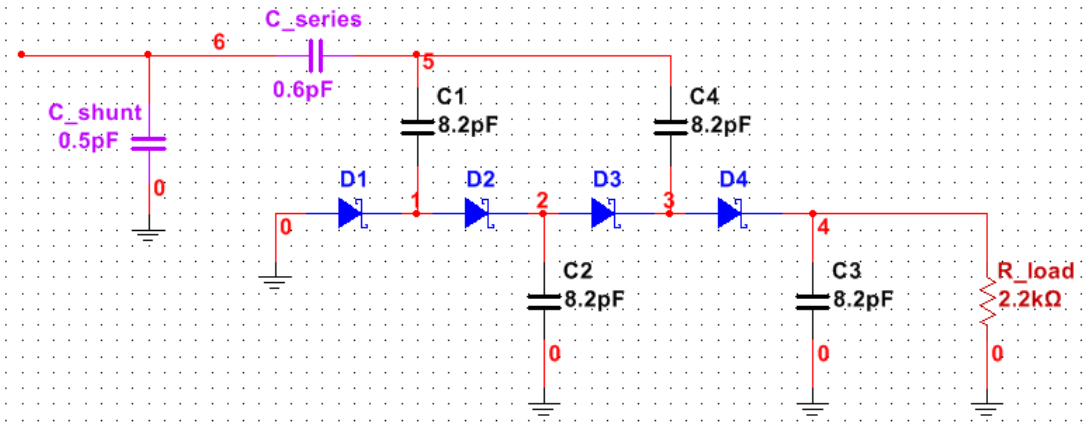

Figure 118. Improved Rectifier Circuitry with Input Shunt and Series Capacitors

5.1.3.3.2 Results

The results from the test can be seen in Figure 119 and Figure 120. In Figure 119 and Figure 120, it can be seen that the input impedance varies with input power and that the S11 parameter varies with input power.

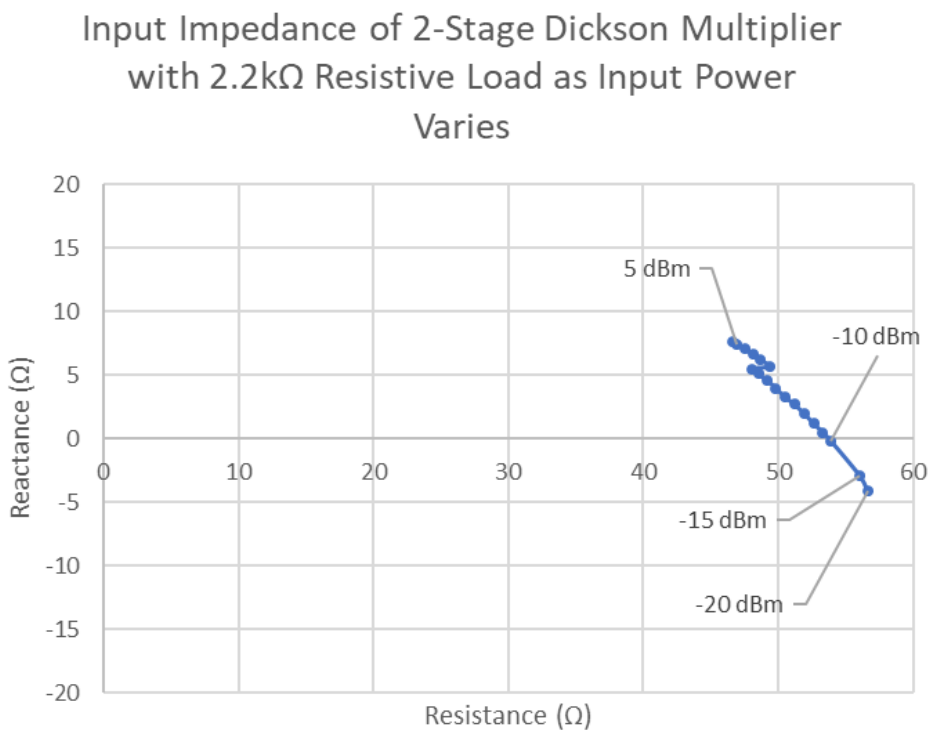

Figure 119. Input Impedance of Rectifier Circuitry with Varying Input Power

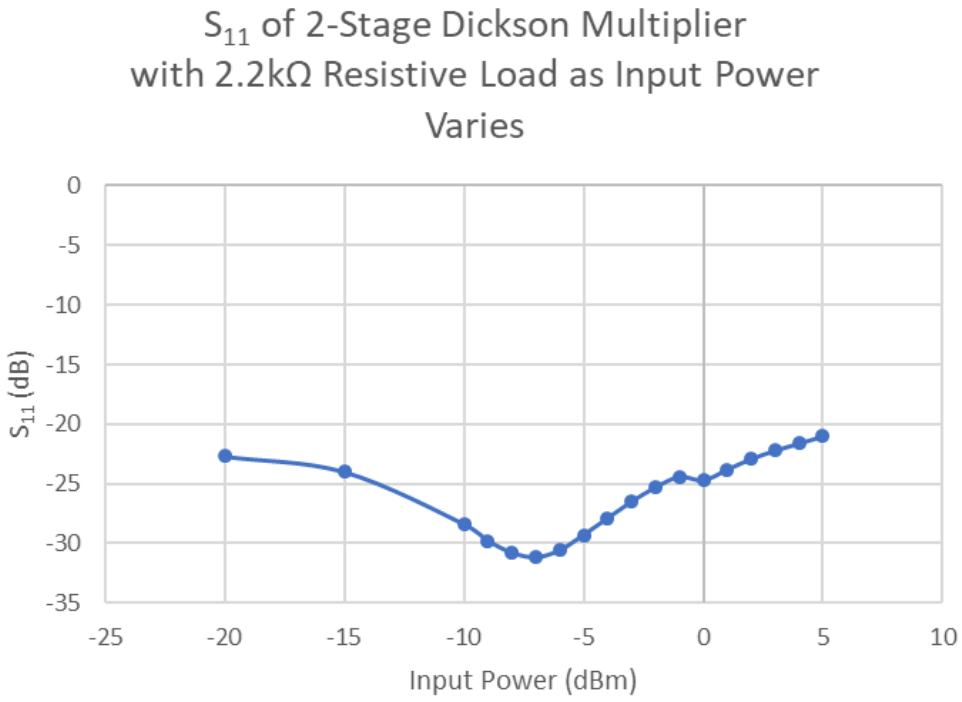

Figure 120. S11 Parameter of Rectifier with Varying Input Power

5.1.3.3.3 Discussion

From Figure 119, it can be seen that the input impedance of the Two-Stage Dickson Multiplier does in fact vary with input power. More notably, perhaps, is that at around -10 dBm input power, the input impedance of the Two-Stage Dickson Multiplier had almost no reactance, which means that the input impedance would almost be perfectly matched — a perfect match meaning that minimum power would be reflected (i.e. minimum return loss). However, after inspecting Figure 120, it can be noted that minimum power reflection actually occurs at approximately -7 dBm input power. Nevertheless, with the addition of the 0.5 pF shunt capacitor at the input of the Two-Stage Dickson Multiplier, it can be seen that the circuit is undoubtedly better matched than with just a series capacitor.

5.1.3.4 Experiment 15: Observing Varying Power Efficiency with Varied Input Power

Recall that, based on the results of Experiment 13, the resistance that produced the optimal power efficiency was around 2.0 kΩ. Recall from Experiment 13 that when a load resistance of approximately 2.0 kΩ was applied as the load to the Two-Stage Dickson Multiplier, optimal power efficiency was achieved. Moreover, irrespective of the input powers tested in Experiment 13, when a 2.0 kΩ load was applied to the rectifier, the voltage that resulted across the load was invariably approximately 40% - 45% of what the open circuit voltage of the rectifier circuit would be.

In Experiment 15, an oscillator was used to evaluate the performance of the rectifier circuit with a larger input power range. However, the circuit in Experiment 15, is slightly different from the circuit in Experiment 13. Recall that the circuit in Experiment 14 evolved from the circuit in Experiment 13 with the addition of a shunt capacitor. Experiment 15 is a continuation of the circuit in Experiment 14.

The aim of Experiment 15 is to establish the loss through the circuit as power input is swept across a larger input power range.

5.1.3.4.1 Set-up

A 2.2kΩ resistor was applied as the load of the rectifier. The resistor was placed in series with a Rigol DM3068 Digital Multimeter (which was set on the ammeter mode). Additionally, a Rigol MSO2202A digital oscilloscope was clipped across the resistor. The rectifier was connected to a male-to-male SMA connector, which was in turn connected to one of the SMA ports of a JFW Industries Inc. attenuator (model 50DR-046). The other SMA Port of the attenuator was connected to a male-to-male SMA connector, which was in turn connected to a 2.4 GHz oscillator that sourced 20dBm of power.

5.1.3.4.2 Procedure

An adjustable attenuator allowed the input power to be attenuated up to 50dB, providing control over how much power was inputted into the rectifier. For a total of 35 trials, the attenuator was varied. Though the nominal input power was 20dBm, the actual measured

power was 19.833dBm. This meant that the test input power was varied from +19.833dBm to -14.167dBm.

Two sweeps were performed: (1) the first sweep utilized a 2.2 kΩ load resistor, with the voltage across the resistor and the current through the resistor measured and logged; (2) the second sweep utilized a no load configuration, measuring and logging only the open circuit voltage of the rectifier.

Using the load voltage and the open circuit voltage, the ratio of the load voltage with respect to the open circuit voltage was calculated, expressed as $\%V_{OC}$. In addition, the power consumed by the load resistor was calculated and converted to mW and dBm. The power loss through the rectifier was also calculated in dBm by subtracting the power consumed by the resistor from the input power. Power loss through the rectifier was used to calculate the power efficiency of the rectifier, displayed as a percentage. And lastly the output resistance of the rectifier was also calculated.

5.1.3.4.3 Results

The numerical results from the test can be seen in Table 5. Some of the data was graphed. For instance, it was of interest to plot out the power loss (in dB) with respect to the input power (in dBm). It was also of interest to plot the open circuit voltage (in mV) of the rectifier with respect to input power (in dBm). Lastly, the power efficiency with respect to $\%V_{OC}$ was also of interest.

The graph plotting the power loss of the rectifier versus the input power at 2.4 GHz can be seen in Figure 121. This graph shows that as the input power decreases, the rectifier becomes less power efficient.

The graph of the open circuit voltage of the rectifier with respect to the input power at 2.4 GHz can be seen in Figure 122. A trendline was included with this graph as an exponential curve; the Excel-generated equation has a correlation coefficient of 99.21%. Note that the y-axis is logarithmic base-10.

The graph of the power efficiency with respect to $\%V_{OC}$ of a 2.2 kΩ resistive load can be seen in Figure 123.

Trial	Attenutator (dB)	P_{in} (dBm)	V_{OC} (mV)	$V_{2.2k\Omega}$ (mV)	$\%V_{OC}$ (V/V)	$I_{2.195k\Omega}$ (mA)	$P_{2.195k\Omega}$ (mW)	$P_{2.2k\Omega}$ (dBm)	P_{loss} (dB)	$\eta_{rectifer}$	R_{out} (Ω)
1	0	19.8333	14000	7260	51.9%	3.268	23.726	13.752	6.081	24.7%	2037.782
2	1	18.8333	13000	6520	50.2%	2.951	19.241	12.842	5.991	25.2%	2181.534
3	2	17.8333	12000	5940	49.5%	2.682	15.931	12.022	5.811	26.2%	2239.343
4	3	16.8333	11100	5310	47.8%	2.396	12.723	11.046	5.787	26.4%	2393.418
5	4	15.8333	10100	4780	47.3%	2.162	10.334	10.143	5.690	27.0%	2442.971
6	5	14.8333	9280	4170	44.9%	1.899	7.919	8.987	5.847	26.0%	2689.796
7	6	13.8333	8570	3750	43.8%	1.703	6.386	8.052	5.781	26.4%	2821.307
8	7	12.8333	7920	3560	44.9%	1.554	5.532	7.429	5.404	28.8%	2688.258
9	8	11.8333	7040	2940	41.8%	1.328	3.904	5.915	5.918	25.6%	3061.054
10	9	10.8333	6400	2670	41.7%	1.195	3.191	5.039	5.795	26.3%	3066.423
11	10	9.8333	5840	2350	40.2%	1.056	2.482	3.947	5.886	25.8%	3259.809
12	11	8.8333	5150	2050	39.8%	0.913	1.872	2.722	6.111	24.5%	3319.268
13	12	7.8333	4520	1770	39.2%	0.79	1.398	1.456	6.377	23.0%	3410.311
14	13	6.8333	3990	1530	38.3%	0.683	1.045	0.191	6.642	21.7%	3529.216
15	14	5.8333	3520	1330	37.8%	0.593	0.789	-1.031	6.864	20.6%	3614.323
16	15	4.8333	3110	1150	37.0%	0.514	0.591	-2.283	7.117	19.4%	3741.043
17	16	3.8333	2720	1020	37.5%	0.453	0.462	-3.353	7.186	19.1%	3658.333
18	17	2.8333	2490	915	36.7%	0.412	0.377	-4.237	7.070	19.6%	3778.279
19	18	1.8333	2110	738	35.0%	0.331	0.244	-6.121	7.954	16.0%	4080.678
20	19	0.8333	1890	642	34.0%	0.29	0.186	-7.301	8.134	15.4%	4266.916
21	20	-0.1667	1810	629	34.8%	0.284	0.179	-7.480	7.314	18.6%	4121.296
22	21	-1.1667	1580	521	33.0%	0.237	0.123	-9.084	7.917	16.2%	4461.622
23	22	-2.1667	1350	429	31.8%	0.194	0.083	-10.797	8.631	13.7%	4712.343
24	23	-3.1667	1150	350	30.4%	0.159	0.056	-12.545	9.379	11.5%	5017.143
25	24	-4.1667	990	298	30.1%	0.135	0.040	-13.954	9.788	10.5%	5097.114
26	25	-5.1667	770	249	32.3%	0.112	0.028	-15.546	10.379	9.2%	4592.751
27	26	-6.1667	689	210	30.5%	0.094	0.020	-17.047	10.880	8.2%	5006.69
28	27	-7.1667	655	177	27.0%	0.08	0.014	-18.489	11.323	7.4%	5927.74
29	28	-8.1667	530	130	24.5%	0.059	0.008	-21.152	12.985	5.0%	6753.846
30	29	-9.1667	460	106	23.0%	0.049	0.005	-22.845	13.678	4.3%	7330.472
31	30	-10.1667	406	117	28.8%	0.053	0.006	-22.075	11.909	6.4%	5421.838
32	31	-11.1667	399	84	21.1%	0.038	0.003	-24.959	13.793	4.2%	8231.25
33	32	-12.1667	328	62	18.9%	0.028	0.002	-27.605	15.438	2.9%	9417.258
34	33	-13.1667	265	45	17.0%	0.021	0.001	-30.246	17.079	2.0%	10731.11
35	34	-14.1667	223	35	15.7%	0.016	0.001	-32.518	18.351	1.5%	11790.29

Table 5. Tabulated results from Experiment 15

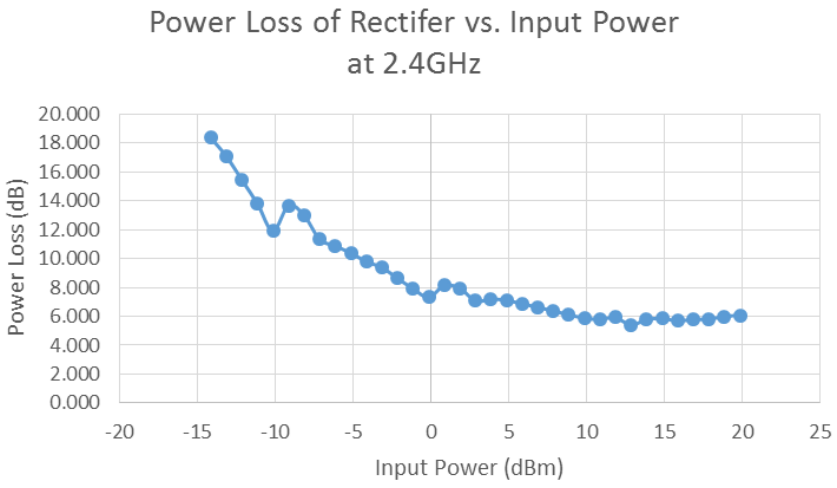

Figure 121. Power loss of rectifier with respect to the input power at 2.4 GHz

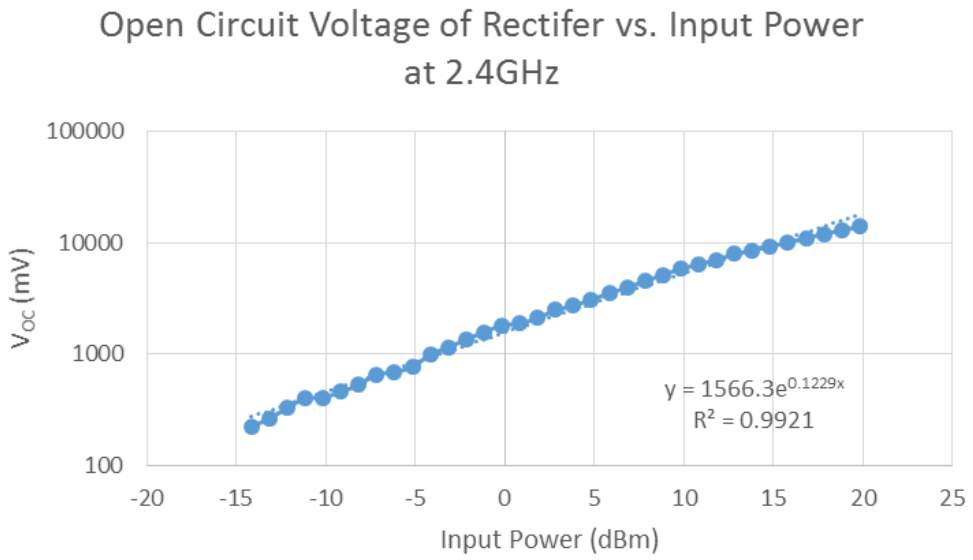

Figure 122. Open circuit voltage of the rectifier with respect to input power at 2.4 GHz

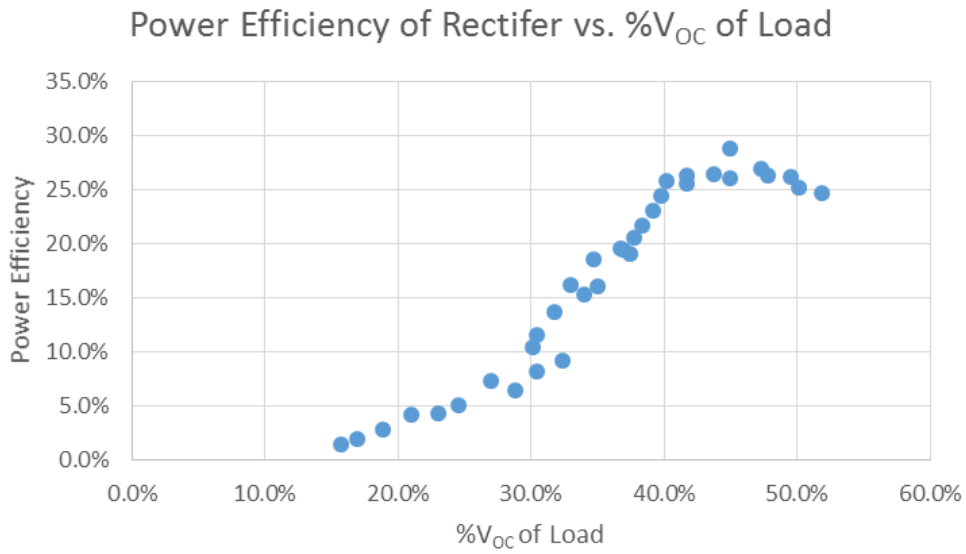

Figure 123. Power efficiency of the rectifier with respect to the $\%V_{OC}$

5.1.3.4.4 Discussion

The first graph, shown in Figure 121, shows that as the input power decreases, the rectifier becomes less power efficient, which is significant because it shows that as power input decreases, the rectifier becomes more power inefficient; said in other words, as power input decreases, the price paid in power loss increases (power loss is not constant with input power!). This relationship is very likely due to the non-linear behavior of the Schottky diodes.

The second graph, shown in Figure 122, shows that as power input increased, the open circuit voltage increased. This relationship was expected. It shows that the open circuit voltage increases as the input power increases, with no flattening of the curve.

The third graph, shown in Figure 123, shows that power efficiency decreases with the $\%V_{OC}$ decreases below 40%. Moreover, this graph shows that for a non-varying resistive load at 2.2 kΩ, the $\%V_{OC}$ changes with respect to input power. Not only does the $\%V_{OC}$ change with input power, power efficiency changes with input power as well. This assessment is important because the BQ25504 utilizes $\%V_{OC}$ to set its input resistance. Looking at this graph, it appears that the maximum power efficiency achieved was somewhere between 40% and 50 %, with the maximum power efficiency just above 25%. For the BQ25504 to draw power from the rectifier circuit at the optimal power efficiency, the $\%V_{OC}$ needs to be set correctly on the BQ25504. The $\%V_{OC}$ is set with a pair of biasing resistors.

5.1.4 Booster Experimentation

This section lays out the experimentation that took place for the booster circuitry. Seven tests were conducted on the BQ25504 evaluation board in conjunction with the two stage Dickson multiplier. All tests take place in the context of Experiment 16.

5.1.4.1 Experiment 16: Booster Experimentation for First Design Approach

The two stage Dickson multiplier implemented in this experimentation utilized only a series 0.6 pF capacitor element for impedance matching. A 6 dB attenuator was implemented at the input of the two stage Dickson multiplier to reduce the power input level to approximately 12.2 dBm. Figure 124 shows the two stage Dickson multiplier in conjunction with the BQ25504 evaluation board.

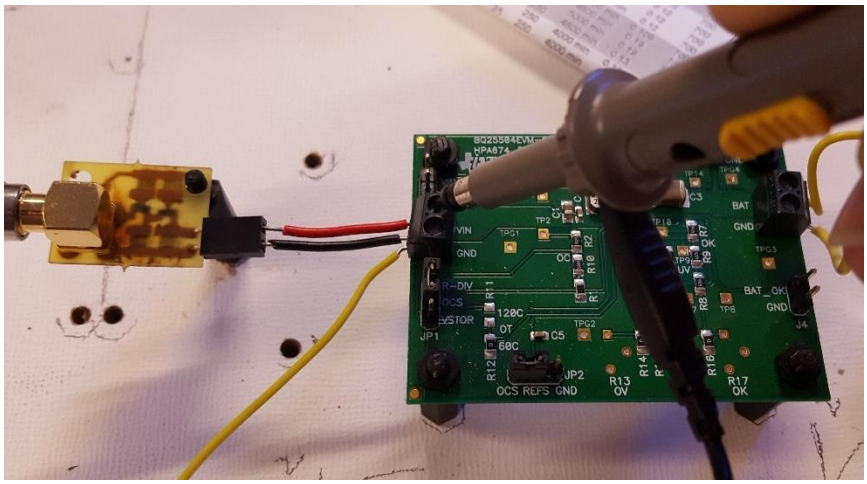

Figure 124. BQ25504 evaluation board in conjunction with the two stage Dickson multiplier for the first design attempt

5.1.4.1.1 Set up

A block diagram of the set-up for Experiment 16 can be seen in Figure 125. Note that this block diagram also shows the measurement points, with a V indicating a voltage measurement, and an I indicating a current measurement.

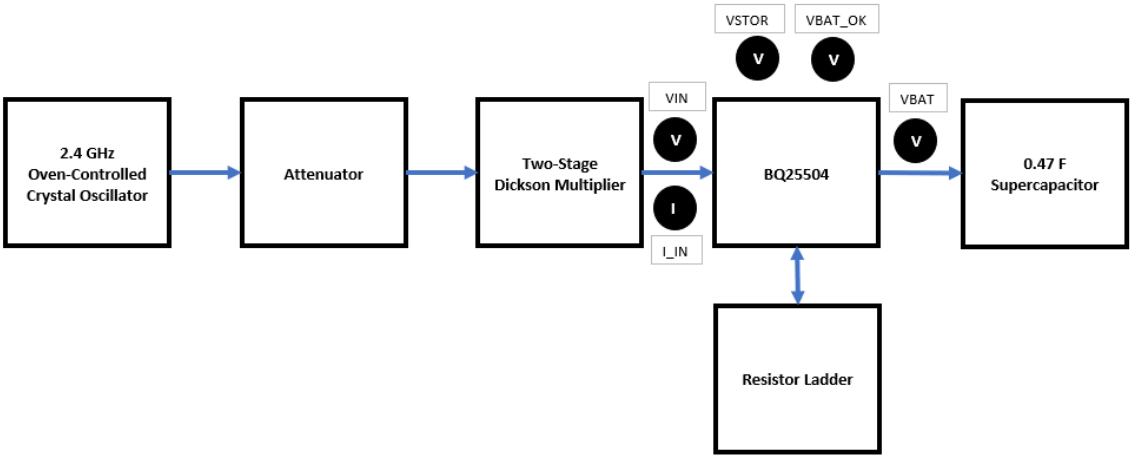

Figure 125. Block Diagram for the Energy Harvesting Circuitry in Experiment 16

A jumper on the 3-pinned J2 connection on the BQ25504 Evaluation Board was left disconnected. An additional breadboard was used to serially stack twenty (20) 1MΩ resistors, creating a 20MΩ resistor ladder with 1MΩ resolution. To provide power to the resistor ladder, V_{IN} and GND from the BQ25504 were jumpered over to the breadboarded resistive ladder. To set open circuit voltage percentage, $\%V_{OC}$, for the MPPT circuit, the OCS pin of the J1 connection on the BQ25504 Evaluation Board was jumpered over to the breadboarded resistor ladder. Four voltages were monitored during the testing using a Tektronix oscilloscope:

- Channel 1 was connected to VSTOR,
- Channel 2 was connected to VBAT,
- Channel 3 was connected to VIN, and
- Channel 4 was connected to VBAT_OK.

The averages for each channel were reported on the oscilloscope screen, as shown in Figure 126. A timestamp for each measurement was issued using macro features in a Microsoft Excel spreadsheet. The timestamps were used to determine how much time (in seconds) had elapsed since the onset of the test session.

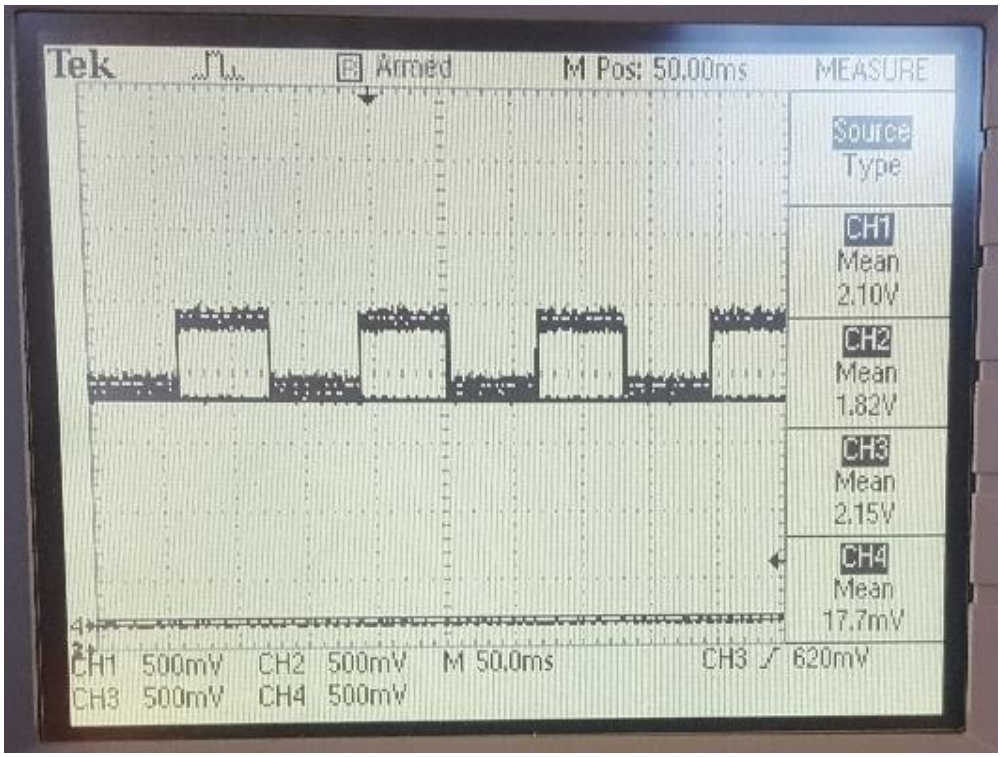

Figure 126. Square waveform that would appear at the end of the cold start stage.

A multimeter was connected in series between the BQ25504 and the two stage Dickson multiplier so that the input current could be measured. Using the voltage input measured from the Tektronix oscilloscope as well as the current input measured from the multimeter, the input power and input resistance were calculated.

5.1.4.1.2 Results

The results for the seven (7) tests run in Experiment 16 are shown in the subsections below.

5.1.4.1.2.1 Test 1 Results

The open circuit voltage percentage for the BQ25504 in test one was set to 55% of the open circuit voltage. Overall, it took the BQ25504 12 minutes and 19 seconds to charge the super capacitor to the point where the VBAT_OK signal pin was set high (indicating the energy storage device is ready to be used). Figure 127 shows the results for Test 1.

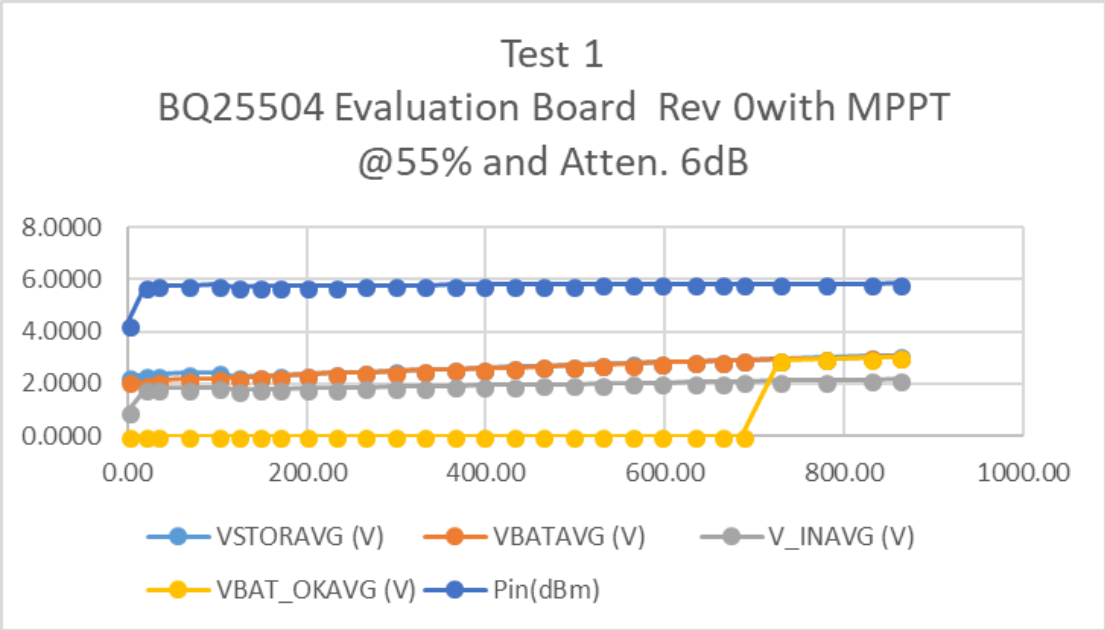

Figure 127. Test 1 of Experiment 16 results

5.1.4.1.2.2 Test 2 Results

The open circuit voltage percentage for the BQ25504 in test two was set to 60% of the open circuit voltage. Overall, it took the BQ25504 12 minutes and 12 seconds to charge the super capacitor to the point where the VBAT_OK signal pin was set high. Figure 128Figure 127 shows the results for Test 2.

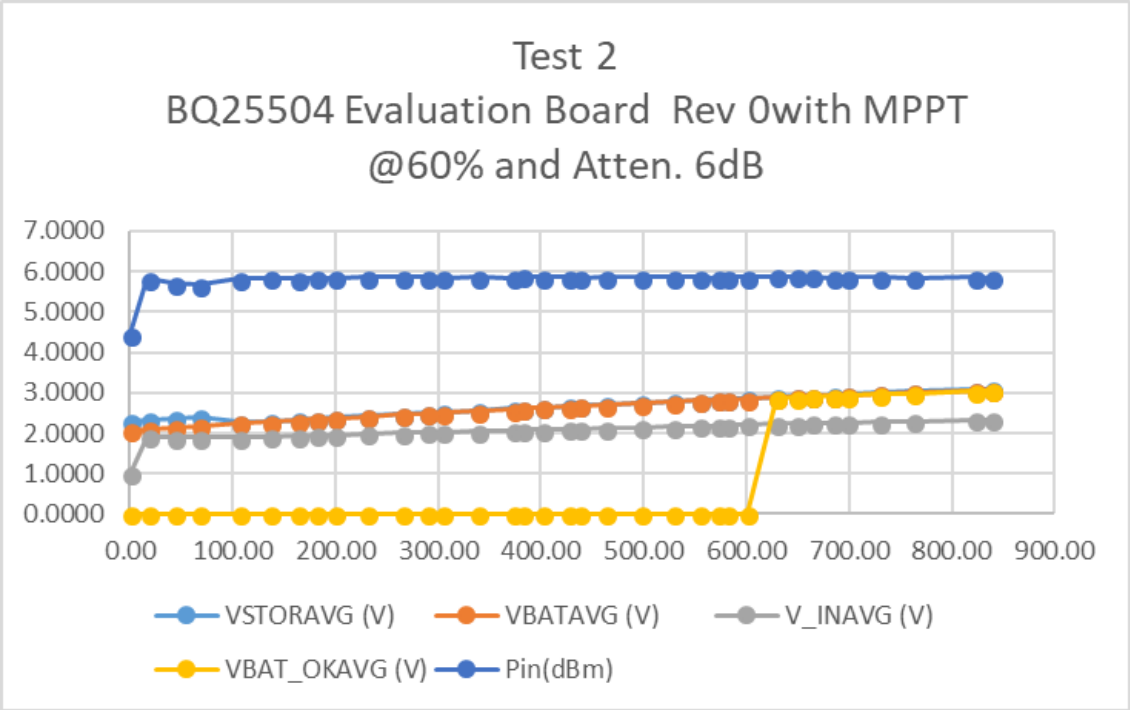

Figure 128. Test 2 of Experiment 16 results

5.1.4.1.2.3 Test 3 Results

The open circuit voltage percentage for the BQ25504 in Test 3 was set to 65% of the open circuit voltage. Overall, it took the BQ25504 13 minutes and 36 seconds to charge the super capacitor to the point where the VBAT_OK signal pin was set high. Figure 129Figure 127 shows the results for Test 3.

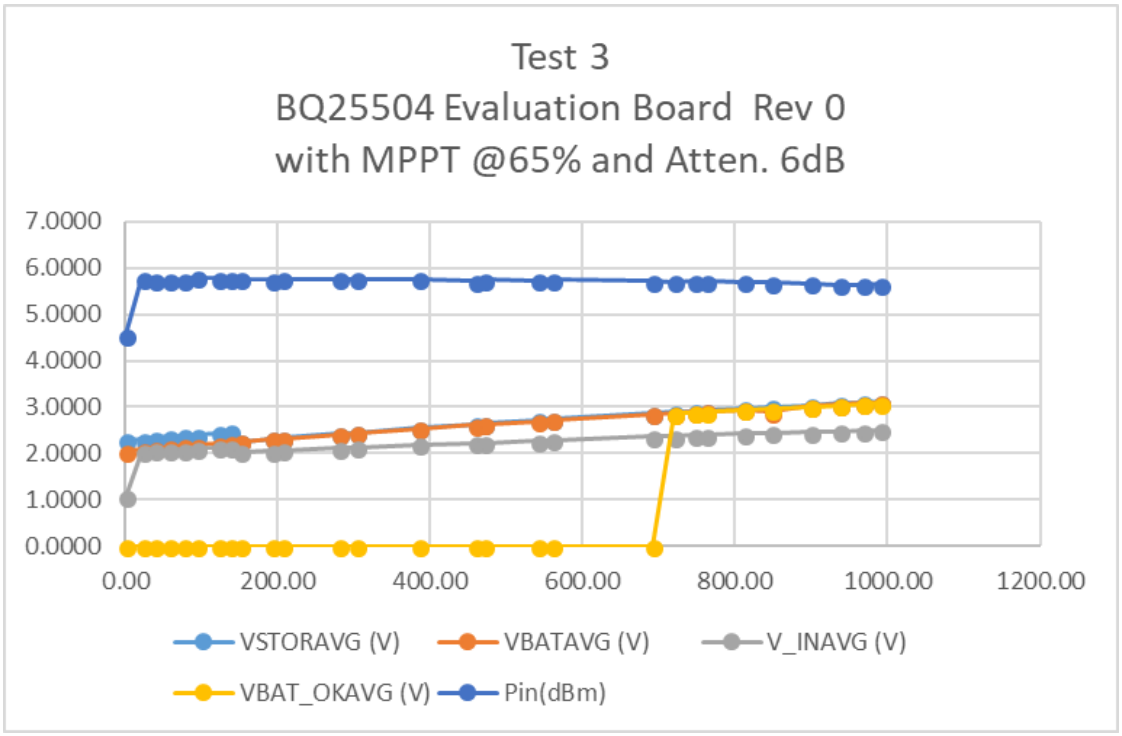

Figure 129. Test 3 of Experiment 16 results

5.1.4.1.2.4 Test 4 Results

The open circuit voltage percentage for the BQ25504 and Test 4 was set to 70% of the open circuit voltage. Overall, it took the BQ25504 12 minutes, 19 seconds to charge the super capacitor to the point where the VBAT_OK signal pin was set high. Figure 130Figure 127 shows the results for Test 4.

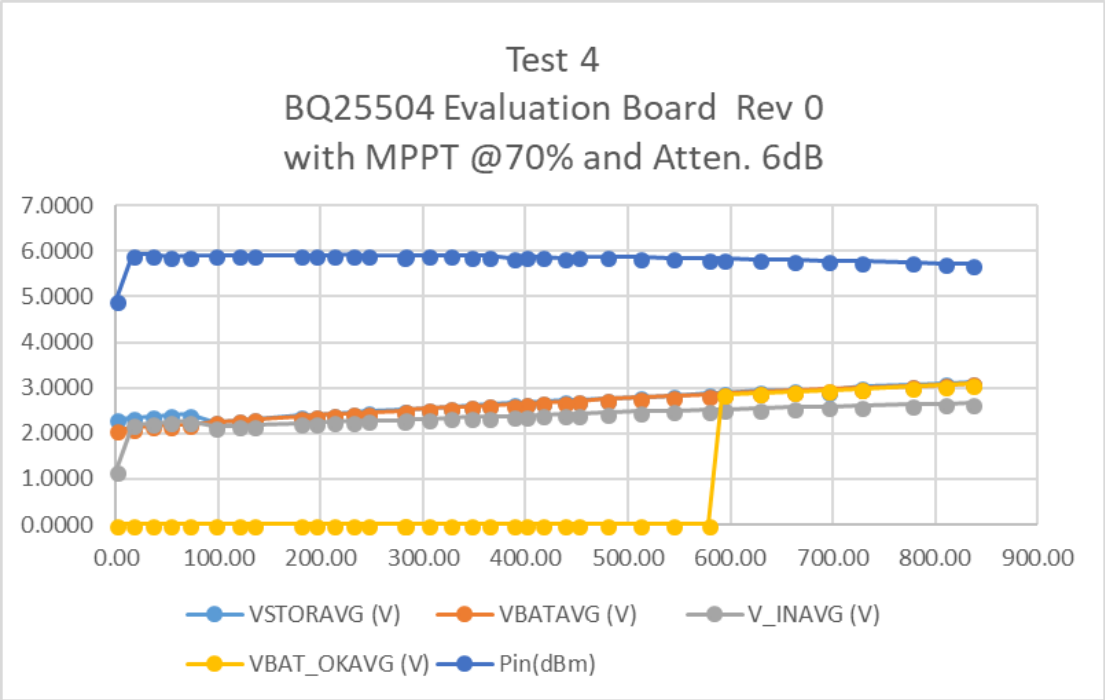

Figure 130. Test 4 of Experiment 16 results

5.1.4.1.2.5 Test 5 Results

The open circuit voltage percentage for the BQ25504 and Test 5 was set to 75% of the open circuit voltage. Overall, it took the BQ25504 12 minutes, 30 seconds to charge the super capacitor to the point where the VBAT_OK signal pin was set high. Figure 131Figure 127 shows the results for Test 5.

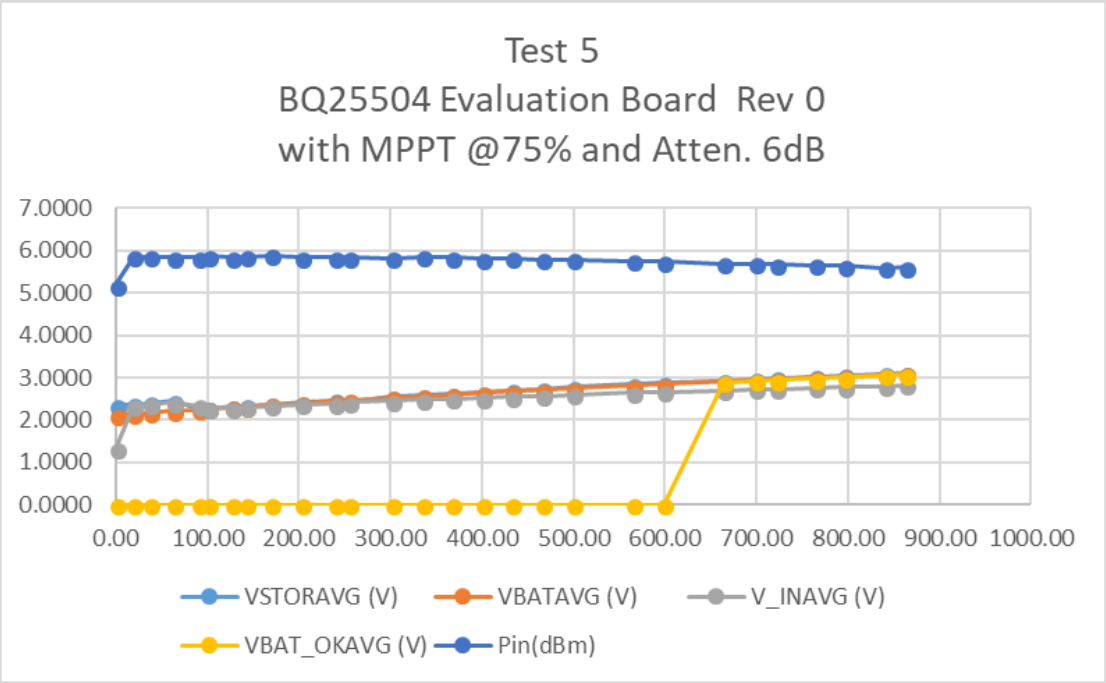

Figure 131. Test 5 of Experiment 16 results

5.1.4.1.2.6 Test 6 Results

The open circuit voltage percentage for the BQ25504 and Test 6 was set to 80% of the open circuit voltage. Overall, it took the BQ25504 11 minutes, 38 seconds to charge the super capacitor to the point where the VBAT_OK signal pin was set high. Figure 132 shows the results for Test 6.

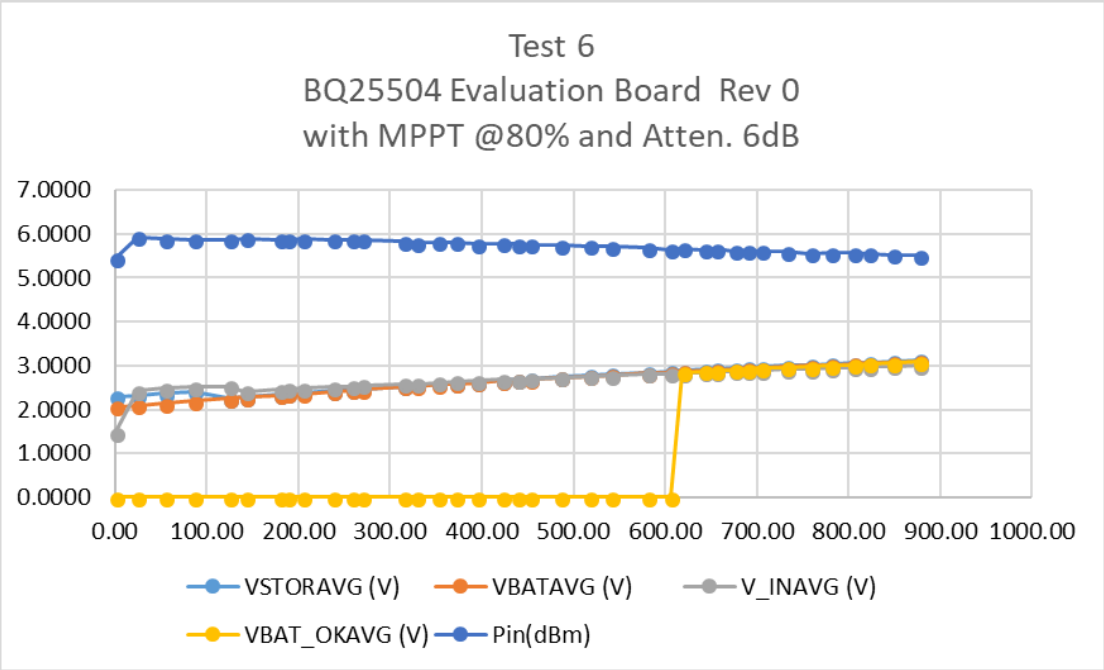

Figure 132. Test 6 of Experiment 16 results

5.1.4.1.2.7 Test 7 Results

The open circuit voltage percentage for the BQ25504 and Test 7 was set to 85% of the open circuit voltage. Overall, it took the BQ25504 12 minutes, 9 seconds to charge the super capacitor to the point where the VBAT_OK signal pin was set high. Figure 133 shows the results for Test 7.

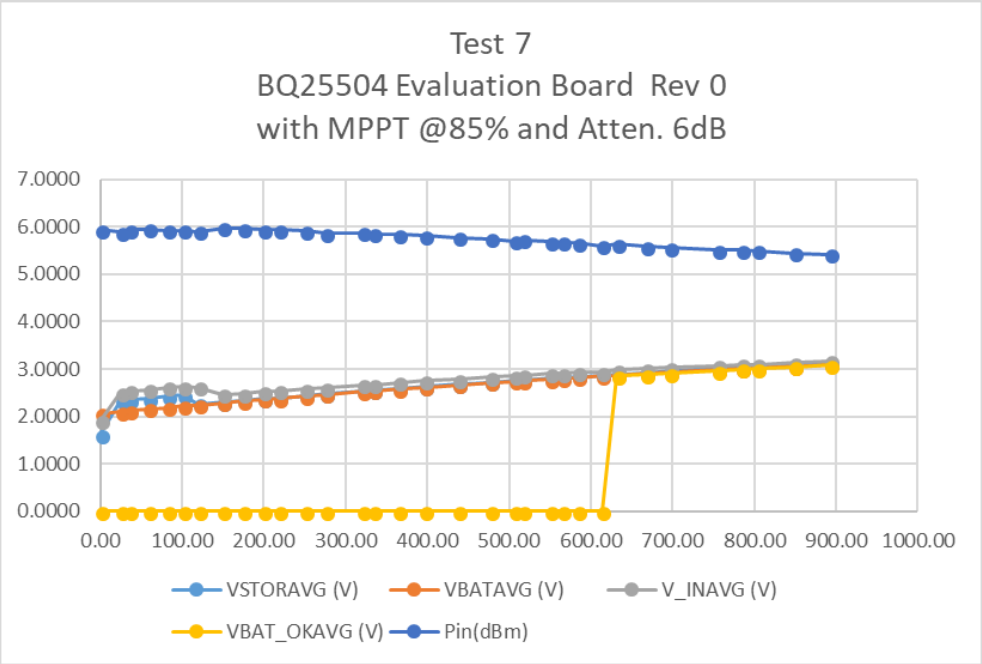

Figure 133. Test 7 of Experiment 16 results

5.1.4.1.3 Discussion

No significant difference could be detected in the time it took to charge the supercapacitor vs the $\%V_{OC}$ set on the BQ25504. Instead, the results seemed to indicate that the $\%V_{OC}$ of the BQ25504 did not matter. Moreover, the input power into the BQ25504 appeared to be constant across the different tests, meaning that the $\%V_{OC}$ setting did not appear to affect the power efficiency.

After later analysis, and after noticing how much better the circuit in Experiment 22 behaved, it was posited that by not changing the value of the C_{HVR} capacitor on the BQ25504 shown in Figure 24 from 4.7 µF to a much lower value (on the order of the 8.2 pF capacitors of the Two-Stage Dickson Multiplier) that the output impedance of the Two-Stage Dickson Multiplier was not well matched with the BQ25504.

5.2 Second Design Attempt: Grounding Clamps at 8 kHz

After it was noted from Experiments 10 and 11 that at lower frequencies significantly more power was able to be transferred through the rebar embedded in a concrete medium, a second design approach was investigated. The second design approach utilized a power and ground probe at each tap point and operated at a frequency of 8 kHz.

5.2.1 Grounding Clamp Experimentation in Concrete and Air

Due to the simplicity of the second design approach and to the low applied frequency, not a lot of experimentation was necessary with air as the dielectric medium to gain an understanding of EMF phenomena. Hence, the first experiments for the second design approach (Experiments 17 – 21) were conducted in concrete.

Experiment 17 was conducted to establish the performance of power transmission across a single length of rebar through concrete. After a flaw with the grounding was discovered in Experiment 17, a revision made to the grounding and was tested in Experiment 18.

In Experiment 19, three changes were imposed on the design: (a) the experiment was conducted without concrete and in the presence of air, (b) grounding clamps were implemented as the tap points onto the rebar, and (b) the length of rebar was changed to a cage. In Experiment 20, a VNA was used to evaluate the rebar cage. In Experiment 21, the rebar cage was embedded in concrete and then tested for performance.

5.2.1.1 Experiment 17: Single Length of Rebar Embedded in Concrete

Once the design of the 2.4 GHz launcher was demonstrated to be insufficient, design alternatives were considered. The frequency span on the VNA was widened so that all frequencies available to the VNA were included into the graph. The VNA can perform measurements from 9 kHz to 6.5 GHz. It was noticed that the lowest frequencies available, on the VNA, in the 9 kHz range, performed the best. Given this revelation, the frequency allocations available for use were assessed. The FCC rules indicate that frequencies below 9 kHz are unallocated, and therefore free to use [27]. To prevent from transmitting above 9 kHz, a frequency of 8.0 kHz was targeted.

5.2.1.1.1 Set-Up

A new pillar of concrete was poured using the same mixture of the prior batches; however, this time the concrete pillar had a longer length of rebar protruding from both the top and the bottom. After five days of drying, the new concrete pillar was transported into the lab. A coaxial cable with BNC connectors was then cut in half; and then both halves of the cable were stripped of the outer sheath, outer conductor, and insulation; and then on both ends of the concrete pillar the center conductor of a half-cable was affixed to the rebar using hose clamps. Figure 135 shows the configuration for Experiment 17.

Figure 134. Top end of concrete pillar with hose clamp connecting BNC cable half to protruding rebar.

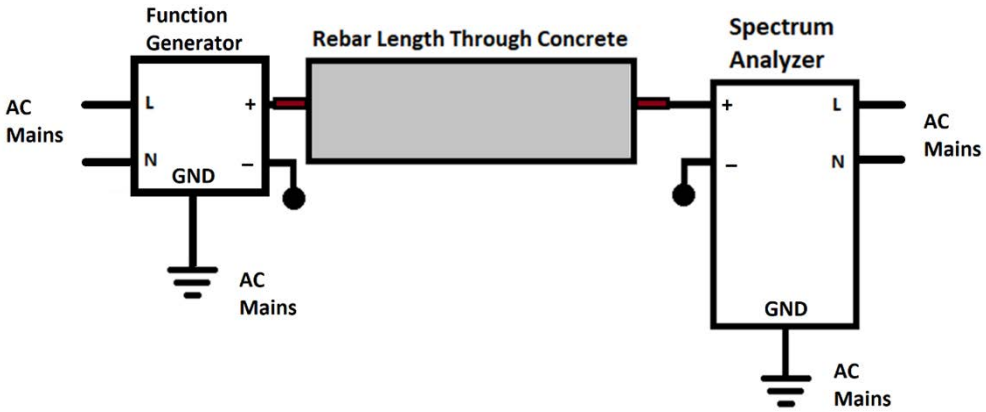

Figure 135. Configuration for Experiment 17

5.2.1.1.2 Results

One of the BNC cable-halves was connected to a Rigol DG4162 Function Generator. The function generator was set to 8.0 kHz at 10 V peak to peak. The other BNC cable-half was connected to s Hewlett-Packard 8562A Spectrum Analyzer. The spectrum analyzer was set to a start frequency of 7.0 kHz and a stop frequency of 20.0 kHz; the reference level was set to 30.0 dBm. The function generator was energized, and a measurement of 23.0 dBm was observed at 8.0 kHz.

Figure 136. Power received by spectrum analyzer from receiving cable half tapping off protruding rebar.

The function generator was then deenergized. The function generator was then directly connected to the spectrum analyzer. With the voltage peak to peak reduced on the function generator, the function generator was set to 8.0 kHz with the big to be gold is reduced. The function generator was then turned on and incrementally increased back up to 10 V peak to peak. (This was done to ensure that the function generator wasn't going to exceed 30 dBm, which was the absolute maximum power input for the spectrum analyzer. The power input was closely monitored with each increase in voltage.) When the function generator was back at 10 V peak to peak, the input power was measured at 24.0 dBm. As can be seen, a very low 1.0 dB power loss was measured.

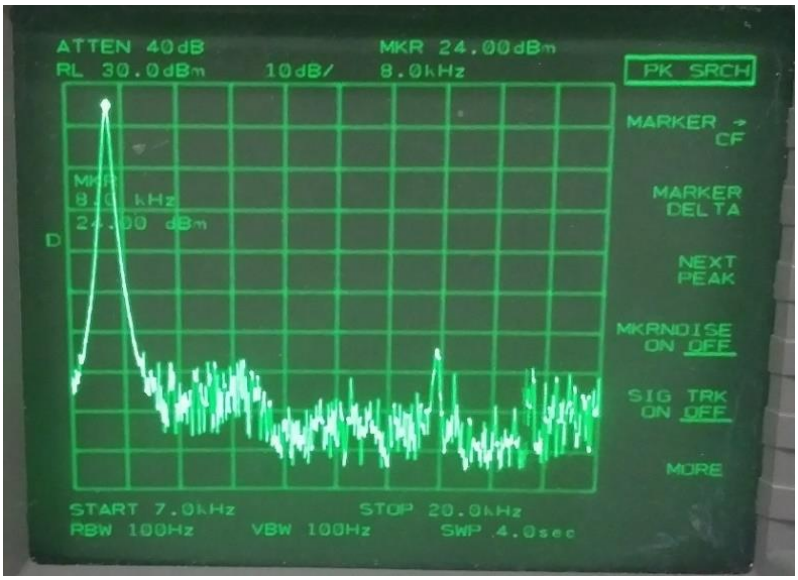

Figure 137. Output power of the function generator at 10 V peak to peak at 8 kHz

5.2.1.1.3 Discussion

Experiment 17 yielded very promising results, showing a power loss of maybe 1.0 dBm. However, a major flaw was noticed after the experiment took place. The function generator utilized Line, Neutral, and Ground from the AC Mains power supply at its power input, as did the spectrum analyzer. This is an important detail.

It is essential practice that at some point in the building that the Ground and Neutral for the AC Mains be tied together — the practice is commonly known among electricians and engineers. Hence, even though as power is routed throughout a given building the electric potential

difference between Neutral and Ground grow some (due to the resistivity of the wire), the resistance between Neutral and Ground is small and is not enough to represent conditions in the field. With the circuit implemented as shown in Figure 136, ground closes the circuit, and means that current is returning from the spectrum analyzer to the function generator, which will not happen in the field, because the ground in the embedded sensors will not be tied to the ground of the power supply.

5.2.1.2 Experiment 18: Single Length of Rebar Embedded in Concrete with Varied Simulated Ground Resistance

Experiment 18 addresses the flaws in Experiment 17 by simulating a resistance to ground. After the results of Experiment 17 were analyzed, it was noticed that the ground of the function generator and the ground of the spectrum analyzer were connected through the AC mains power supply of the building. Given that the embedded sensor would be within the concrete affixed to the rebar, and that the nearest ground would be through the concrete and then through the soil, it was determined that the design approach should be investigated with a varied resistance to ground.

5.2.1.2.1 Set-Up

Figure 138 is a diagram of the set up for Experiment 18.

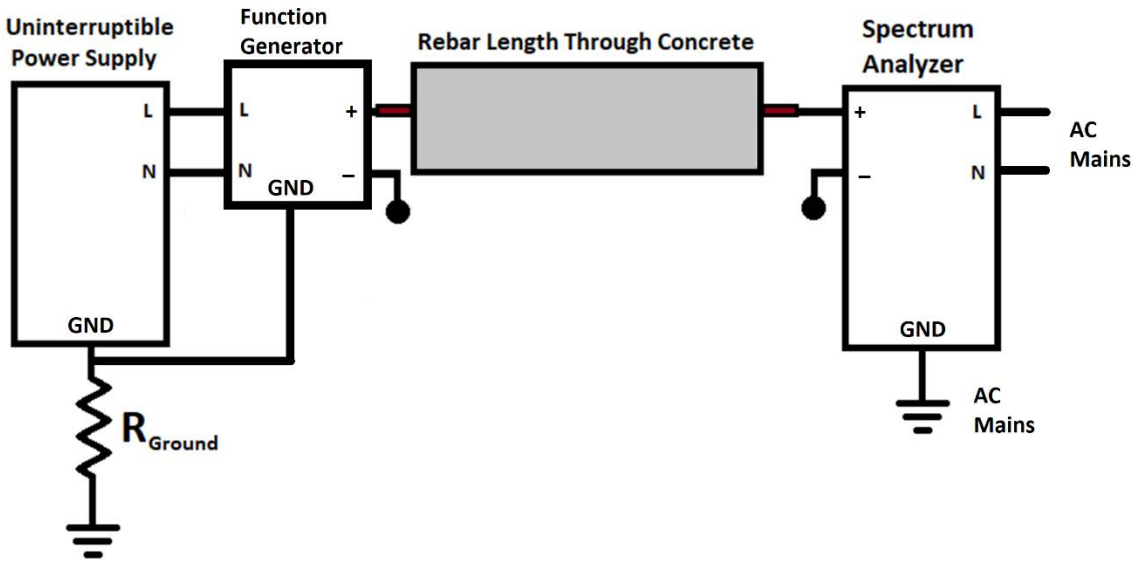

Figure 138. Diagram of the Experiment 18 set up

In Experiment 18, an uninterruptible power supply supplied AC power to a function generator. Meanwhile, the spectrum analyzer was powered through the AC mains supply from the building. Using two banana alligator clips and a given resistor, the ground of the uninterruptible power supply and AC mains was connected, with the value of the resistor modeling the ground resistance. The uninterruptible power supply was energized and the function generator transmitted a 24 dBm 8 kHz signal through the rebar.

5.2.1.2.2 Results

Figure 139 shows the plotted results of the power loss with respect to the modeled ground resistance. It can be seen that after 100 Ω of ground resistance significant power loss occurs.

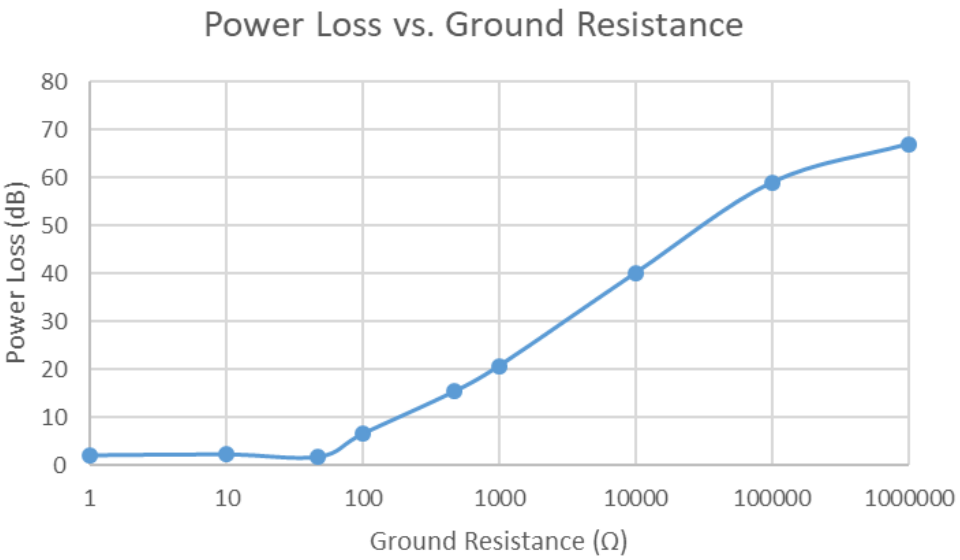

Figure 139. Plotted results for Experiment 18

Table 6 shows the received power and the calculated power loss with respect to the applied ground resistance.

Resistance (Ω)	$P_{received}$ (dBm)	P_{loss} (dB)
1	21.83	2.17
10	21.67	2.33
47	22.17	1.83
100	17.33	6.67
470	8.5	15.5
1000	3.17	20.83
10000	-16.17	40.17
100000	-35	59
1000000	-43	67
Open Circuit	-44.67	68.67

Table 6. Results for Experiment 18

5.2.1.2.3 Discussion

The results of Experiment 18 shows that the ground resistance affects the power loss through the circuit dramatically. As long as the ground resistance stays below 100 Ω of resistance, about most of the power will transfer across the rebar embedded in concrete. When the ground resistance exceeds 100 Ω, significant power losses begin to emerge, increasing by approximately 20 dB as the resistance increases an order of magnitude.

The ground resistance for a sensor embedded in concrete is not known, and likely cannot be guaranteed for any given location or time due to variance in moisture over time at a given location, and variance in ground moisture levels across geography. Not to mention, such a structure might not necessarily be submerged in a soil environment, so relying on a ground resistance being less than 100 Ω might not even be an option. Hence, Experiment 19 through Experiment 21 investigated transferring power through a rebar cage itself, using grounding clamps to tap to two different legs, and at two different electric potentials (positive and negative).

5.2.1.3 Experiment 19: Evaluating the Rebar Cage with a Vector Network Analyzer

The aim of Experiment 19 was to establish how the Rebar cage behaved with and without a load of approximately 50 Ω. Two parameters of interest were (1) the input impedance and (2) the standing wave ratio. The aim of these two parameters was to (a) qualitatively determine how well matched 50 Ω was to the characteristic impedance of the rebar cage, and (b) determine how much reflection would result with and without an approximately 50 Ω load.

5.2.1.3.1 Set-Up

Input Impedance and Standing Wave Ratio measurements were made on the rebar cage at 8 kHz. The impedance measurements were made using a VNA designed for the UHF bands; the manufacturer of the VNA is Array Solutions.

Grounding clamps were installed onto the legs of the rebar. These were used as termination points for connections. The rebar cage was then laid on to a lab bench. Any connections made to the rebar were done through the grounding clamps.

The configuration for Experiment 19 for the first measurement can be seen in Figure 140. The configuration for Experiment 19 for the second and third measurement can be seen in in Figure 141.

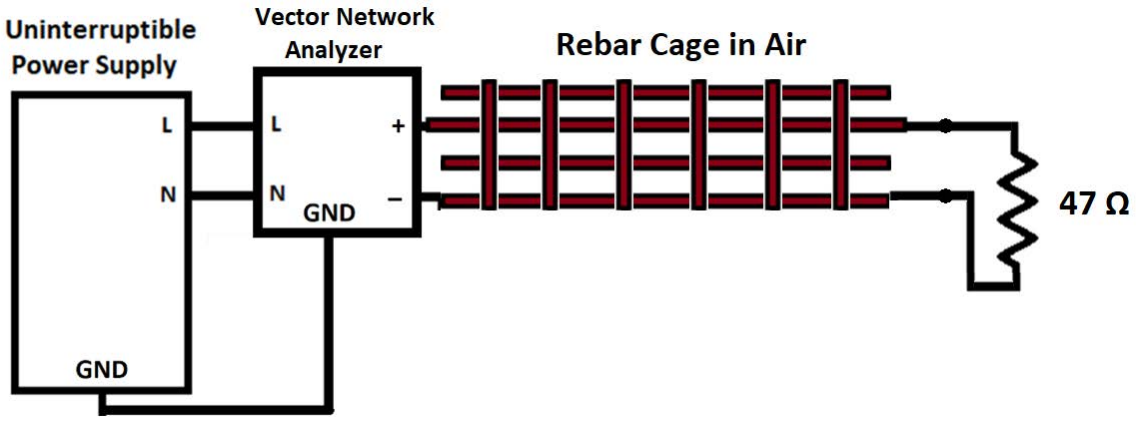

Figure 140. Diagram of the set-up for Experiment 19 for the first measurement

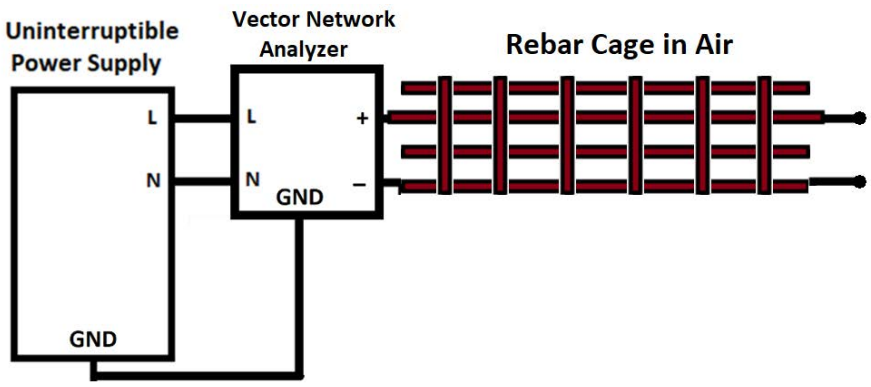

Figure 141. Diagram of the set-up for Experiment 19 for the second and third measurement

5.2.1.3.2 Results

The first measurement used a 47 Ω test resistor to terminate the rebar connections. At 8 kHz, the equivalent series resistance was measured to be 2.823 Ω; the equivalent series reactance was measured to be 0.378 Ω; and the standing wave ratio was measured to be 17.7484.

The second measurement removed the 47 Ω resistor. The same vector network analyzer was used to make measurements of the rebar cage. At 8 kHz, the equivalent series resistance was measured to be 3.148 Ω; the equivalent series reactance was measured to be 0.248 Ω; the standing wave ratio was measured to be 15.9141.

The third measurement was made after the rungs were de-wired and then re-wired; the purpose of this was to restructure the rebar cage so that the legs were more equidistant from each other. The same vector network analyzer was used to make measurements of the rebar cage. At 8 kHz, the equivalent series resistance was 2.707 Ω; the equivalent series reactance was 0.342 Ω; the standing wave ratio was measured to be 18.5111.

5.2.1.3.3 Discussion

The input impedance varies across all three measurements on the order of approximately 1 Ω; that is, the input impedance varied with (a) a 47 Ω load applied, (b) no load applied, and (c) no load applied, but the cage was manipulated and shaken before measurement. From this, it can be drawn that the input impedance of the cage is likely around 3.0 + j 0.3 Ω. Moreover, the standing wave ratio was greater than 15 for all three measurements, which indicates that significant power reflection is resulting.

5.2.1.4 Experiment 20: Evaluating the Rebar Cage with a Function Generator and Spectrum Analyzer

With Experiment 19 establishing how the rebar cage behaved with and without an approximately 50 Ω applied to the end of the rebar cage, Experiment 20 aimed to establish how much power was received by an approximately 50 Ω by utilizing a function generator as a power source and a spectrum analyzer as a 50 Ω load.

5.2.1.4.1 Set-Up

A Rigol DG4162 function generator was connected to one end of the rebar cage at the grounding clamp terminals; the frequency was set to 8 kHz, and the peak to peak voltage was set to 10 V. A Hewlett-Packard 8562A spectrum analyzer was connected to the other end of the rebar cage to measure the power measurements. All connections were made using SMA cables with alligator clips terminated at the end.

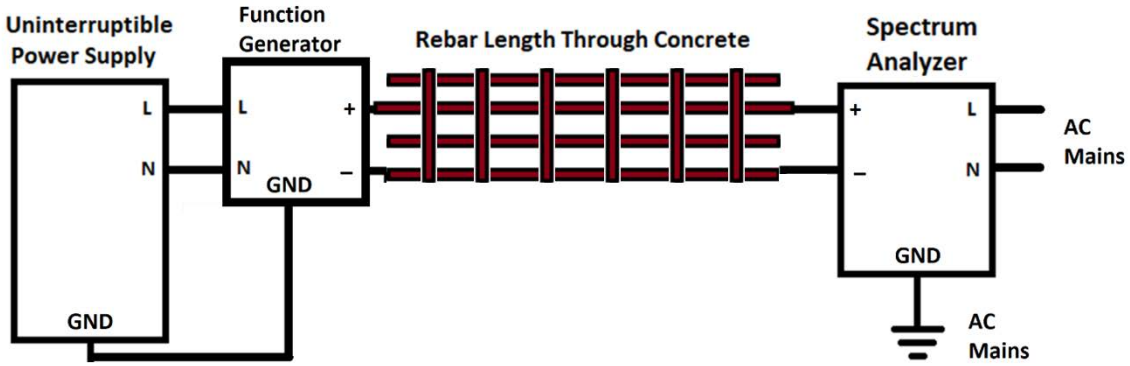

Figure 142. A diagram of the set-up for Experiment 20

5.2.1.4.2 Results

When a 10 V peak to peak voltage was applied to one end of the terminals, a power of 4.50 dBm was detected on the function generator, as can be seen in Figure 143.

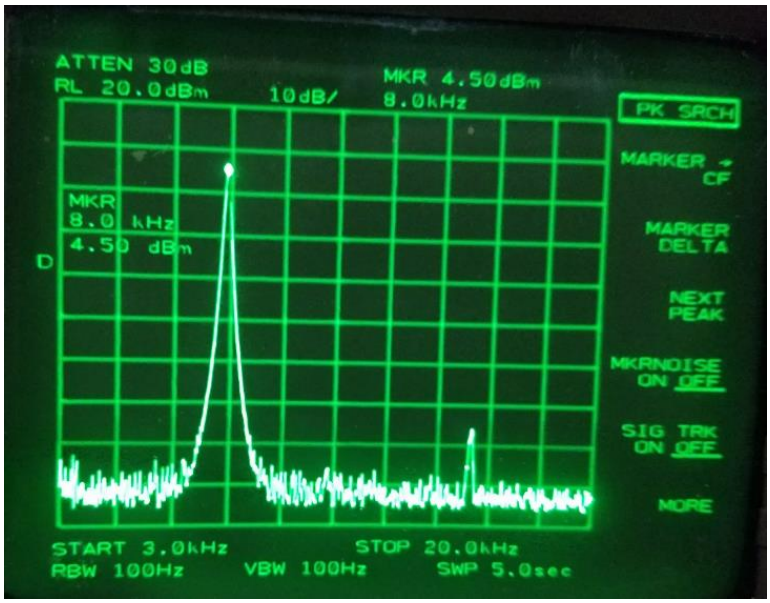

Figure 143. Power received by spectrum analyzer in Experiment 20 directly after powering circuit

After some time had passed, and the function generator was left on at the same frequency in voltage, the detected power at the output had risen to 6.17 dBm, as can be seen in Figure 144.

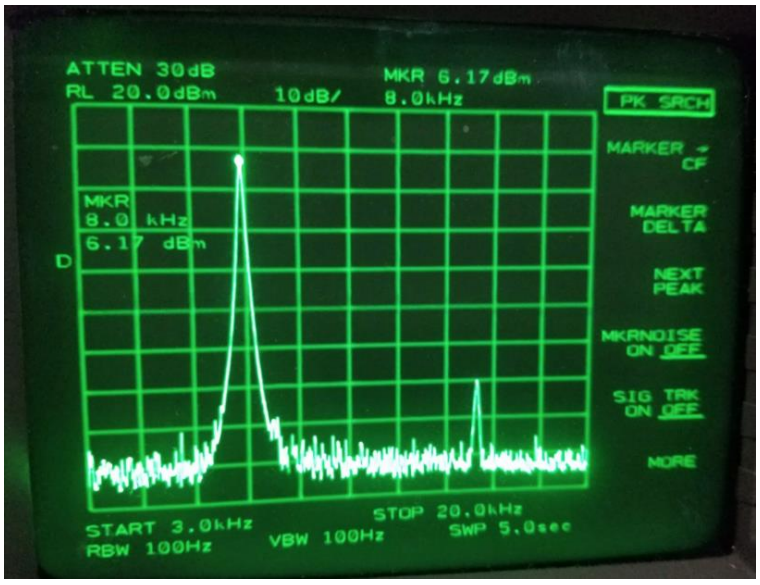

Figure 144. Power received by the spectrum analyzer in Experiment 20 after a few minutes passed

5.2.1.4.3 Discussion

Before making these measurements, the rebar cage configuration was manipulated and examined while the function generator was still on: many sensitivities were noticed as different parts of the cage were moved and manipulated (e.g. rotated, inclined, scooted, suspended, lifted, etc.). The power dropped well below -20 dBm without any clear indication which specific manipulation would cause the power drop to occur. Furthermore, it was noted that the tightness with which the grounding clamps were affixed to the rebar affected the power received by the spectrum analyzer: the relationship appears to be that when the grounding clamps are screwed tighter (especially at the site where power was sourced from) more power transfer occurred through the rebar cage.

5.2.1.5 Experiment 21: Transferring Power Through the Rebar Cage in Air and Concrete

Experiment 21 tested power transfer to the rebar cage in both air and concrete. Experiment 21 was conducted in two parts, one part in air and one part in concrete. Both parts of the experiment were set up the same way, the only difference being the median in which the rebar cage was immersed.

5.2.1.5.1 Set-Up

Experiment 21 was set up such that three pairs of grounding clamps were connected to the same pair of rebar legs. As shown in Figure 145, one pair of grounding clamps was for the source, another pair of grounding clamps was for a tap point located at the center of the rebar cage, and another pair of grounding clamps was for a tap point located at the end of the rebar cage.

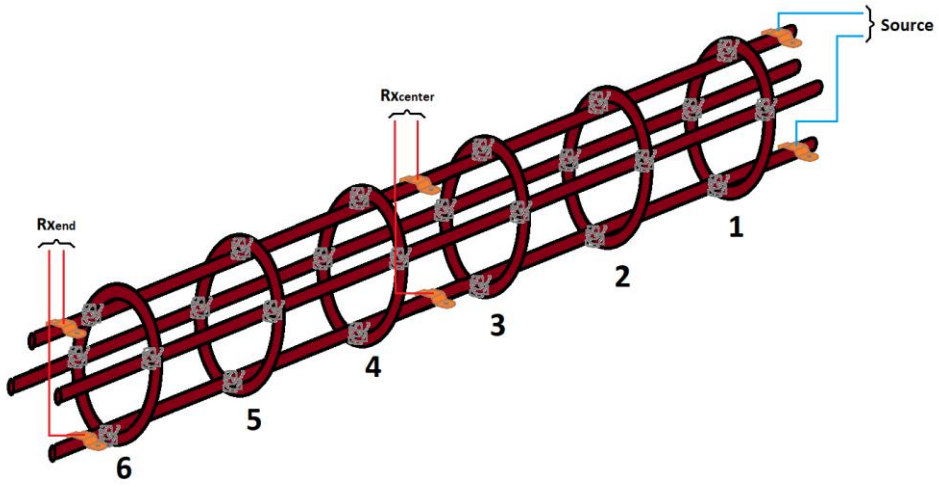

Figure 145. Diagram identifying the connections for the Rebar Cage Test Set Up for 8 kHz

To provide a connection between the grounding clamps and the test equipment, a 16 AWG wire was affixed to the grounding clamp at the screw terminal, after which sealant was applied to the grounding clamp at the point where the 16 AWG wire was affixed, as can be seen in Figure 146. The purpose of the sealant was to prevent any ingress of moisture from the concrete mixture upon the pouring of the material.

Figure 146. Duct sealant applied on the grounding clamp where the 16 AWG wire was affixed

A Universal Power Supply (UPS) provided power to the function generator. AC Mains provided power to the Spectrum Analyzer. The function generator transmitted a signal at one end of the rebar cage, while a spectrum analyzer measured the power received at the one of two points along the cage: (1) at the opposite end of the rebar cage, and (2) at the center of the cage. The power received was measured at one location at a time.

In air, the measurements were taken on a lab table with a wooden surface. In concrete, the measurements were taken with the concrete pillar vertically standing on a pallet, which can be seen in Figure 147. What is not clearly visible in Figure 147 are the wires exiting the concrete molding tube; the wires are exiting through cord grips that were installed on the concrete molding tube, which allows for the wires to be accessed.

Figure 147. Experiment 21 embedded in concrete standing on a pallet

5.2.1.5.2 Results

The results of the experiment can be seen in Figure 148. From this figure, the power loss at the center tap point is 24.74 dB without concrete present (in air); however, power loss of the center tap point is 54.50 dB with concrete present. The center tap point is approximately 2 feet away from the power source. Approximately 2 feet further away from the power service is the end tap point. At the end tap point the measured power loss was 18.67 dB without concrete present (in air); however, with concrete presents the measured power loss was 60.33 dB.

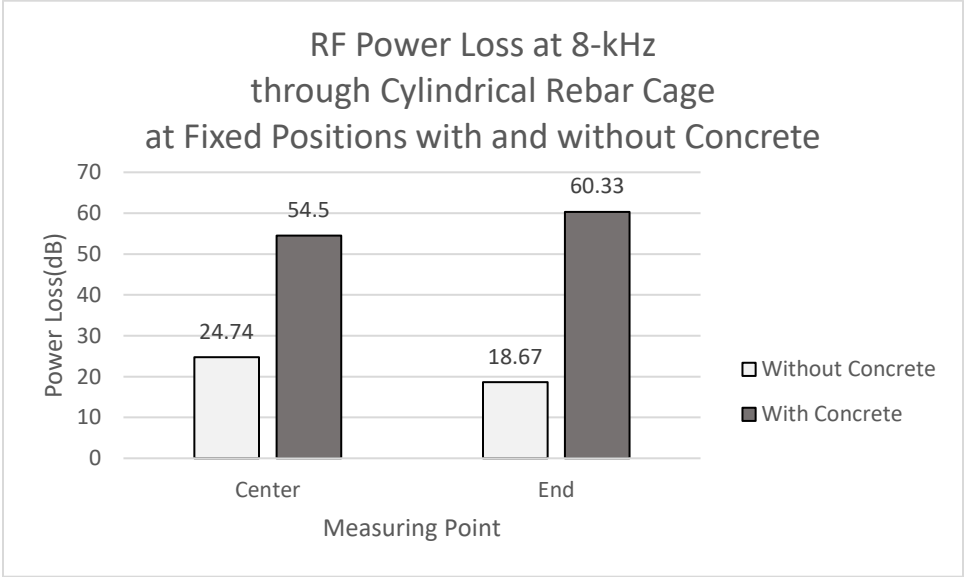

Figure 148. Results of the Rebar Cage 8 kHz test both in and out of concrete.

5.2.1.5.3 Discussion

Note that in air, the power loss for the tap point at the end was less than the power loss for the tap point in the center. This is believed to be a result of the rebar cage being manipulated by hand. As the test lead clips for the spectrum analyzer measurement were detached and reattached from the grounding clamps at the center and the grounding clamps at the end of the rebar cage, the cage was moved causing the rungs and the legs to make either stronger or weaker connections. Note that the structure was expected to have greater power loss at the end rather than at the center due to the longer resistance path. However, this is not what was observed for the part of the experiment that was conducted in air.

5.2.2 Rectifier and Booster Experimentation at 8 kHz

Recall that for the rectifier circuit, the 8.2pF capacitors were changed to 2.2uF capacitors so that the reactance of approximately 8 Ω was preserved going from 2.4 GHz to 8kHz. Additionally, because the frequency was so low for the second design attempt in comparison to the first design attempt, the impedance matching wasn't as crucial. The wavelength of an 8 kHz signal is 300,000 times longer than that of a 2.4 GHz signal and also much longer than the length of a rebar cage. As a result any reflections due to mismatched impedances were not a concern. Nevertheless, functionality of the new circuit needed to be established, so series of tests were performed for Experiment 22.

All tests for the rectifier and booster experimentation for the second design attempt utilized (a) a modified the rectifier circuit and (b) the BQ25504 evaluation board. The following materials were used:

- Tektronix TDS-224 Four Channel Oscilloscope,
- Rigol DM3068 Digital Multimeter,
- Xantrex Duel HPD 60-5 DC Power Supply,
- Communication Technologies Inc. 2.4 GHz OCXO, and
- BQ25504 Evaluation Board
  Rectifier Circuitry

5.2.2.1 Experiment 22: Evaluating the Performance of the Modified Rectifier and Booster

The aim of Experiment 22 was to evaluate the performance of the new rectifier circuit in conjunction with the BQ25504. The new rectifier circuit utilized 2.2 µF charging capacitors for the Two Stage Dickson Multiplier. The BQ25504 evaluation board has a 4.7 µF filtering capacitor at the input of the circuit. The significance of this is that the impedance of the filtering capacitor at 8 kHz might be better suited than at the 2.4 GHz applied in Experiment 16.

5.2.2.1.1 Set-Up

A function generator was connected to the input of an adjustable attenuator. The output of the adjustable attenuator was connected to the input of the modified Two-Stage Dickson Multiplier. The output of the modified Two-Stage Dickson Multiplier was connected to the input of the BQ25504 Evaluation Board. Figure 149 shows a block diagram for the set up for Experiment 22. Shown in this diagram are the measurement points; a V indicates a voltage measurement, while an I indicates a current measurement. The function generator was set to a 19.83 dBm output.

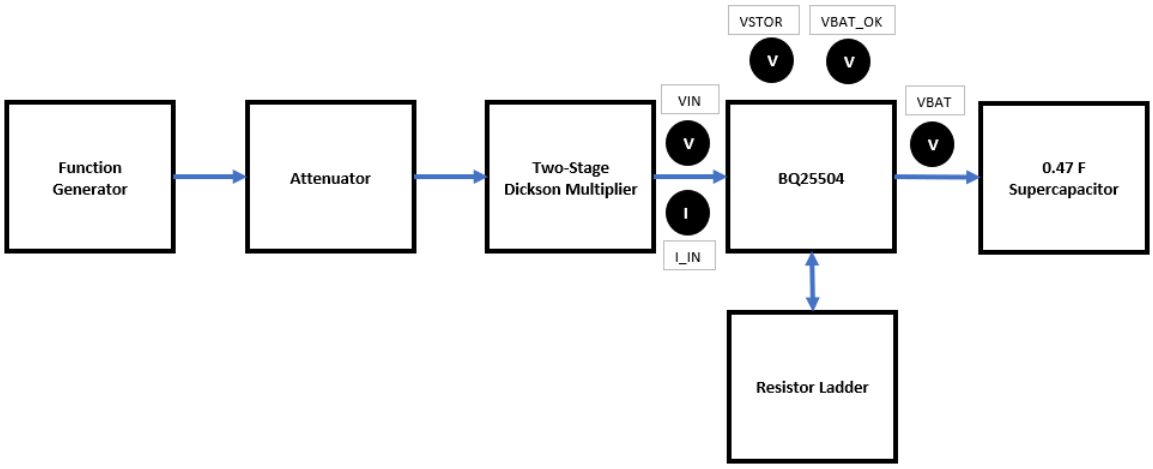

Figure 149. Block Diagram of Test Set-Up for Experiment 22

Sitting next to the BQ25504 was a breadboard with twenty (20) 1 MΩ resistors serially connected to create a 20MΩ resistor ladder. The resistor ladder was used to set the $\%V_{OC}$ value for the MPPT circuity in the BQ25504 IC. To set this value, V_{IN} and GND from the BQ25504 were jumpered over to the breadboard, and then the Open Circuit Sample (OCS) pin from the

J1 header on the BQ25504 Evaluation Board was jumpered over to the resistor ladder to set the $\%V_{OC}$.

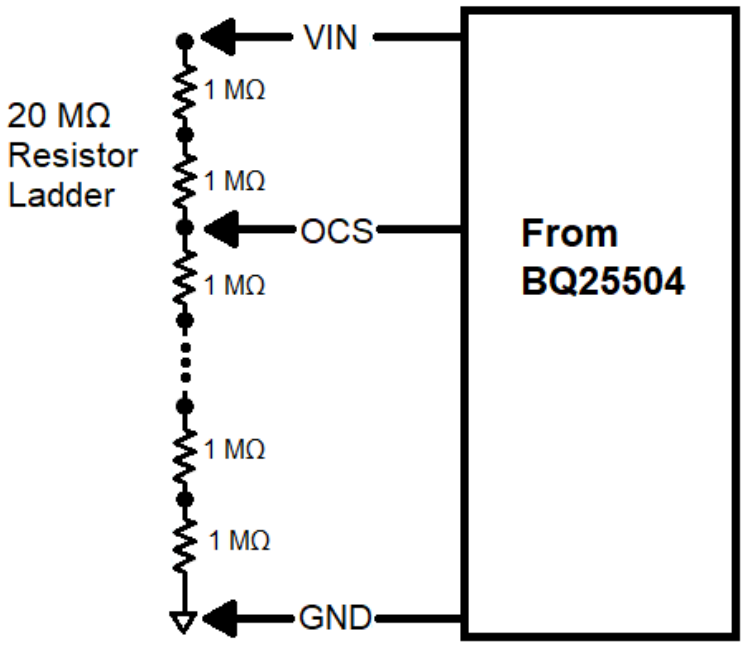

Figure 150. Diagram of the Resistor Ladder

In total, 9 tests were performed. Tests 1 through Test 6 utilized 0 dB attenuation, with the main focus on varying the $\%V_{OC}$ parameter to find the optimal $\%V_{OC}$ setting. After selecting a perceived optimal $\%V_{OC}$ setting of 85%, Test 7 utilized an 8 dB attenuation. Using the same $\%V_{OC}$ setting, Test 8 utilized a 12 dB attenuation. However, after an undesirable amount of charge time was observed, in Test 9, the 12 dB attenuation was used again, but the $\%V_{OC}$ was changed to 45%.

5.2.2.1.2 Results

The results section is sub-sectioned into the nine (9) tests that were performed. The main parameter of interest is the amount of time it would take to charge the supercapacitor to 4.83 V, which is the voltage of the supercapacitor that the BQ25504 has been modified to signal that the supercapacitor is sufficiently charged for operations. When the supercapacitor is sufficiently charged, the V_{BAT_OK} signal goes to a logic high.

5.2.2.1.2.1 Test 1 Results

For this test, the OCS pin was connected to the 20 MΩ resistor ladder so that a $\%V_{OC}$ of 45% was being sensed (R_{OC1} = 9MΩ, R_{OC2} = 11MΩ). The input voltage (V_{IN}) to the BQ25504 would repeatedly excite and then exponentially decay, taking approximately 15 to 20 seconds for re-excitation, as shown in Figure 151. The current, however, stayed relatively constant, consistently exceeding 6 mA, even when the input voltage had fully decayed. This all indicated that no charging occurred.

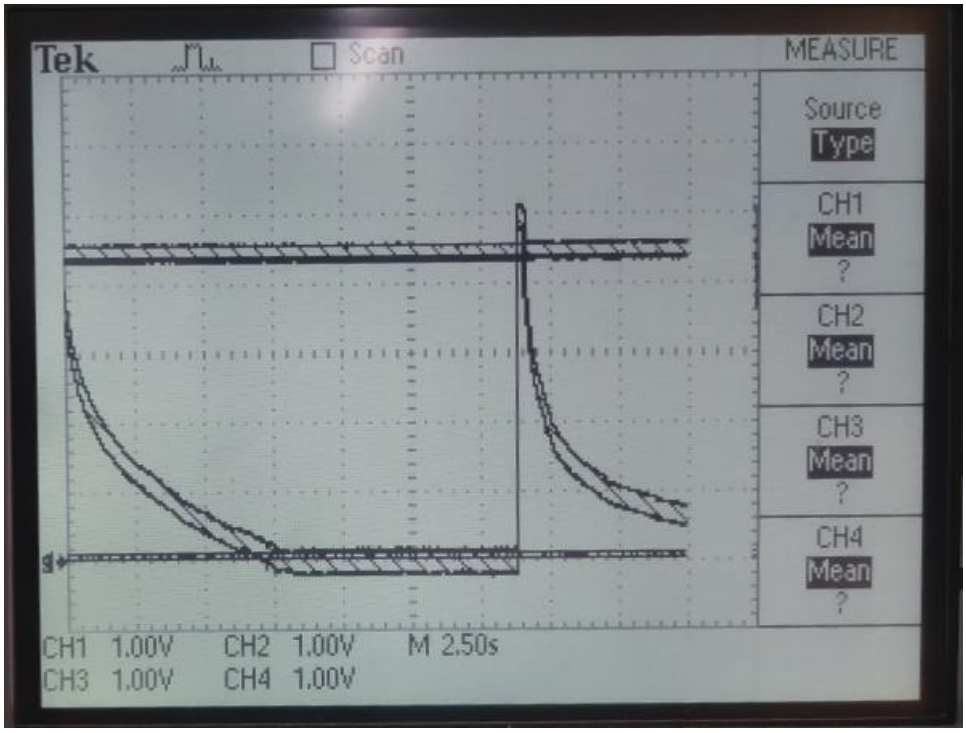

Figure 151. Example of V_{IN} repeatedly exciting and then exponentially decaying

In total, it took 29 minutes, 29 seconds for the BQ25504 to charge a 0.47F capacitor above 4.83 V, which is the voltage that the battery is deemed okay for operations. Figure 152 shows a graph of the recorded results.

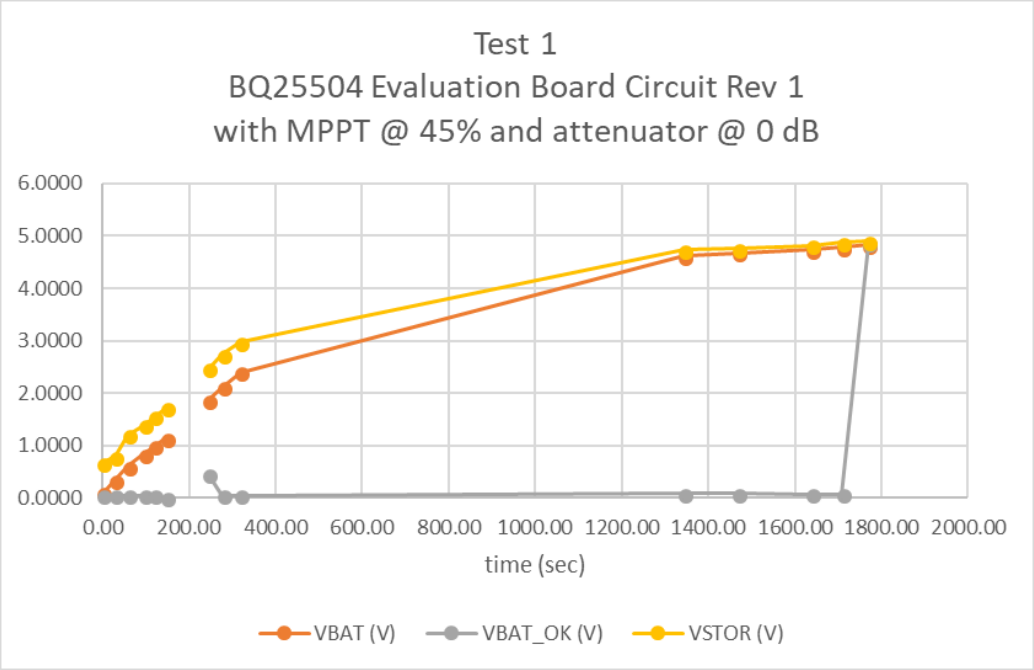

Figure 152. Test 1 of Experiment 22 results

5.2.2.1.2.2 Test 2 Results

For this test, the OCS pin was connected to the 20 MΩ resistor ladder so that a $\%V_{OC}$ of 45% was being sensed (R_{OC1} = 9MΩ, R_{OC2} = 11MΩ). Unlike in Test 1, the input voltage (V_{IN}) did not experience repetitive excitation followed by exponential decay. Instead, the circuit behaved as expected. Eventually, the anticipated square wave was observed for the V_{STOR} waveform oscilloscope trace. In total, it took 10 minutes and 55 seconds for the BQ25504 to charge a 0.47 F capacitor above 4.83 V, which is the voltage that the supercapacitor is deemed okay for operations. Figure 153 shows a graph of the recorded data for Test 2.

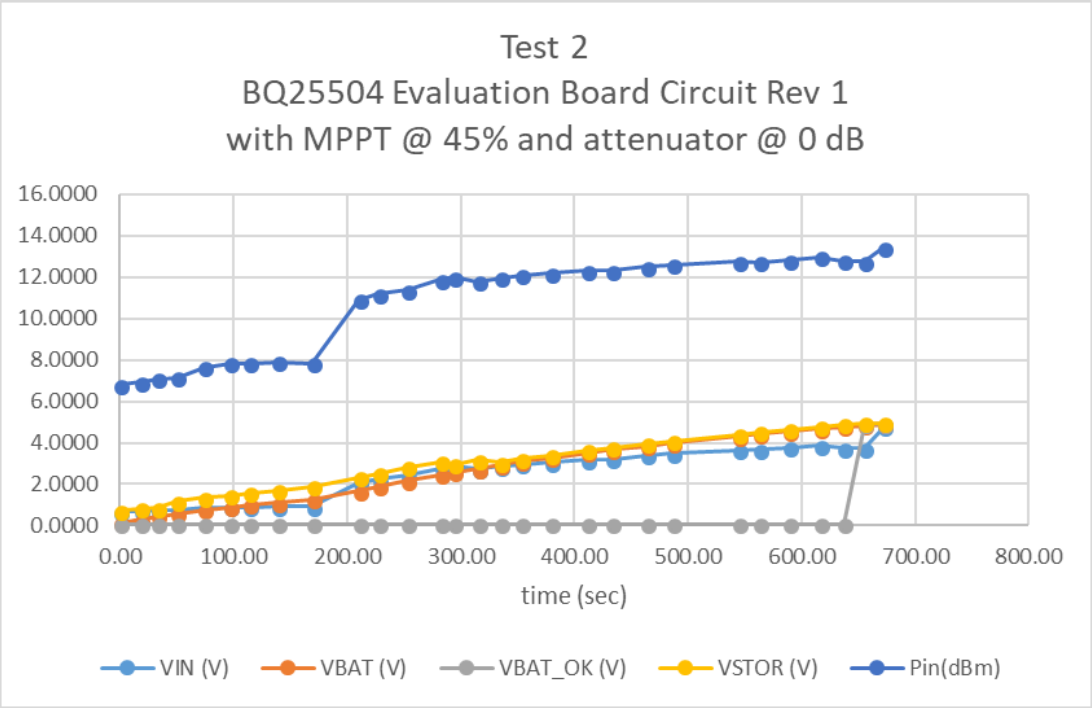

Figure 153. Test 2 of Experiment 22 results

5.2.2.1.2.3 Test 3 Results

For this test, the OCS pin was connected to the 20 MΩ resistor ladder so that a $\%V_{OC}$ of 55% was being sensed (R_{OC1} = 11MΩ, R_{OC2} = 9MΩ). In total, it took 9 minutes and 43 seconds for the BQ25504 to charge a 0.47 F supercapacitor above 4.83 V, which is the voltage that the battery is deemed okay for operations. Figure 154 shows a graph of the recorded data for Test 3.

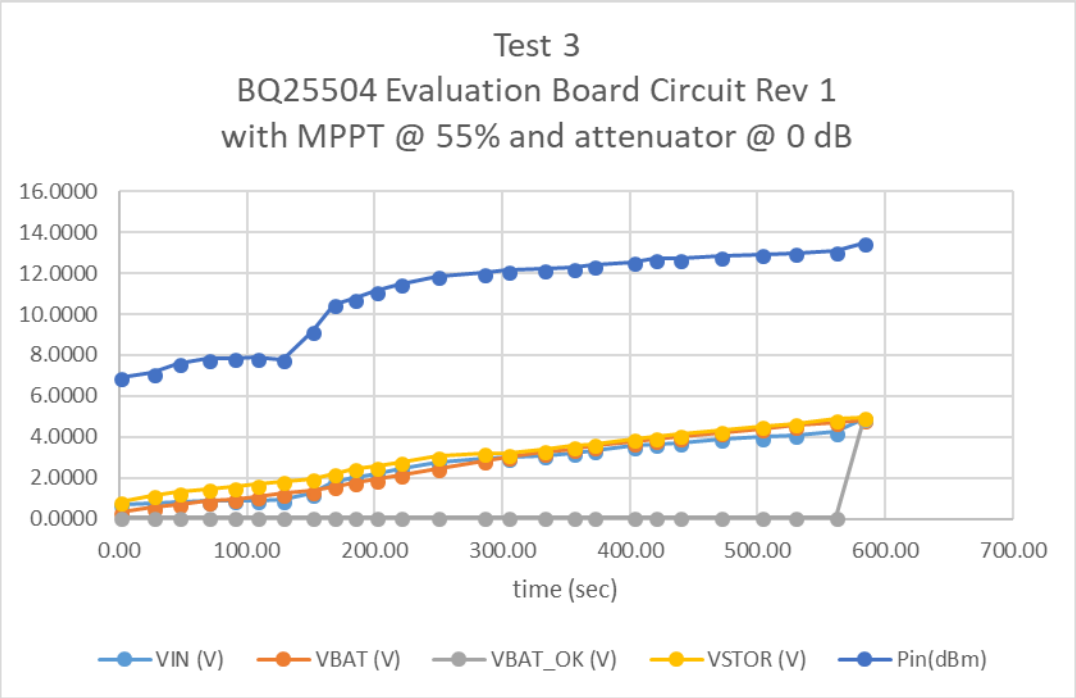

Figure 154. Test 3 of Experiment 22 results

5.2.2.1.2.4 Test 4 Results

For this test, the OCS pin was connected to the 20 MΩ resistor ladder so that a $\%V_{OC}$ of 65% of the V_{IN} voltage was being sensed (R_{OC1} = 13MΩ, R_{OC2} = 7MΩ). In total, it took 10 minutes, 0 seconds for the BQ25504 to charge a 0.47F capacitor above 4.83 V, which is the voltage that the battery is deemed okay for operations. Figure 155 shows a graph of the recorded data for Test 4.

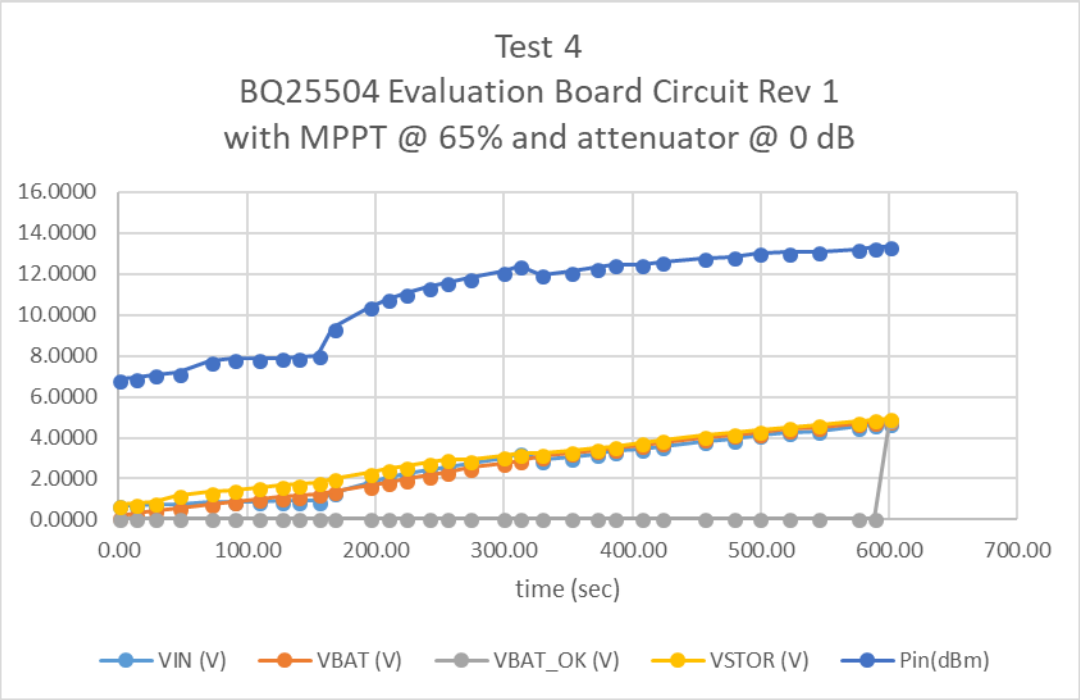

Figure 155. Test 4 of Experiment 22 results

5.2.2.1.2.5 Test 5 Results

For this test, the OCS pin was connected to the 20 MΩ resistor ladder so that a $\%V_{OC}$ of 75% was implemented. In total, it took 9 minutes, 29 seconds for the BQ25504 to charge a 0.47F capacitor above 4.83 V, which is the voltage that the battery is deemed okay for operations. Figure 156 shows a graph of the recorded data for Test 5.

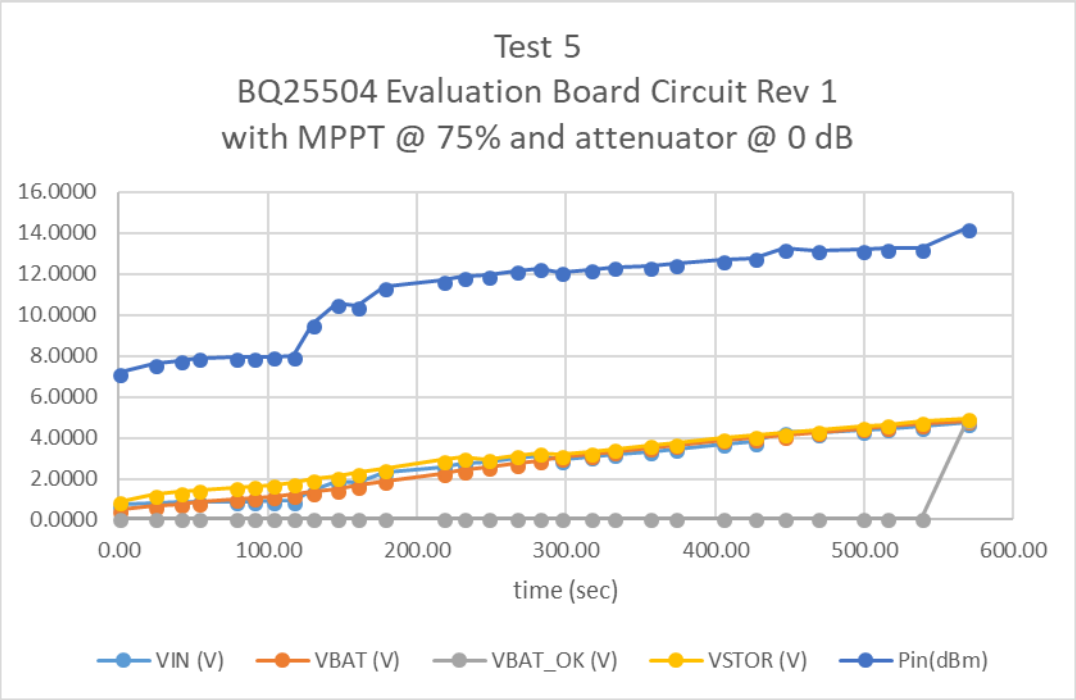

Figure 156. Test 5 of Experiment 22 results

5.2.2.1.2.6 Test 6 Results

For this test, the OCS pin was connected to the 20 MΩ resistor ladder so that a $\%V_{OC}$ of 85% was being sensed (R_{OC1} = 17MΩ, R_{OC2} = 3MΩ). In total, it took 9 minutes, 23 seconds for the BQ25504 to charge a 0.47F capacitor above 4.83 V, which is the voltage that the battery is deemed okay for operations. Figure 157 shows a graph of the recorded data for Test 6.

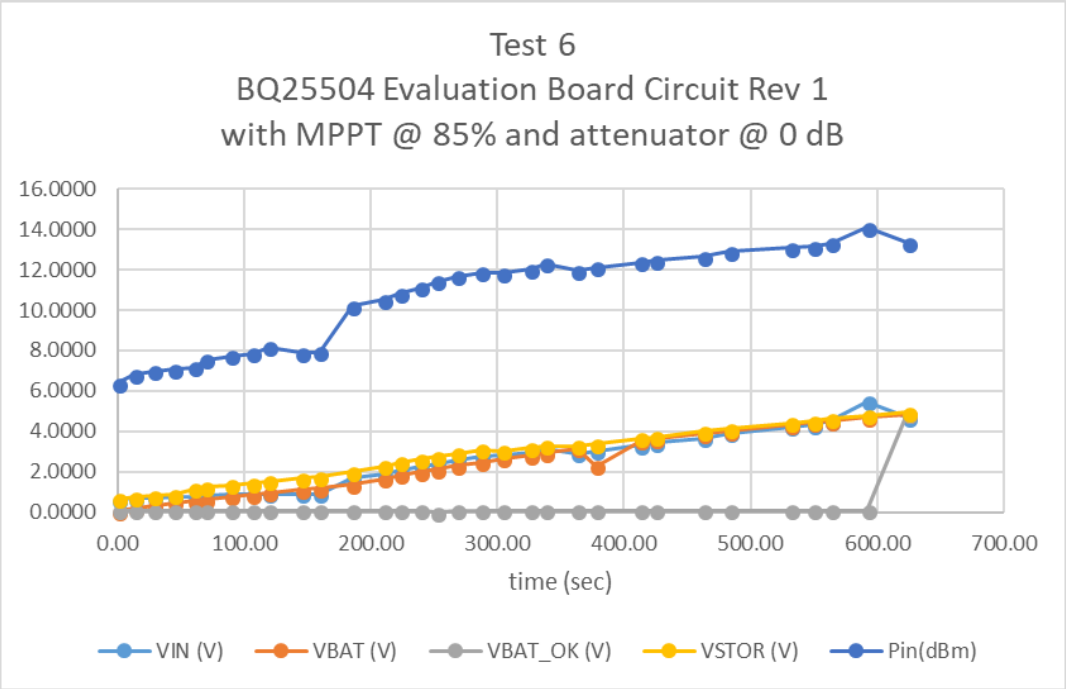

Figure 157. Test 6 of Experiment 22 results

5.2.2.1.2.7 Test 7 Results

The aim of this test was to see if the circuit would perform better with a lower input power (11.83 dBm), but with the MPPT circuit still set to 85%. For this test, the OCS pin was connected to the 20 MΩ resistor ladder so that a $\%V_{OC}$ of 85% was being sensed (R_{OC1} = 17MΩ, R_{OC2} = 3MΩ). The attenuator was set to 8 dB. In total, it took 1 hour, 48 minutes, and 28 seconds for the BQ25504 to charge a 0.47F capacitor above 4.83 V, which is the voltage that the battery is deemed okay for operations. Figure 158 shows a graph of the recorded data for Test 7.

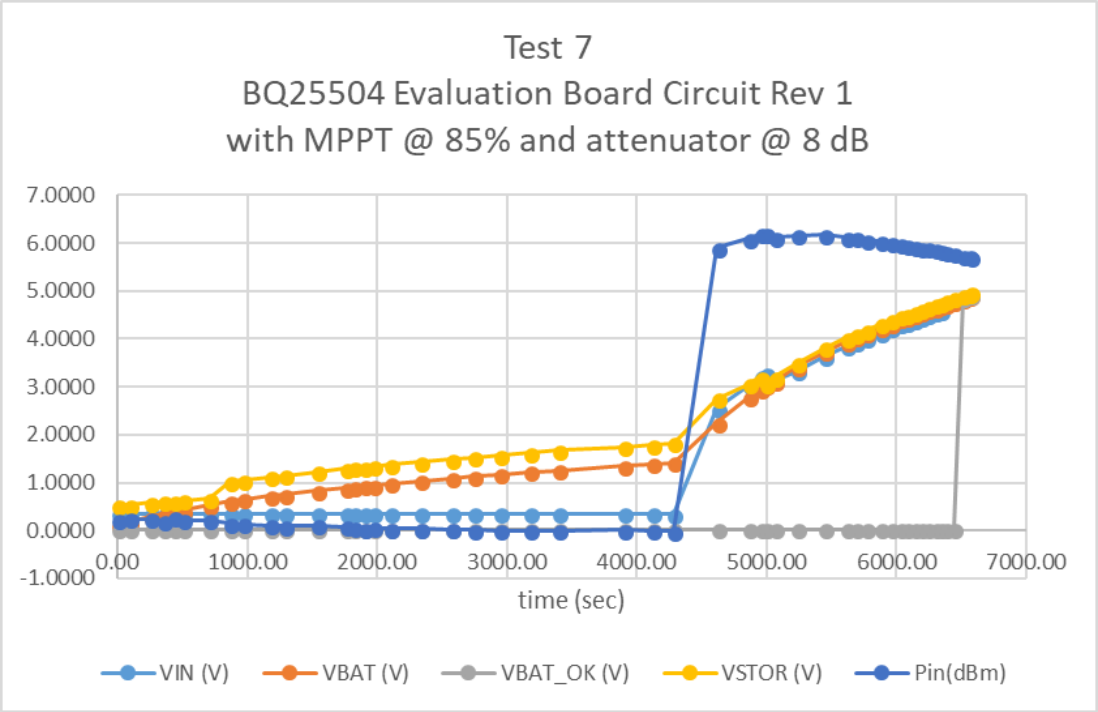

Figure 158. Test 7 of Experiment 22 results

5.2.2.1.2.8 Test 8 Results

The aim of this test was to see if the circuit would perform better with an even lower input power (7.83 dBm), but with the MPPT circuit still set to 85%. For this test, the OCS pin was connected to the 20 MΩ resistor ladder so that a $\%V_{OC}$ of 85% was being sensed (R_{OC1} = 17MΩ, R_{OC2} = 3MΩ). The attenuator was set to 12 dB. In total, it took 1 hour, 57 minutes, and 36 seconds for the BQ25504 to charge a 0.47 F capacitor above 4.83 V, which is the voltage that the battery is deemed okay for operations. Figure 159 shows a graph of the recorded data for Test 8. With the open circuit voltage percentage for the MPPT circuit set to 85%, the input impedance was driven higher as the super capacitor became more charged.

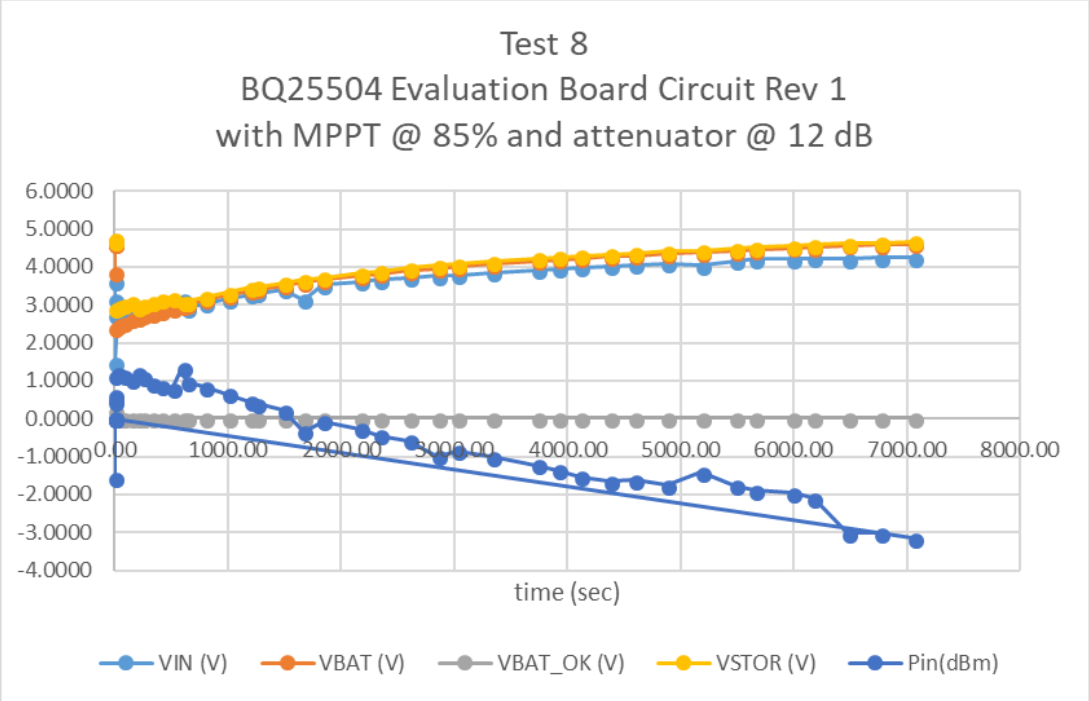

Figure 159. Test 8 of Experiment 22 results

5.2.2.1.2.9 Test 9 Results

The aim of this test was to see if the circuit would perform better with the same input power as Test 8 (7.83 dBm), but with the $\%V_{OC}$ of the MPPT circuit set to 45%. The reason the $\%V_{OC}$ was lowered to 45% was to see if the input impedance could be lowered to prevent the input power from being driven so low as in Test 8. For this test, the OCS pin was connected to the 20 MΩ resistor ladder so that a $\%V_{OC}$ of 45% was being sensed (R_{OC1} = 9MΩ, R_{OC2} = 11MΩ). The attenuator was set to 12 dB. In total, it took 35 minutes, and 6 seconds for the BQ25504 to charge a 0.47 F capacitor to approximately 3.25 V; the cap was not charged to 4.83 V in this test. Moreover, the overall power input was approximately the same; this is in contrast to Test 7 where the power input dropped across time. Figure 160 shows a graph of the recorded data for Test 9.

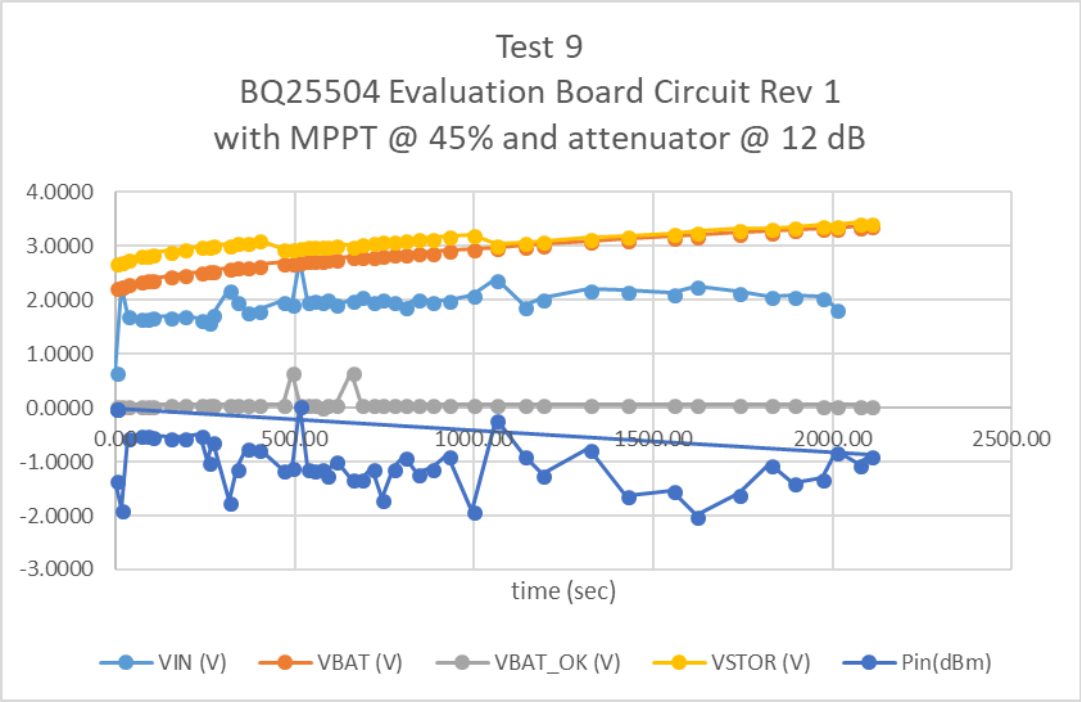

Figure 160. Test 9 of Experiment 22 results

5.2.2.1.3 Discussion

At first, based on the results of Tests 1 through 6, it appeared that the $\%V_{OC}$ for the quickest charge time was 85%. This was simply based on what $\%V_{OC}$ setting resulted in the quickest charge time. Since the charge times were very close for Tests 1 – 6, it was difficult to determine if 85% $\%V_{OC}$ did in fact produce the quickest charge time.

Tests 7 and 8 utilized an 85% $\%V_{OC}$; these tests showed that when the input power was lowered, the amount of time for charging was significantly increased.

Test 9 showed that when a $\%V_{OC}$ was set to 45% and the input power was kept at the same value as in Test 8, the BQ25504 input voltage does not need to increase to maintain charging the supercapacitor. What's more is that for Test 9, it appears that the Two-Stage Dickson Multiplier and the BQ25504 has never functioned better. For Test 9, this is the lowest input power that the rectifier and BQ25504 have ever been successfully subjected to. In part, it is believed that the reason for this is the $\%V_{OC}$ that the BQ25504 was set to the proper setting for the rectifier output. However, it is also believed that at 8.0 kHz, the higher valued charging capacitors in the Two-Stage Dickson Multiplier happened to be closer to the value of the filtering capacitor used in the BQ25504 Evaluation Board — this is believed to have greatly contributed to the success of the circuit in Test 9 of Experiment 22. On the other hand, in Experiment 16, the same filtering capacitor in the BQ25504 Evaluation Board is now believed to have compromised the Two-Stage Dickson Multiplier circuity at 2.4 GHz by causing such a low impedance (effectively creating a short at the output of the rectifier).

6 Conclusion

In the end, the concrete medium proved to be too lossy for either the first design attempt (single line conduction at 2.4 GHz via a rebar cage) or the second design attempt (using two legs of the rebar cage for conventional two-line conduction at 8.0 kHz). The overall problem posed this study was to charge remotely embedded devices using some form of RF energy harvesting so that these embedded devices could make a measurement of the degradation of concrete — and then communicate the results. Unfortunately, restrictions conferred by the material properties of concrete prevent the two design attempts in this report from being successful. Simply put, the concrete medium attenuates RF power too much.

Hypothetically, if design improvements can be made to the power transfer methods used in this report, then the next challenge would be to ensure that the energy harvesting circuitry can adequately harvest the input power at a low enough power. A design improvement is posited in the Future Work subsection below.

6.1 Achievements

Even though the design approaches presented in this this research did not work, there were accomplishments made in the investigation of the functionality. Firstly, the development of the TM Coupler (2.4 GHz launcher) was successfully achieved and showed to be functional when embedded in air. On the road to this achievement was a necessary lesson in the importance of impedance matching, which itself was a time-consuming and iterative process. Moreover, the benefits of single line conduction were able to be seen with the observation that the power loss of the TM Coupler system was significantly less (~25 dB less) than the free space path loss of an identically spaced system with isotropic antennas. Another achievement is the recognition that a single line conduction system embedded in concrete is, for energy harvesting purposes, highly improbable due to the losses that are incurred by the concrete medium.

Another achievement is the recognition that at lower frequencies (below 1.5 GHz), power transmission is more viable for a single line conduction system. This led to the development of the second design approach, which showed that when only the rebar cage is used to propagate RF power at very low frequencies, that power transfer and energy harvesting may be viable.

On the Energy Harvesting end of things, it was demonstrated in Experiment 16 and Experiment 22 that in order for the Two Stage-Dickson Multiplier and the BQ25504 Energy Harvesting Circuit to function optimally together, the input filtering capacitor of the BQ25504 needed to be on the same order of magnitude as the charging capacitors of the Two-Stage Dickson Multiplier. Moreover, when operating at 2.4 GHz, it was shown that the best way to match the input impedance of the Two-Stage Dickson Multiplier to 50 Ω was to utilize a shunt and series capacitor.

6.2 Future Work

Another design approach is inspired by the ubiquitous coaxial cable. By analogizing the rebar cage to the outer conductor of a coaxial cable and the concrete medium as the dielectric of a coaxial cable, it may be easily conceivable that if a center conductor was applied to this configuration, then one could essentially have a scaled-up version of a coaxial cable. An illustration of this concept is shown in Figure 161, Figure 162, and Figure 163.

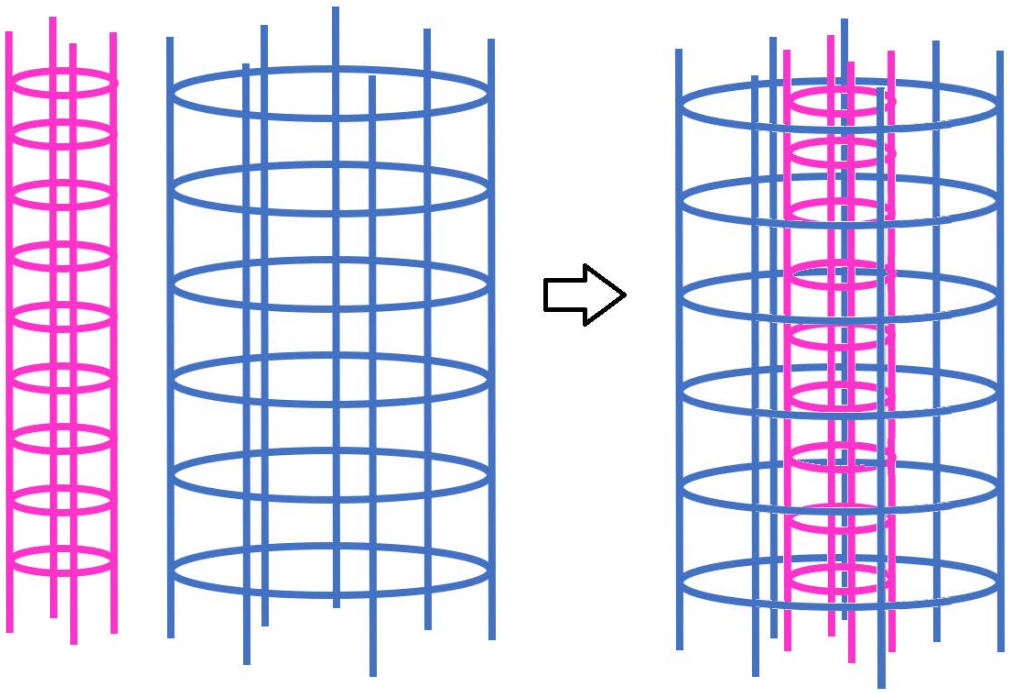

Figure 161. Illustration of the inner and outer rebar cages both separated (left) and combined (right)

As seen in Figure 161, an inner conductor can be supplied in the form of a cage; however, a cage need not be the form that the inner conductor takes. Another possibility for an inner conductor could simple be a length of rebar or some other conductor. The advantage of a cage would be the potential to set the characteristic impedance of the medium by setting the diameter of the inner conductor. That is, since the dielectric medium is concrete is known to a range, and since the diameter of the outer conductor will likely be set, the diameter of the inner conductor can be fabricated as needed to achieve a 50 Ω characteristic impedance. Having the characteristic impedance of the waveguide set will allow for the input impedances of sources and loads be able to be set so that maximum power transfer can be achieved.

Figure 162 shows a possible configuration of such a system; note that though this figure does not show the presence of a concrete medium, the concrete medium would be of crucial importance for setting the characteristic impedance. In such a system, the Charger/Interrogator (C/I) would input power with the application of a sinusoidal waveform at a sufficiently low frequency. On the other hand, several embedded Remote Sensors (RSs) would receive the power and store it as energy. After a sufficient amount of time, the C/I would interrogate the RSs with a status query, one RS at a time. Once interrogated, the RS would (a) make a measurement, and then (b) communicate that measurement back to the C/I.

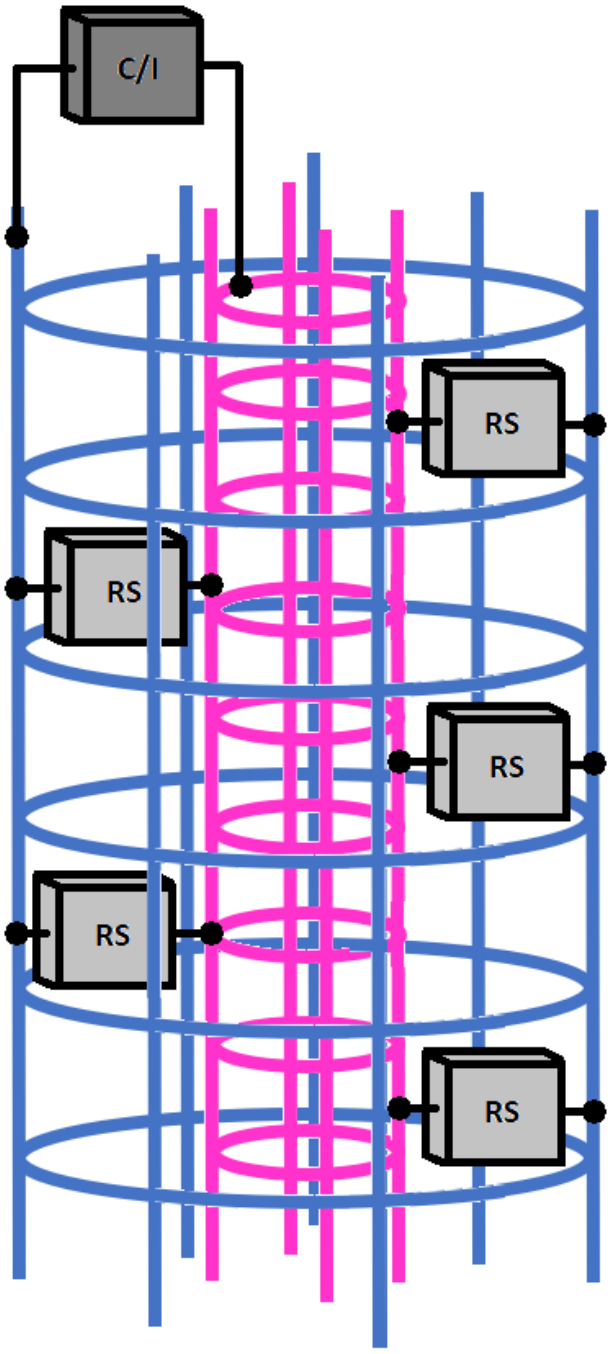

Figure 162. Illustration of the Remote Sensors (RS) and Charger/Interrogator (C/I) affixed to the inner and outer rebar cages.

Figure 163 shows a bird's eye view of the third approach with the presence of a concrete medium but without the presence of the C/I or RSs. It may be clearer from this illustration that by setting the diameter of the inner cage, the characteristic impedance of the waveguide can be

set. From Equation 4 [28], it can be seen that the characteristic impedance, Z_0, of a coaxial transmission line can be when the following parameters are known: the outer diameter, D; the inner diameter, d; and the relative permittivity of concrete, $\epsilon_{r,concrete}$.

$$Z_0 = \frac{138\ \Omega}{\sqrt{\epsilon_r}} \log_{10}\left(\frac{D}{d}\right) \tag{4}$$

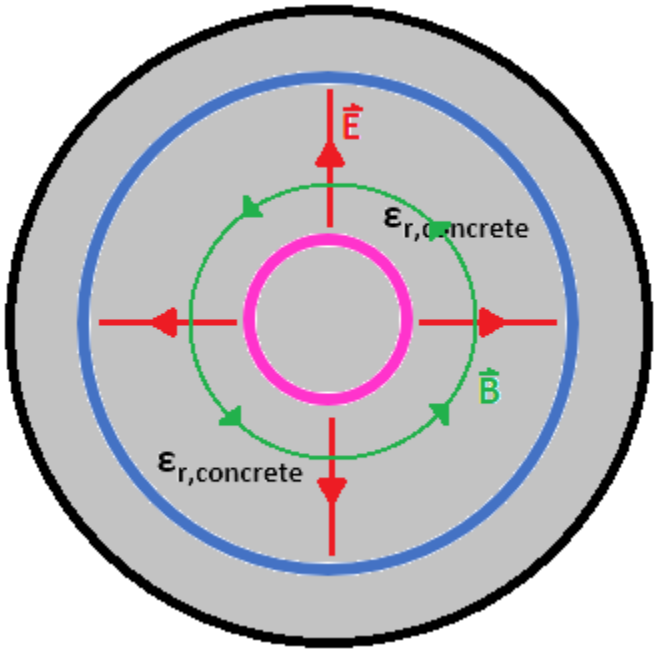

Figure 163. Illustration of the outer conductor (blue) and inner conductor (pink) embedded in a concrete medium; also shown is the electric and magnetic fields.

7 Work Cited

Below is the list of sources used for this research.

[1] N. J. Carino and J. R. Clifton, "Prediction of Cracking in Reinforced Concrete Structures," *NISTIR 5634,* 1995.

[2] American Society of Civil Engineers, "2013 Report Card for America's Infrastructure," American Society of Civil Engineers, 2013.

[3] S. Jiang, . S. V. Georgakopoulos and H. Jin, "Effects of Periodic Reinforced-Concrete Structures on Power Transmission," *IEEE,* 2012.

[4] G. J. Goubau, "Single-Conductor Surace-Wave Transmission Lines," *NDT&E International 44,* 1951.

[5] G. J. Goubau, "Surface Wave Transmission Line". United States of America Patent 2,685,068, 27 July 1954.

[6] G. J. Goubau, "Surface Waves and Their Application to Transmission Lines," *Journal of Applied Physics ,* vol. 21, 1950.

[7] Texas A&M, "Reinforced Concrete Design," [Online]. Available: http://faculty.arch.tamu.edu/media/cms_page_media/4198/NS22-1cncrtdesign_3.pdf. [Accessed 28 March 2017].

[8] M. C. Jack, B. H. Russell and , in *Design of Reinforced Concrete*, USA, Wiley, 2014, pp. 1-35.

[9] H. Bohni, "Corrosion in Reinforces Concrete Structures," *CRC Press | Woodhouse Publishing Limited,* 2005.

[10] E. Possan, W. Thomaz, G. Aleandri, E. Felix and A. Dos Santos, "CO2 Uptake Potential Due To Concrete Carbonation: A Case Study," *Case Studies in Construction Materials,* vol. 6, pp. 147 - 161, 2017.

[11] R. L. Pickholtz, D. L. Shilling and L. B. Milstein, "Measured Complex Permittivity of Walls with Different Hydration Levels and the Effect on Power Estimation of TWRI Target Returns," *Progress In Electromagnetics Research,* vol. 30, no. 5, 1982.

[12] G. Elmore, "Introduction to the Propagating Wave on a Single Conductor," Corridor Systems Inc., 2009.

[13] S. Chalasani and J. M. Conrad, "A Survey of Energy Harvesting Sources for Embedded Systems," *IEEE.*

[14] T. Soyata, L. Copeland and W. Heinzelman, "RF Energy Harvesting for Embedded Systems: A Survey of Tradeoffs and Methodology," *A IEEE Circuits and Systems Magazine,* vol. 1, 2016.

[15] C. R. Valenta and G. D. Durgin, "Harvesting Wireless Power," *IEEE Microwave Magazine,* vol. June, p. 108, 2014.

[16] K. Gudan, S. Chemishkian, J. J. Hull, S. J. Thomas, J. Ensworth and M. S. Reynolds, "A 2.4GHz Ambient RF Energy Harvesting System with -20dBm Minimum Input Power and NiMH Battery Storage," in *IEEE RFID Technology and Applications Conference*, 2014.

[17] K. Gudan, S. Shao, J. J. Hull, J. Ensworth and M. S. Reynolds, "Ultra-low Power of 2.4 GHz RF Energy Harvesting and Storage System with -25 dBm Sensitivity," in *IEEE International conference on RFID*, 2015.

[18] D. V. Ragone, "Review of Battery Systems for Electrically Powered Vehicles," in *Mid-Year Meeting of the Society of Automotive Engineers*, Detroit, MI, 1968.

[19] R. V. Prasad, S. Devasenapathy, V. S. Rao and J. Vazifehdan, "Reincarnation in the Ambiance: Devices and Networks with Energy Harvesting," *IEEE Communications Surveys & Tutorials,* vol. 16, no. 1, 2014.

[20] R. L. Pickholtz, D. L. Schilling and L. B. Milstein, "Theory of Spread-Spectrum Communications-A Tutorial," *IEEE TRANSACTIONS ON COMMUNICATIONS,* vol. 30, no. 5, pp. 855-884, May 1982.

[21] R. E. Ziemer, Fundamentals of Spread Spectrum Modulation, Synthesis Lectures on Communications.

[22] ARC Electronics, "Bell Modem Standards: Bell 103, 202T, 202S, 201B, 201C, 208 A, 208 B," [Online]. Available: https://arcelect.com/bell.htm. [Accessed 13 May 2018].

[23] K. Kurokawa, "Power Waves and the Scattering Matrix," *IEEE Trans. Micr. Theory & Tech,* pp. 194-202, 1965.

[24] J. Wetherell, "Impedance Matching Network Designer," University of San Diego, 30 Oct. 1997. [Online]. Available: https://home.sandiego.edu/~ekim/e194rfs01/jwmatcher/matcher2.html. [Accessed 15 Nov. 2017].

[25] Texas Instruments, "bq25504 Ultra Low-Power Boost Converter With Battery Management for Energy Harvester Applications," June 2015. [Online]. Available: http://www.ti.com/lit/ds/symlink/bq25504.pdf. [Accessed 5 May 2017].

[26] University of Victoria, "Derivation the dB version of the Path Loss Equation for Free Space," 19 September 2000. [Online]. Available: http://www.ece.uvic.ca/~peterd/35001/ass1a/node1.html. [Accessed 12 08 2018].

[27] Federal Communications Commission, "FCC ONLINE TABLE OF FREQUENCY ALLOCATIONS," 12 June 2018. [Online]. Available: https://transition.fcc.gov/oet/spectrum/table/fcctable.pdf. [Accessed 8 August 2018].

[28] W. C. Elmore, M. A. Heald and , Physics of Waves, 1969.

[29] S. Jiang and S. V. Georgakopoulos , "Optimum Wireless Powering of Sensors Embedded in Concrete," *IEEE TRANSACTIONS ON ANTENNAS AND PROPAGATION,* vol. 60, no. 2 , 2012 .

[30] A. Ogunsola, U. Reggiani and L. Sandrolini, "Modelling Shielding Properties of Concrete," in *17th International Zurich Symposium on Electromagnetic Compatibility*, 2006.

[31] J. F. Shackelford, W. Alexander and , CRC Materials Science and Engineering Handbook, Third Edition, Boca Raton: CRC Press, 2001.

8 Appendix A – Refining the λ/4 Stub Distance and Determining the Permittivity of PVC at 2.4 GHz

Two TM Couplers separated by a distance of 110.5 cm were implemented as shown in Figure 52. As can be seen from Figure 52, anechoic chamber padding was placed on the surface to ensure that no reflections were caused by the table. (It was later determined that most of there was no detectable reflection induced by the table when the same results were observed without the anechoic chamber padding present.)

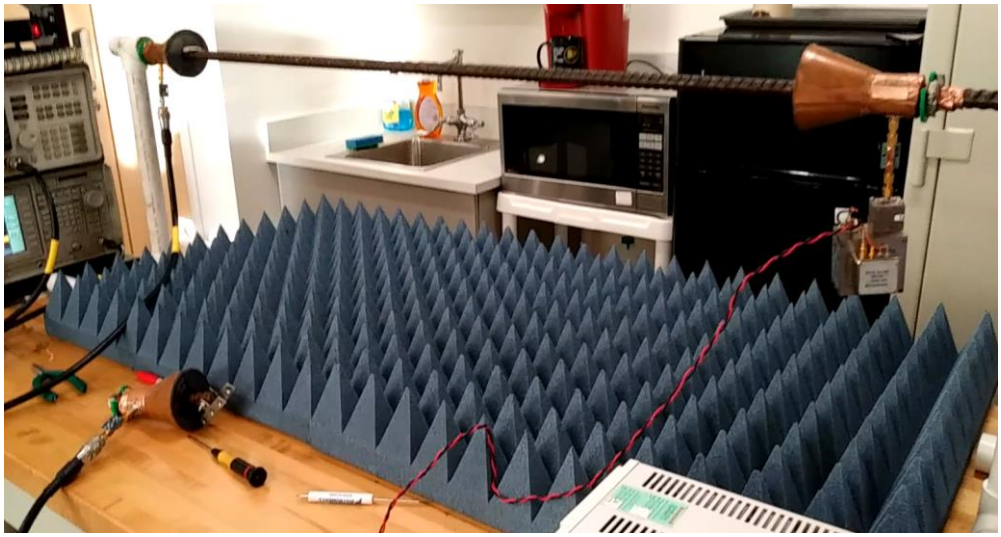

Figure 164. Two TM Coupler system in Experiment 1

The S12 and S21 traces show that the performance of system is optimal at 1.2 GHz, which is half the frequency that the TM Couplers were designed for. The traces also show that the system is performing undesirable at 2.4 GHz, with the peak forward gain (S12, S21) in that local region happening at 2.35 GHz. Also note that at approximately 600 kHz, the S21 parameter of the system is at a local maximum. Figure 165 and Figure 166 show yes parameter results from the VNA before any modifications were made.

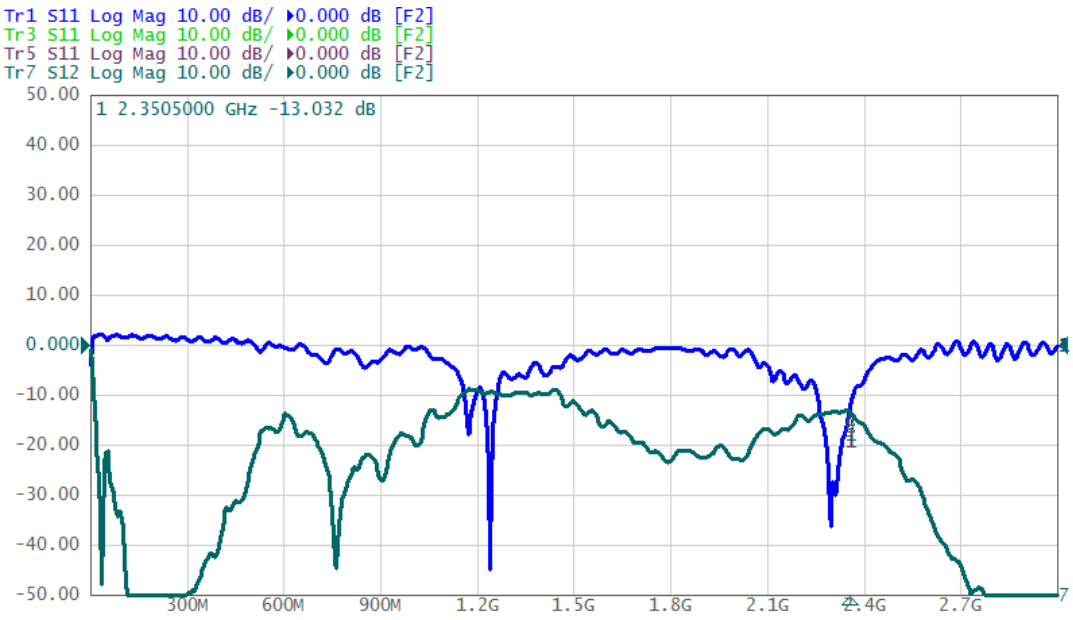

Figure 165. The S11 and S12 parameters before the modifications

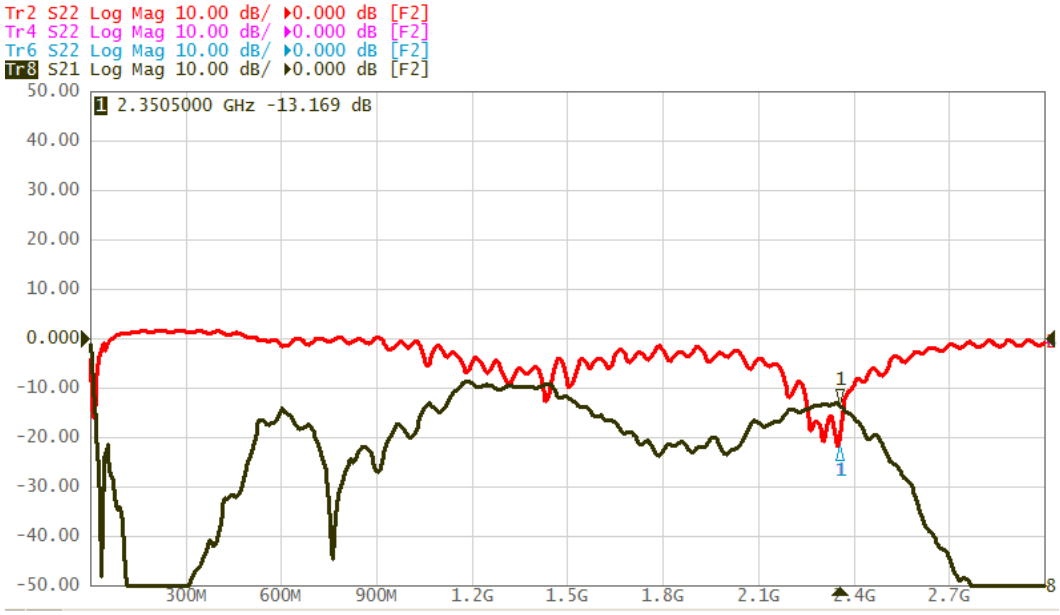

Figure 166. The S22 and S21 parameters before the modifications

A hypothesis has been generated to explain these results. A critical guideline for the design of this device, given by Goubau, is to implement a quarter wavelength trap at the rear of the TM Coupler. The quarter wavelength trap is meant to reflect input RF power so that the reflected RF power is constructively interfering with the non-reflected RF power. This feature ensures

that the device is transmitting unidirectionally. At 1.2 GHz, the device is functioning at half the frequency it was designed for, which results in a wavelength that is twice the length that the device was designed for. Likewise, for 600 kHz the device is functioning at a quarter of the frequency was designed for, which results in a wavelength that is four times as long as the device was designed for. Somehow, with these wavelengths there must be enough constructive interference so that the TM Coupler is able to transmit at these frequencies.

8.1 First Modification to the Stub Distance

A supposed solution to this problem is to put a small section of the backplane off so that the distance between the tap point and the backplane is reduced by a fraction of an inch. This should effectively translate the S12 and S21 traces shown above in the rightward direction on the frequency domain. The amount that should be cut off should be determined by the relative permittivity of the PVC material. Figure 167 and Figure 168 show the S-parameters results from the VNA after the first modification.

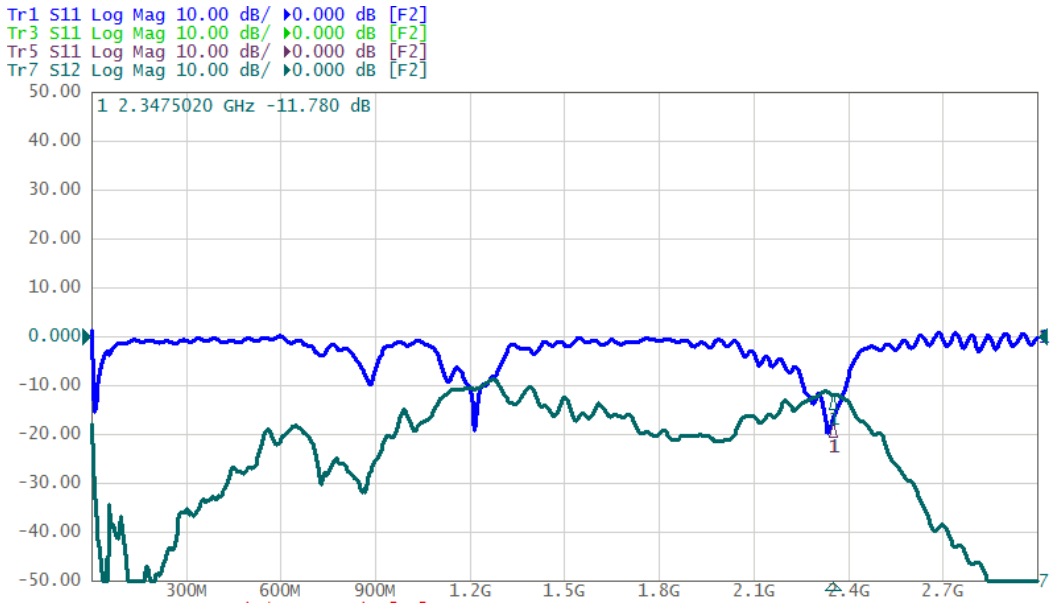

Figure 167. The S11 and S12 parameters of experiment after the first modification

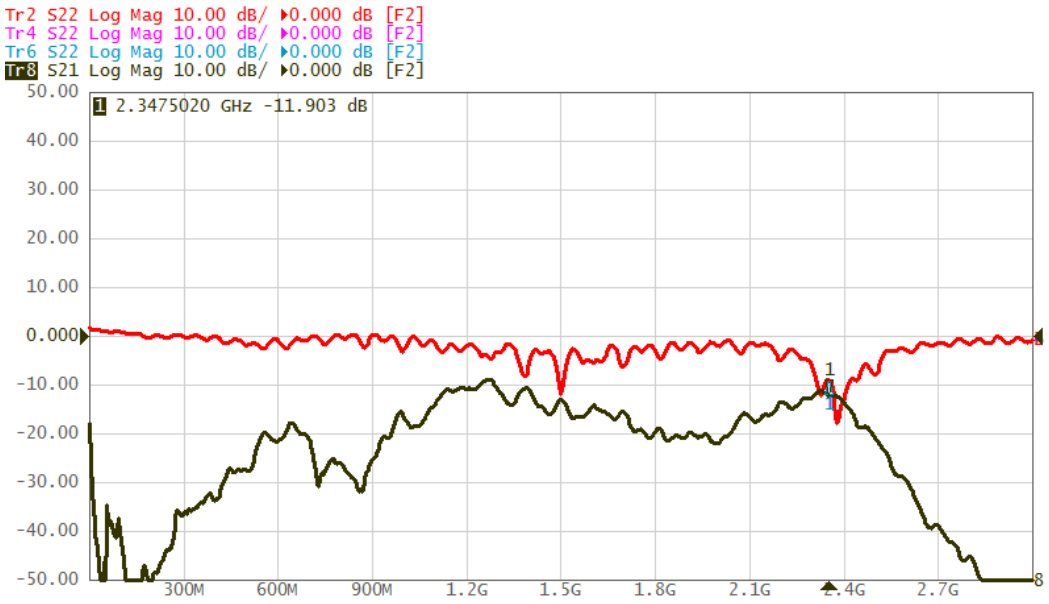

Figure 168. The S22 and S21 parameters of the experiment after the first modification

The trace above shows the S-Parameters for the original test set-up. Note that the 2.4 GHz measurements are equivalent to the 1.2 GHz measurements. Specifically note that the S21 and S12 parameters are at a maximum near 2.34 GHz. Again it is supposed that the location of this peak on the frequency domain is a result of the distance between the tap point and the backplane. Again, it is hypothesized that if the backplane were to be cut so that the distance between the tap point and the backplane was reduced, the traces for the S21 and S12 parameters would move in the rightward direction.

The difficulty with designing the TM Couplers is the mystery of the permittivity of PVC at 2.4 GHz. The permittivity of any material can vary with frequency, which results in a varied effect of the wavelength across frequency. Not knowing the permittivity introduces guesswork into the design, which can be corrected after a number of fabrication iterations demonstrates the correct tap-point to backplane distance.

8.2 Second Modification to the Stub Distance

The trace shown below is the result of a set of modified TM Couplers. The TM Couplers were modified so that the distance between the tap point and the backplane was reduced. To reduce the distance between the tap point and the backplane, the PVC was shaved down so that the

distance between the tap point in the backplane was approximately 1.7272 cm. Figure 169 and Figure 170 show the S parameter results from the VNA after the second modification.

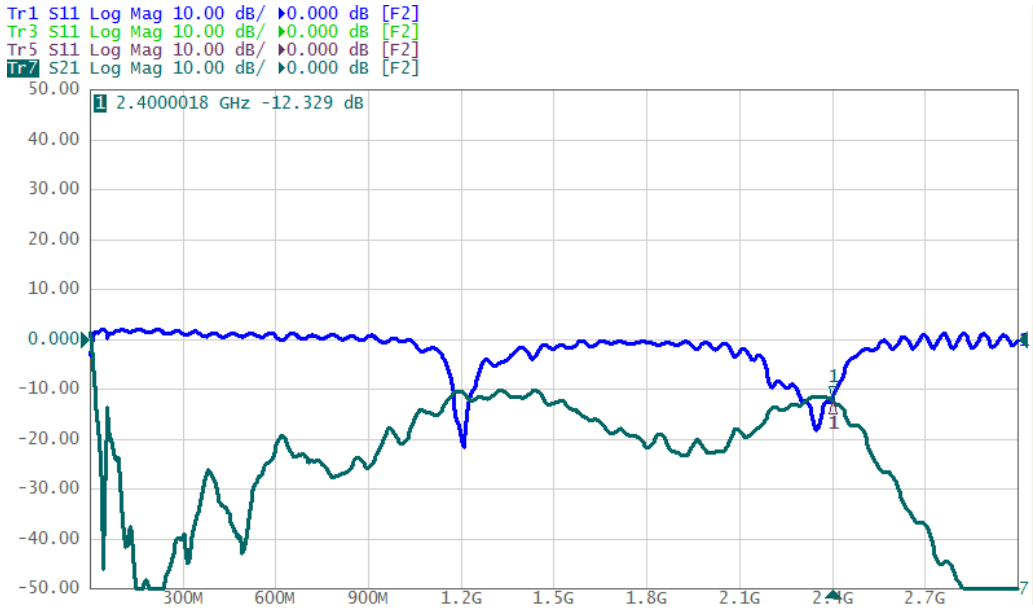

Figure 169. The S11 and S12 parameters of the experiment after the second modification

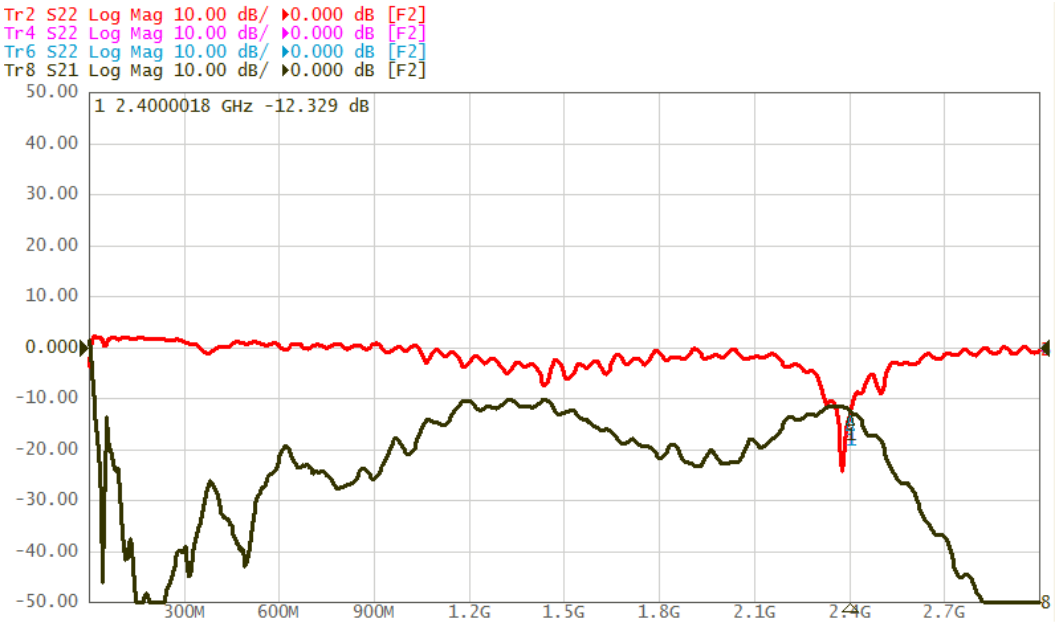

Figure 170. The S22 and S21 parameters of the experiment after the second modification

8.2.1 Determining the Relative Permittivity of PVC

The wavelength through a dielectric medium at a given frequency can be calculated with the following formula:

$$c = \lambda \cdot f \cdot \sqrt{\epsilon_r}$$

In the formula shown above, λ is the wavelength, f is the frequency, and ϵ_r is relative permittivity of the material; c is the speed of light. Using the trace shown in the prior experiments, it was assumed that the optimal frequency at which reflection was occurring was 2.35 GHz (because that's where the S12 curve is at a maximum); this means that at 2.35 GHz the wavelength that resulted within the PVC medium was such that the distance was between the tap point and the backplane was one quarter of the wavelength. That distance happen to be 1.8796 cm; using this number to calculate the wavelength within the PVC medium at 2.35 GHz, the relative permittivity of the PVC material was calculated and found to be 3.0969.

8.2.2 Shaving down the PVC

Once the relative permittivity of the PVC was found, the optimal distance at 2.4 GHz through a PVC medium could be calculated. The calculated wavelength was 7.0993 cm; therefore, one quarter of a wavelength should be approximately 1.7526 cm.

9 Appendix D – Expanded Results for Experiment 11

This section displays the results for Experiment 11 in concrete. The results are in the form of superimposed graphs. The superimposed graphs include: an admittance Smith chart and an impedance Smith chart of the input impedance, and XY graphs of the S-Parameters. Only two measurements were taken over the span of two days. As indicated in Experiment 11: Three TM Couplers in Concrete, three different 2-port configurations were used for the several measurements; in other words, for each configuration, a set of measurements was taken.

Configuration 1	Configuration 2	Configuration 3
	Port 1	Port 2
Port 2	Port 2	
Port 1		Port 1

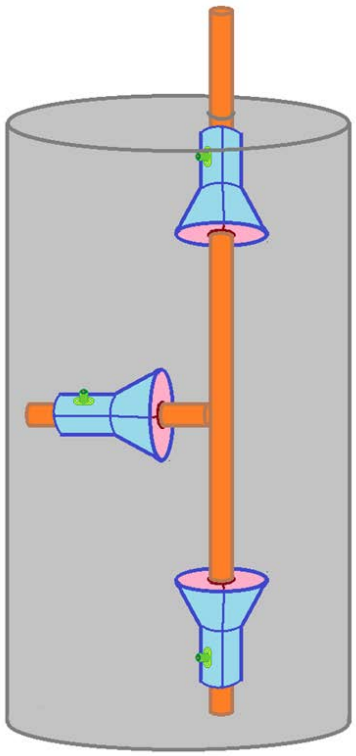

Figure 171. The Setup for Experiment 11

Three different configurations are measured. For each configuration, one set of measurements was taken centered at 2.4 GHz. Another set of measurements was taken at the full span of the VNA.

9.1 Measurement 1

Measurement 1 occurred 11 days after the concrete pour.

9.1.1 Measurement 1, Configuration 1, 2.4 GHz

These are the results for Measurement 1, Configuration 1 at 2.4 GHz with a 20 MHz span.

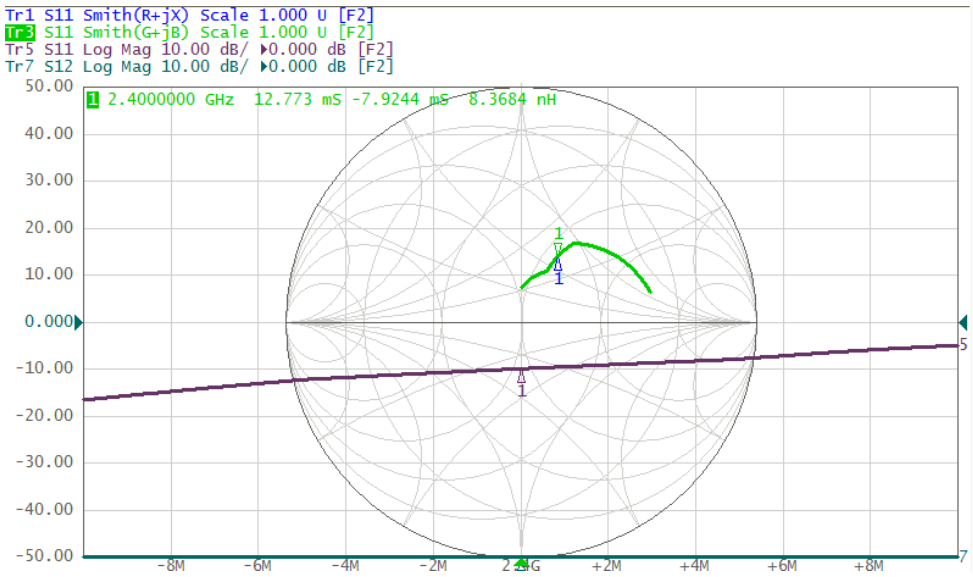

Figure 172. Port 1 for Measurement 1, Configuration 1, 2.4 GHz

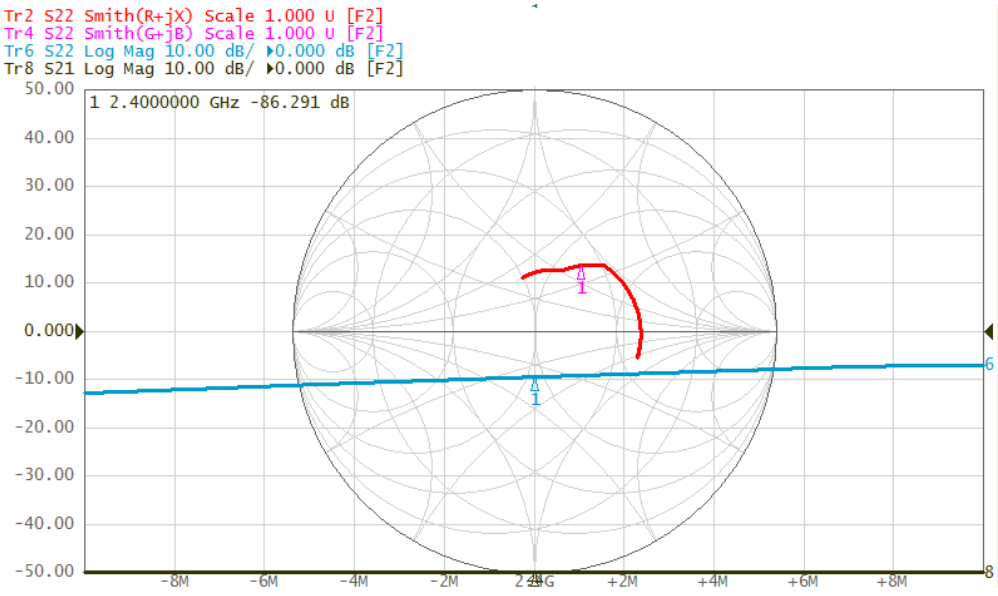

Figure 173 . Port 2 for Measurement 1, Configuration 1, 2.4 GHz

9.1.2 Measurement 1, Configuration 1, Full Span

These are the results for configuration 1 at full span.

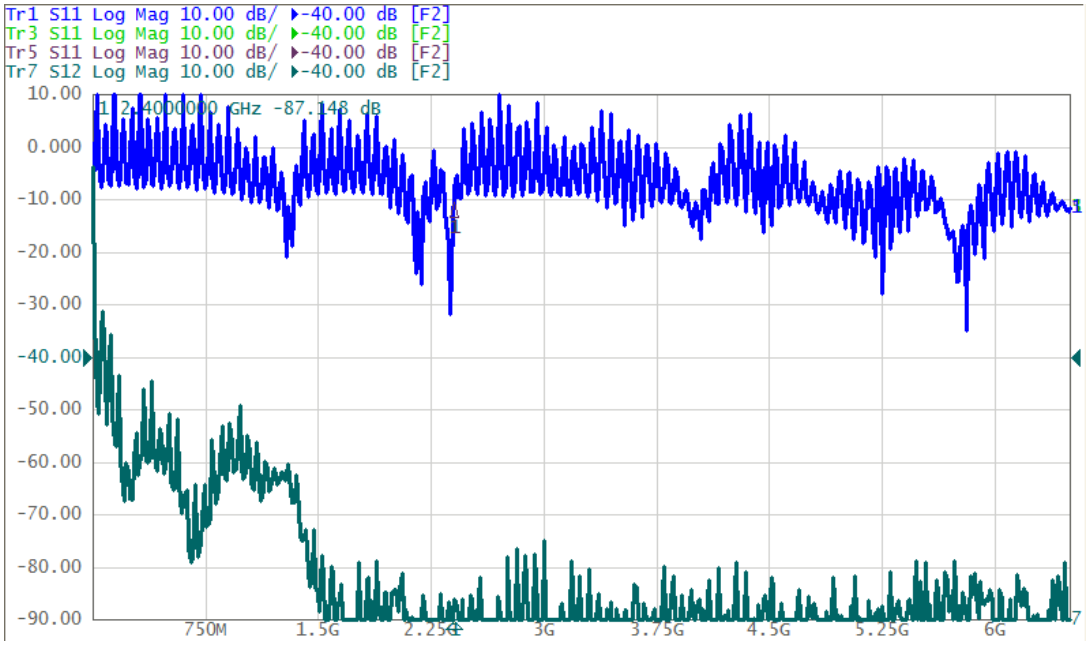

Figure 174. Port 1 for Measurement 1, Configuration 1, Full Span

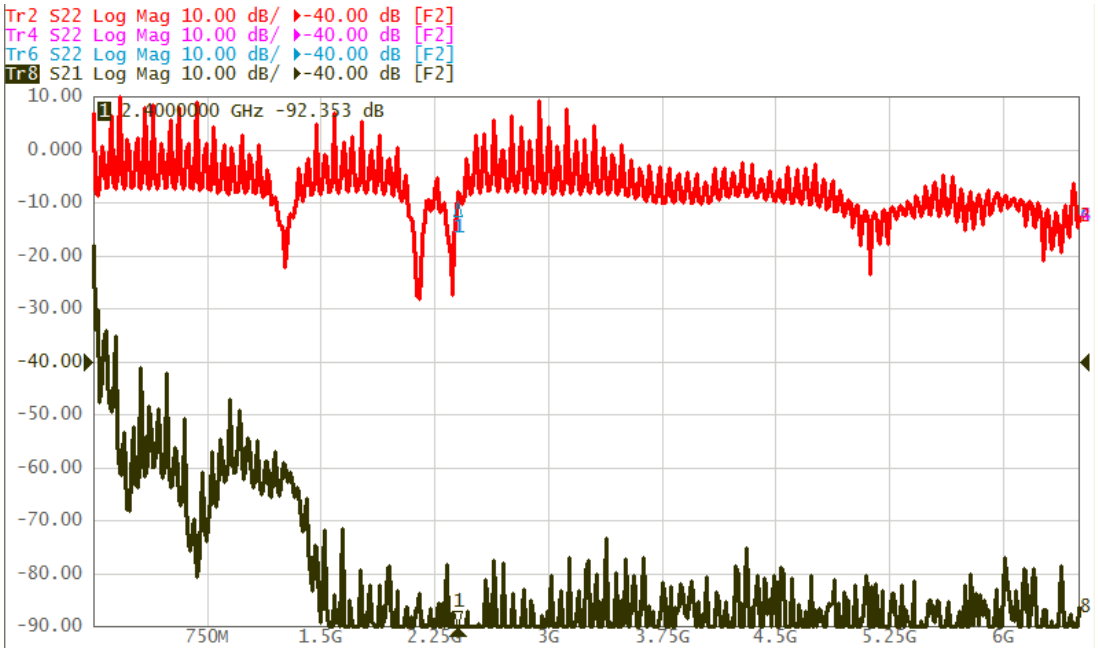

Figure 175. Port 2 for Measurement 1, Configuration 1, Full Span

9.1.3 Measurement 1, Configuration 2, 2.4 GHz

These are the results for configuration 2 at 2.4 GHz.

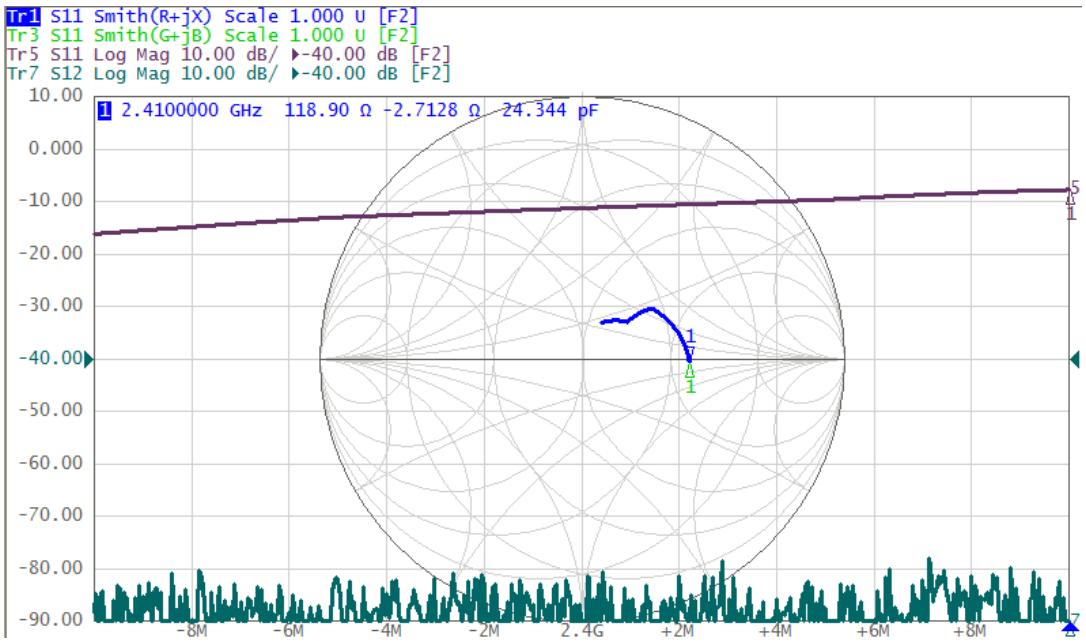

Figure 176. Port 1 for Measurement 1, Configuration 2, 2.4 GHz

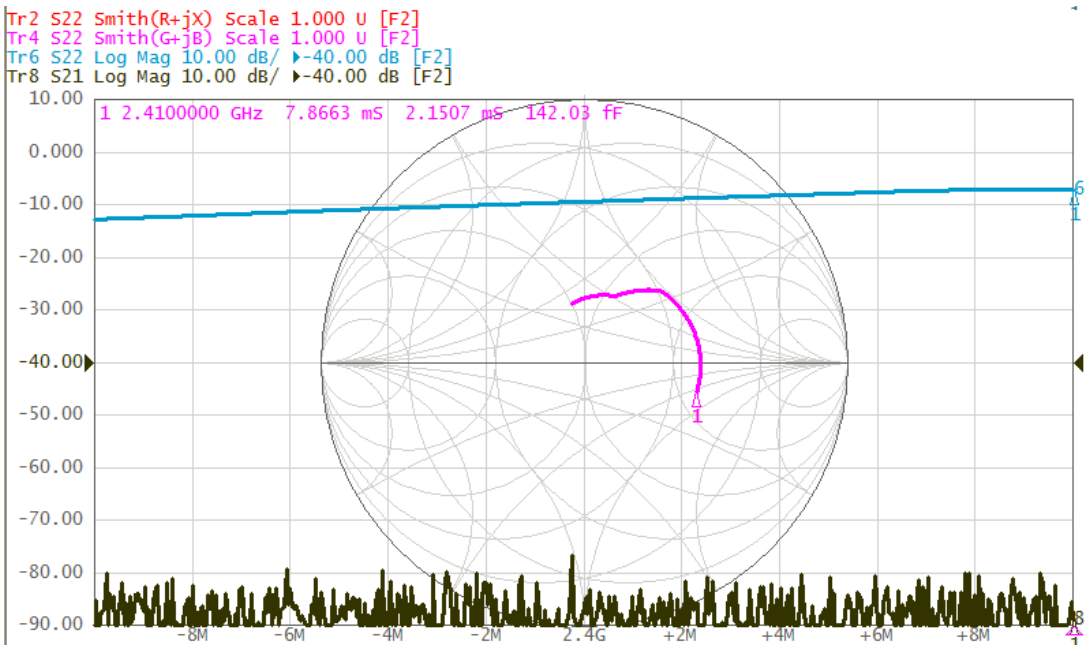

Figure 177. Port 2 for Measurement 1, Configuration 2, 2.4 GHz

9.1.4 Measurement 1, Configuration 2, Full Span

These are the results for configuration 2 at full span.

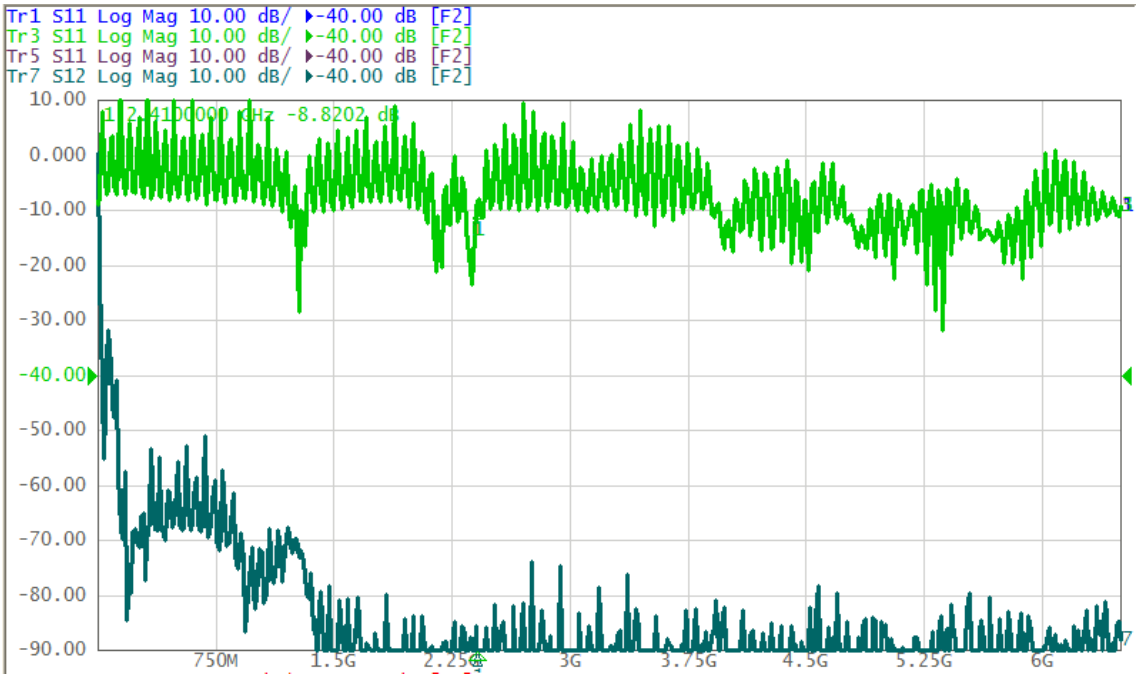

Figure 178. Port 1 for Measurement 1, Configuration 2, Full Span

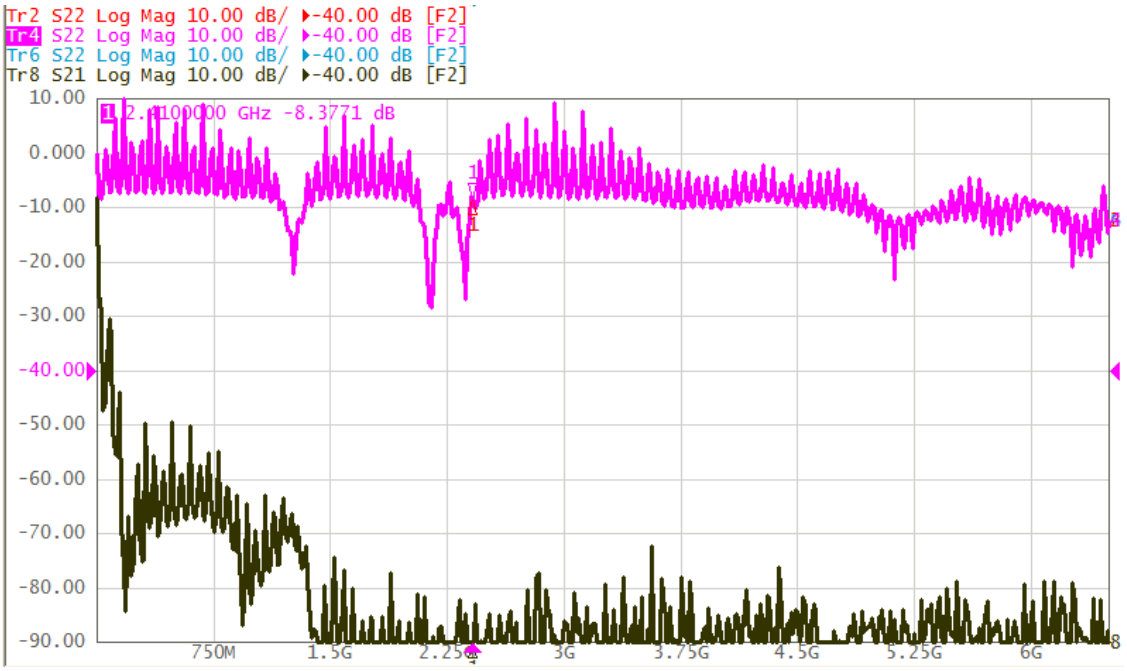

Figure 179. Port 2 for Measurement 1, Configuration 2, Full Span

9.1.5 Measurement 1, Configuration 3, 2.4 GHz

These are the results for configuration 3 at 2.4 GHz.

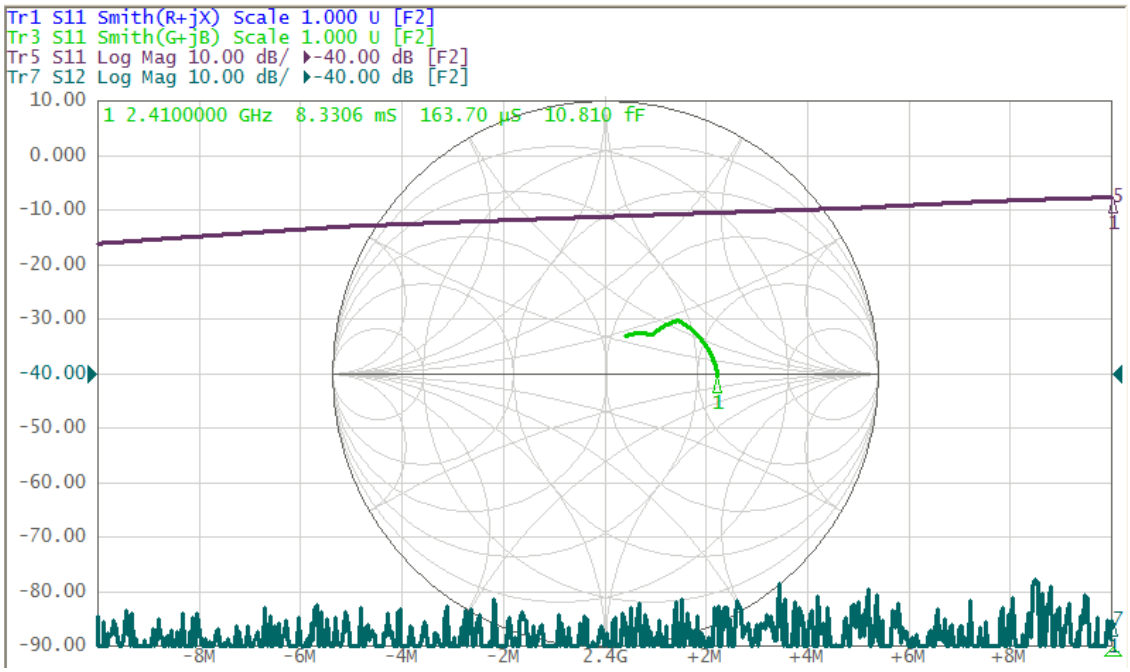

Figure 180. Port 1 for Measurement 1, Configuration 3, Full Span

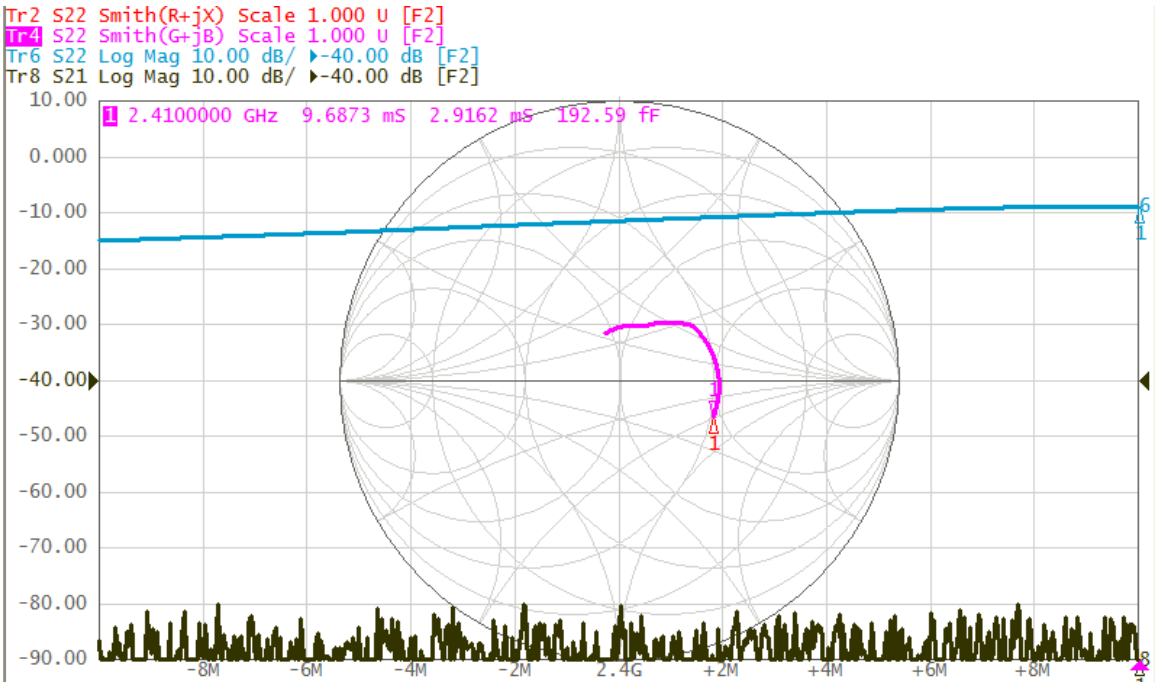

Figure 181. Port 2 for Measurement 1, Configuration 3, Full Span

9.1.6 Measurement 1, Configuration 3, Full Span

These are the results for configuration 3 at full span.

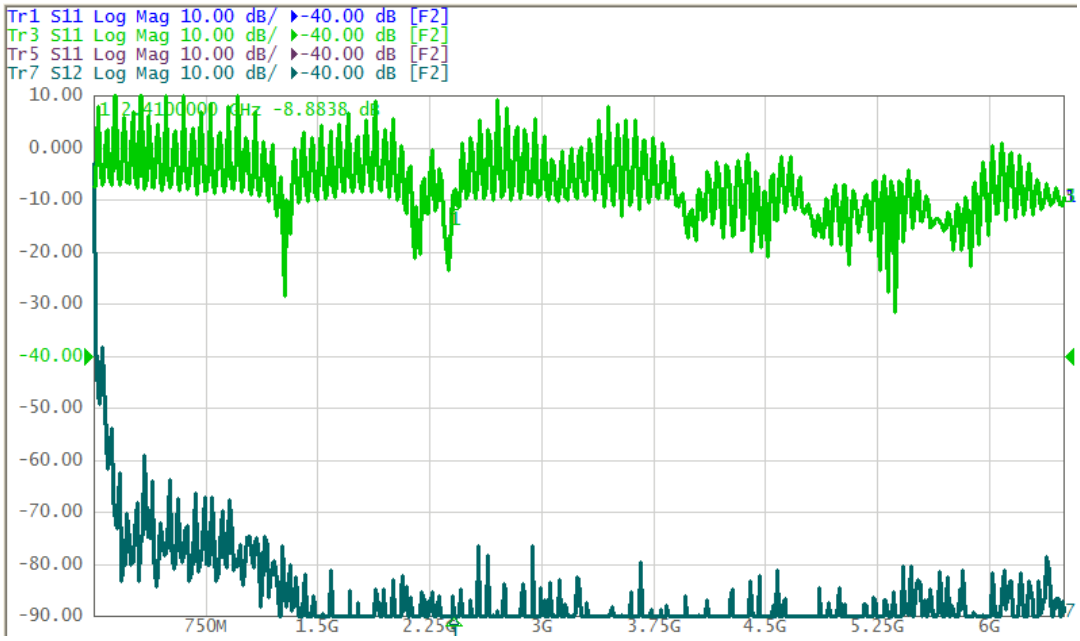

Figure 182. Port 1 for Measurement 1, Configuration 3, Full Span

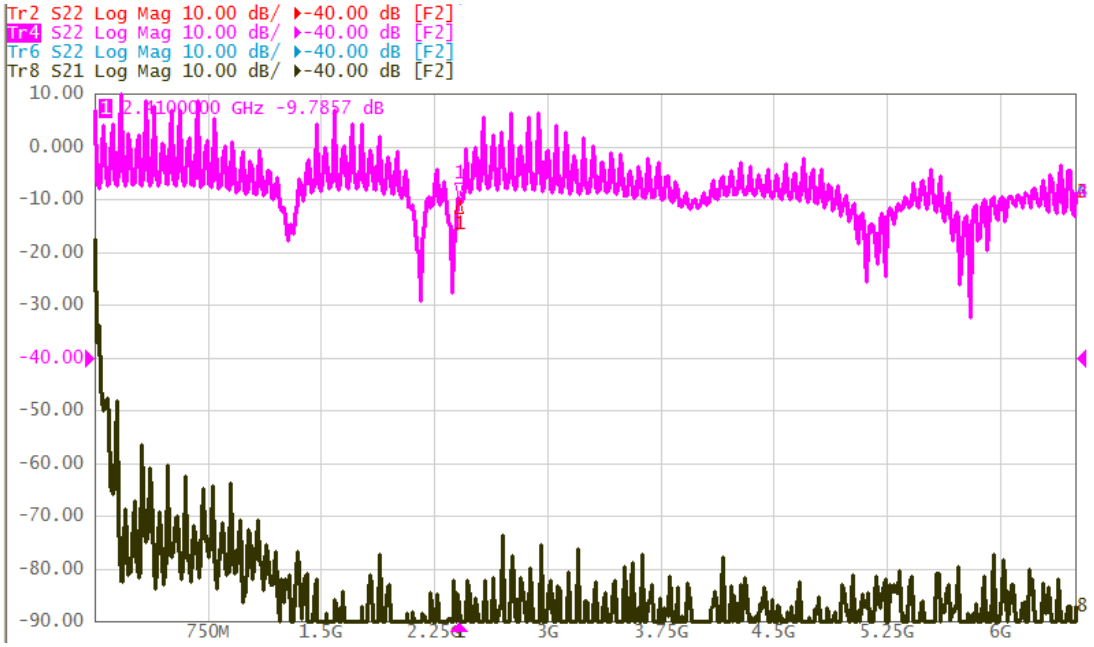

Figure 183. Port 2 for Measurement 1, Configuration 3, Full Span

9.1.7 Measurement 2, Configuration 1, 9kHz to 200MHz

These are the measurements taken from 9kHz to 200MHz. (Note: Minimal S_{11}, locally, occurs at 3.25MHz.)

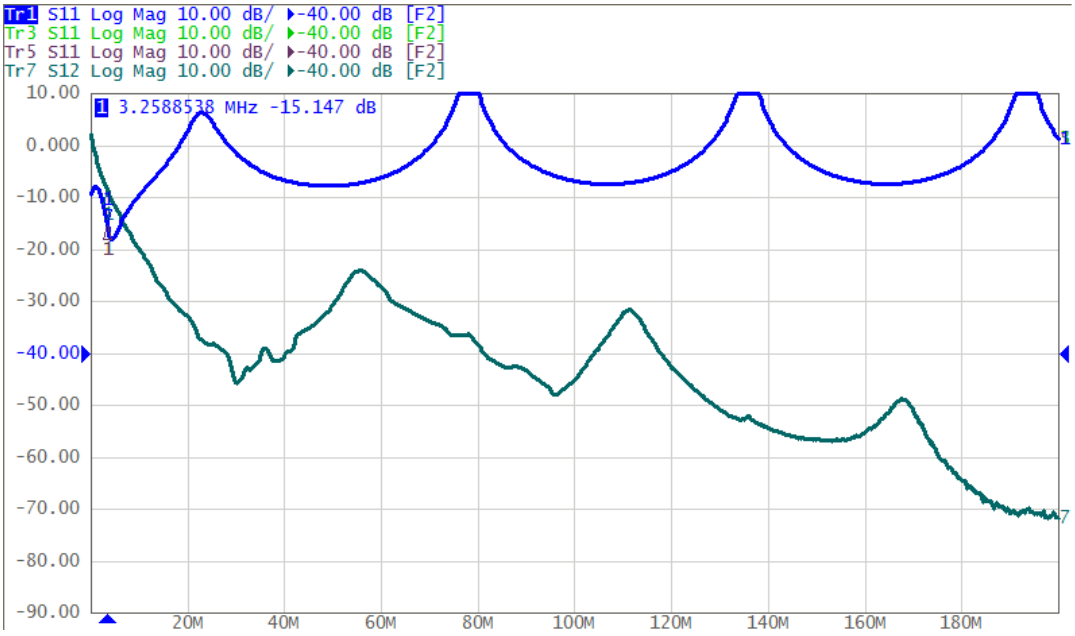

Figure 184. Port 1 for Measurement 2, Configuration 1, 9kHz to 200MHz

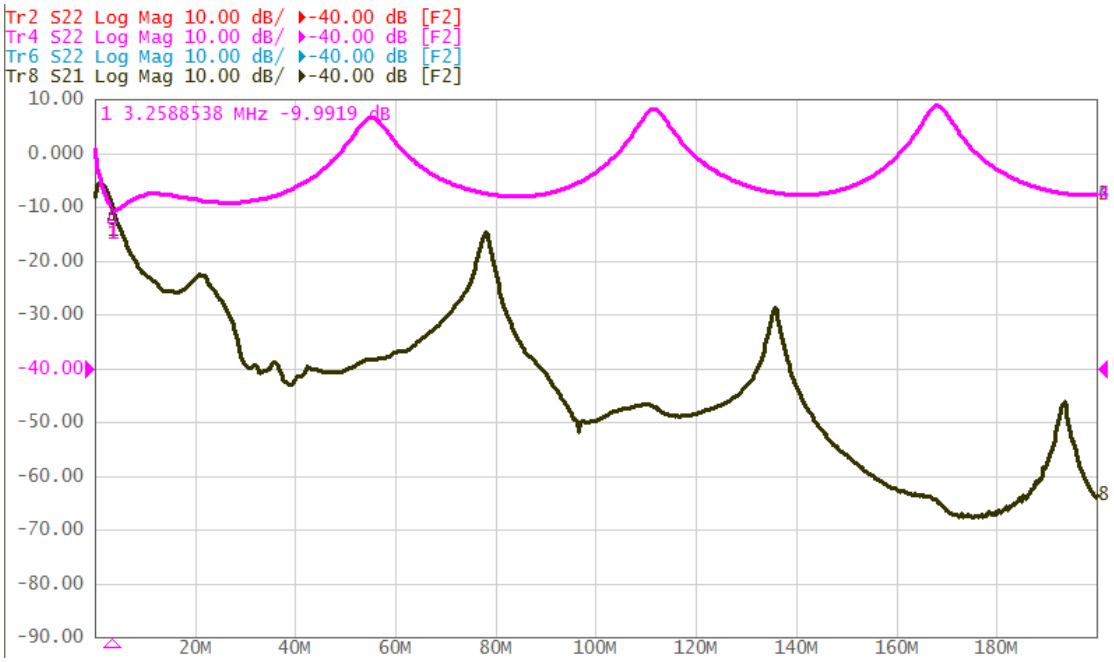

Figure 185. Port 2 for Measurement 2, Configuration 1, 9kHz to 200MHz

9.2 Measurement 2

Measurement 2 was taken 12 days after the pour.

9.2.1 Measurement 2, Configuration 1, 2.4 GHz

These are the results for configuration 1 at 2.4 GHz.

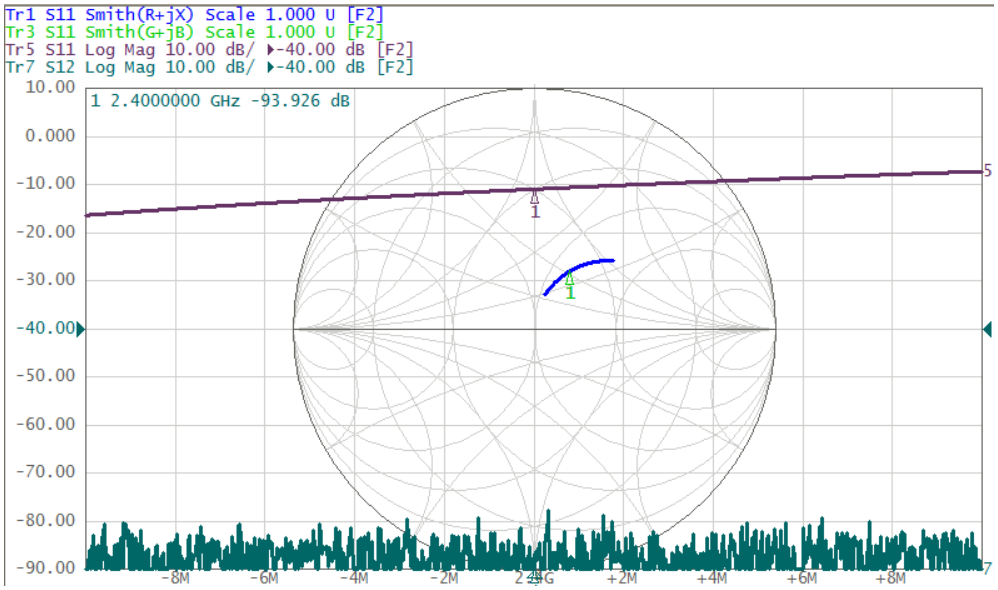

Figure 186. Port 1 for Measurement 2, Configuration 1, 2.4 GHz

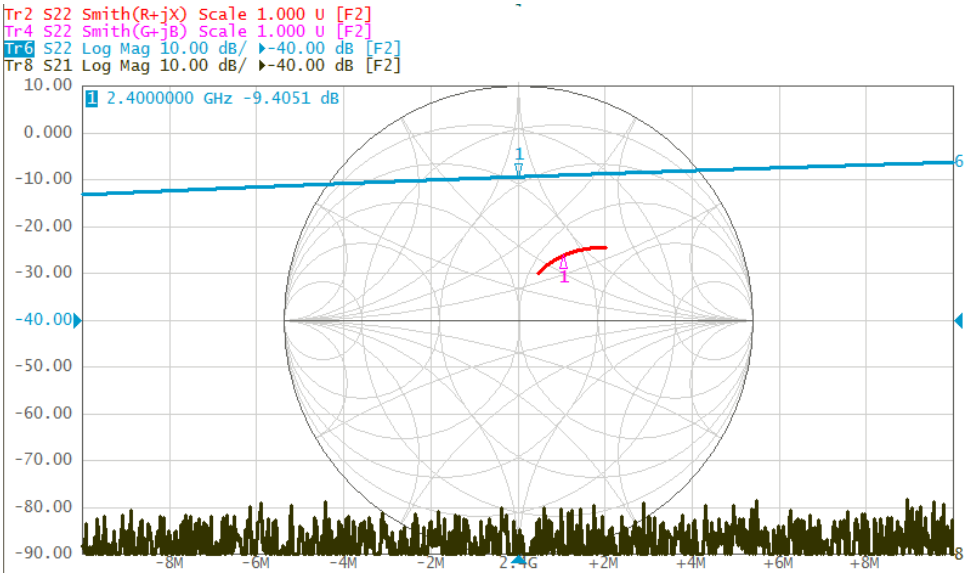

Figure 187. Port 2 for Measurement 2, Configuration 1, 2.4 GHz

9.2.2 Measurement 2, Configuration 1, Full Span

These are the results for measurement 2 at full span.

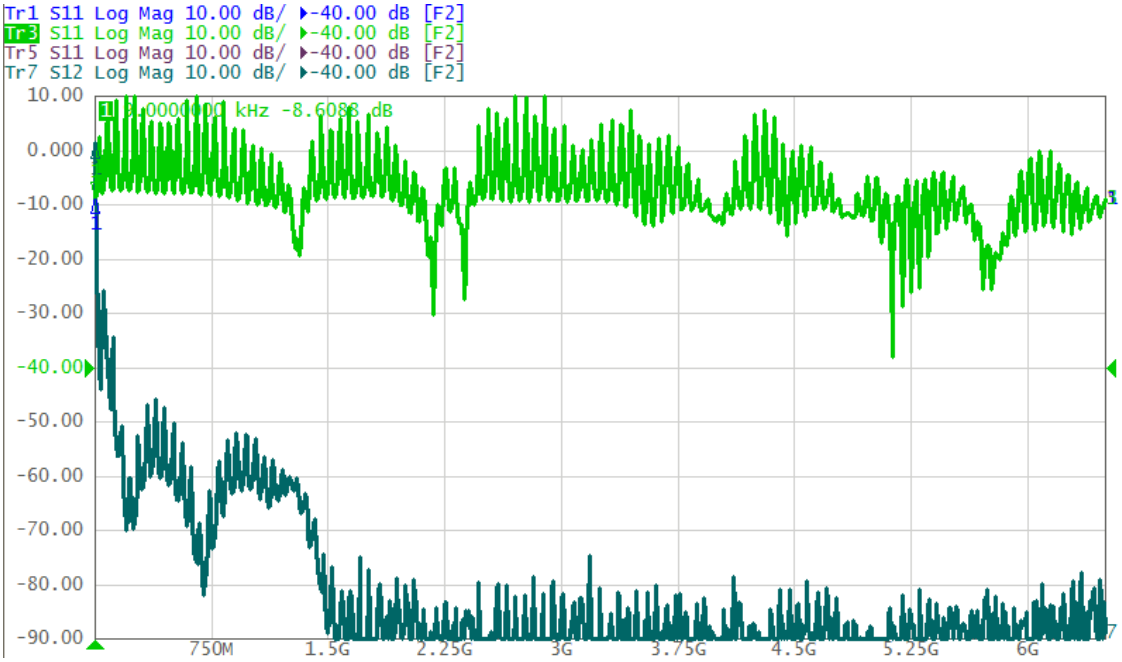

Figure 188. Port 1 for Measurement 2, Configuration 1, Full Span

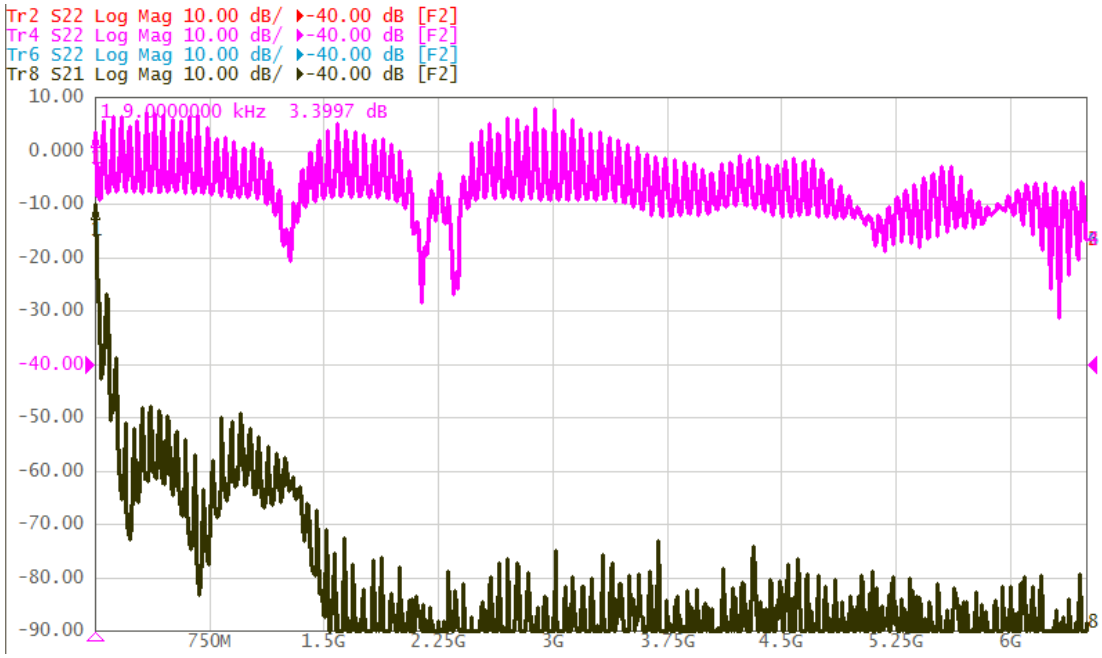

Figure 189. Port 2 for Measurement 2, Configuration 1, Full Span

9.2.3 Measurement 2, Configuration 1, 9kHz to 1.5GHz

These are the measurements taken from 9kHz to 1.5GHz.

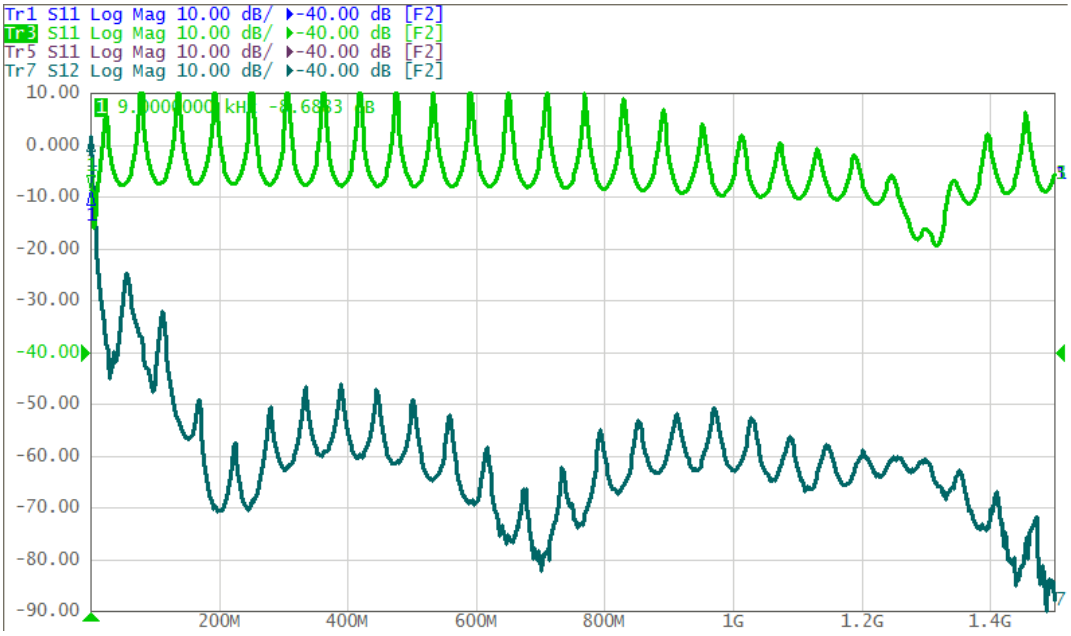

Figure 190. Port 1 for Measurement 2, Configuration 1, 9kHz to 1.5GHz

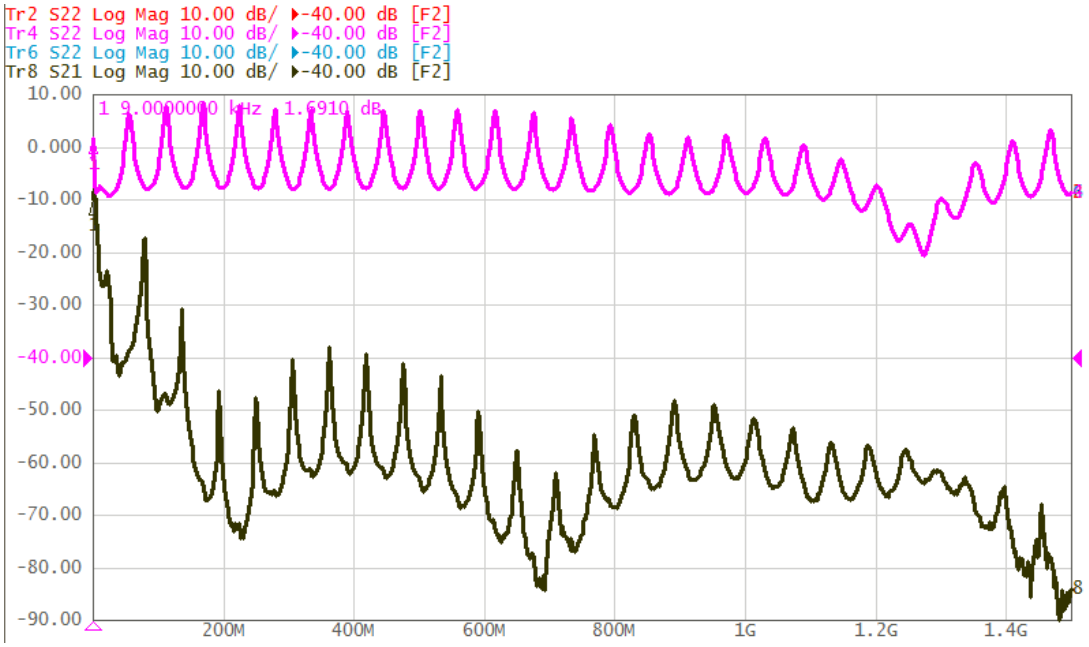

Figure 191. Port 2 for Measurement 2, Configuration 1, 9kHz to 1.5GHz

9.2.4 Measurement 2, Configuration 2, 2.4 GHz

These are the results for configuration 2 at 2.4 GHz.

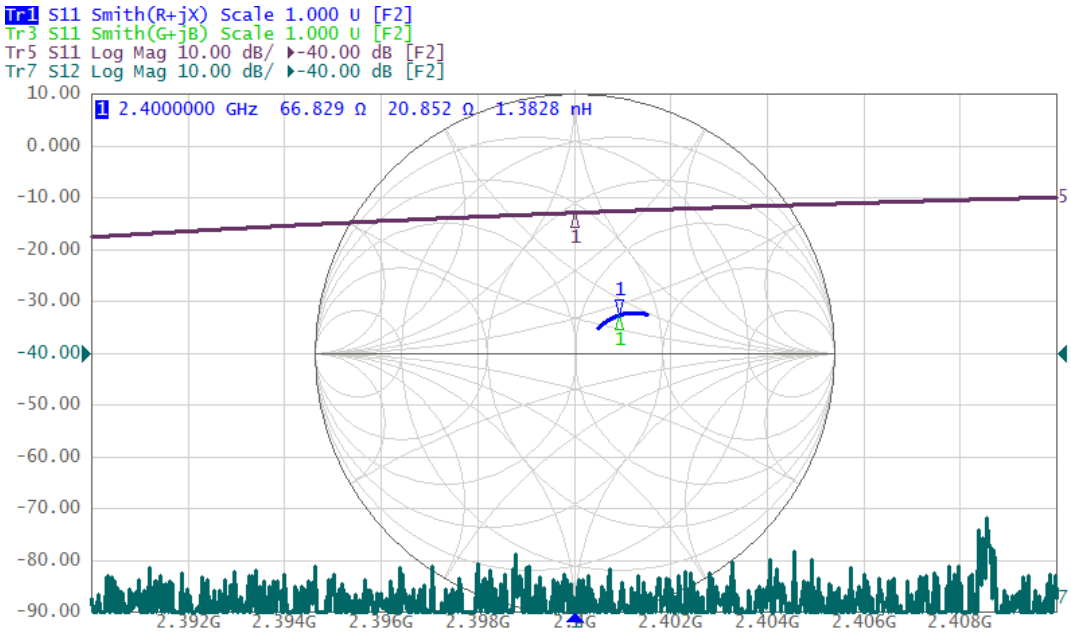

Figure 192. Port 1 for Measurement 2, Configuration 2, 2.4 GHz

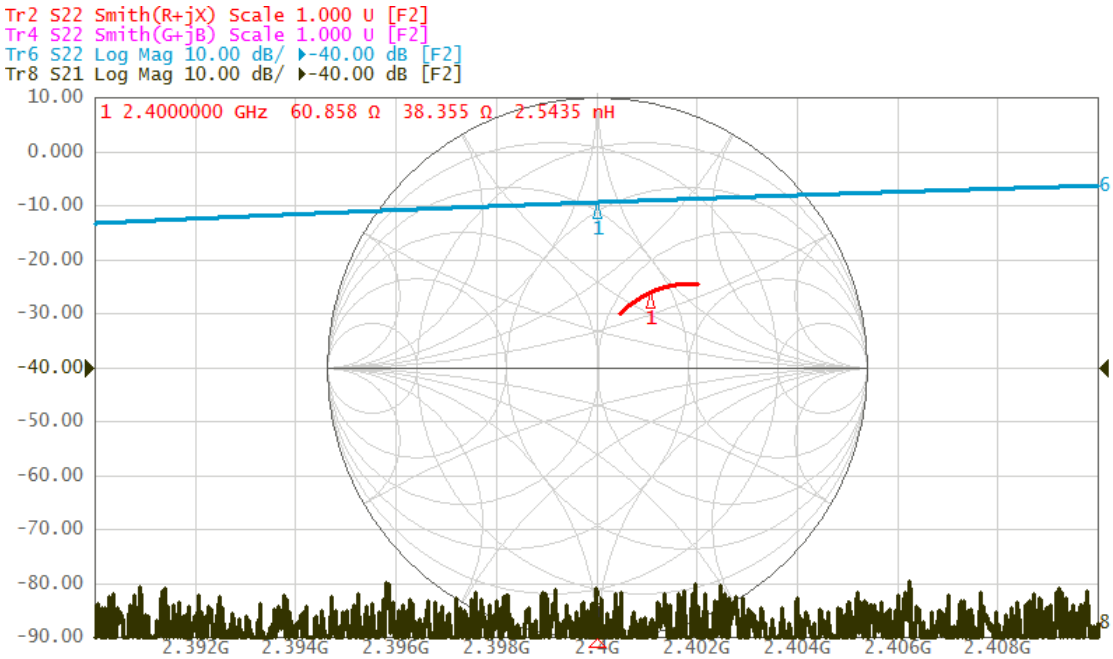

Figure 193. Port 2 for Measurement 2, Configuration 2, 2.4 GHz

9.2.5 Measurement 2, Configuration 2, Full Span

These are the results for configuration 2 at full span.

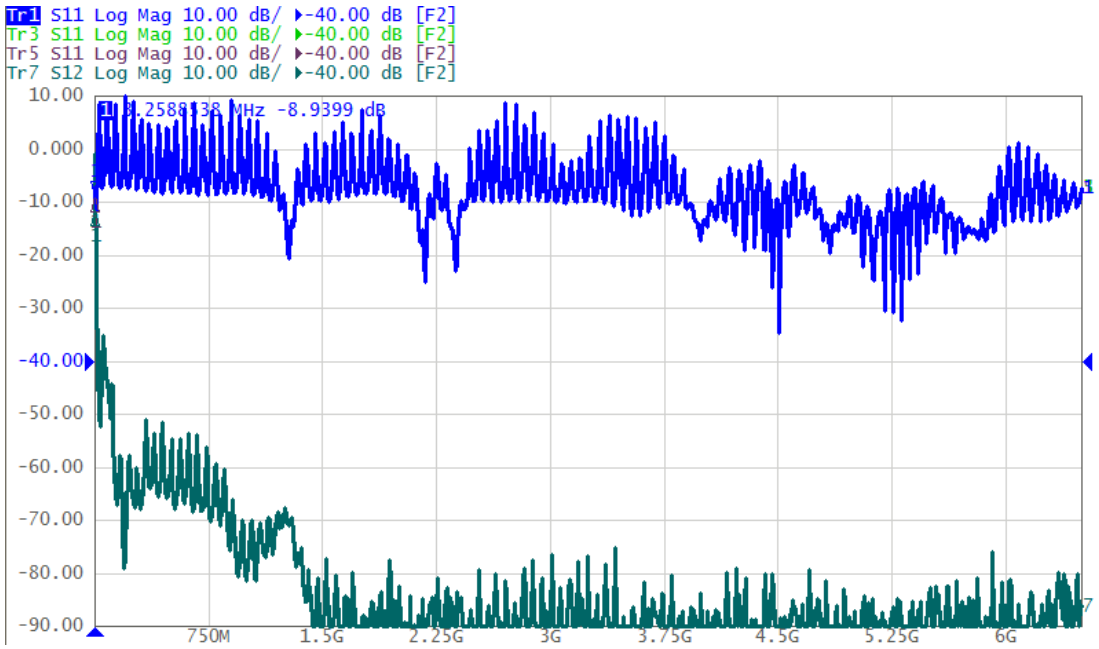

Figure 194. Port 1 for Measurement 2, Configuration 2, Full Span

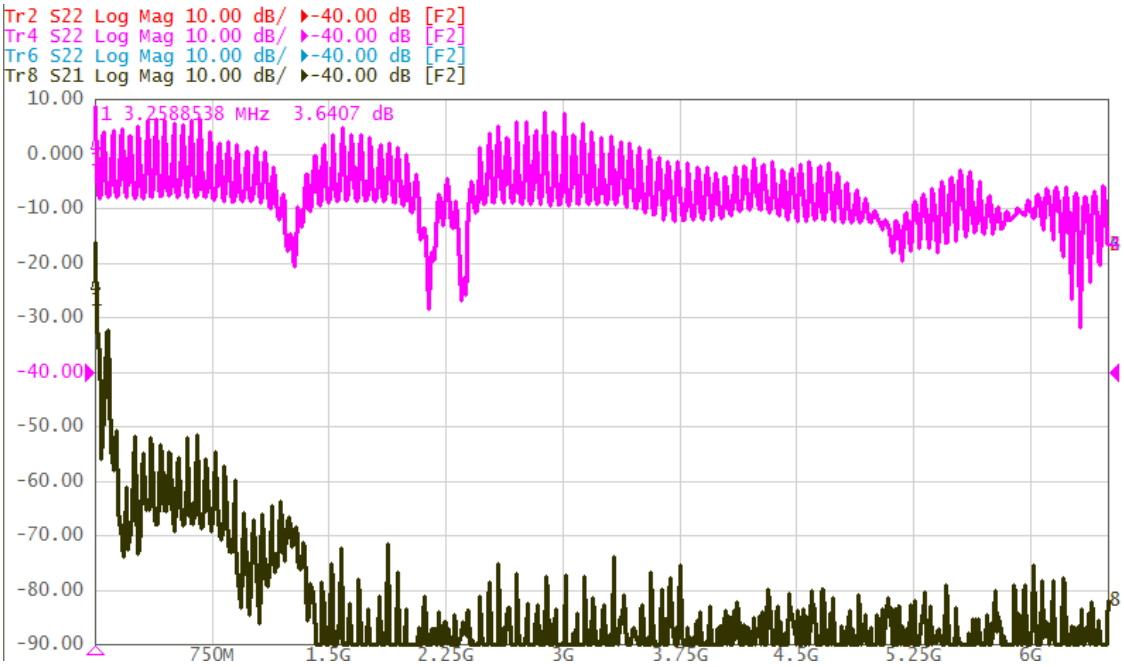

Figure 195. Port 2 for Measurement 2, Configuration 2, Full Span

9.2.6 Measurement 2, Configuration 2, 9kHz to 1.5GHz

These are the results for configuration 2 from 9kHz to 1.5GHz.

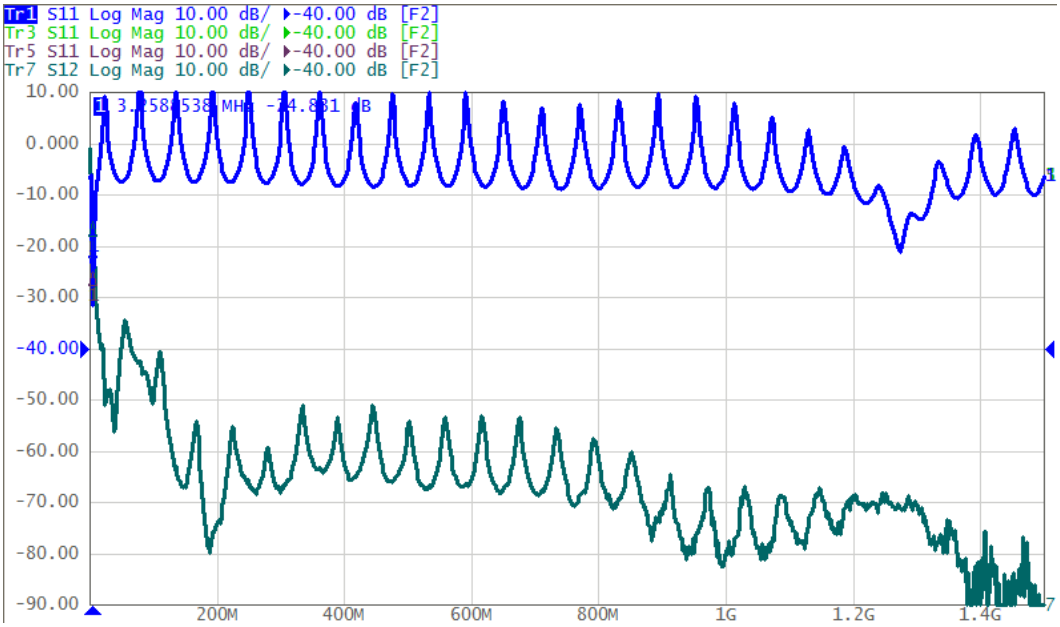

Figure 196. Port 1 for Measurement 2, Configuration 2, 9kHz to 1.5GHz

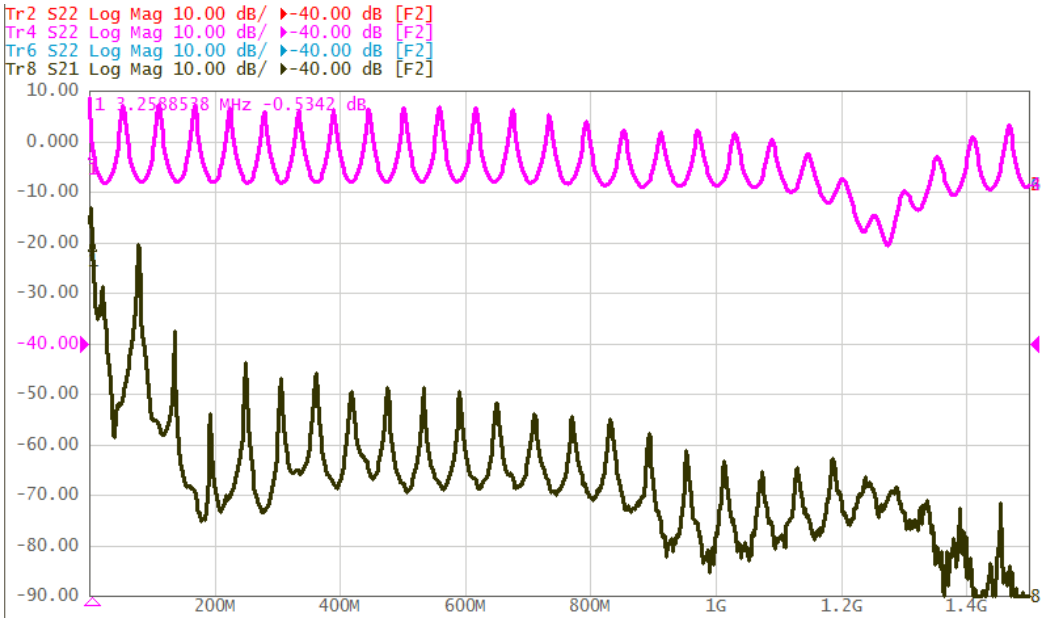

Figure 197. Port 2 for Measurement 2, Configuration 2, 9kHz to 1.5GHz

9.2.7 Measurement 2, Configuration 2, 9kHz to 200MHz

These are the results for configuration 2 from 9kHz to 200MHz.

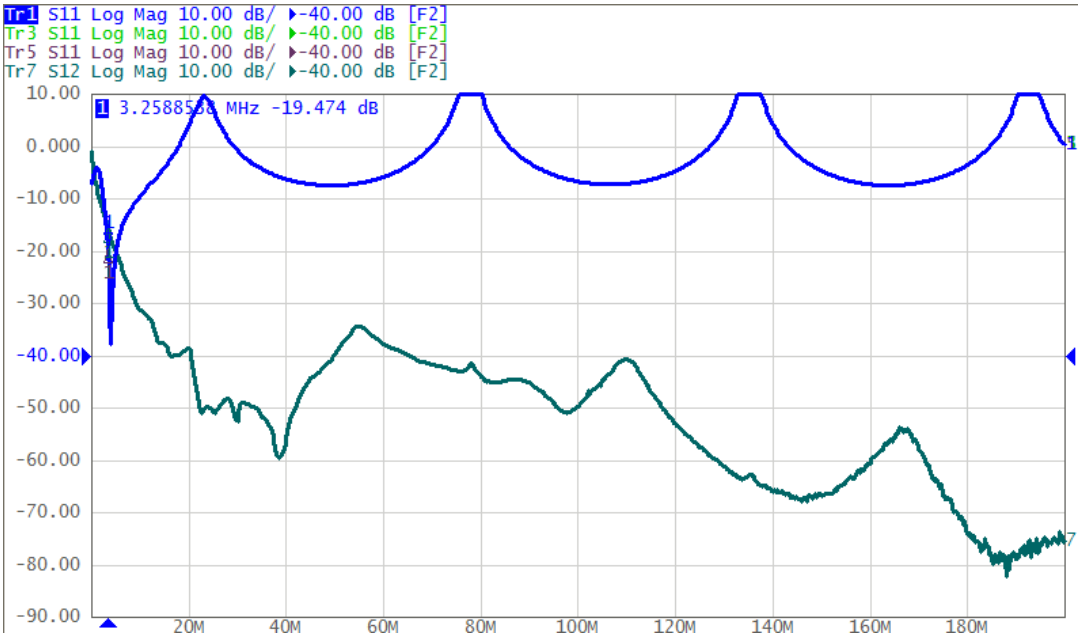

Figure 198. Port 1 for Measurement 2, Configuration 2, 9kHz to 200MHz

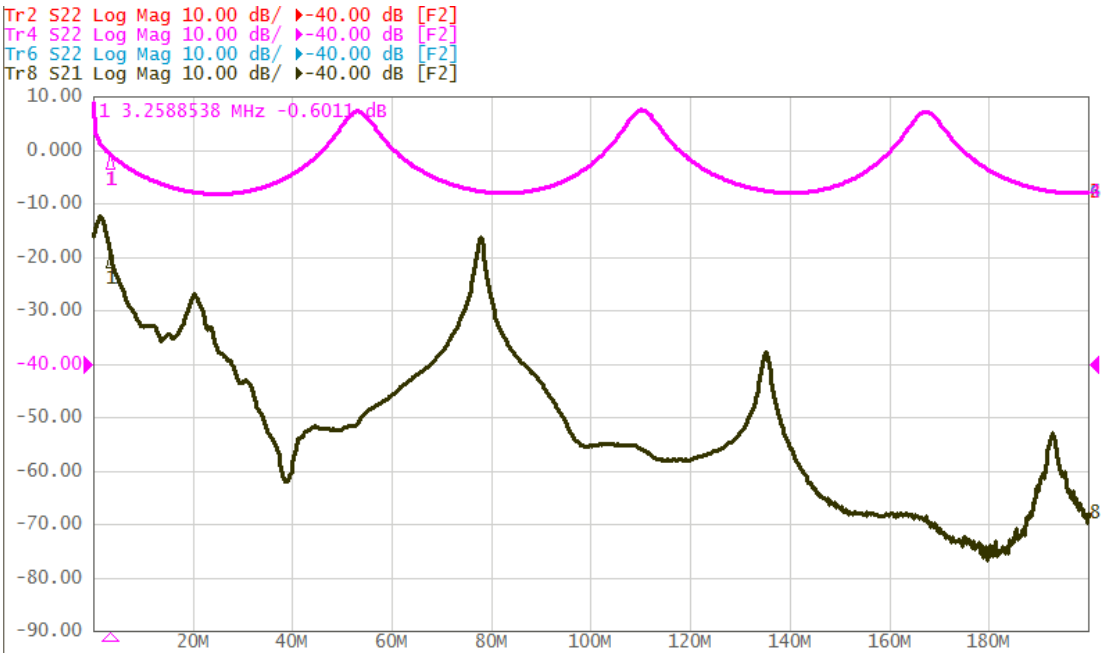

Figure 199. Port 2 for Measurement 2, Configuration 2, 9kHz to 200MHz

9.2.8 Measurement 2, Configuration 3, 2.4 GHz

These are the results for configuration 3 at 2.4 GHz.

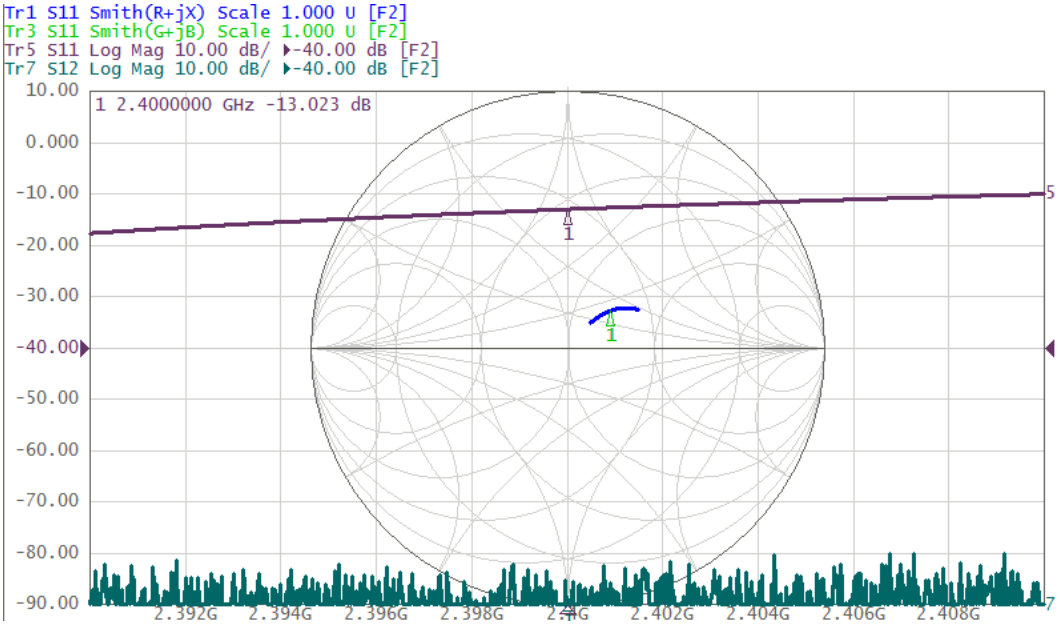

Figure 200. Port 1 for Measurement 2, Configuration 3, 2.4 GHz

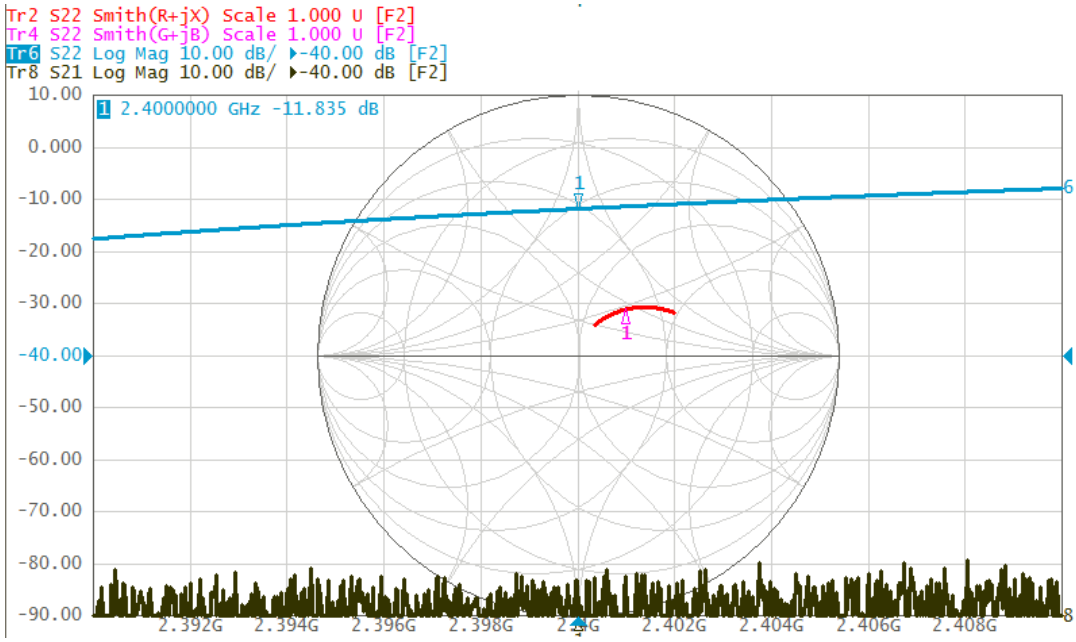

Figure 201. Port 2 for Measurement 2, Configuration 3, 2.4 GHz

9.2.9 Measurement 2, Configuration 3, Full Span

These are the results for configuration 3 at full span.

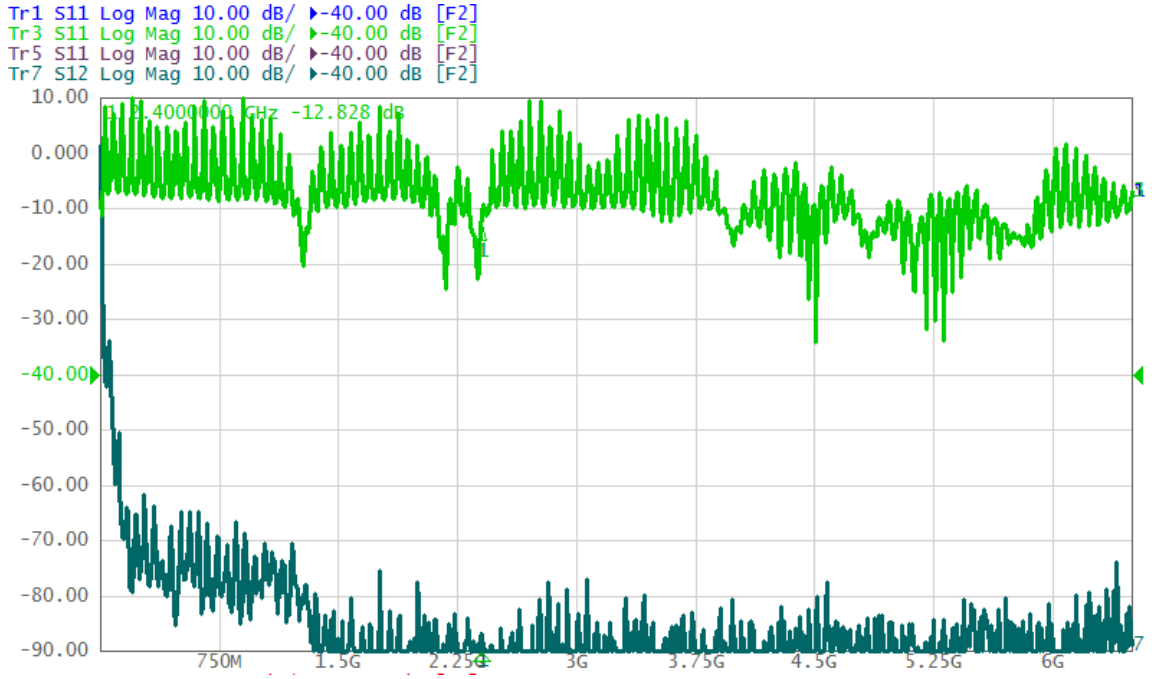

Figure 202. Port 1 for Measurement 2, Configuration 3, Full Span

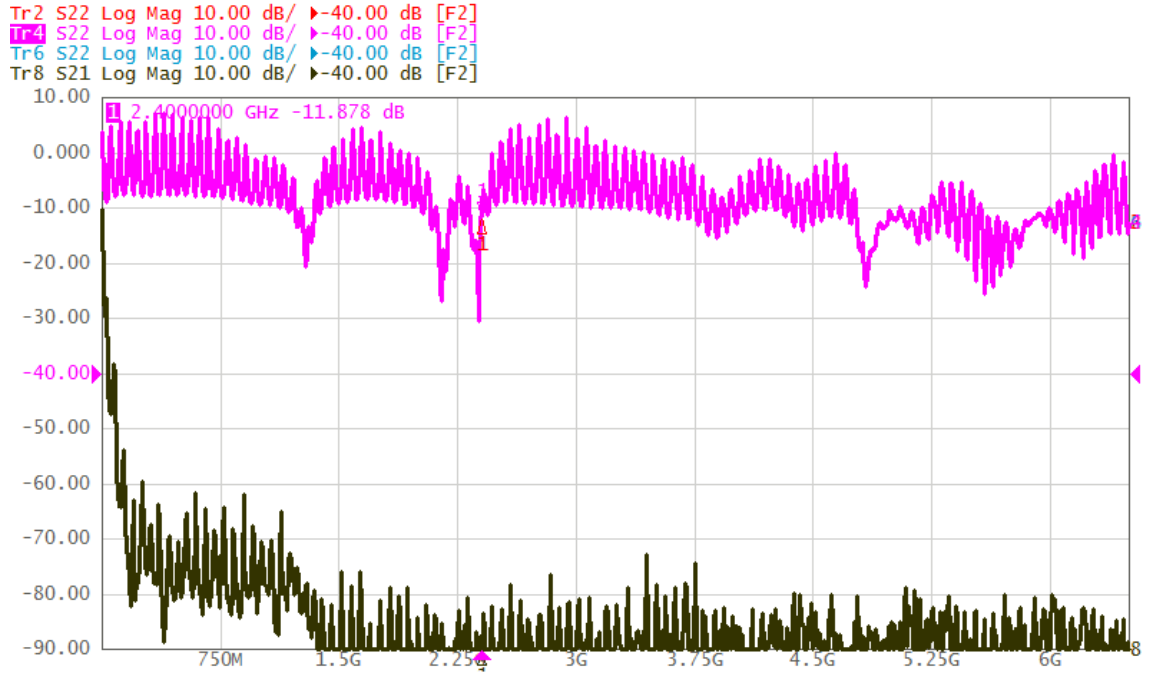

Figure 203. Port 2 for Measurement 2, Configuration 3, Full Span

9.2.10 Measurement 2, Configuration 3, 9kHz to 1.5GHz

These are the results for configuration 2 from 9kHz to 1.5GHz.

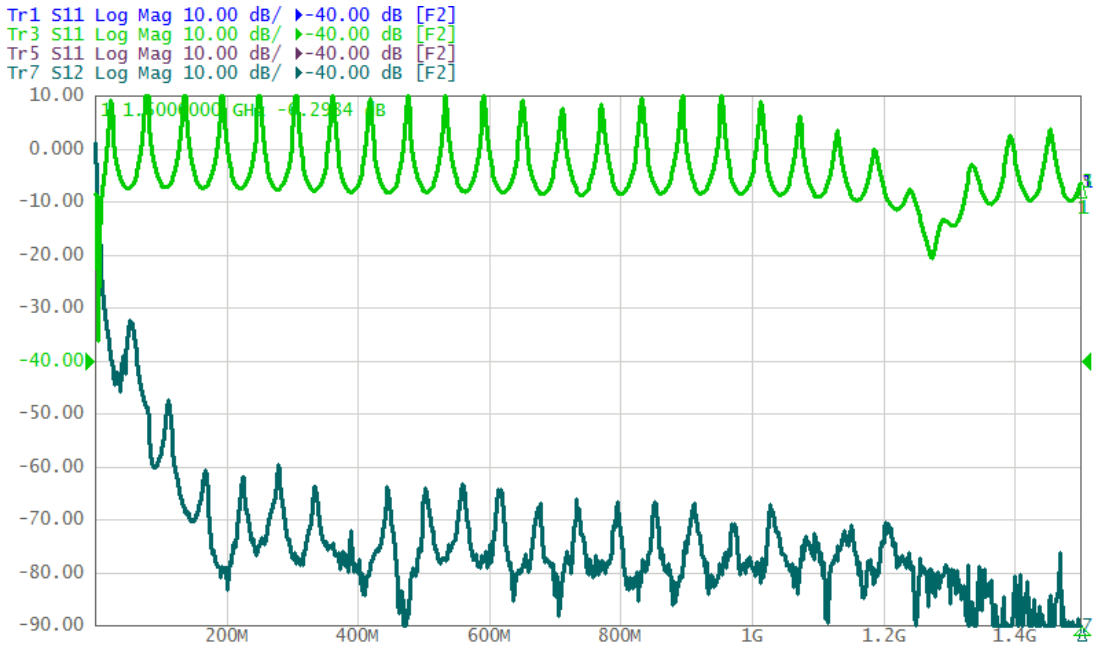

Figure 204. Port 1 for Measurement 2, Configuration 3, 9kHz to 1.5GHz

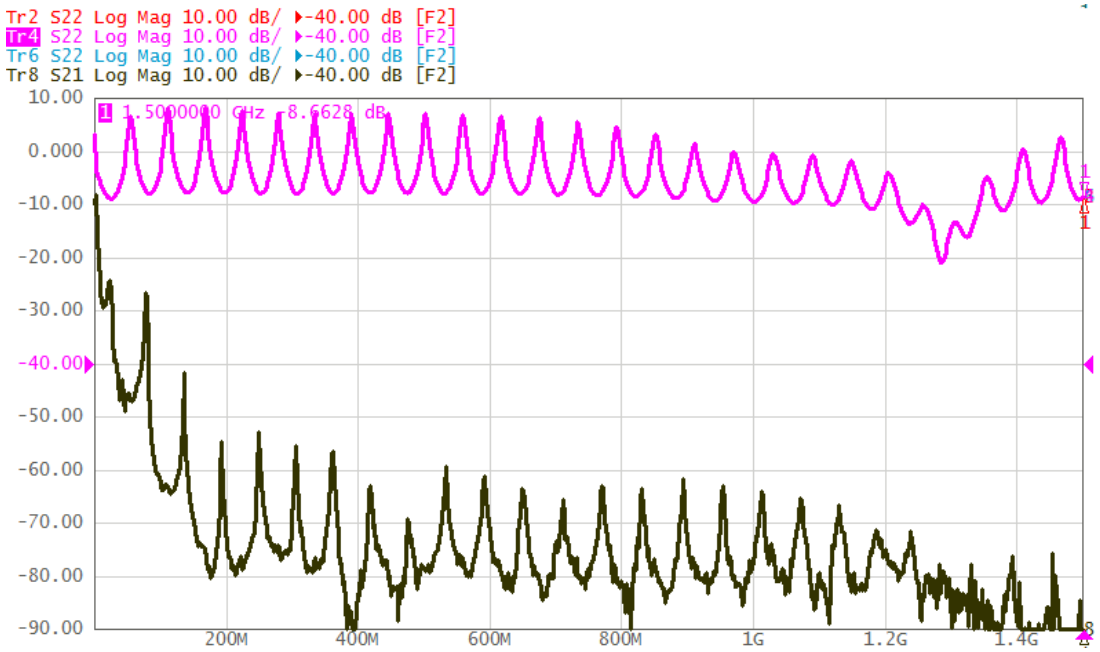

Figure 205. Port 2 for Measurement 2, Configuration 3, 9kHz to 1.5GHz

9.2.11 Measurement 2, Configuration 3, 9kHz to 200MHz

These are the results for configuration 2 from 9kHz to 200MHz.

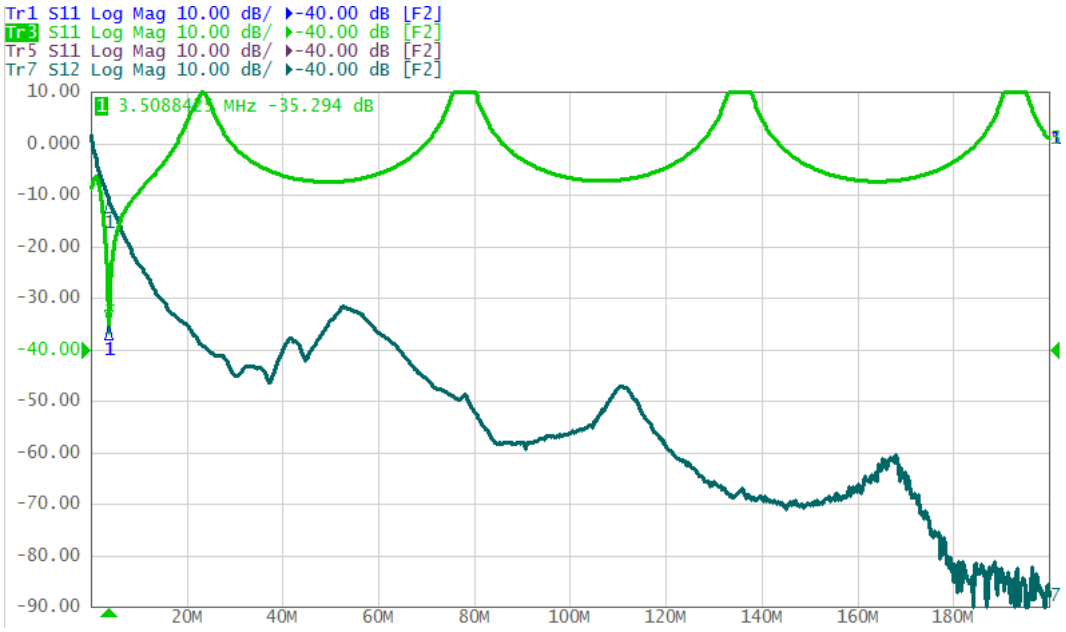

Figure 206. Port 1 for Measurement 2, Configuration 3, 9kHz to 200MHz

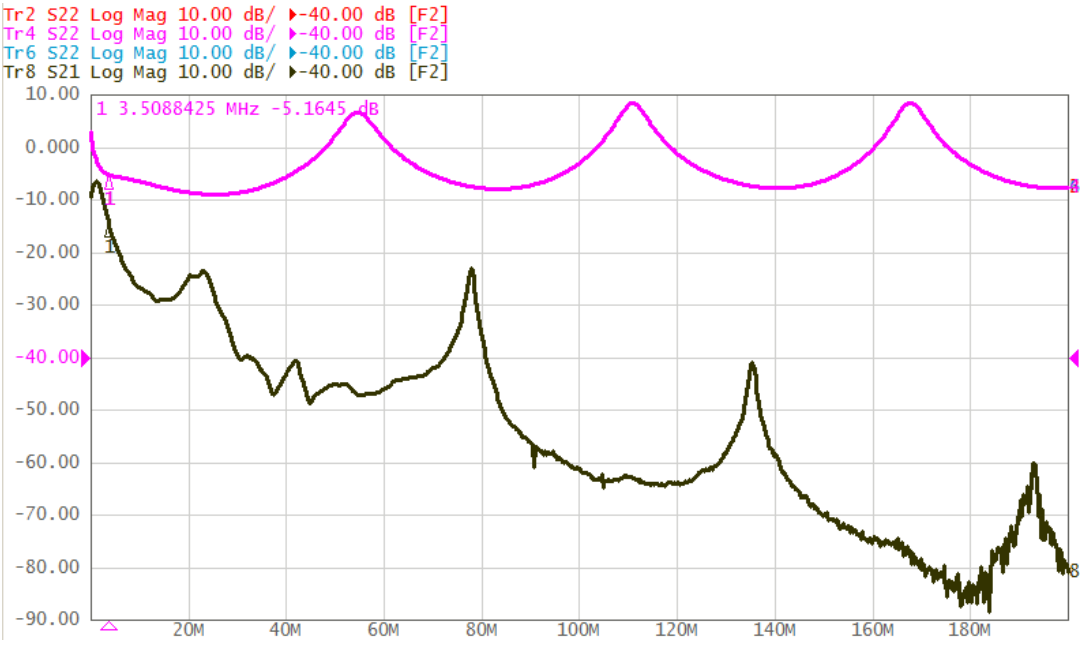

Figure 207. Port 2 for Measurement 2, Configuration 3, 9kHz to 200MHz

9.2.12 S-parameters and Smith Chart

Below an image shows the S-Parameters and the Smith chart for the two modified TM Couplers separated by distance 110.5 cm; the graph on the top is for port one, wrapping the bottoms to Note that the S11 and S22 parameters are not ideally matched (there's a little bit of reactance present on the input impedance); nevertheless, the traces indicate that between 90% and 99% of the power is not reflected. Furthermore, the traces for the S12 and S21 parameters indicate that there is only about a 12 dB power loss.

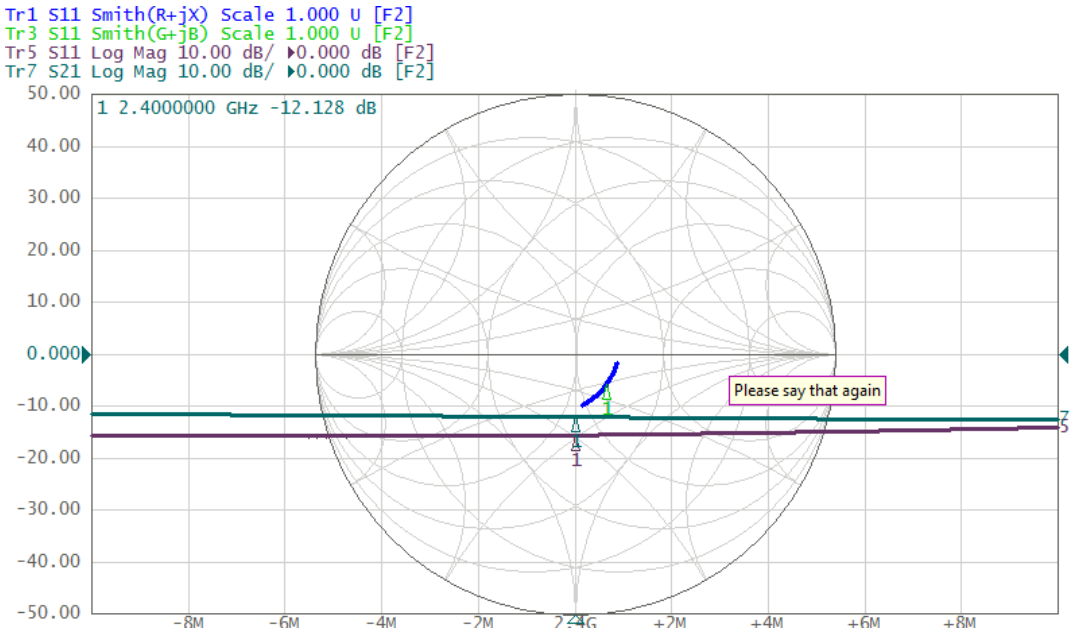

Figure 208. S11 and S21 parameters after the Second Modification

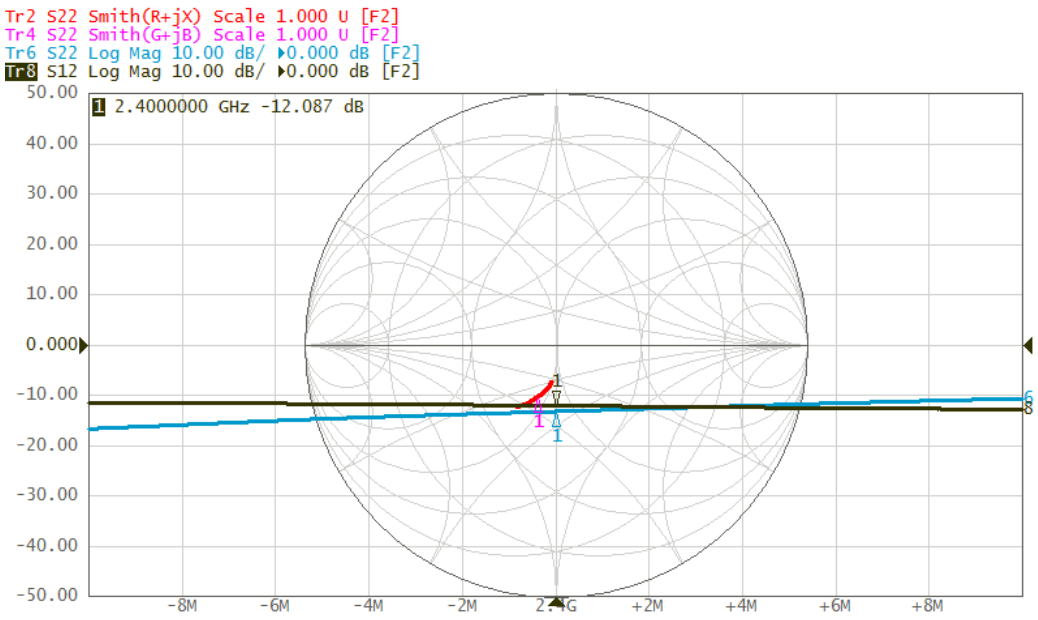

Figure 209. S22 and S12 parameters after the Second Modification

10 Appendix B – Embedding the First Design Approach in Concrete

Both test set ups for the TM couplers need to be embedded in concrete. To embed both test setups and concrete, both set ups were installed in 4 foot tall Sakrete cardboard tubes, which are made for molding concrete pillars. Due to the individual size of both test set ups, each Test Set up required a different diameter concrete tube.

For Experiments 10 and 11, the test apparatus first needed to be constructed so that concrete could be introduced into a mold. Second, the concrete needed to be prepared and then poured. The section first discusses the construction of the testing apparatus, and then discusses the preparation and pouring of the concrete.

10.1 Construction of the Testing Apparatus

For Experiment 2, a 12” x 48” Sakrete cardboard tube was employed as a concrete mold. Three holes were drilled into the Sakrete cardboard tube, as shown in Figure 210, so that cord grips could be installed for the SMA cables to have an entry point.

Figure 210. Hole drilled in the Sakrete cardboard tube for cord grip installation.

After the court grips were installed, the three TM couplers set up was inserted into the tube. The SMA cables were run through the court grips; the court grips were then tightened so that a seal would be formed around the SMA cable preventing any potential leakage. The bottom of the tube was then sealed with excessive packing tape wrapped around a separate piece of cardboard placed at the bottom of the tube (also seen in Figure 210). The Sakrete cardboard tube was then wrapped with orange plastic shrink-wrap sheeting, as shown in Figure 211; the purpose of this sheeting was to reinforce the structure and prevention of any leaks that may occur. Also shown in Figure 211, is a customized PVC jig employed to center the three TM coupler set up while concrete is poured and settles.

Figure 211. Sakrete cardboard tube with three TM coupler set up installed and shrink wrap sheeting applied

10.2 Preparation and Pouring the Concrete

Given that the Sakrete cardboard molding tube has a diameter of 12 inches and a height of 48 inches, applying a simple geometric formula for the volume of a cylinder, it is found that the volume is 3.14159 ft^3. To achieve the desired properties for the concrete in this project, the density ratios shown in Table 7 dictated how much of each material (in lbs) was required. The numbers in this table were driven by the requirement to have a water to cement ratio of 0.3.

Material	**lb/ft^3**
Water	12.4
Cement	31.0
Fine Aggregate	34.4
Coarse Aggregate	63.6

Table 7. Ratios desired for the concrete in this project

To find out how much of each material was required, the volume of the cylinder was multiplied by each density ratio. As shown in Table 8, for one 12" x 48" Sakrete cardboard tube, a total of 444.28 lbs of material was needed.

Material	**M_{1tube} (lbs)**
Water	38.96
Cement	97.45
Fine Aggregate	108.07
Coarse Aggregate	199.81
TOTAL	**444.28**

Table 8. Amount of mass (in lbs.) required for each material for Experiment 2

11 Appendix C – Pouring Concrete for the Second Design

The cylindrical concrete was poured on March 21, 2018. Overall, the process probably took about 4 hours, from set up to clean up. As can be seen in Figure 212, the top of the concrete was flattened smoothly. The same concrete material ratios were used as the ratios applied in Appendix B – Embedding the First Design Approach in Concrete.

Figure 212. Top of Concrete Pillar

The bottom of the concrete molding tube was secured with two layers of cardboard. Figure 213 shows the second layer of cardboard before the packing tape was applied.

Figure 213. Bottom of concrete molding tube before packing tape was applied to the second layer of cardboard

To help support the weight, some scrap wood was cut so that the rebar protruding from the bottom could slide through a slit. The weight of the pillar would be supported by the scrap wood piece, which was resting on two pallets. The cut scrap wood resting atop the two pallets can be seen in the image below. Overall, the process probably took about 4 hours, from set up to clean up. The set-up of the pallets allowed the rebar to rest some distance below the concrete molding tube, as shown Figure 214.

Figure 214. Cut scrap wood resting on top of two pallets with concrete molding tube and rebar visible with rebar extending to the ground

12 Appendix E – Improving the Rectifier Circuit

Two circuits are shown in this section: one circuit with just a series component for the matching element, and another component with a series and shunt component for the matching elements. The circuits are ideally matched at 50 Ω.

12.1 Rectifier with Series Capacitor with a 2.2kΩ Load

The previous best performance rectifier circuit before the final circuit was landed on is shown in Figure 215. Figure 216 through Figure 220 show graphs produced by the VNA.

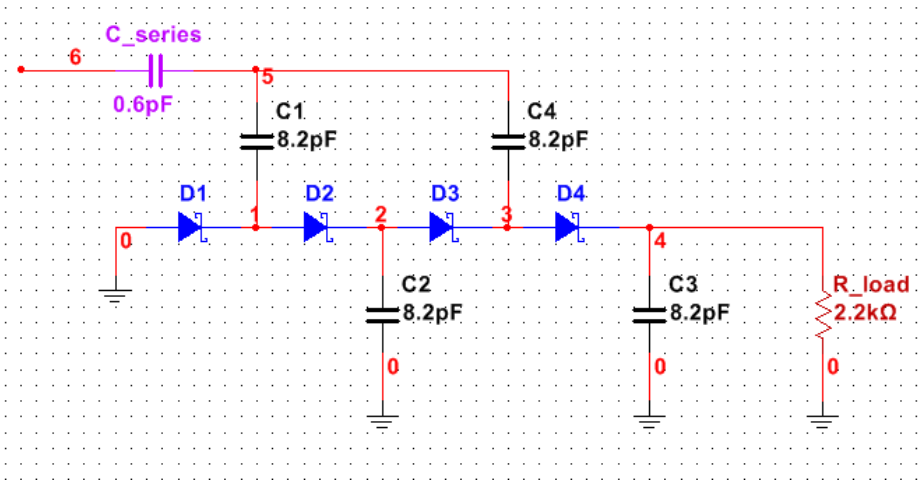

Figure 215. Rectifier Circuit with Series Capacitor as Matching Element

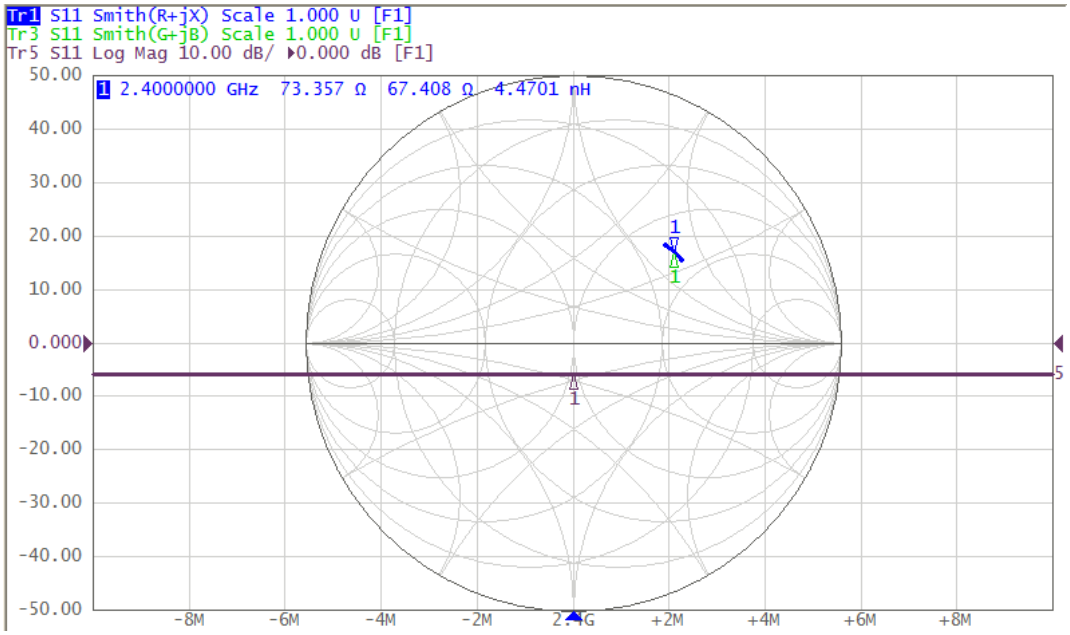

Figure 216. -15dBm Input Power into rectifier with Series Capacitor.

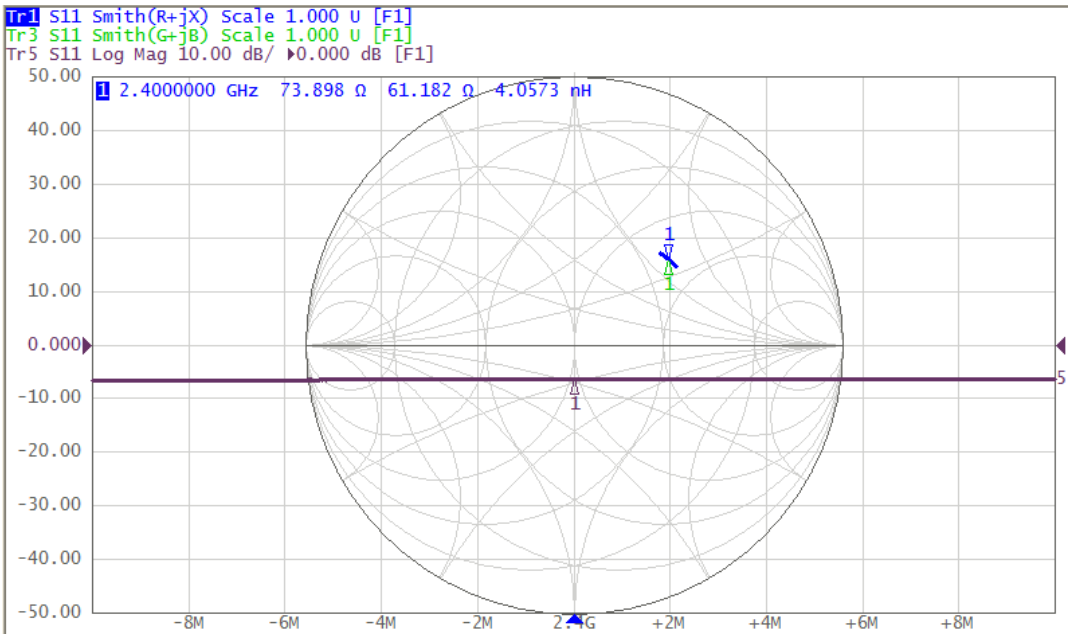

Figure 217. -10dBm Input Power into rectifier with Series Capacitor.

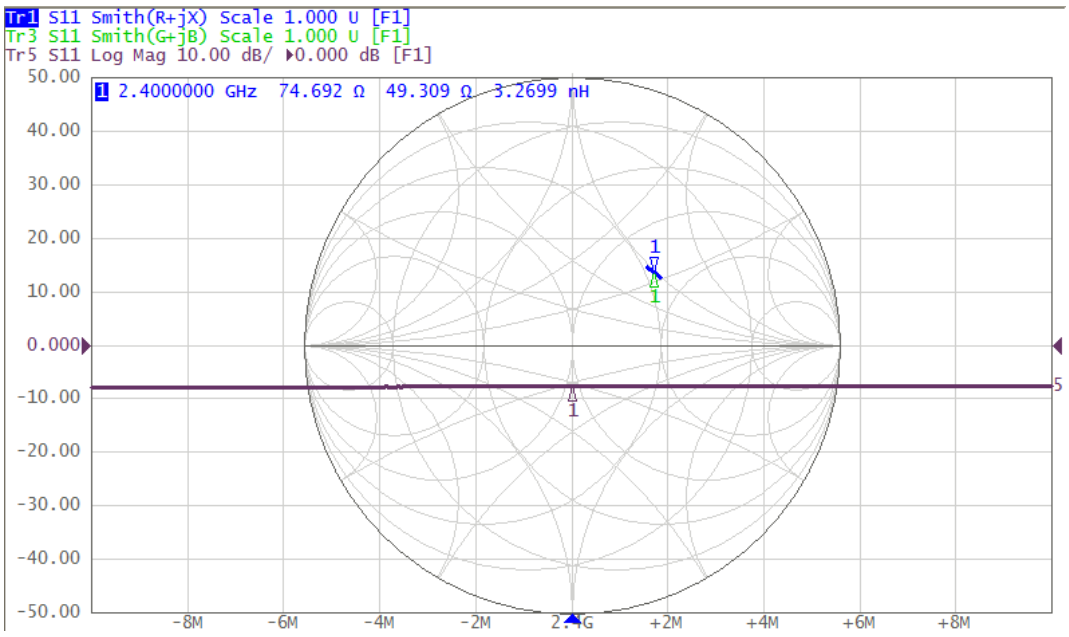

Figure 218. -5dBm Input Power into rectifier with Series Capacitor.

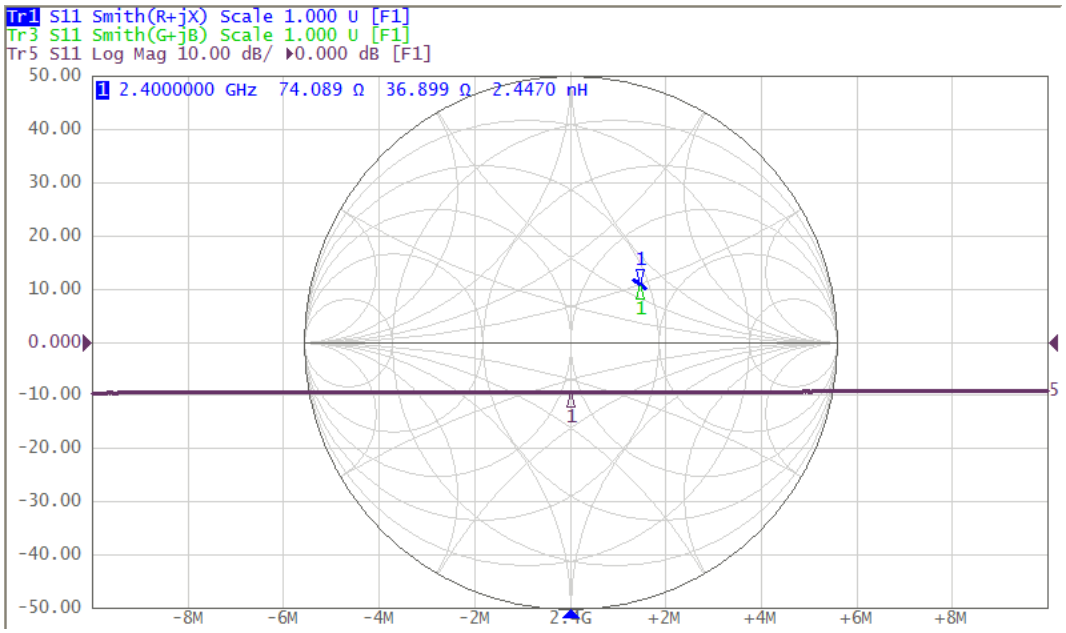

Figure 219. 0dBm Input Power into rectifier with Series Capacitor.

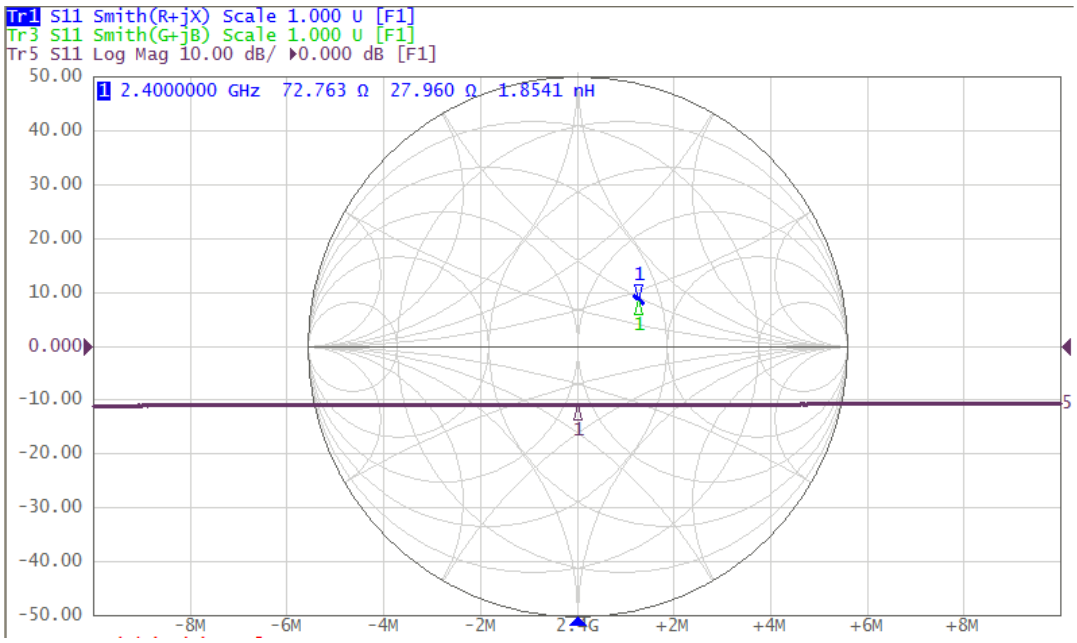

Figure 220. 5dBm Input Power into rectifier with Series Capacitor.

12.2 Series Capacitor and Shunt Capacitor with 2.2kΩ Load

Figure 221 shows a circuit diagram for the rectifier circuit that resulted in an improved performance. This circuit employed a 0.5pF shunt capacitor and a 0.6pF series capacitor.

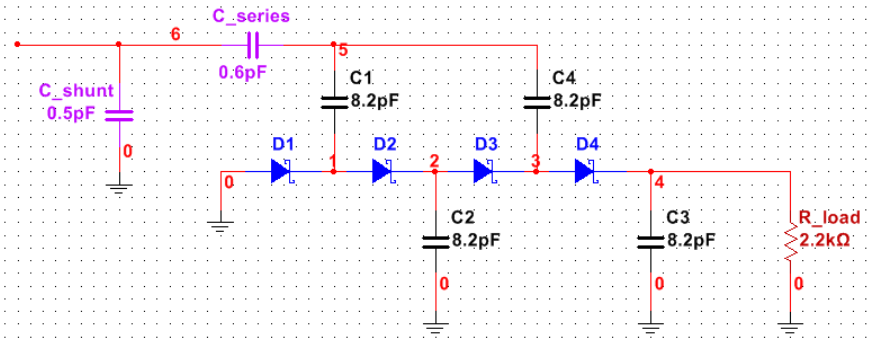

Figure 221. Rectifier Circuit with Series and Shunt Capacitor as Matching Elements

Figure 222 through Figure 226 display the smith charts for the result of this circuit connected to the VNA with the input power varying from figure to figure.

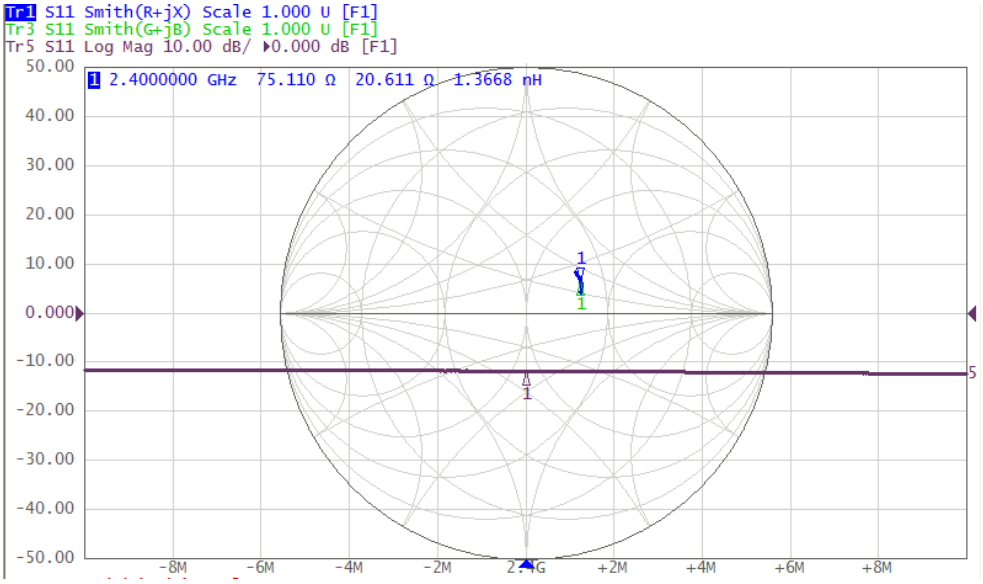

Figure 222. -15dBm Input Power into rectifier with Series and Shunt Capacitors

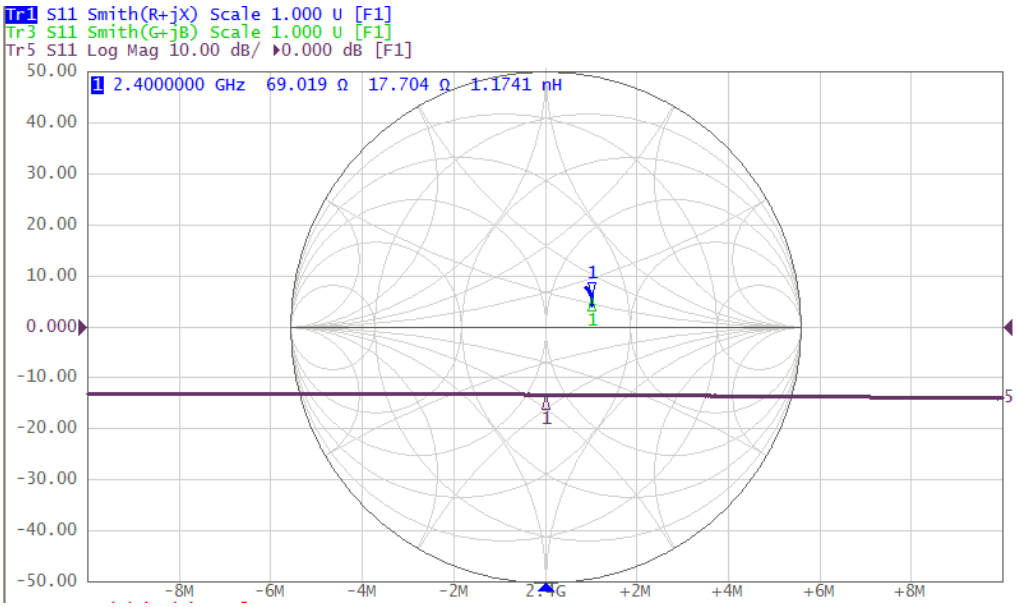

Figure 223. -10dBm Input Power into rectifier with Series and Shunt Capacitors

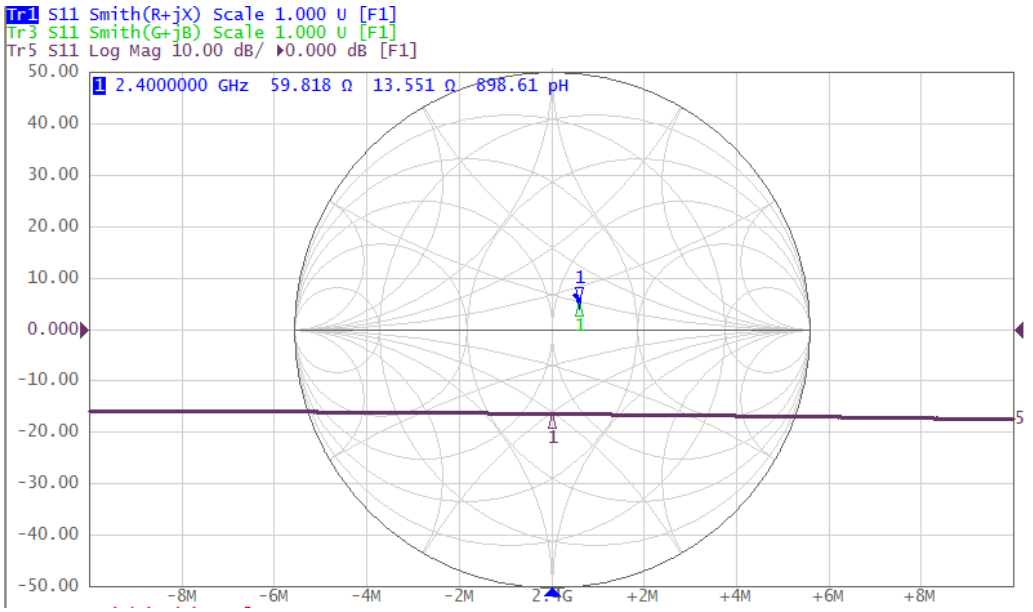

Figure 224. -5dBm Input Power into rectifier with Series and Shunt Capacitors

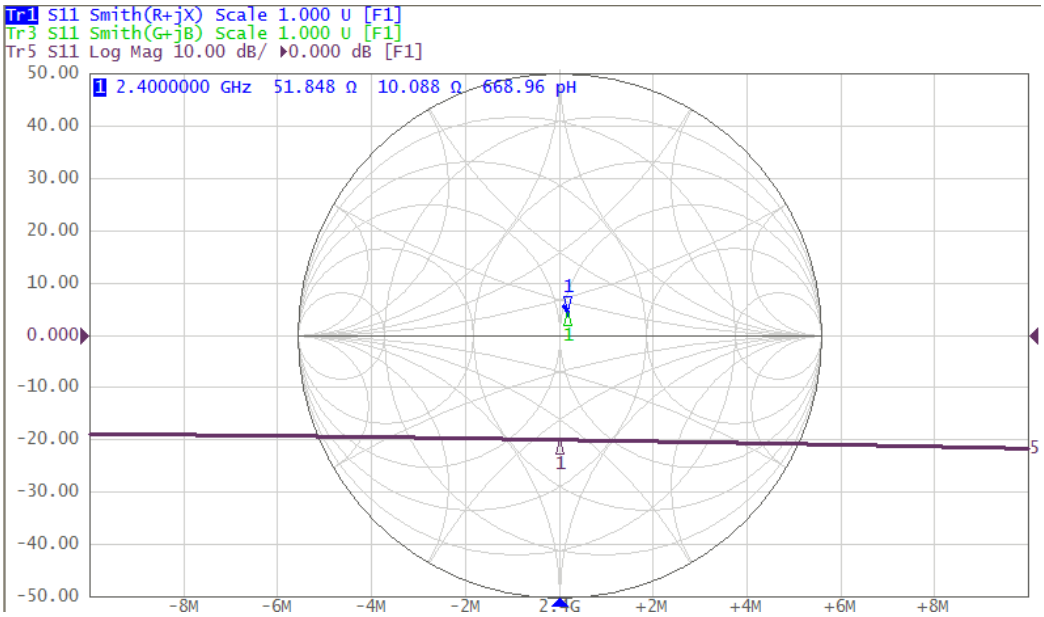

Figure 225. 0dBm Input Power into rectifier with Series and Shunt Capacitors

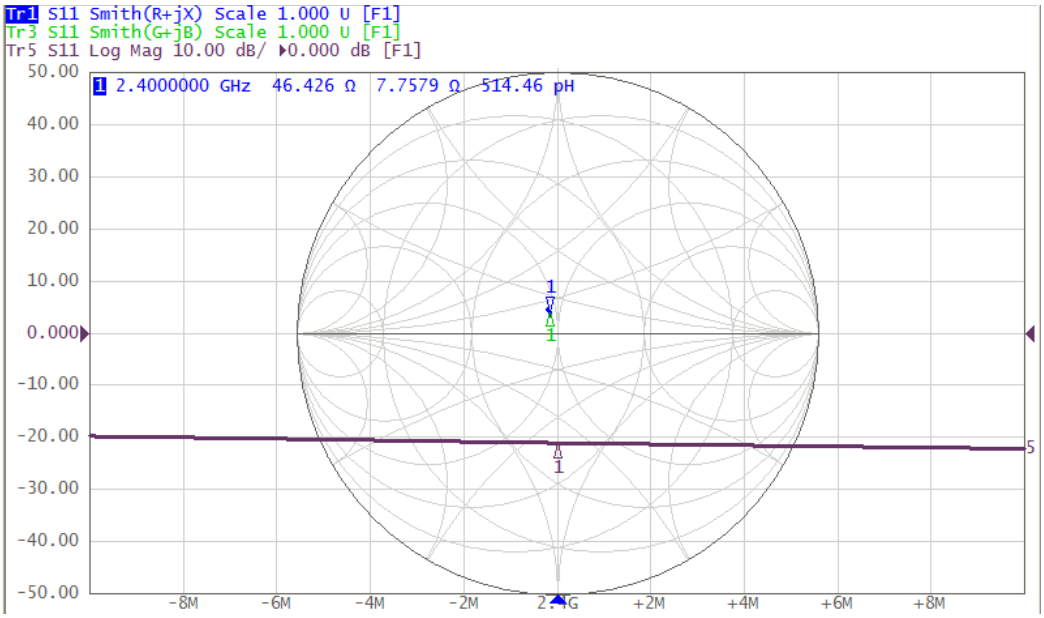

Figure 226. 5dBm Input Power into rectifier with Series and Shunt Capacitors

13 Appendix F – Simulating the Rectifier Circuit

Before fabricating the rectifier circuitry, the rectifier circuitry was simulated using NI Multisim. The original goal of this simulation was to find the value of the inductor that could eliminate the reactance from the rectifier circuitry. Hence, an inductor denoted L_match1 was applied in series to the circuit, as shown in Figure 227. Input impedance of 50 ohms was not used for the voltage source

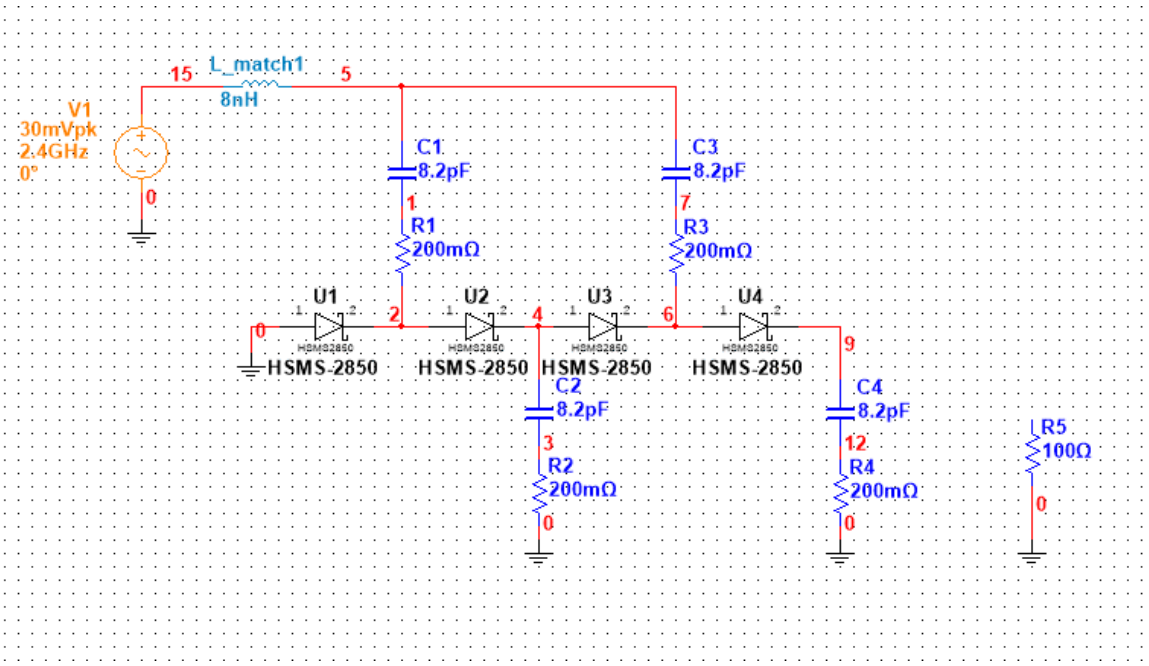

Figure 227. Screenshot of NI Multisim for the voltage rectification/multiplication circuitry

Two independent variables were applied to the circuit: load resistance and input voltage. By varying the input voltage, it was reasoned that the input power would be varied. By varying the load resistance, it was reasoned that the output power would be varied. At a given input voltage, the goal is to find the load resistance that would result in the maximum power efficiency. So for a given input voltage and load resistance the following parameters were calculated: input power, output power, power efficiency, output resistance, and the percentage of the load resistance with respect to the open circuit voltage, or $\%V_{out,OC}$.

The output resistance was calculated by monitoring the output voltage waveform and the output current waveform. By using the Grapher tool the phase difference between these two

waveforms and the amplitude of these two waveforms could be found to calculate what the output impedance was — provided that the load resistance was known. The output impedance was calculated using a voltage divider circuit as the model. Figure 228 shows a screenshot of the Grapher tool that was utilized to find the phase difference and amplitudes for the voltage and current waveforms. The Grapher tool was also utilized in the same manner at the input to understand which series matching inductor most closely aligned the voltage and current input waveforms, thus eliminating the reactance as intended.

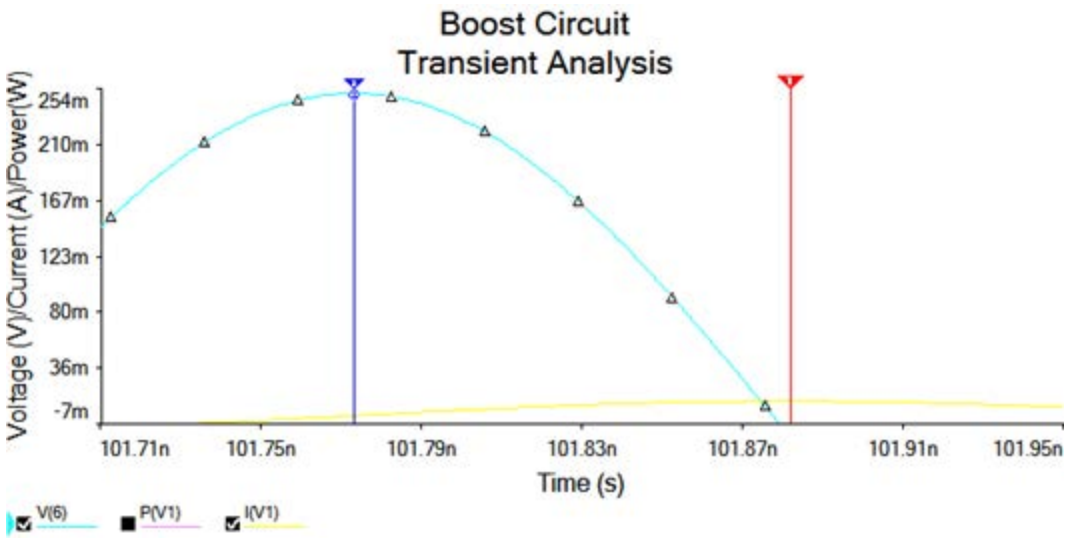

Figure 228. Utilizing the Grapher Tool to find the phase difference between the voltage and current as well as their amplitudes

Table 9 through Table 14 show the results of the simulations. Looking at these tables, it can be seen that for each voltage input column there is a single highlighted cell. The cell that is highlighted corresponds to the load resistance that yielded the maximum power efficiency for that particular input voltage. Table 12 is the origin of the highlighted cells, and for this reason the highlighted cells are formatted differently for this table than all of the others.

Load Resistance (Ω)	V_{in} (mV)	30	50	60	120	240	480	960
100	$V_{out,load}$ (mV)	1.53	3.49	4.90	12.00	26.00	56.00	119.00
400	$V_{out,load}$ (mV)	6.04	13.72	18.48	47.46	104.50	222.55	465.78
1600	$V_{out,load}$ (mV)	22.83	51.88	74.30	181.94	401.38	858.81	1812.00
3500	$V_{out,load}$ (mV)	39.54	105.82	142.87	370.87	837.10	1808.20	3790.20
4500	$V_{out,load}$ (mV)	48.97	132.23	179.23	472.19	1071.40	2289.00	4667.20
5500	$V_{out,load}$ (mV)	57.73	157.55	214.65	574.16	1301.00	2718.50	5353.50
6400	$V_{out,load}$ (mV)	77.14	179.70	268.00	690.06	1523.70	3073.20	5800.60
10240	$V_{out,load}$ (mV)	93.62	270.68	379.70	1052.00	2156.20	3902.70	6805.40
14080	$V_{out,load}$ (mV)	116.59	460.40	520.92	1367.80	2515.10	4260.60	7004.10
17920	$V_{out,load}$ (mV)	137.00	570.88	675.93	1585.60	2707.70	4443.70	7076.90
21760	$V_{out,load}$ (mV)	155.33	697.26	831.14	1729.80	2823.80	4535.40	7123.20
25600	$V_{out,load}$ (mV)	172.69	701.48	973.48	1832.80	2904.80	4592.10	7158.20
40000	$V_{out,load}$ (mV)	225.29	1074.40	1260.20	2008.30	3034.60	4687.50	7205.90
60000	$V_{out,load}$ (mV)	288.07	1271.50	1412.50	2102.50	3105.80	4747.90	7237.20
80000	$V_{out,load}$ (mV)	357.39	1352.70	1498.00	2154.90	3145.60	4784.30	7228.90
102400	$V_{out,load}$ (mV)	475.00	1400.30	1546.60	2190.80	3179.40	4819.30	7276.30
409600	$V_{out,load}$ (mV)	1138.20	1511.60	1643.30	2265.20	3251.40	4891.00	7304.10

Table 9. Voltage of the load with respect to the load resistance in the input voltage

Load Resistance (Ω)	V_{in} (mV)	30	50	60	120	240	480	960
100	P_{in} (μW)	10.27	22.80	31.20	87.00	267.00	951.00	4039.00
400	P_{in} (μW)	10.28	22.82	31.29	88.26	268.05	950.99	4039.00
1600	P_{in} (μW)	10.29	22.82	34.13	103.29	324.08	1050.00	4039.00
3500	P_{in} (μW)	9.77	24.44	35.40	128.58	444.74	1603.50	5918.40
4500	P_{in} (μW)	9.77	25.45	37.40	143.24	515.52	1872.80	6685.80
5500	P_{in} (μW)	9.77	26.46	39.43	158.49	583.41	2076.10	7029.00
6400	P_{in} (μW)	10.29	27.38	46.26	181.80	654.97	2214.40	7023.20
10240	P_{in} (μW)	9.77	31.56	50.24	231.38	762.30	2170.10	6100.60
14080	P_{in} (μW)	9.77	42.74	61.26	269.45	746.13	1891.30	5692.60
17920	P_{in} (μW)	9.77	50.69	74.75	281.19	687.22	1822.20	5551.90
21760	P_{in} (μW)	9.77	60.61	88.54	278.37	637.65	1791.60	5479.90
25600	P_{in} (μW)	9.77	60.91	100.04	269.18	624.13	1773.60	5441.60
40000	P_{in} (μW)	10.29	86.47	111.82	232.69	605.30	1741.60	5367.50
60000	P_{in} (μW)	11.58	88.72	105.81	224.63	596.77	1725.10	5330.30
80000	P_{in} (μW)	13.41	84.65	98.84	221.73	592.99	1717.50	5309.00
102400	P_{in} (μW)	17.77	80.18	92.25	220.04	590.62	1712.50	5180.40
409600	P_{in} (μW)	41.46	65.15	83.62	216.11	584.73	1700.10	5269.80

Table 10. Input power with respect to the load resistance in the input voltage

Load Resistance (Ω)	V_{in} (mV)	30	50	60	120	240	480	960
100	P_{out} (μW)	0.043	0.156	0.287	1.500	7.000	32.000	144.000
400	P_{out} (μW)	0.096	0.480	0.960	5.660	27.360	124.030	543.140
1600	P_{out} (μW)	0.327	1.687	3.450	20.720	100.850	461.690	2056.200
3500	P_{out} (μW)	0.448	3.207	5.845	39.384	200.642	936.157	4113.400
4500	P_{out} (μW)	0.534	3.894	7.157	49.682	255.811	1167.500	4852.900
5500	P_{out} (μW)	0.607	4.524	8.403	60.136	308.800	1347.900	5225.700
6400	P_{out} (μW)	0.933	5.060	11.310	74.770	364.510	1482.100	5276.600
10240	P_{out} (μW)	0.857	7.181	14.159	108.756	456.416	1493.500	4537.100
14080	P_{out} (μW)	0.970	11.898	19.429	133.919	451.868	1294.700	3494.900
17920	P_{out} (μW)	1.054	15.093	25.779	141.533	411.563	1106.500	2804.000
21760	P_{out} (μW)	1.117	19.181	32.191	138.767	368.621	949.265	2338.700
25600	P_{out} (μW)	1.173	19.363	37.499	132.196	331.180	826.454	2006.200
40000	P_{out} (μW)	1.284	29.173	40.460	101.794	231.580	551.559	1301.800
60000	P_{out} (μW)	1.407	27.249	33.897	74.373	161.711	377.220	875.411
80000	P_{out} (μW)	1.619	23.129	28.373	58.439	124.272	287.157	656.445
102400	P_{out} (μW)	2.250	19.367	23.554	47.062	98.971	227.275	517.881
409600	P_{out} (μW)	3.297	5.644	6.647	12.578	25.876	58.566	130.461

Table 11. Output power with respect to the load resistance in the input voltage

Load Resistance (Ω)	V_{in} (mV)	30	50	60	120	240	480	960
100	η	0.004	0.007	0.009	0.017	0.026	0.034	0.036
400	η	0.009	0.021	0.031	0.064	0.102	0.130	0.134
1600	η	0.032	0.074	0.101	0.201	0.311	0.440	0.509
3500	η	0.046	0.131	0.165	0.306	0.451	0.584	0.695
4500	η	0.055	0.153	0.191	0.347	0.496	0.623	0.726
5500	η	0.062	0.171	0.213	0.379	0.529	0.649	0.743
6400	η	0.091	0.185	0.244	0.411	0.557	0.669	0.751
10240	η	0.088	0.228	0.282	0.470	0.599	0.688	0.744
14080	η	0.099	0.278	0.317	0.497	0.606	0.685	0.614
17920	η	0.108	0.298	0.345	0.503	0.599	0.607	0.505
21760	η	0.114	0.316	0.364	0.498	0.578	0.530	0.427
25600	η	0.120	0.318	0.375	0.491	0.531	0.466	0.369
40000	η	0.125	0.337	0.362	0.437	0.383	0.317	0.243
60000	η	0.121	0.307	0.320	0.331	0.271	0.219	0.164
80000	η	0.121	0.273	0.287	0.264	0.210	0.167	0.124
102400	η	0.127	0.242	0.255	0.214	0.168	0.133	0.100
409600	η	0.080	0.087	0.079	0.058	0.044	0.034	0.025

Table 12. Power efficiency with respect to the load resistance in the input voltage

Load Resistance (Ω)	V_{in} (mV)	30	50	60	120	240	480	960
100	R_{out} (Ω)	75599.35	44149.64	32230.61	18200	12138.46	8533.929	6052.94118
400	R_{out} (Ω)	76301.99	44546.08	33890.04	18108.22	11779.9	8290.182	5887.9471
1600	R_{out} (Ω)	79570.39	45956.14	32514.67	17711.86	11084.24	7407.813	4865.34216
3500	R_{out} (Ω)	99027.2	47505.64	35308.51	17223.97	9804.276	5858.755	3261.38462
4500	R_{out} (Ω)	101941.3	47981.74	35275.24	16427.81	8864.756	5005.242	2559.69318
5500	R_{out} (Ω)	104845.7	48334.98	35092.18	15536.02	7951.96	4282.049	2022.36854
6400	R_{out} (Ω)	89691.26	48521.27	31431.64	13966.92	6965.361	3668.983	1678.61256
10240	R_{out} (Ω)	116442.8	48097.98	32483.35	11135.51	4871.622	2446.192	777.321539
14080	R_{out} (Ω)	125794.3	33081.15	28739.75	8525.41	3733.431	1898.219	639.058837
17920	R_{out} (Ω)	133580.7	30486.91	24079.52	6898.567	3138.995	1577.986	620.63785
21760	R_{out} (Ω)	140487.7	26365.91	19715.72	5864.558	2760.263	1437.425	607.295597
25600	R_{out} (Ω)	146094.5	30677.88	16060.52	5073.069	2442.963	1354.117	585.8009
40000	R_{out} (Ω)	165639.4	17412.51	10284.08	3738.485	1942.925	1258.667	644.471891
60000	R_{out} (Ω)	181235.5	12769.17	7293.451	2668.252	1472.084	1100.697	703.034323
80000	R_{out} (Ω)	179259.8	11201.3	4603.471	1525.825	925.7375	847.7729	1030.3089
102400	R_{out} (Ω)	147283.5	10369.44	2489.487	243.0528	83.73907	333.592	643.140057
409600	R_{out} (Ω)	7197.329	8264.62	-14730.9	-12512.9	-8742.77	-4689.76	1003.79787

Table 13. The rectifier's output resistance with respect to the load resistance in the input voltage

Load Resistance (Ω)	V_{in} (mV)	30	50	60	120	240	480	960
100	$\%V_{out,OC}$	0.001	0.002	0.003	0.005	0.008	0.012	0.016
400	$\%V_{out,OC}$	0.005	0.009	0.012	0.022	0.033	0.046	0.064
1600	$\%V_{out,OC}$	0.020	0.034	0.047	0.083	0.126	0.178	0.247
3500	$\%V_{out,OC}$	0.034	0.069	0.090	0.169	0.263	0.374	0.518
4500	$\%V_{out,OC}$	0.042	0.086	0.113	0.215	0.337	0.473	0.637
5500	$\%V_{out,OC}$	0.050	0.102	0.135	0.261	0.409	0.562	0.731
6400	$\%V_{out,OC}$	0.067	0.117	0.169	0.314	0.479	0.636	0.792
10240	$\%V_{out,OC}$	0.081	0.176	0.240	0.479	0.678	0.807	0.929
14080	$\%V_{out,OC}$	0.101	0.299	0.329	0.623	0.790	0.881	0.957
17920	$\%V_{out,OC}$	0.118	0.370	0.427	0.722	0.851	0.919	0.967
21760	$\%V_{out,OC}$	0.134	0.452	0.525	0.788	0.887	0.938	0.973
25600	$\%V_{out,OC}$	0.149	0.455	0.614	0.835	0.913	0.950	0.978
40000	$\%V_{out,OC}$	0.195	0.697	0.795	0.915	0.954	0.969	0.984
60000	$\%V_{out,OC}$	0.249	0.825	0.892	0.957	0.976	0.982	0.988
80000	$\%V_{out,OC}$	0.309	0.877	0.946	0.981	0.989	0.990	0.987
102400	$\%V_{out,OC}$	0.410	0.908	0.976	0.998	0.999	0.997	0.994
409600	$\%V_{out,OC}$	0.983	0.980	1.037	1.032	1.022	1.012	0.998

Table 14. Percentage of the output voltage referenced to the open circuit output voltage with respect to the load resistance in the input voltage

To visualize these results in another way, the power efficiency of the circuit was plotted with respect to the voltage input and load resistance, as can be seen in Figure 229. In this figure, it

can be seen that if maximum power efficiency is to be achieved, then as the input voltage is varied the load resistance should in turn vary so that the maximum of this topological graph is achieved.

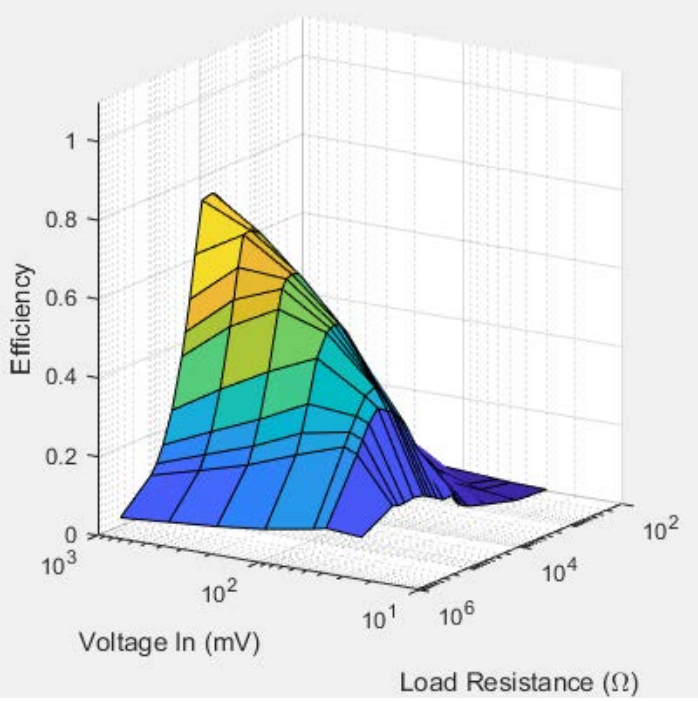

Figure 229. Power efficiency of the circuit with respect to the voltage input and load resistance.

14 Appendix G – Evaluating the performance of a Scaled Up Square Rebar Cage

A square rebar cage was constructed as shown in Figure 230. The length of the rebar legs were just over 4 feet. The length of the side of a square rung was 18 inches. With respect to the rebar cage, one leg was the positive terminal, while the other leg was the negative terminal.

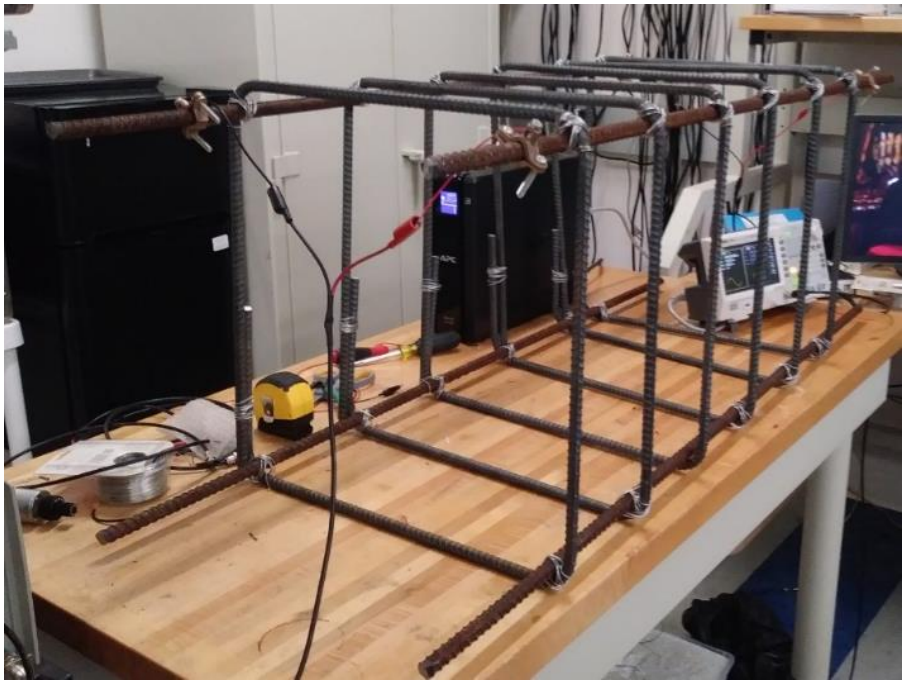

Figure 230. Square Rebar Cage with Grounding Clamps Connected to Legs

At one end of the rebar cage, the positive lead of a BNC-to-Alligator Clip coaxial cable was connected to one leg by clamping the alligator clip to a 16-AWG wire that was clamped onto the alligator clamp, while the negative lead of the BNC-to-Alligator Clip coaxial cable was connected to another leg in the same fashion. On the other end of the rebar cage, on the same respective legs a positive and negative connection was established with another BNC-to-Alligator Clip coaxial cable. One cable was connected to a Rigol Function Generator, while the other cable was connected to a spectrum analyzer.

14.1 Process and Results

With the leads on the very end of the cage, the input power from the function generator was set to its maximum at 23.98 dBm, while the output power read by the spectrum analyzer was measured at 5.86 dBm. This results in a power loss through the cage of 18.12 dB.

However, when the cage was jostled and shaken with the same input power of 23.98 dBm, the output power measured by the spectrum analyzer was measured at 12.56 dBm. This results in a power loss through the cage of 11.42 dB.

Afterwards, the grounding clamps connected to the spectrum analyzer were re-clamped to the section of the rebar legs where there were three rungs between it and the grounding clamps connected to the function generator. The input power was still set to 23.98 dBm, while the output power was measured at 4.07 dBm. This results in a power loss through the rebar cage of 19.91 dB.

14.2 Discussion

Given that power loss varied to precipitously and without clear explanation, it stands to reason that the rebar cage connection is not the most stable connection. Considering that the power loss through the cage could be affected so significantly just by jostling the cage during a measurement indicates that the rebar cage can be potentially very unreliable. Even when the grounding clamps were moved closer to the source of power, there was not an increase of power, but a drop in power.

15 Vita

For as long as he can remember, Ryan Campiz has quietly had a tangential interest in a variety of science and engineering topics. After high school, Ryan did not have a lot of direction other than academics, even though he was not the best high school student. After earning his Associates in Arts at Florida Stage College at Jacksonville, Ryan enrolled at the University of North Florida with a major in Philosophy. Eventually, his curiosity led him to independently study the field of Electrical Engineering — and after some trepidation, Ryan switched majors to Electrical Engineering. In the Spring term of 2016, Ryan Campiz graduated from the University of North Florida with his Bachelor of Science (B.Sc.) in Electrical Engineering. Many who knew him 10 years before that time would not have guessed that he would have ended up studying Electrical Engineering, even though the interest was always quietly there. Upon receiving his B.Sc. in Electrical Engineering, Ryan got the opportunity — and privilege — to study at the University of North Florida for his graduate degree. In doing so, Ryan has gained not only new knowledge, but also a little bit of wisdom in how to better conduct his thinking and properly investigate new ideas.

[THIS PAGE IS INTENTIONALLY LEFT BLANK.]